



Optimising Magnetostatic Assemblies

Insinga, Andrea Roberto; Bahl, Christian; Bjørk, Rasmus; Smith, Anders

Publication date:
2016

Document Version
Publisher's PDF, also known as Version of record

[Link back to DTU Orbit](#)

Citation (APA):

Insinga, A. R., Bahl, C., Bjørk, R., & Smith, A. (2016). Optimising Magnetostatic Assemblies. Department of Energy Conversion and Storage, Technical University of Denmark.

DTU Library

Technical Information Center of Denmark

General rights

Copyright and moral rights for the publications made accessible in the public portal are retained by the authors and/or other copyright owners and it is a condition of accessing publications that users recognise and abide by the legal requirements associated with these rights.

- Users may download and print one copy of any publication from the public portal for the purpose of private study or research.
- You may not further distribute the material or use it for any profit-making activity or commercial gain
- You may freely distribute the URL identifying the publication in the public portal

If you believe that this document breaches copyright please contact us providing details, and we will remove access to the work immediately and investigate your claim.

Optimising Magnetostatic Assemblies

Andrea Roberto Insinga

Department of Energy Conversion and Storage
Ph.D. Thesis, July 2016

Thermoelectrical Generators / Superconducting Components
High Temperature Polymer Electrolyte Membrane Fuel Cells

Energy Conversion

Colloidal Chemistry/Electrochemistry
Magnetism
Electrochemistry
Defect Chemistry

Polymer Solar Cells
Solid State Physics

Ceramic Membranes
Electron Microscopy

Solid Oxide Fuel Cells
Modeling / Heterostructures
Synthesis / Colloidal Chemistry / Solid State Physics / Computational Materials Science

Solid Oxide Electrolysis Cells
Computational Materials Design
X-Ray and Neutron Scattering

High Temperature Polymer Electrolyte Membrane Electrolysis Cells
Fuel Cells and Hydrogen Test Center

Shaping Processes / Defect Chemistry

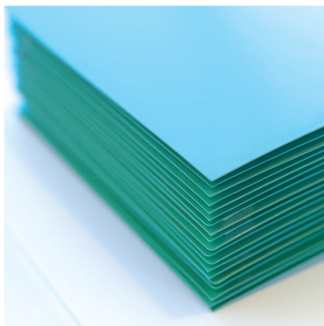
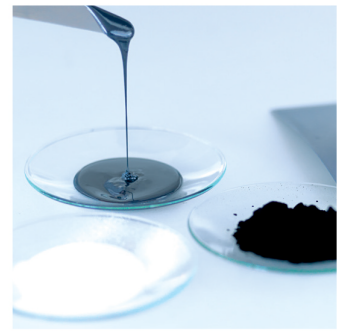
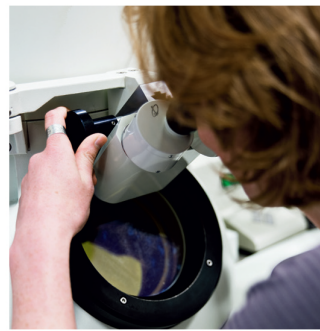
Electrochemical Flue Gas Purification
Batteries / Hydrogen Storage
Synthesis / Colloidal Chemistry / Heterostructures / X-Ray and Neutron Scattering

Magnetic Refrigeration

Energy Storage

Sintering

Synthetic Fuels
Magnetism
Synthesis
Modelling



Abstract

The aim of this thesis is to investigate a framework to design and optimise magnetostatic systems. Over the course of the last decades the range of applications of permanent magnets expanded considerably, thanks to the development of powerful rare-earth permanent magnets. Concurrently, the research on methods to optimise permanent magnet based magnetic systems intensified. The increase in computational power, and the emergence of new optimisation algorithms provided new instruments for the design of magnetic systems. All these factors contribute in making the optimisation of magnetic systems a very lively sector of modern research.

The main focus of this work are magnetic systems based on permanent magnets, although hybrid systems combining permanent magnets with electromagnets are also considered. Many optimisation approaches presented here are derived within a framework based on the reciprocity theorem. This theorem formulates an energy equivalence principle with several implications concerning the optimisation of objective functionals that are linear with respect to the magnetic field. Linear functionals represent different optimisation goals, e.g. maximising a certain component of the field averaged over a region of space. In general, a linear functional can be expressed as the integral over a given region of the scalar product between the magnetic field and an arbitrarily defined objective vector field. It has been known for some time that the reciprocity theorem can be used to determine the optimal remanence distribution with respect to a linear objective functional.

Additionally, it is shown here that the same formalism can be applied to the optimisation of the geometry of magnetic systems. Specifically, the border separating the permanent magnet from regions occupied by air or soft magnetic material can be optimised within this framework. Since in the practice most structures are realized by assembling uniformly magnetized pieces of permanent magnet, it is relevant to address the question of how a given region of space is best subdivided. This problem is investigated here within the framework of the reciprocity theorem. Analytical derivations will be used to show that, for segmentations controlled by a single parameter, the globally optimal solution to this problem can be determined for almost arbitrary geometries. The case of segmentations depending by two parameters has been approached employing a heuristic algorithm, which led to new design concepts. Some of the procedures developed for linear objective functionals have been extended to non-linear objectives, by employing iterative techniques.

Even though most the optimality results discussed in this work have been derived analytically, the different approaches have been implemented in combination with finite element methods, resulting in flexible and computationally efficient algorithms. Most of the optimisation approaches could only be proven under the assumption of linear magnetic behavior. The last part of this thesis also investigates some of the effects on the performance of magnetic systems, due to non-linear magnetic phenomena. In particular, the non-linear demagnetization effects caused by the finite coercivity of the permanent magnet material will be examined.

All the optimisation techniques will be illustrated with example magnetic systems for different applications, thus showing the versatility and efficacy of the various approaches. The Halbach cylinder geometry, relevant for many applications, will be often used as example, also because of the many symmetries and optimality properties exhibited by this geometry. Despite

the fact that this system has already been subject of many publications, some of the aspects considered in this thesis have not been investigated before. The ultimate goal of the PhD project is to apply the optimisation techniques developed during this research to the design of the magnetic system for the prototype of heat pump based on the magnetocaloric effect. Magnetic systems for room temperature magnetic refrigeration will thus frequently be used as illustrative examples along the course of this thesis.

Primarily because of the theoretical relevance of linear functionals, the results presented here lead to a deeper understanding of the magnet optimisation process. One of the perspectives considered in this work is the trade-off between field intensity and field quality, as the choice of a particular optimisation approach may favour one or the other. The general framework discussed here provides a set of useful tools aiding the magnet design process. This research also opened new scientific questions which would be worth investigating in future studies.

Resumé (Danish)

Målet med denne afhandling er at undersøge rammerne for design og optimering af magnetostatiske systemer. I løbet af de sidste årtier er anvendelsesmulighederne for permanente magneter udvidet betydeligt takket være udviklingen af stærke sjælden-jordarts permanente magneter. Samtidig er forskningen i metoder til at optimere permanent magnet-systemer intensiveret. Væksten i computerkraft, samt udviklingen af nye optimeringsalgoritmer har givet nye muligheder for designet af magnetiske systemer. Alle disse faktorer bidrager til at gøre optimeringen af magnetsystemer til en livlig aktivitet i moderne forskning.

Hovedfokus i dette arbejde er magnetsystemer baseret på permanente magneter, men hybridsystemer hvor permanente magneter kombineres med elektromagneter betragtes også. Mange af optimeringstilgangene præsenteret her er afledt i rammen af reciprocitetsteoremet. Dette teorem formulerer et energiækvivalensprincip med adskillige implikationer for optimeringen af objekt-funktioner, som er lineære med hensyn til magnetfeltet. Lineære objekt-funktioner repræsenterer forskellige mål for optimeringen, fx maksimering af en bestemt komponent af feltet, midlet over et volumen. Generelt, kan en lineær objekt-funktion udtrykkes som skalarproduktet af magnet feltet med et arbitrært defineret objekt vektorfelt integreret over en given region. Det har været kendt i nogen tid at reciprocitetsteoremet kan benyttes til at finde den optimale remanensfordeling med hensyn til en lineær objekt-funktion.

Derudover vises det her at den same formalisme kan anvendes til optimering af geometrien af magnetiske systemer. Specifikt kan grænsen der adskiller regioner med permanent magnet fra regioner med luft eller blødt magnetisk materiale optimeres. Idet de fleste magnetstrukturer realiseres ved at samle blokke af uniformt magnetiseret magnetmateriale er det relevant at undersøge hvordan et område bedst opdeles i blokke. Dette problem undersøges her i rammerne af reciprocitetsteoremet. Analytiske udledninger bruges til at vise at for segmenteringer afhængig af en enkelt parameter kan den globalt optimale løsning findes for næsten vilkårlige geometrier. Det tilfælde hvor segmenteringen afhænger af to parametre gribes an med en heuristisk algoritme, hvilket fører til nye designkoncepter. Nogle af procedurerne som er udviklet til lineære objekt-funktioner er blevet udvidet til ikke-lineære objekt-funktioner, ved at bruge en iterativ teknik.

Selvom de fleste optimerings resultater der diskuteres i dette arbejde er afledt analytisk er de forskellige tilgange implementeret i kombination med finite element metoder hvilket resulterer i fleksible og beregningsmæssigt effektive algoritmer. De fleste af optimeringstilgangene kunne kun bevises under antagelse af magneter med en lineær opførsel. I den sidste del af denne afhandling undersøges nogle af de effekter på ydelsen fra et magnetsystem, som skyldes ikke en ikke-lineær opførsel af magnet materialet. Specifikt undersøges den ikke-lineære demagnetisering der skyldes den endelige koercivitet i virkelige magnet materialer.

Alle optimerings teknikker illustreres med eksempler på magnetsystemer fra forskellige anvendelser, for således at vise alsidigheden og effektiviteten af de forskellige tilgange. Halbach-cylinderen, som er relevant for mange anvendelser, benyttes ofte som et eksempel på grund af de mange symmetrier og optimalitets egenskaber af denne geometri. Selvom dette system allerede har været belyst i mange publikationer indeholder denne afhandling aspekter der ikke er belyst før. Det ultimative mål for dette ph.d. projekt er at anvende de udviklede optimerings teknikker til at designe et magnetsystem til en varmepumpe prototype baseret på den

magnetokaloriske effekt. Således vil magnetsystemer fra stue temperatur magnetisk køling ofte anvendes som illustrative eksempler i denne afhandling.

Primært på grund af den teoretiske relevans af lineære objekt-funktioner fører resultaterne præsenteret her til en dybere forståelse af magnetsystem optimerings processen. Et af de perspektiver der betragtes her er afvejningen imellem feltstyrke og kvaliteten af feltet, idet valget af en optimerings tilgang kan favorisere enten den ene eller den anden. De generelle ideer der diskuteres her giver et set nyttige værktøjer der hjælper magnet designprocessen. Denne forskning har også åbnet op for ny videnskabelige spørgsmål som vil kunne belyses i fremtidige studier.

Acknowledgements

I would like to start by thanking my family. Besides supporting me and encouraging me over the course of the years, they thought me the importance of being curious and passionate about what one does.

I would like to express my deepest gratitude to my PhD supervisors Christian Bahl, Rasmus Bjørk and Anders Smith. They have always been ready to help me, and they constantly motivated me to pursue new ideas. Not only they have been wonderful people to work with, but it has been a real pleasure to share with them many personal experiences, travels, and dinners. I simply cannot imagine better supervisors than them, and I truly admire them, as scientists and as persons.

I had the good luck of meeting Henrique Neves Bez, a great person, and a true friend. We started the PhD around the same time, we have been officemate and flatmates. I learned many things from him, and we shared numberless stimulating conversations, life experiences, and everyday events. He helped me in many occasions during the course of the work, and more importantly, this whole experience would not have been the same without him, and I will always be grateful.

I would like to thank my MSc supervisor, Bjarne Andresen. It is with him that I moved my first steps as scientist, and I will always look up to him, and consider him a friend.

My gratitude goes to all the members of the Electrofunctional Materials section, and guest students. All of them contributed in creating a stimulating and friendly environment. Everyone has always been generously available to help me, and I had the pleasure of working with many nice and brilliant researchers. A special thank goes to the ones with whom I share most time during travels, lunches, meetings and other occasions: Nini Pryds, Kaspar Nielsen, Kurt Engelbrecht, Dan Eriksen, Stefano Dallolio, Jaka Tusek, Stefano Soprani, Tian Lei, Barbara Torregrosa and Urban Tomc. A big thank you goes also to the section secretary Anita Voss, a very nice person who has helped me many times.

This work was financed by the ENOVHEAT project which is funded by Innovation Fund Denmark (contract no 12-132673).

List of publications

Papers in peer-reviewed journals

D. Eriksen, K. Engelbrecht, C. R. H. Bahl, R. Bjørk, K. K. Nielsen, A. R. Insinga and N. Pryds, *Design and experimental tests of a rotary active magnetic regenerator prototype*, International Journal of Refrigeration **58**, 14-21, (2015). Attached in section [B.1](#).

A. R. Insinga, C. R. H. Bahl, R. Bjørk and A. Smith, *Performance of Halbach magnet arrays with finite coercivity*, Journal of Magnetism and Magnetic Materials **407**, 369-376, (2016). Attached in section [B.2](#).

A. R. Insinga, R. Bjørk, A. Smith and C. R. H. Bahl, *Globally Optimal Segmentation of Permanent-Magnet Systems*, Physical Review Applied **5**, (6), 064014, 1-16, (2016). Attached in section [B.3](#).

A. R. Insinga, R. Bjørk, A. Smith and C. R. H. Bahl, *Optimally segmented permanent magnet structures*, accepted for publication in IEEE Transactions on Magnetics, (2016). Attached in section [B.4](#).

R. Bjørk, C. R. H. Bahl and A. R. Insinga, *Topology optimized permanent magnet systems*, submitted for publication in IEEE Transactions on Magnetics, (2016). Attached in section [B.5](#).

Conference proceedings

A. R. Insinga, A. Smith, C. R. H. Bahl and R. Bjørk, *Performance-oriented analysis of a hybrid magnetic assembly for a heat-pump magnetocaloric device*, 6th IIF-IIR International Conference on Magnetic Refrigeration at Room Temperature, Thermag VI, Victoria, Canada, (2014). Attached in section [B.6](#).

A. R. Insinga, R. Bjørk, A. Smith and C. R. H. Bahl, *Optimization of Hybrid Magnetic Systems*, AIM 2016 - Advances In Magnetics Conference, Bormio, Italy, (2016). Attached in section [B.7](#).

R. Bjørk, A. R. Insinga, A. Smith and C. R. H. Bahl, *Generating the optimal magnetic field for magnetic refrigeration*, 7th IIF-IIR International Conference on Magnetic Refrigeration at Room Temperature, Thermag VII, Turin, Italy, (2016). Attached in section [B.8](#).

Contents

Abstract	iii
Resumé (Danish)	v
Acknowledgements	vii
List of publications	ix
0 Notations and units	xv
0.1 Units	xv
0.2 Notation	xv
0.3 Notation used in the figures	xvi
1 Introduction	1
1.1 Background	1
1.1.1 Rare earth permanent magnets and applications	1
1.1.2 Magnet optimisation approaches	3
1.2 Scope of this work	5
2 Framework	7
2.1 Fundamental equations	7
2.2 Materials	8
2.2.1 Non magnetic materials	9
2.2.2 Permanent magnets	9
2.2.3 Soft magnetic materials	13
2.2.4 Insulators	14
3 Magnetic Circuit Model	15
3.1 Introduction	15
3.2 Single-Loop magnetic circuit	18
3.3 Application to magnetocaloric heat pump	20
3.4 Flux leakage	24
3.5 Cogging torque minimization	27
3.6 Boundaries and surface current	30
4 Magnet design and optimisation	33
4.1 Magneto-static equations	33
4.1.1 Scalar potential formulation	34
4.1.2 Vector potential formulation	34
4.1.3 Boundary Conditions	35
4.2 Solving the equations	36
4.2.1 Formal solution	36
4.2.2 Analytically solvable geometries - Halbach cylinders	38

4.2.3	Finite Element Method	40
4.2.4	Validation	43
4.3	Theorems	46
4.3.1	Remanence Reciprocity theorem	46
4.3.2	Current reciprocity theorem	47
4.4	Objectives	48
4.4.1	Linear Objectives	48
4.4.2	Magnetic Inverse problem	50
5	Flux Sources Optimization	53
5.1	Pre-segmented systems	53
5.1.1	Permanent magnet systems	53
5.1.2	Hybrid systems	56
5.1.3	Linear Objectives	58
5.1.4	Illustrative examples	59
5.1.5	Cylinders segmentations	60
5.2	Continuously varying remanence field	64
5.2.1	Abele's approach	64
5.2.2	The virtual magnet method	68
5.2.3	Energy considerations	70
5.2.4	Non-Linear Objectives	71
6	Geometry Optimization	75
6.1	Air-magnet border	75
6.2	Iron-magnet border	78
6.2.1	Yoked Halbach cylinders	80
6.2.2	Multipoles pole-pieces	82
6.2.3	Three dimensional designs	84
6.3	Optimal Segmentation	85
6.3.1	Segment-segment border	85
6.3.2	Segment-segment border - three dimensional case	89
6.3.3	General coordinate transformation	90
6.3.4	Two-parameters segmentation	91
6.3.5	One-parameter segmentation	96
6.3.6	Invertibility issues and starting point	100
6.4	Examples	102
6.4.1	Halbach cylinder	102
6.4.2	Rectangular Cavity	104
6.4.3	Quadrupole magnet for beam focusing	105
6.4.4	Comparison with uniform field magnets	106
6.4.5	Electric Motor	109
6.4.6	Magnetic refrigeration 1	110
6.4.7	Magnetic refrigeration 2	111

7 Non Linear effects	115
7.1 Finite Coercivity	115
7.1.1 Halbach cylinder	116
7.1.2 Magnetic refrigeration	123
7.2 Iron Saturation	124
8 Conclusions	127
8.1 Discussion of the results	127
8.2 Outlook	130
A Appendices	133
A.1 Segmentations of the ENOVHEAT prototype	133
A.2 Final design	138
B Published or submitted papers	145
B.1 Design and experimental tests of a rotary active magnetic regenerator prototype	146
B.2 Performance of Halbach magnet arrays with finite coercivity	155
B.3 Globally Optimal Segmentation of Permanent-Magnet Systems	164
B.4 Optimally segmented permanent magnet structures	181
B.5 Topology optimized permanent magnet systems	189
B.6 Performance-oriented analysis of a hybrid magnetic assembly for a heat-pump magnetocaloric device	200
B.7 Optimization of Hybrid Magnetic Systems	203
B.8 Generating the optimal magnetic field for magnetic refrigeration	206
Bibliography	211

Notations and units

0.1 Units

In thesis it is adopted the International System of Units. In particular, the magnetic flux density \mathbf{B} will be expressed in teslas (symbol T), and the magnetic field \mathbf{H} and magnetization \mathbf{M} will be expressed in ampere over meters (symbol A/m). However, it will be often more convenient to consider the product of \mathbf{H} with the vacuum permeability μ_0 . This product can be expressed in teslas, and similarly for $\mu_0\mathbf{M}$. Many of the results will be presented in terms of adimensional relative quantities.

0.2 Notation

This section briefly introduces the mathematical notation used in this work.

Vectors, and vector fields:

$$\mathbf{H} \tag{1}$$

Norm of vector:

$$H = \|\mathbf{H}\| \tag{2}$$

Normalized vectors:

$$\hat{\mathbf{H}} = \frac{\mathbf{H}}{H} \tag{3}$$

Rank-2 tensors, and tensor fields:

$$\underline{\underline{\mu}} \tag{4}$$

Cartesian coordinates

$$x, y, z \tag{5}$$

Cartesian coordinates unit vectors:

$$\hat{\mathbf{e}}_x, \hat{\mathbf{e}}_y, \hat{\mathbf{e}}_z \tag{6}$$

Cylindrical coordinates:

$$\rho, \phi, z \tag{7}$$

Cylindrical coordinates unit vectors:

$$\hat{\mathbf{e}}_\rho, \hat{\mathbf{e}}_\phi, \hat{\mathbf{e}}_z \tag{8}$$

Functionals having a scalar or vector field as input argument and a real number as output:

$$\mathcal{S}[\mathbf{H}] \tag{9}$$

Operators having a scalar or vector field as input argument and output.

$$\mathbf{F}[\mathbf{H}] \tag{10}$$

0.3 Notation used in the figures

Figure 1 has the purpose of illustrating the notation used in many of the figures presented in this thesis. Both the panels represent two dimensional systems. Two dimensional geometries will be described in Cartesian coordinates x and y , or in polar coordinates ρ and ϕ . The coordinate z indicates the direction going out of the plane. Figure 1a represents a square magnet delimited by the thick black lines. The remanent flux density vector, introduced in section 2.2.2, is indicated by the black arrow. The filed lines of the magnetic flux density are represented as thin black lines. The colour of the background indicates the norm of the flux density according to the colour-scale shown on the bottom of the figure: white corresponds to zero, and the darker shades correspond to higher values of the norm. Figure 1b shows a pair of two dimensional electromagnets with circular cross section, delimited by the black thick lines. For two-dimensional systems, the only relevant component of the current density is the z component. The value of the z component is indicated by the colour scale shown on the bottom of the figure. The shades of red indicate the direction pointing out of the plane, while the shades of blue indicate the direction pointing into the plane. The colour grey corresponds to zero current density.

This notation will be employed for many figures shown in this thesis, usually representing results of Finite Element Methods (FEM), calculations.

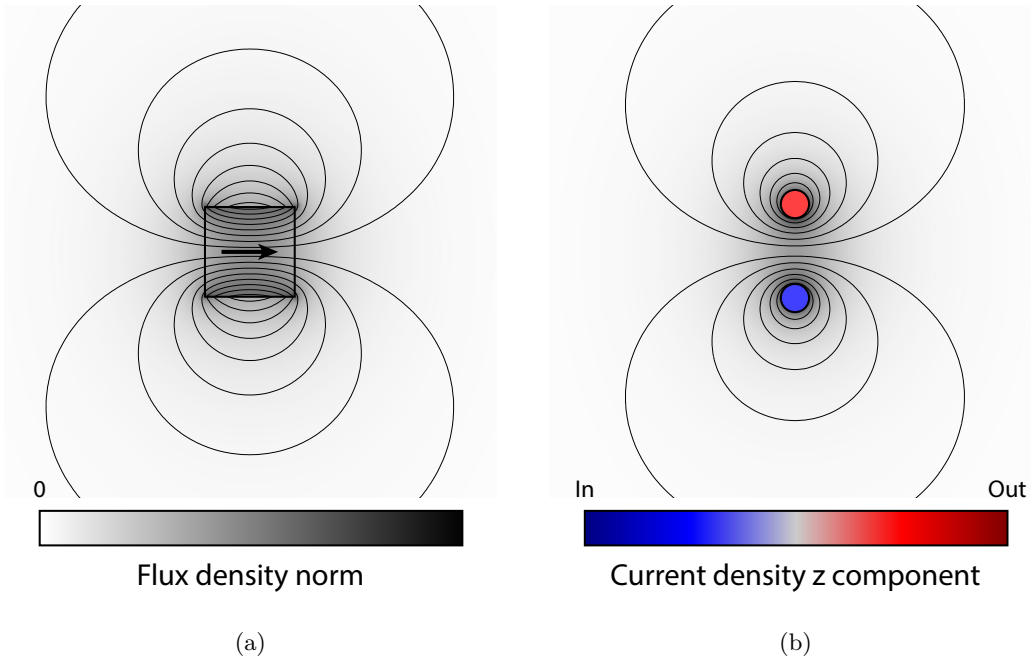


Fig. 1: Illustration of the notation which is going to be used to illustrate the magnetic structures presented in this work.

Optimising Magnetostatic Assemblies

Andrea Roberto Insinga

July 31, 2016

Introduction

Magnetic systems play a crucial role in many important scientific and technological applications. Optimising these systems is always important, especially for energy conversion systems, where achieving a high efficiency is crucial, and for emerging or developing technologies, such as magnetic levitation or magnetic refrigeration.

The purpose of this thesis is to study a general framework for the optimisation of magneto-static systems. While the field of design and optimisation of magnetic systems has been subject of intense scientific investigation over the course of the years, the shifting technological landscape keep introducing new questions and provides new possibilities, thus creating the necessity for new research. In particular, the range of applications of permanent magnet flux sources has been constantly broadening during the last decades, as new powerful magnetic materials have been developed. This thesis addresses permanent magnet based systems or hybrid systems including permanent magnets combined with electro magnets.

Rather than focusing on the optimisation of a specific magnetic system, the perspective adopted in this work is to derive general results and illustrate the resulting optimisation approaches using example magnetic systems from applications in different fields, although with a special focus on magnetic refrigeration.

1.1 Background

1.1.1 Rare earth permanent magnets and applications

Before the discovery of rare earth based permanent magnets revolutionized the sector in the 1970s, ferrites and Ni-Co based alloys were among the most frequently used permanent magnet materials [3]. The study of rare earth based compounds led to the development of modern permanent magnet materials, such as Sm-Co magnets and Nd-Fe-B magnets [3, 2, 1]. Besides having a larger remanent flux density than previously known magnets, these materials greatly surpass their predecessors for what concerns anisotropy field, coercivity, energy product and temperature stability [1]. All together this set of qualities unlocked the use of permanent magnets for applications which were previously unfeasible [4]. Dysprosium is another rare-earth element which is important for the magnet industry since its addition to the composition of Nd-Fe-B magnets can increase its coercivity and temperature stability [1, 17].

The design of magnetic systems exploiting these new possibilities has been subject of intense research during the last decades. As it is stressed in [28], a grand part of the electrical energy is produced with and consumed by rotary devices performing electromechanical energy conversion. For their ability of generating magnetic fields at no energy-cost, permanent magnets are crucial for the development of a sustainable and efficient energy system [67]. Because of the precision and stability of the fields, magnetic actuators [29, 71], magnetic gears [23, 20, 73, 23], and

magnetic bearings [21, 22] realized with permanent magnets are also reaching many other industrial applications, especially with the ongoing advancements in the fields of automation and robotics. Nuclear magnetic resonance is applied in many scientific techniques, most notably for medical imaging, and the usage of permanent magnets for this application has been considered by different scientific publications [31, 32]. In the field of beam physics permanent magnets are being used for beam focusing [35, 37] because of their ability to efficiently deliver stable and precise multipole fields, and are also present inside insertion devices such as wigglers and undulators [36].

Among the emerging technologies employing permanent magnets, room temperature magnetic refrigeration is particularly relevant with respect to this thesis. The PhD project has been in fact carried out within the magnetic refrigeration research group of the Technical University of Denmark, with the ultimate goal of designing the magnetic system for the prototype of a heat pump based on the magnetocaloric effect¹. Refrigerators and heat pumps exploiting the magnetocaloric effect are being investigated as alternatives to conventional devices based on vapour-compression thermodynamic cycles [98]. The main motivation behind this research is the attempt of reducing the negative impact on the environment associated with greenhouse gases and ozone-depleting gases frequently used as refrigerants in conventional devices [27, 26]. Currently, the challenge is to achieve the same levels of performance reached by vapour-compression refrigeration [99, 103]. It is worth mentioning that the magnetocaloric materials, i.e. the materials exhibiting the magnetocaloric effect, are frequently rare earth compounds as well [100].

Achieving sustainability is certainly the most important objective that modern society should confront. As mentioned above, rare-earth materials became crucial for clean energy applications. It is therefore important to consider some strategic issues with the production and availability of these materials. Particularly after 2011, the price of rare earth materials has been subject to sharp fluctuations [17]. The global production of these materials is vastly dominated by the Chinese output, which is limited by export quotas. This situation raises concerns over the supply risk associated with these materials. It is essential to consider also the ecological footprint associated with mining and processing rare earth elements, as many of the industrial processes involved have a negative effect on the environment [19].

Because of these reasons, the newest trend of the research is also to investigate strategies to diversify the supply and to limit the use of the most critical materials, such as Neodymium and Dysprosium [19]. Among the possibilities being explored, research on recycling end-of-life rare earth magnets is currently ongoing [14, 15, 16]. It is also being studied the possibility of replacing the use of these materials with alternatives which are not interested by the same issues [18].

The field of design and optimisation of magnetic systems is also affected by this relatively new trend. One of the priorities is to minimise the amount of permanent magnet used in a given magnetic system. Another challenge is to design the magnetic systems such that they can be realized with rare-earth free [69] or recycled [68] permanent magnet materials, which are generally less versatile.

¹The PhD project is in fact a work package of the ENOVHEAT project ([link to the project website](#)), which involves a collaboration between DTU and other universities and companies.

1.1.2 Magnet optimisation approaches

The field of magnet design and optimisation has been subject of important innovations over the course of the last decades.

The computational power available for scientific computations has been steadily improving, thus expanding the range of application of numerical approaches, such as finite element methods, to more complex physical systems. The main advantage of numerical techniques over analytical approaches is in fact the capacity to predict the behaviour of systems characterized by complex geometries, interplay between different physical processes, and non-linear phenomena. Starting from the 1960s different numerical simulation programs were developed and became available as open source or commercial packages. The availability of these computational tools is one of the factors that simplified the implementation of optimisation algorithms for design problems.

Another significant break-through came from the development of a new class of optimisation algorithms inspired by physical or biological processes. Some examples include genetic algorithms, simulated annealing, machine learning approaches, and artificial-colony-type algorithms [43]. These algorithms are usually of heuristic nature. Deterministic gradient-based algorithms are another possible way to address an optimisation problem when an exhaustive sampling of the search space is infeasible. This class of algorithms, such as steepest descent, exploits the information given by the gradient of the objective function to gradually converge to a stationary point [45]. The main disadvantage of gradient-based algorithms compared to heuristic algorithms is the risk of convergence to a locally optimal point instead of the desired globally optimal solution. One of the purposes of heuristic algorithms is to avoid this problem by employing effective strategies to explore a larger region of the search space with a relatively limited number of evaluations of the objective function. Many scientific studies investigated the application of these approaches to magnet design and optimisation problems.

Topology optimisation is a class of optimisation approaches that has also been considered for the purpose of designing magnetic systems. Since in topology optimisation the arrangement of materials with different properties is not constrained by a predefined topological configuration, this family of methods potentially leads to novel design concepts. As the implementation usually relies on numerical approaches to simulate the magnetic system, topology optimisation approaches are versatile and do not require imposing restrictive assumptions about the physical behaviour of the system. The optimisation scheme may be performed by gradient based methods [58, 59, 60] or heuristic approaches [61, 66, 62, 63], such as genetic algorithms. Even though in principle topology optimisation can be applied to any magnet design problem, this optimisation method has yet to reach its full potential. One limitation is the trade-off between computational time and the resolution of the mesh underlying the simulation. Moreover, some care has to be taken in order to avoid solutions characterized by finely subdivided or jagged shapes, which may sometimes be produced as result of the topology optimisation procedure.

It is important to stress that the rise of new promising numerical optimisation techniques did not diminish the relevance of more well-established approaches based on analytical derivations. In some cases it is possible to derive closed form expressions of the physical quantities that are relevant to the optimisation problem, expressed as function of the optimisation parameters to be varied. These expressions can only be obtained starting from simplifying assumptions, which are generally more idealized than the assumptions required for numerical procedures. However, finding the optimal set of parameters with respect to the optimisation objective is

considerably easier when closed-form expressions are available. The analytical calculation of the field may be based on solving the partial differential equation governing the magnetic potential [72, 73, 54, 55, 56], often by means of spectral methods. Alternatively, the calculation might be based on a simplified model of the magnetic system [52, 53, 70], such as the lumped parameter magnetic circuit model.

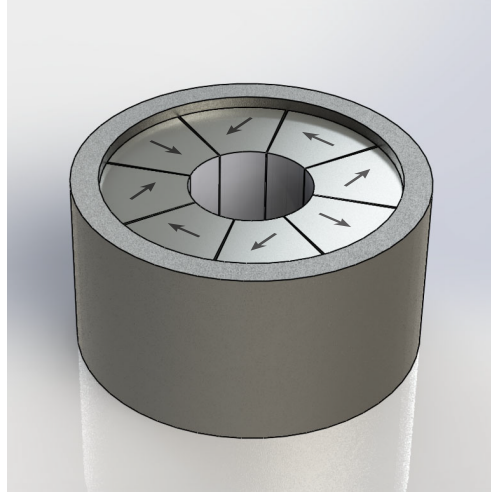


Fig. 1.1: Halbach cylinder.

An important landmark in the design of permanent magnet based systems is the invention of a novel geometrical arrangement of permanent magnet blocks which generates a field with many desirable features [64]. These geometrical arrangements are currently known as Halbach arrays or Halbach cylinders [65]. In the ideal scenario of smoothly varying magnetization direction, these configurations are theoretically able to produce multipole fields of arbitrary intensity and precision, provided that a sufficiently large volume of magnet is used. The Halbach arrays have been developed employing analytical approaches, originally under the assumption that the permanent magnet material is characterized by zero magnetic susceptibility [65]. This simplified model, which would have been an unrealistic description if applied to pre-70s magnetic materials, is surprisingly accurate when applied to rare-earth based permanent magnets whose development initiated around the same time of the invention of the Halbach cylinder. Variations of Halbach-type designs have been used extensively. Some of the applications include [4]: NMR spectroscopy [40, 32, 30, 31], cyclotrons [33], electric motors and actuators, generators, magnetic levitation, and magnetic refrigeration [98, 27, 92].

In more recent times an analytical framework starting from similar assumptions has been employed to derive conditions obeyed by the maximally energy-efficient magnetization distribution which generates a given magnetic field [86]. These insightful results also provide a way to calculate the optimal magnetization distribution whose norm and direction are smoothly varying functions of the position. The same authors investigate the generation of a perfectly uniform field inside a closed cavity by combining uniformly magnetized wedges [87, 89].

Of particular relevance with respect to the optimisation approaches considered in this thesis, is the application of the energy equivalence relation known as reciprocity theorem [74] to magnet optimisation problems. This perspective proves to be insightful from a theoretical point of view,

and practically useful for the optimisation of real magnetic systems [80, 81]. Many ramifications of the reciprocity theorem concerning the optimal geometry of magnetic systems have not been explored by previous works.

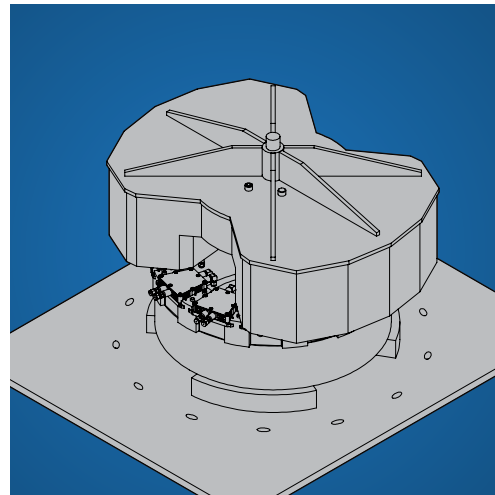
1.2 Scope of this work

As stressed above, many factors contribute in stimulating the research in the field of design and optimisation of magnetic systems, leading to a vast variety of techniques. The strategy adopted in this thesis is to break down the optimisation procedure into easier problems which can then be tackled by relatively simple approaches. The idea of starting with the easier questions is applied by introducing rather restrictive assumptions and by initially addressing the most fundamental optimisation problems. The results derived within these assumption provide the starting point to generalize the optimisation procedures to more complex cases. In this thesis some of the implications of the theoretical approaches mentioned in the last part of section 1.1.2 will be explored in greater depth. As will be shown, this framework has important implications with respect to the optimisation of the flux sources and the geometry of magnetic systems [105, 106].

One of the fundamental assumptions adopted in this work, is that the magnetic systems under consideration are described by the equations of magnetostatics. Despite the name this mathematical description is applicable, at least to some extent, to the analysis of magnetic systems including moving parts or slowly varying currents.



(a) Prototype previously developed at DTU.



(b) Prototype being developed for the ENOVHEAT project.

Fig. 1.2: Rotary devices for room temperature magnetic refrigeration.

The different methods will be illustrated with examples of magnet optimisation problems from different scientific and technological fields. These examples have the purpose of clarifying the procedures and showing the efficacy and flexibility of the optimisation methods. A detailed analysis of the technical issues concerning specifically the different applications goes beyond

the scope of this thesis. Because of its relevance for many different applications, the Halbach cylinder geometry is considered many times through the thesis under different perspectives and in relation with different optimisation strategies. This geometry exhibit several symmetries, and many calculations can be performed analytically for this case. The Halbach cylinder is thus a particularly convenient example for illustrating various concepts [104].

The other group of recurrent examples which will be analysed through the thesis comes from the field of room-temperature magnetic refrigeration. The focus will be on design concepts for rotary devices. The purpose of these magnetic system is to cyclically vary the intensity of the field experienced by the magnetocaloric material which is collected in many independent cassettes. This is accomplished by rotating the permanent magnet with respect to the cassettes enclosing the magnetocaloric material. Two different design concepts will be analysed in particular. The first design corresponds to a prototype previously developed by the magnetic refrigeration research group at DTU [103]. Figure 1.2a shows a picture of the prototype whose geometry is inspired by the Halbach cylinder. During this work, the field produced by the magnetic system of figure 1.2a has been measured and compared with the finite element method calculation.

The second design concept is illustrated in figure 1.2b, and presents similarities with the designs discussed in [25, 24]. The figure represents the drawing of the prototype of the heat-pump device currently being designed within the ENOVHEAT project by the magnetic refrigeration research group. As optimising the magnetic system for this device is the ultimate goal of the PhD project, this system occupies a central role among the examples considered in this thesis.

Framework

This section introduces the mathematical framework describing the magnetic systems discussed in this work. The fundamental equations governing magnetostatic phenomena are introduced in section 2.1. The following section describes the magnetic properties of the materials considered in the thesis.

2.1 Fundamental equations

Electromagnetic phenomena in the macroscopic scale are described by a set of four fundamental equations, known as macroscopic Maxwell's equations. The macroscopic Maxwell's equations expressed in differential form are given by:

Gauss's law:

$$\nabla \cdot \mathbf{D} = \rho_{\text{free}} \quad (2.1)$$

Gauss's law for magnetism:

$$\nabla \cdot \mathbf{B} = 0 \quad (2.2)$$

Maxwell-Faraday equation:

$$\nabla \times \mathbf{E} = -\frac{\partial}{\partial t} \mathbf{B} \quad (2.3)$$

Ampère's law with Maxwell's addition:

$$\nabla \times \mathbf{H} = \mathbf{J}_{\text{free}} + \frac{\partial}{\partial t} \mathbf{D} \quad (2.4)$$

Where the vector fields \mathbf{E} , \mathbf{D} , \mathbf{B} , and \mathbf{H} denote the electric field, electric displacement field, magnetic flux density, and magnetic field, respectively. The symbols ρ_{free} and \mathbf{J}_{free} denote, respectively, the electric charge density and current density not associated with the collective response of macroscopic bodies.

The macroscopic Maxwell's equations imply the continuity equation, which expresses conservation of electric charge:

$$\nabla \cdot \mathbf{J}_{\text{free}} = -\frac{\partial}{\partial t} \rho_{\text{free}} \quad (2.5)$$

This equation is derived by applying the divergence operator to equation 2.4, and using equation 2.1. The interaction between macroscopic bodies and electromagnetic fields is due to complex collective phenomena happening at the nano-scale, which can only be analysed within the theory of quantum mechanics. The macroscopic equations reduce the complexity of these phenomena to the relation between the macroscopic fields \mathbf{D} and \mathbf{H} and the microscopic field \mathbf{E} and \mathbf{B} . These relations are called constitutive relations. The difference between macroscopic and

microscopic fields is due to microscopic distributions of polarization charges and magnetization currents within the bodies, which are not included in the quantities ρ_{free} and \mathbf{J}_{free} . The response of macroscopic bodies to electromagnetic field may be predicted employing a statistical quantum description of the material, or based on phenomenological models.

The focus of this thesis is on steady state magnetostatic phenomena, described by a set of two equations derived from Maxwell's equations. The steady state regime is expressed by the requirement that the free currents are not varying with time, and the time derivative \mathbf{D} is null, thus generating a static magnetic field. In this regime the electric equations for \mathbf{E} and \mathbf{D} decouple from the magnetic equations for \mathbf{B} and \mathbf{H} , leading to the equations of magnetostatics:

Gauss's law for magnetism:

$$\nabla \cdot \mathbf{B} = 0 \quad (2.6)$$

Ampère's law:

$$\nabla \times \mathbf{H} = \mathbf{J}_{\text{free}} \quad (2.7)$$

The simplified continuity equation which is consistent with the steady state requirement, can be derived from Ampère's law:

$$\nabla \cdot \mathbf{J}_{\text{free}} = 0 \quad (2.8)$$

The constitutive relation between \mathbf{H} and \mathbf{B} describes the magnetic behaviour of macroscopic bodies, and is often expressed in functional form as $\mathbf{B} = f(\mathbf{H})$. The formalism is commonly based on the introduction of the auxiliary field \mathbf{M} , called magnetization, and defined by:

$$\mathbf{M} = \frac{1}{\mu_0} \mathbf{B} - \mathbf{H} \quad (2.9)$$

Where μ_0 denotes the vacuum magnetic permeability, given by $\mu_0 = 4\pi \times 10^{-7} \text{ N/A}^2$. The magnetization expresses the density of magnetic dipoles in a magnetic material.

As can be immediately derived from equations 2.6 and 2.7, if the geometry is rescaled isometrically by a factor λ the flux densities and magnetic field spatial distributions rescaled by the same factor are still a valid solution:

$$\mathbf{B}(\mathbf{x}) \rightarrow \mathbf{B}(\lambda \mathbf{x}); \quad \mathbf{H}(\mathbf{x}) \rightarrow \mathbf{H}(\lambda \mathbf{x}) \quad (2.10)$$

Here \mathbf{x} denotes a generic point of space. The vector fields \mathbf{M} and \mathbf{J}_{free} scale in the same way. Exploiting this invariance, the geometrical parameters describing the magnetic systems analysed in this thesis will often be expressed in terms of relative lengths and volumes, rather than reporting the particular values used for the calculations. When the actual size of the system is relevant, the absolute geometrical parameters will be explicitly reported.

2.2 Materials

As mentioned in the previous section, the magnetic response of a material is described by a constitutive relation. The simplest relation is direct proportionality, expressed as:

$$\mathbf{B} = \mu \mathbf{H} \quad (2.11)$$

where the proportionality factor μ is the magnetic permeability characterizing the material. Introducing the magnetic susceptibility χ_m , and writing μ as $\mu_0(1 + \chi_m)$, the definition of \mathbf{M} given by equation 2.9, implies the following direct proportionality between \mathbf{M} and \mathbf{H} :

$$\mathbf{M} = \chi_m \mathbf{H} \quad (2.12)$$

The ratio between the permeability of a material and the vacuum permeability is called relative permeability, and denoted by $\mu_r = \mu/\mu_0$. Relation 2.11 can be generalized to the case of anisotropic response by considering the rank-2 permeability tensor denoted as $\underline{\underline{\mu}}$ and the corresponding susceptibility tensor $\underline{\underline{\chi}}_m$. Even considering the anisotropic case, the behaviour described by equation 2.11 does not apply to all cases, as will be discussed in sections 2.2.2 and 2.2.3.

2.2.1 Non magnetic materials

The vacuum permeability, introduced in the previous section, describes the magnetic behaviour of empty space, thus given by:

$$\mathbf{B} = \mu_0 \mathbf{H} \iff \mathbf{M} = \mathbf{0} \quad (2.13)$$

Non magnetic materials are characterized by the same constitutive relation as vacuum space. This implies that the relative permeability is equal to 1 and the susceptibility is zero. Many materials are characterized by a null or almost null magnetic response. Since the relative permeability of air is only very slightly greater than 1, the parts of a magnetic systems that are filled with air have almost the same magnetic behaviour as if they were completely empty. Similarly, the relative permeability of copper is only very slightly smaller than 1, and the same is true for other weakly magnetic metals, such as aluminium or non-magnetic steel. Copper is relevant for hybrid magnetic systems involving electro-magnets, as their coils are generally composed of this highly conductive material. Aluminium and steel are also relevant since the weight bearing and structural elements of magnetic structures are often composed of these materials.

2.2.2 Permanent magnets

Permanent magnets are materials that exhibit a magnetic behaviour even in absence of an applied field. For their ability to generate an external magnetic flux density they are also called permanent magnet flux sources.

In the data-sheets provided by the magnet manufacturers the non-linear properties of a permanent magnet material are usually described by the B - H curve for the easy axis of magnetization. The assumption behind this model is that the non-linear effects are negligible in the transverse directions, which is a good approximation as long as the transverse field is not too intense [5]. An example of B - H graph and the corresponding M - H graph are shown in figures 2.1a and 2.1b, respectively. The graph represents a hysteresis loop, shown as thick lines, and the virgin curve that is the thinner line passing by the point $(0, 0)$. The graphs of the magnetization relations are also called intrinsic curves, while the graphs of the flux density relations are called normal curves. Figure 2.1a also shows an example load line and the corresponding working point of the B - H curve [76], shown in grey.

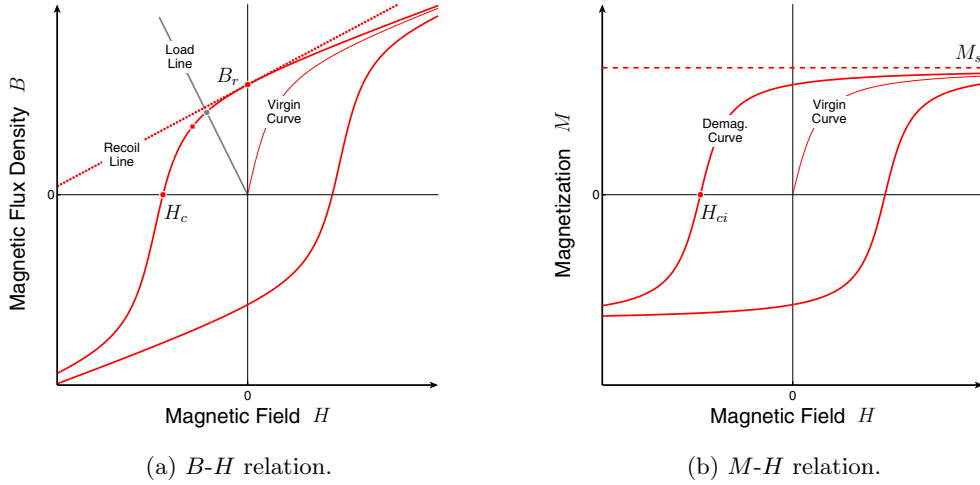


Fig. 2.1: Prototypical B - H curve, 2.1a, and M - H curve, 2.1b, representing the magnetic behaviour of permanent magnets along the easy axis of magnetization. Different geometrical features of the curves are associated with parameters commonly reported in permanent magnet data sheets.

The most relevant part of the graph for modelling of permanent magnet based system is usually the demagnetization curve, indicated in figure 2.1b, and the corresponding curve of the B - H graph of figure 2.1a. If memory effects play an important role and the permanent magnet is subject to an oscillating field, the trajectory of the working point on the B - H plane describes minor hysteresis loops, enclosed by the major loop [76]. A detailed analysis of this situation requires more complex models [7]. However for modern rare earth permanent magnets these effects are usually less significant [76].

Some of the parameters reported by the data-sheets of permanent magnets correspond to geometrical features of the curves.

- The *remanent flux density*, or remanence, is denoted by B_r . In figure 2.1a this parameter corresponds to the intersection point between the demagnetization B - H curve and the $H = 0$ axis.
- The *coercive force*, or coercivity, is denoted by H_c . In figure 2.1a this parameter corresponds to the intersection point between the demagnetization B - H curve and the $B = 0$ axis.
- The *recoil permeability* is denoted by μ_{rec} . In figure 2.1a this parameter corresponds to the slope of the line indicated as *recoil line*, which is the tangent to the demagnetization B - H curve at its point of intersection with the $H = 0$ axis¹.
- The *intrinsic coercive force*, or intrinsic coercivity, is denoted by H_{ci} . In figure 2.1b this parameter corresponds to the intersection point between the demagnetization M - H curve and the $M = 0$ axis.

¹If minor loops are taken into account the recoil line intercepts the major hysteresis loop [76].

- The *saturation magnetization* is denoted by M_s and is the value of magnetization corresponding to the horizontal asymptote shown in figure 2.1b as a dashed line.
- The point of maximum energy product is denoted by $(BH)_{\max}$ and is the point of the demagnetization B - H curve indicated by a square marker in figure 2.1a.

There is a wide variety of commercially available permanent magnet materials with different magnetic characteristics. The curves of figures 2.2a and 2.2b are representative of some of the features exhibited by real materials. The values of the parameters that describe these curves are listed in table 2.1, and are within the range of commonly used materials [10, 12, 13]:

	μ_{rec}/μ_0	B_r [T]	$\mu_0 H_c$ [T]	$\mu_0 H_{ci}$	$\mu_0 M_s$ [T]
Mat. 1	1.05	1.4	0.95	1.05	1.45
Mat. 2	1.05	1.2	1.05	1.59	1.28
Mat. 3	2.00	0.7	0.10	0.10	0.80
Mat. 4	997	0	0	0	1.77
Air	1	0	0	0	0

Table 2.1: Parameters of the magnetic materials

For the purpose of numerical computations it is sometimes convenient to describe the B - H relations using a phenomenological model function [6], such as:

$$M(H) = \frac{2M_s}{\pi} \arctan\left(\frac{H + H_{ci}}{\Delta H}\right) \quad (2.14)$$

The arctangent functions approximately reproduces the behaviour of magnetization curves, but other choices of sigmoid functions could have been possible. This model function is controlled by the three parameters M_s , ΔH , H_{ci} , determining respectively the vertical scale, the horizontal scale, and the horizontal shift, determining the intersection between $M(H)$ and $M = 0$. The parameters M_s and H_{ci} are often included in the permanent magnet data sheets, while the parameter ΔH can be fixed by imposing some additional condition, such as the slope of the corresponding $B(H)$ curve at $H = 0$, given by μ_{rec} , or the intersection of the $B(H)$ curve with $B = 0$, given by H_c . The same model function could also have been parametrized in terms of different quantities, such as B_r instead of M_s . However, the variety of possibilities is limited by the number of free parameters. For example is not possible to modify the hardness of the knee-point without altering other geometrical features of the graph. More elaborate model functions with additional degrees of freedom would increase the range of possibilities.

We will now discuss some general features exhibited by real permanent magnet materials, by considering the prototypical curves shown in figure 2.2a. The slope of the demagnetization B - H curve of materials 1 and 2 is constant over a wide region of the second quadrant around the point of intersection with the axis $H = 0$. This property is typical among modern rare-earth based hard permanent magnets such as Sm-Co and Nd-Fe-B magnets. In many cases it is justifiable to linearise the B - H curve around this point:

$$B = \mu_{\text{rec}}H + B_{\text{rem}} \quad (2.15)$$

This linear relation describes the recoil line indicated in figure 2.1a. If the recoil permeability is very close to μ_0 as in these two example materials, the relation can be approximated even

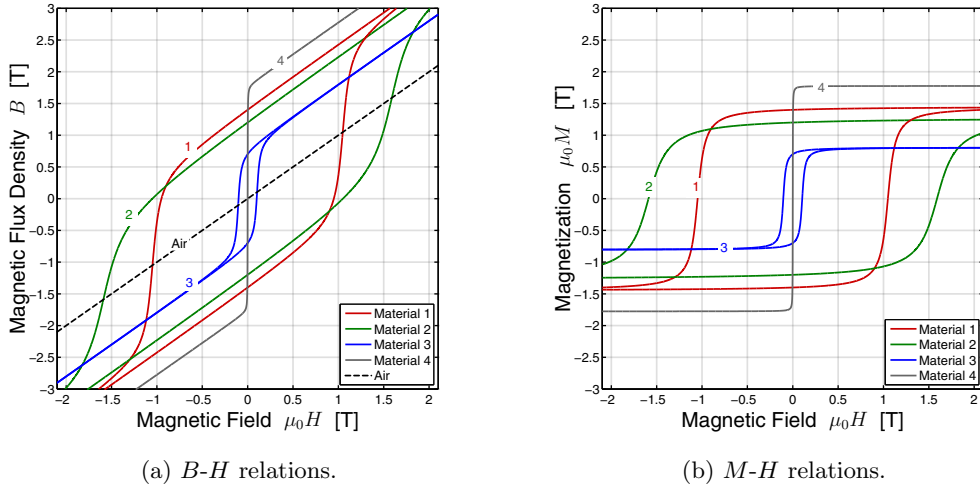


Fig. 2.2: B - H curves, 2.2a, and M - H curves, 2.2b, representing the magnetic behaviour of the prototypical materials whose properties are listed in table 2.1. These curves correspond to the phenomenological model function given by equation 2.14. As discussed in the text, the different features of the curves are important to determine which materials might be suitable for a given application.

more by assuming:

$$\mu \rightarrow \mu_0 \quad (2.16)$$

This is for many purposes a fairly accurate model of hard permanent magnets [65, 87]. In this limit the M - H curve is reduced to a horizontal line and $\chi_m \rightarrow 0$. Using this approximation may simplify significantly the mathematical difficulties of modelling a magnetic system. The demagnetization B - H curve of material 1 presents a knee point in the second quadrant of the graph and therefore might exhibit a non-linear behaviour more easily than material 2 that has the knee point in the third quadrant. For material 3 linearising the B - H curve around its point of intersection with the $H = 0$ axis would not be very realistic approximation. The magnetic behaviour due to non linearity of the B - H curve for the easy axis of magnetization will be considered in section 7.1. The three dimensional generalization of equation 2.15 is expressed by the following equation:

$$\mathbf{B} = \underline{\underline{\mu}}\mathbf{H} + \mathbf{B}_r \quad (2.17)$$

The remanent flux density vector, denoted by \mathbf{B}_r , is oriented along the easy axis and has norm equal to B_r . The rank-2 permeability tensor, $\underline{\underline{\mu}}$, describes the general linear dependence between \mathbf{H} and \mathbf{B} . This general relation may include, e.g., different permeabilities along the easy axis and the hard axes. When the slope of the B - H curve remains constant inside the second quadrant, i.e. when the knee point is in the third quadrant, the permeability for the easy axis, denoted by μ_{\parallel} , can be expressed in terms of B_r and H_c :

$$\mu_{\parallel} = \frac{B_r}{H_c} \quad (2.18)$$

The permeability for the hard axes, denoted by μ_{\perp} is related to the anisotropy field H_A . The following relation is often a good approximation [65]:

$$\mu_{\perp} = \mu_0 + \frac{B_r}{H_A} \quad (2.19)$$

Typical values of anisotropy field for modern rare earth permanent magnets range from ≈ 5 T to ≈ 40 T [4, 65], making these materials quite stable with respect to transverse fields. Often using a scalar permeability provides a sufficiently realistic model.

It is worth mentioning that the versatility of a given permanent magnet material depends on other physical properties as well. Thermal stability is an extremely important factor, especially for applications such as electric motors. Since the magnetic behaviour is due to the ordering of the magnetic spins within the crystal lattice, thermal fluctuation may obscure the relatively small energy advantage of the ordered state. A too high temperature will cause the material to completely lose its magnetic properties. Increasing the thermal stability of permanent magnet materials is one of the most studied aspects of the research on permanent magnet materials [1]. Thermal coefficients describing the temperature dependence of the magnetic properties are often reported in the permanent magnet data sheets [10], and can also be included in numerical models of magnetic systems [6]. Electrical conductivity must also be considered when the material is subject to time varying fields, which would induce electromotive forces. Depending on its conductivity, eddy currents may establish inside the permanent magnet material and the Joule heating associated with such currents would have a harmful effect on the magnetic properties. Typical values of electrical resistivity for Neodymium magnets are around $140 \mu\Omega \text{ cm}$ [13].

2.2.3 Soft magnetic materials

Soft ferromagnets are widely used as passive element inside magnetic structures, since they are excellent magnetic conductors. Even though the magnetic effects exhibited by these materials in absence of an external field are usually negligible, they are extremely useful for their ability of channelling, shielding, or shaping the field generated by permanent magnets or electromagnets. Iron is a prototypical material belonging to this category, broadly used in the applications because of its magnetic properties and relatively low price.

Soft magnetic materials are characterized by a very small value of coercivity. If the effects of magnetic hysteresis are completely neglected, corresponding to the limit $H_c \rightarrow 0$, the B - H relation for soft magnetic materials exhibits approximately the behaviour of material 4, shown in figures 2.2a and 2.2b. In this limit the remanent flux density is also zero. It has to be stressed that the behaviour of soft magnetic materials is usually nearly isotropic. If the magnetic field is decomposed into its norm H and its direction, given by the unit vector \hat{H} , the isotropic non linear relation can be expressed in vector form as:

$$\mathbf{B} = \hat{H} f(H) \quad (2.20)$$

Generally it is desirable to avoid the phenomenon of magnetic saturation, corresponding to the almost flat regions of the B - H curve. This implies that is generally advantageous to increase the magnetic saturation of soft magnetic materials. When the working point is expected to remain in the nearly vertical region of the curve, i.e. far from the saturation magnetization of the material, the non linearities play a minor role, and it is thus justified to approximate the

B - H relation with a linear dependence, expressed by:

$$\mathbf{B} = \mu \mathbf{H} \quad (2.21)$$

As mentioned, this relation describes the B - H curve in its region of highest slope. The values of permeability of soft magnetic materials are in fact by several order of magnitude larger than the values of hard permanent magnets. As can be seen from table 2.1, the relative permeability parametrizing the B - H curve of material 4 is 997, which is a typical value for materials commonly used in magnetic structures. Materials specifically designed for high permeability can reach even higher values [11]. For modelling purposes, and especially when using analytical techniques, the high values of permeability justify the use of the approximation [85, 86]:

$$\mu \rightarrow \infty \quad (2.22)$$

This approximation has important consequences from the theoretical point of view, which will be exploited in different derivations discussed in this work. Section 7.2 presents an example of how the generated field may be distorted because of the saturation of the soft magnetic material.

The development eddy currents due to time varying fields is usually a more important issue for soft magnetic materials than it is for permanent magnets. For example, the joule dissipation associated with the eddy currents inside the iron cores may decrease significantly the performance of an electrical machine or a transformer. One possible solution is to laminate the cores combining layers of ferromagnet separated by thin layers of electrical insulator which have the purpose of breaking the current loops. The orientation of the layers has thus to be determined from the distributions of induced currents inside the different parts of magnetic structure. However the choice of orientation must also be based on the path described by the field lines of the magnetic flux density, since laminations that are transversal to the field lines might decrease the total flux across the part. Even when the layers are parallel to the field lines an over-reduction of the cross-section area filled with ferromagnet might induce magnetic saturation, thus again reducing the flux.

2.2.4 Insulators

Magnetic insulators could in principle have a symmetrical role with respect to the role of soft magnetic materials for the design of magnetic structures. This symmetry is highlighted by the discussion of section 4.1.3. Unfortunately, the permeability of conventional room temperature materials can be only slightly below μ_0 , making their insulating properties almost negligible.

The picture changes drastically if superconductivity is considered. In the superconducting regime the field lines cannot penetrate the surface of a superconductor, meaning that the magnetic permeability is almost exactly zero. This unlocks many possibilities, such as the impressive results presented by Prat-Camps et al. in [8, 9] which consider combining layers of superconductor alternated with layer of ferromagnetic material to realise a metamaterial with highly anisotropic magnetic properties. Thanks to these properties it is possible to perfectly channel the magnetic flux, making these metamaterials ideal for the purposes of magnetic cloaking and flux concentration. Since superconducting magnets are not within the scope of this work, these possibilities are not explored in this thesis.

Magnetic Circuit Model

3.1 Introduction

The magnetic circuit model is an approximate description of the behaviour of a magnetic system. It often provides the most intuitive way to understand a magnetic system. Different scientific studies apply this framework to magnet design problems [52, 53].

The magnetic circuit model approximates a magnetic system with a collection of interconnected components, analogously to the lumped element model approximation of an electrical system. As will be discussed in sections 4.1 and 4.2, an exact calculation of the spatial dependence of the magnetic field in a magnetic system requires solving a partial differential equation. This calculation cannot always be performed analytically, and it is often necessary to resort to numerical approaches such as finite element methods. With the magnetic circuit model the problem is reduced to a discrete set of algebraic equations. If the constitutive relations of all the materials in the system are assumed to be linear, the problem is represented by a system of linear equations. Not all the magnetic systems can be realistically described by the magnetic circuit model. The fundamental assumption is that the magnetic flux is constrained into a series of interconnected channels, such that the flux across their lateral surfaces is zero. This is an adequate model of structures mostly composed by high-permeability material, such as iron, surrounded by a medium of very low permeability, typically air.

Figure 3.1a shows a simple example of such a structure. As can be seen from the figure, the magnetic circuit is composed by a permanent magnet block connected to two iron cores. A small air gap located in the right side of the loop separates the two iron cores. Figure 3.1a represent a realistic situation, calculated with FEM analysis. Figure 3.1b represents the idealized situation described by the magnetic circuit model. As can be noticed from figure 3.1a, the field lines are not perfectly constrained within the different components of the circuit. Particularly around the air gap, the magnetic flux leaks into the regions which the magnetic circuit model would assume to be perfectly insulated. In section 3.4 we will examine more realistic examples of magnetic circuit, which incorporate leakage across the lateral surfaces of the structures. For now this effect will be neglected. As can be seen from the circuit diagram on the top-right corner of figure 3.1b, the magnetic system has been modelled with a single loop magnetic circuit composed by four elements all connected in series: the permanent magnet, the two iron cores, and the air gap.

It is assumed that the geometry of each component is characterized by its length L , measured along the direction of the field lines, and its cross-sectional area S . The magnetic field and magnetic flux density are always oriented in the direction of the length of the component, and their norm is constant. The field H and the flux density B are thus related by a scalar equation $B = f(H)$. This leads to a relation between the magnetic flux $\Phi = BS$ through the component

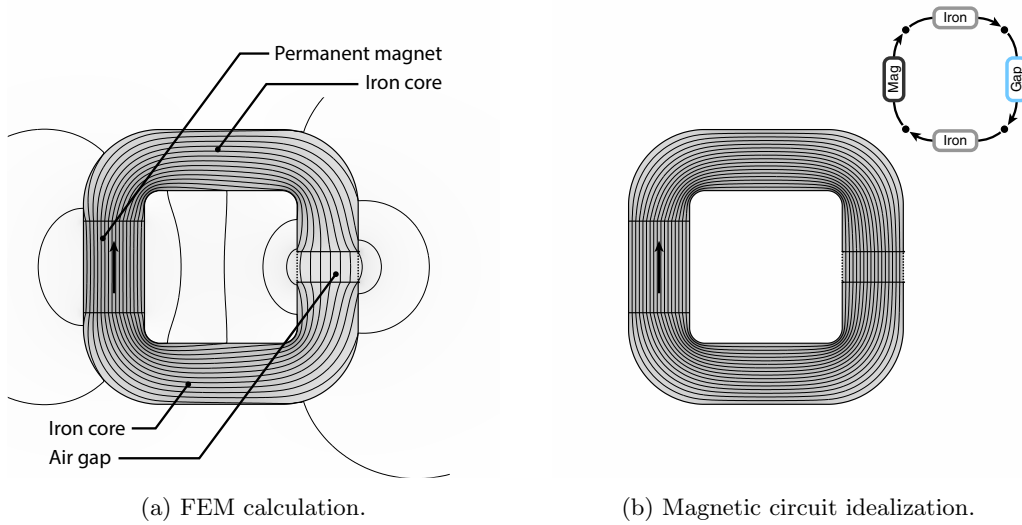


Fig. 3.1: Single loop magnetic circuit composed by four component connected in series: the permanent magnet, two iron cores, and an air gap. **3.1a**: FEM calculation taking into account magnetic flux leakage across the lateral surfaces of the circuit. **3.1b**: illustration of the fundamental assumption on which the magnetic circuit model is based, i.e. the magnetic flux cannot leak from the circuit. The circuit diagram is shown on top right corner of figure 3.1b.

and the magnetomotive force $\mathcal{F} = HL$ across it:

$$\Phi = S f(\mathcal{F}/L) = F(\mathcal{F}) \quad (3.1)$$

Flux and magnetomotive force are the analogous of the electric current flowing through a component and the voltage across it, respectively. Gauss's law for magnetism leads to the magnetic equivalent of Kirchhoff's current law: it implies that the algebraic sum of the magnetic fluxes Φ_k of all the components connected to the same node is zero:

$$\sum_k \Phi_k = 0 \quad (3.2)$$

Ampère's law leads to the magnetic equivalent of Kirchhoff's voltage law: it implies that the directed sum of the magnetomotive forces \mathcal{F}_k across the components that form a closed loop is equal to the total electric current I flowing through the loop.

$$\sum_k \mathcal{F}_k = I \quad (3.3)$$

The mathematical techniques that are normally applied to analyse electrical circuits can also be applied to the analysis of magnetic circuits. It is possible to combine two components in series or in parallel, and calculate the Φ - \mathcal{F} relation for the series or parallel combination. Two components, labelled by A , and B are considered, and the component obtained by connecting A and B in series is labelled by C . The following two equations relate flux and magnetomotive force for component C , with the corresponding quantities for A and B .

$$\Phi_C = \Phi_A = \Phi_B; \quad \mathcal{F}_C = \mathcal{F}_A + \mathcal{F}_B \quad (3.4)$$

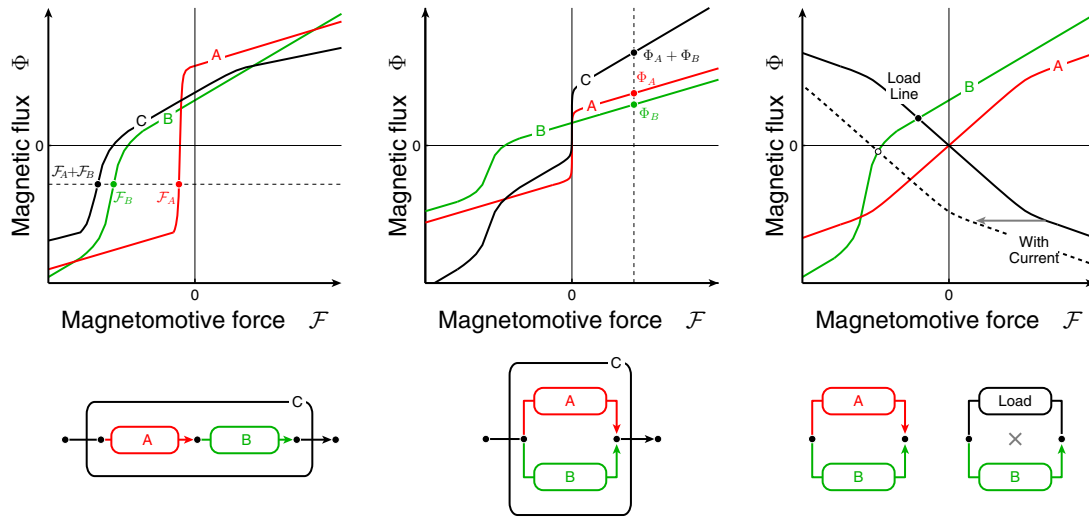


Fig. 3.2: Graphical interpretation of the parallel and series composition between two circuit elements. The left and middle panel represent the series sum and parallel sum, respectively. The right panel shows how to graphically determine the solution for a single loop circuit composed by two elements. This lead to the concept of load line, which is shown in the figure.

Therefore the relation between the magnetomotive force across C and its flux is given by:

$$\mathcal{F}_C = F^{-1}(\Phi_C) = F_A^{-1}(\Phi_C) + F_B^{-1}(\Phi_C) \quad (3.5)$$

The left panel of figure 3.2 shows the geometric interpretation of this equation on the Φ - \mathcal{F} graph. The curve Φ_C - \mathcal{F}_C , plotted in black, is obtained by summing *horizontally* point by point the two curves corresponding to the components A and B , plotted in red and green, respectively.

If C denotes instead the component obtained by connecting A and B in parallel, it is possible to apply a similar argument as long as the current flowing through the loop formed by A and B is zero.

$$\Phi_C = \Phi_A + \Phi_B; \quad \mathcal{F}_C = \mathcal{F}_A = \mathcal{F}_B \quad (3.6)$$

The magnetic response of component C is then given by:

$$\Phi_C = F(\mathcal{F}_C) = F_A(\mathcal{F}) + F_B(\mathcal{F}) \quad (3.7)$$

The middle panel of figure 3.2 shows the geometric interpretation of this equation on the Φ - \mathcal{F} graph. The curve Φ_C - \mathcal{F}_C , plotted in black, is obtained by summing *vertically* point by point the two curves corresponding to the components A and B .

Let us now consider a simple circuit, only composed by a component labelled by A connected to a component B as shown in the right panel of figure 3.2. The component B represents a permanent magnet and the component A , represents the rest of the circuit attached to it, which we will call load. For the illustrative example of figure 3.1, the component A would be the series sum of the air gap with the two iron cores. If the current flowing through the loop formed by

A and B is zero, the following two relations must be satisfied:

$$\Phi_A = -\Phi_B; \quad \mathcal{F}_A = \mathcal{F}_B \quad (3.8)$$

The black curve of the third panel of figure 3.2, labelled *Load Line*, has been obtained from the Φ_A - \mathcal{F}_A curve by reflecting it around the horizontal axis, $\Phi = 0$. The actual values of Φ_B and \mathcal{F}_B when B is connected to A are given by the intersection of the load line with the curve Φ_B - \mathcal{F}_B . This point is shown as a black circle in the right panel of figure 3.2. The corresponding point of the B - H curve of component B is referred to as *working point*, or operating point. If a current I is flowing through the loop formed by A and B , Ampere's law is modified, resulting in the following relations:

$$\Phi_A = -\Phi_B; \quad \mathcal{F}_A = \mathcal{F}_B + I \quad (3.9)$$

Geometrically this correspond to horizontally translating the load line by a distance that is equal to the current I . The translated curve is shown as a black dashed line, and the new working point is indicated by a white circle.

For a linear material with zero remanence the relation between B and H is:

$$B = \mu H \quad (3.10)$$

Defining the magnetic reluctance \mathcal{R} of the component as $\mathcal{R} = \frac{L}{\mu S}$, the relation between \mathcal{F} and Φ can be written analogously to Ohm's law:

$$\Phi = \frac{1}{\mathcal{R}} \mathcal{F} \quad (3.11)$$

As for an electrical circuit, the total reluctance \mathcal{R}_C of two components A and B connected in series is the the sum of the two individual reluctances \mathcal{R}_A and \mathcal{R}_B :

$$\mathcal{R}_C = \mathcal{R}_A + \mathcal{R}_B \quad (3.12)$$

For two components connected in parallel, if the current flowing through the loop formed by the two components is zero, the total reluctance \mathcal{R}_C is given by:

$$\mathcal{R}_C^{-1} = \mathcal{R}_A^{-1} + \mathcal{R}_B^{-1} \quad (3.13)$$

If equation 3.10 is modified to include the remanence of the permanent magnet, i.e. $B = \mu H + B_r$, equation 3.11 modifies accordingly.

3.2 Single-Loop magnetic circuit

It is instructive to analyse in more detail the simple magnetic circuit introduced in the previous section. As mentioned, the geometry is decomposed into four components: the permanent magnet, labelled by the letter m , the air gap, labelled by g , and the upper and lower parts of the iron core, labelled by $I1$ and $I2$, respectively. For a single loop circuit, the magnetic flux Φ , which is conserved, has the same value for all the components. Applying equation 3.3 leads to:

$$\Phi = \frac{B_r L_m / \mu_m}{\mathcal{R}_m + \mathcal{R}_g + \mathcal{R}_{I1} + \mathcal{R}_{I2}} \quad (3.14)$$

The remanence of the permanent magnet is indicated by B_r , and the reluctance \mathcal{R} of each component is defined in terms of the area S of the cross section, the length L , and the permeability μ . The volume of each component is denoted by V and given by the product between length and cross-section area. The sum of the reluctances of all the components except the permanent magnet is indicated by $\mathcal{R}_{\text{Load}}$:

$$\mathcal{R}_{\text{Load}} = \mathcal{R}_g + \mathcal{R}_{I1} + \mathcal{R}_{I2} \quad (3.15)$$

It is interesting to consider the optimization problem of maximizing the flux Φ , with respect to the geometric proportions of the magnet, while keeping the total magnet volume V_m constant. Since the ratio L_m/S_m is proportional to the reluctance \mathcal{R}_m , the optimization problem is equivalent to optimizing \mathcal{R}_m for a fixed V_m . Starting from equation 3.14, it is possible to show that the optimal reluctance \mathcal{R}_m is equal to the total reluctance $\mathcal{R}_{\text{Load}}$ of the rest of the circuit. This implies that the magnetic flux density inside the permanent magnet is exactly half of its remanence. We define the quantity U_m , related to the magnetic energy associated with the permanent magnet:

$$U_m = -B_m H_m V_m \quad (3.16)$$

The point of the B - H curve corresponding to the maximum value of U_m is given by:

$$H = -\frac{1}{2\mu} B_r ; \quad B = \frac{1}{2} B_r \quad (3.17)$$

This is the same working point leading to the maximum flux across the magnet. This gives:

$$U_m \leq \frac{1}{4\mu} B_r^2 V_m \quad (3.18)$$

Maximizing the magnetic flux through a magnet with a given volume with respect to its aspect ratio is equivalent to maximizing its energy product.

Since the permeability of the iron is very high, the corresponding reluctance is generally much smaller than the reluctance \mathcal{R}_g of the air gap. This means that it is possible to consider the following approximation:

$$\mathcal{R}_{\text{Load}} \approx \mathcal{R}_g = \frac{L_g}{\mu_g S_g} \quad (3.19)$$

Within this approximation the air gap flux density B_g generated with the optimal magnet reluctance, $\mathcal{R}_m = \mathcal{R}_g$, obeys the following relation:

$$\mathcal{M} = \frac{V_g B_g^2}{V_m B_r^2} = \frac{1}{4} \quad (3.20)$$

The efficiency figure of merit \mathcal{M} is a measure of the amount of magnetic energy that is associated with the field that the magnet generates outside of itself. Since V_g is assumed to be constant, maximising the flux Φ across the circuit is equivalent to maximising the quantity $V_g B_g^2$, related to the magnetic energy associated with the air gap field. Moreover, since V_m and B_r are also constant, maximizing Φ is also equivalent to maximizing \mathcal{M} . In conclusion, maximising the energy product inside the permanent magnet also results in the maximum air gap energy. In fact the principle that a well designed magnetic system utilizes the permanent magnets as close as possible to their maximum energy point is widely known.

These results, derived within a very simple model, have to be interpreted as an upper limit to the performance of real magnetic systems. As it is shown in [86], and will be discussed in section 5.2.1, the inequality $\mathcal{M} \leq 1/4$ is always verified. Also the equivalence between maximising the permanent magnet energy product and maximising the magnetic energy stored outside the magnet applies to general magnetic systems.

3.3 Application to magnetocaloric heat pump

In this section we will consider a magnetic circuit composed by two loops, and in particular its application for a magnetocaloric device. Some of the general concepts introduced here apply to all the magnetocaloric devices which will be used as illustrative examples in the course of the thesis. The magnetic circuit considered here is a hybrid system combining a permanent magnet with electromagnets. This section mostly reproduces the discussion reported in the paper attached in section B.6.

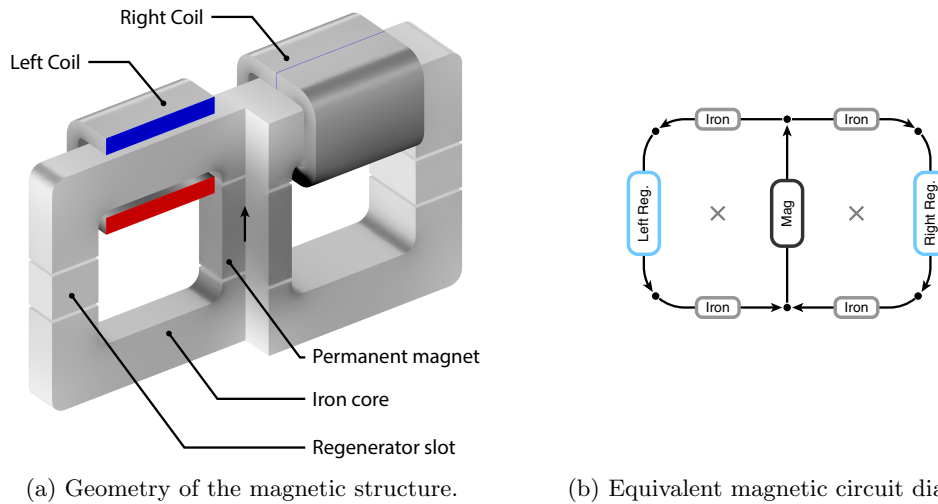
Conventional active-regenerator magnetocaloric devices include moving parts, with the purpose of generating an oscillating magnetic field in the magneto-caloric material, placed inside the regenerator. In this section a different design concept is analysed, for application in a magnetocaloric heat pump. In this design all the parts of the machine are static and the oscillating field is generated by varying the currents of the electromagnets included in the hybrid magnetic assembly. The use of different permanent magnet materials is compared with the perspective of maximizing the coefficient of performance of the device.

Magnetic assemblies designed for magnetocaloric refrigeration are necessarily realized without using electromagnets, since the heat produced by the Joule effect would decrease the overall performance of the device. In order to work, any magnetocaloric device must produce a time oscillating magnetic field inside the magnetocaloric material. When the magnetic assembly is realized without the use of electromagnets, there are two main options to produce the field oscillation inside the material [93]: rearrange different parts of the magnetic assembly to modify the field, or displace the material itself in different positions characterized by different values of magnetic field. Both the options present some disadvantages: additional design challenges are introduced, the lifespan of some components of the machine is reduced because of friction and vibrations associated with the motion. A magnetocaloric heat pump does not share this limitation with the refrigerators and the use of a hybrid magnetic assembly, which includes also electromagnets, is feasible. The Joule dissipation in the coils of the electromagnets will generate an additional heating output. Moreover a new option is available to produce the oscillating field inside the magnetocaloric material: the coil-current of the electromagnets can be varied to alter the magnetic field while all the parts of the device are stationary. This design solution is not affected by the disadvantages of moving machines, and would also result in a minor noise production. One prototypical geometry for a static machine with hybrid magnetic assembly will be analysed, with the perspective of maximizing the net performance of the magnetocaloric heat pump.

Here we consider one prototypical geometry for static machines with hybrid magnetic assembly and describe the methods we employed to model this system. The geometry is schematically illustrated in 3.3a and consists in a high-permeability material (iron) core composed by two loops (left and right loop). A permanent magnet magnetized in the vertical direction is placed in the central branch of the circuit. Two air gaps, which will host the magnetocaloric regen-

erators, are located in the middle of the left and right branches. Finally, two electric coils are wrapped around the left and right branches of the circuit. The circuit diagram representing this magnetic structure is shown in figure 3.3b. Because of the symmetry of the circuit, without coils the magnetic flux generated by the permanent magnet would split equally between the two loops.

The investigation discussed in this section has the main purpose of showing the usefulness of the magnetic circuit approach, and to illustrate how this framework can be applied for the analysis of magnetocaloric devices. The results given by the magnetic circuit model are less realistic than what could be obtained with a finite element analysis of the geometry, but the computational cost is much lower, making it a suitable tool for a preliminary analysis. The specific values of the parameters used for the calculation are not relevant for this qualitative discussion, and will not be reported here.



(a) Geometry of the magnetic structure.

(b) Equivalent magnetic circuit diagram.

Fig. 3.3: Double loop magnetic system, applied in a static magnetocaloric heat pump. The geometry, shown in figure 3.3a, can be represented by the magnetic circuit diagram shown in figure 3.3b. The system involves a single permanent magnet block, located in the central branch, and two coils wrapped respectively around the left and right branches of the iron core. The magnetocaloric material is collected inside the two symmetrical regenerators shown in figure 3.3a. In a given moment, one of the regenerators is in the high field state and the other one is in the low field state. The time varying current applied to the coils switches the high field region from the left regenerator to the right regenerator or vice-versa.

For this analysis it is important to model the non linear characteristics of the B - H curves of different possible permanent magnet materials, and to solve the circuit equations for the diagram shown in figure 3.3b. This has been achieved by developing a Matlab routine, applicable to any circuit that can be solved using a series-parallel analysis. The B - H curves of the prototypical materials used for the calculations are shown in figure 3.4. It is also considered the possibility of entirely replacing the permanent magnet with iron.

The operation of the device (i.e. the time dependence of the coil-currents) is determined

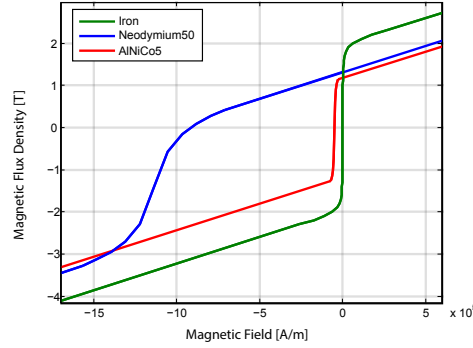


Fig. 3.4: B - H relations of the three materials considered for this study. It is also investigated the possibility of entirely replacing the permanent magnet with iron, leaving the coils as the only flux source. As we will see, the coercivity of the material is one of the parameters having the greatest influence on the final performance of the device considered here.

by the characteristics of the thermodynamical cycle of the magnetocaloric material. The focus of this study will be on cycles for which the materials spend half of the cycle time in high-field state and the other half in a low-field state. For half the duration of a cycle, the coils augment the field in one of the air gaps while simultaneously reducing it in the other one. During the other half of the cycle the high-field and low-field air gaps are switched.

The current flowing in the left and right coils are indicated by I_L and I_R , respectively. The two currents are parametrized by ϕ_I and I_{Tot} , according to the following relations:

$$I_L = I_{\text{Tot}} \cos(\phi_I) \quad (3.21)$$

$$I_R = I_{\text{Tot}} \sin(\phi_I) \quad (3.22)$$

In this way the net power, \dot{W}_{Joule} , spent by the machine by Joule dissipation, is not dependent on the current-angle Φ_I , but only on the square of the current-amplitude, i. e. $I_{\text{Tot}}^2 = I_L^2 + I_R^2$. Denoting the resistance of each coil by R , the power is given by $\dot{W}_{\text{Joule}} = RI_{\text{Tot}}^2$. The top-left panel of figure 3.5 shows the dependence on ϕ_I of the magnetic flux densities of the left and right coil, denoted by B_L and B_R , respectively. As can be noticed from the graph, for the choice of I_{Tot} corresponding to this curve the field can be reduced to zero by some particular values of ϕ_I , depending on the permanent magnet material. As we will see, this is a desirable situation for the performance of the device. The cooling power provided by the heat pump can in fact be expressed as [101, 102]:

$$\dot{Q}_C = \gamma_C \left(\langle B_{\text{High}}^{2/3} \rangle - \langle B_{\text{Low}}^{2/3} \rangle \right) \quad (3.23)$$

The symbol $\langle B_{\text{High}}^{2/3} \rangle$ denotes the average norm of the flux density inside the regenerator in the high field state, and $\langle B_{\text{Low}}^{2/3} \rangle$ the average for the low field regenerator. The proportionality factor γ_C depends on the geometrical and operating characteristics of the regenerators, and on the magnetocaloric material collected inside them. The $2/3$ exponent realistically models the dependence on B of the cooling power provided by devices employing Gadolinium [101].

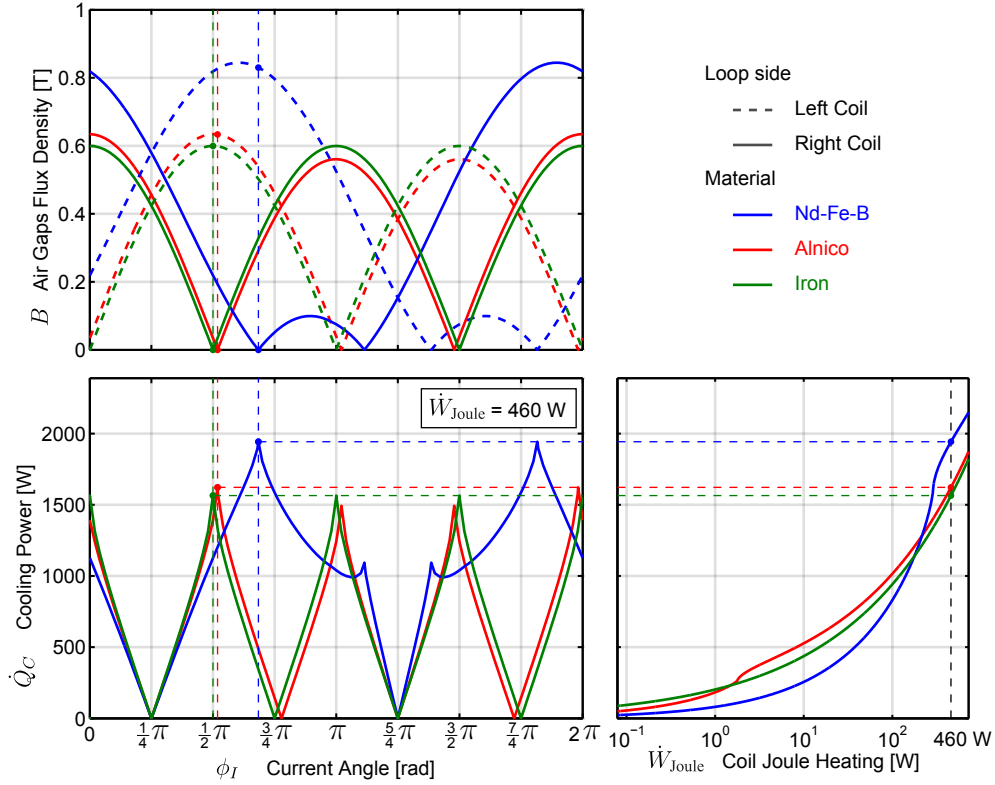


Fig. 3.5: The left panels show the dependence of flux density B and cooling power \dot{Q}_C , on the parameter ϕ_I , which controls how the current is subdivided between the left and right coil. The optimal values ϕ_I with respect to \dot{Q}_C are indicated by the vertical dashed lines, corresponding to the different materials. The left and right panel correspond to a particular choice of total coil power \dot{W}_{Joule} . The location of the optimal points is also affected by the total power. The bottom right panel shows the dependence of the optimal cooling power on the coil power \dot{W}_{Joule} .

This material is widely used as benchmark magnetocaloric material for room temperature applications. The dependence of \dot{Q}_C on ϕ_I is shown in the bottom-left panel of figure 3.5. The optimal value of ϕ_I with respect to \dot{Q}_C is indicated for the three materials by the vertical dashed lines which are also shown in the top-left panel. As can be noticed, the $2/3$ exponent implies that the optimal point always corresponds to the field being zero in one of the regenerators. The extra available coil power is then spent to increase the field intensity in the other regenerator. The bottom-right panel shows the dependence of \dot{Q}_C on \dot{W}_{Joule} , plotted on a logarithmic scale. The curves for Nd-Fe-B and Alnico show a knee point corresponding to the minimum value of coil power necessary to complete cancel the field in one of the regenerator. Because of its lower coercivity, Alnico presents the knee point at a lower power. The curve for iron does not show this feature since without current the field is zero on both sides, which is also the reason why iron gives a better cooling power at low currents.

The performance of the device is expressed by the Coefficient Of Performance, COP, which

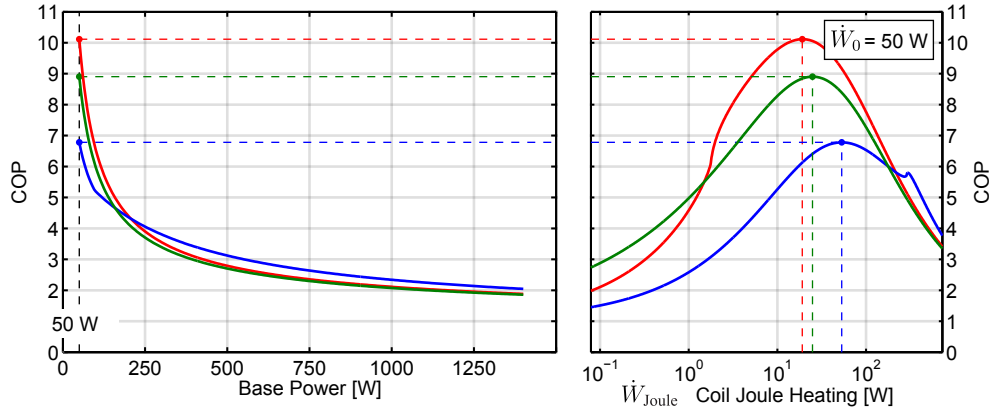


Fig. 3.6: The right panel shows the dependence of the COP on the coil power \dot{W}_{Joule} . The COP is affected by the base power \dot{W}_0 which is consumed by the remaining components of the device; the right panel corresponds to a particular choice. The optimal value of \dot{W}_{Joule} with respect to the COP depends on \dot{W}_0 and on the choice of material. The left panel shows the dependence of the optimal COP on the base power \dot{W}_0 . As can be seen, depending on this parameter, it might be more convenient to select a material or another one.

is defined as the ratio between the output heating power and the input power [99, 103]:

$$\text{COP} = \frac{\dot{Q}_C + \dot{W}_0 + \dot{W}_{\text{Joule}}}{\dot{W}_0 + \dot{W}_{\text{Joule}}} \quad (3.24)$$

The symbol \dot{W}_0 denotes the power spent by the machine in other parts than the electric coils, such as the pump for the heat-exchange fluid. This contribution to the total power will be called base power. The bottom right panel of figure 3.6 shows the dependence of the COP on the coil power, for a particular value of \dot{W}_0 . These curves can be used to select the optimal value of \dot{W}_{Joule} , with respect to the COP. As can be noticed the optimal coil power, indicated by the vertical dashed lines, is also affected by the choice of material. The dependence of the optimal COP on the value of \dot{W}_0 is shown in the left panel of figure 3.6. Depending on the base power one material or another may give the best performance.

3.4 Flux leakage

The magnetic circuit model can also be used to estimate the magnetic leakage in a given structure, provided that the geometry is not too complex. However, the assumption at the base of the circuit model is that the flux across the lateral surfaces of the circuit component is zero. The leakage can only be estimated by including in the circuit diagram extra elements describing the leakage paths. Let us consider the example shown in figure 3.7b. The purpose of this magnetic system is to focus the field generated by the two permanent magnet blocks. The objective is thus to maximise the field inside the central square region delimited by the dotted lines, which is represented in figure 3.7a as a blue shaded region. The focussing is achieved by

the two trapezoidal iron poles visible in both the figures. The circuit closes from the left to the right side, due to the periodic boundary condition imposed at this border, which is indicated by the vertical grey lines.

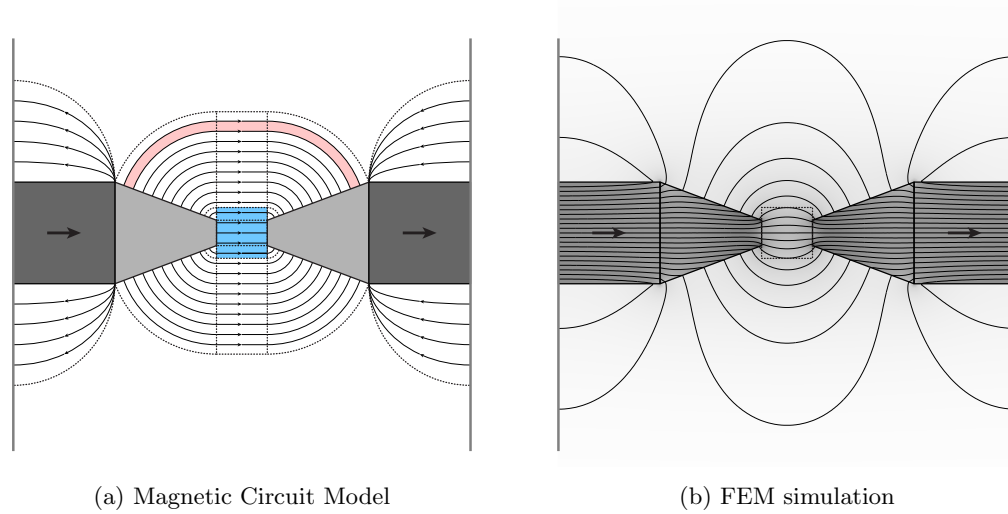


Fig. 3.7: Magnetic system corresponding to the purpose of focusing the field generated by the magnet blocks inside the central square region, indicated in figure 3.7a by the blue shaded area. The focusing is accomplished by means of the two trapezoidal iron poles located on the sides of the air gap. Periodic boundary conditions are imposed at the left and right borders, as symbolically indicated by the vertical grey lines. Figure 3.7b shows the result of the FEM calculation, while figure 3.7a shows the diagram including the different leakage paths.

As can be seen from these figures, the leakage field lines go through two different paths: either bypassing the air gap on its sides, or backstreaming on the sides of the magnet. Using the techniques described in [51] it is possible to include these leakage paths in the magnetic circuit diagram. The permeability of the iron poles by far exceeds the permeability of the other parts of the system, which essentially means that their reluctance is negligible. In practice they can be modelled as nodes of the magnetic circuit. Let us now consider the particular channel, indicated in figure 3.7a as a red shaded region connecting the two iron poles. The flux density is assumed to be oriented along this channel, which approximately reproduces the behaviour visible in figure 3.7b. The cross-section area of the pink-shaded path is constant, and its length can easily be calculated. All the analogous channels can thus be added in parallel, while considering the specific length of each of them. In the continuous limit, the closed form expression of the total reluctance of that region is calculated by integrating “in parallel” the individual infinitesimal paths.

Figure 3.8a shows the circuit diagram including the various leakage paths corresponding to the different regions. For this analysis the magnetic behaviour of the permanent magnets is modelled using a linear B - H relation with $B_r = 1$ and $\mu = 1.05\mu_0$. The two permanent magnets adjacent to the left and right boundaries are square blocks with side $2L$. The horizontal length and the larger base of the trapezoidal iron poles have the same size as the side of the magnet blocks. The length of shorter base of the trapezoids is denoted by a_2 . As mentioned, the goal

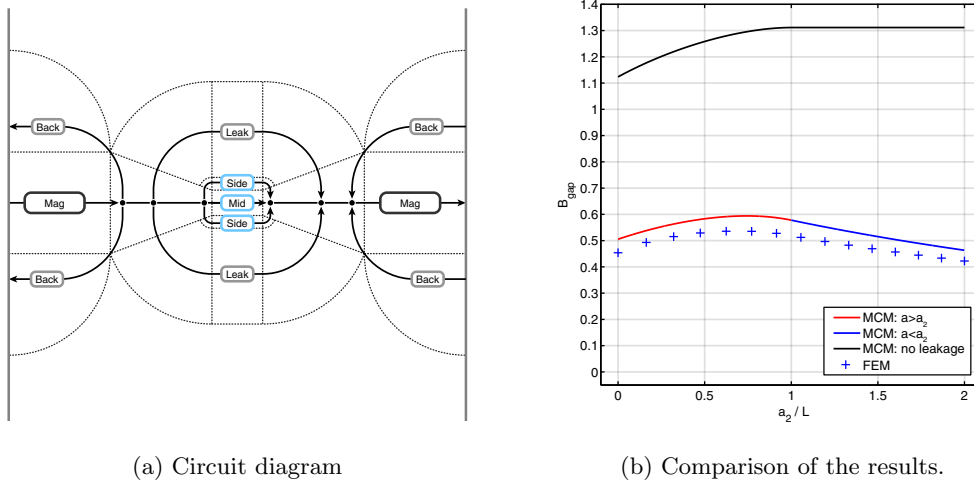


Fig. 3.8: **3.8a**: circuit diagram corresponding to the decomposition shown in figure 3.7a. The circuit elements corresponding to the square region between the iron poles are indicated by the light blue border and labelled as “Mid” and “Side”. The various leakage paths are indicated by the grey border and are labelled as “Leak” or “Back”. **3.8b**: comparison between the results calculated with the FEM analysis, indicated by the blue crosses, and the results given by the magnetic circuit model, indicated by the red and blue lines. The solid black line indicates the prediction given by the magnetic circuit model when the flux leakage is not taken into account.

is to focus the field inside the square blue shaded region, whose side is equal to L . We will consider how the field is affected by length of the shorter base of the trapezoid, a_2 . When a_2 is equal to L , the shorter base of the trapezoids has the same size as the side of the square blue shaded region.

The prediction given by the magnetic circuit model has been compared with the result of the finite element method calculation. In particular, we will consider the norm of the flux density B averaged over the blue shaded region. The closed form expression given by the magnetic circuit analysis is very complicated and not particularly insightful, and is not reported here. The results are shown in figure 3.8b, as function of a_2/L . The FEM calculation is shown as blue crosses, and the magnetic circuit model calculation is represented by the blue and red solid lines. The two different colours separate the regions $a_2 < L$ and $a_2 > L$. The circuit diagram is different when $a_2 > L$, since the two components labelled as *Side* in figure 3.8a, belonging to the blue shaded region, are not present. The black solid line shown in figure 3.8b represents the prediction given by the magnetic circuit model when the leakage is not considered, i. e. when all the components labelled as *Leak* or *Back* are removed from the diagram of figure 3.8a. When the leakage is considered, the magnetic circuit model only slightly overestimates the result of the FEM calculation, and the qualitative dependence on a_2 is reproduced correctly. Disregarding the flux leakage leads to a gross overestimation of the field intensity. This example shows that the magnetic circuit model can be used to obtain quite realistic results, with all the advantages brought by a closed form expression. However, some care must be taken to correctly include the different leakage paths in the circuit diagram.

3.5 Cogging torque minimization

Forces and torques between different magnetizable parts of a magnetic structure can also be calculated within the magnetic circuit model. In this section we will consider a simple magnetic system which will be used to investigate the phenomenon of cogging torque. Rotary magnetic machines are composed by a stationary part, called stator, and a rotating part, called rotor. If the system includes flux sources, the two parts will experience a relative torque, attempting to minimise the total reluctance of the magnetic circuit, thus increasing the total flux. If the part that is moving with respect to the flux sources presents a periodic structure, the torque will exhibit a corresponding periodic behaviour. This phenomenon is called cogging torque, and is generally disadvantageous for different reasons. The vibrations induced by this oscillatory torque increase the noise, and are harmful for lifespan of the machine. Especially at low frequencies this effect can be very important and decrease the resulting performance of a magnetic device.

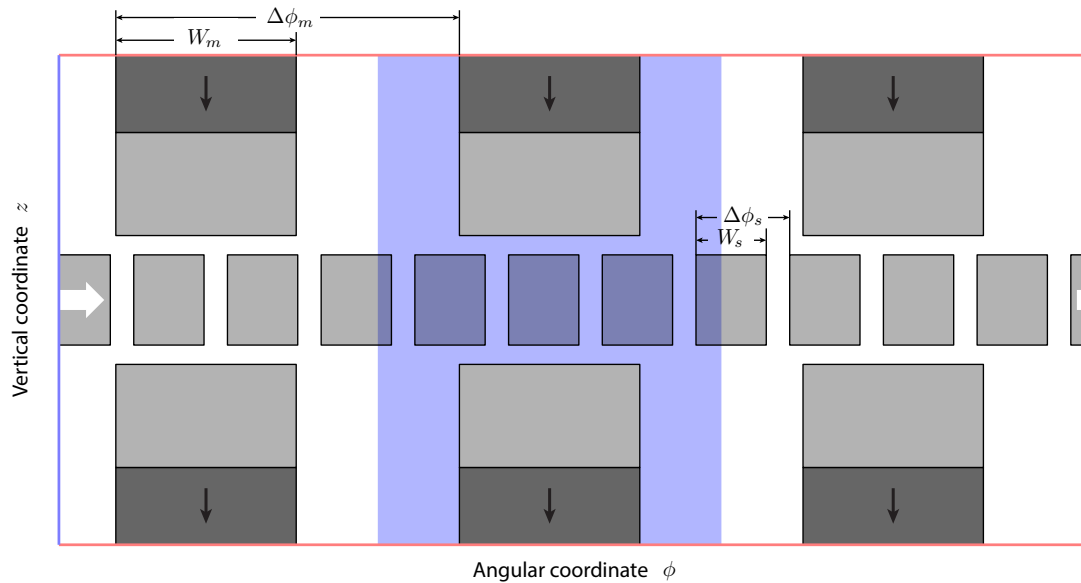


Fig. 3.9: Illustration of the prototypical magnetic system used to predict the qualitative dependence of the cogging torque amplitude on the parameters controlling the geometry. The figure shows three independent magnetic circuits, i. e. $N_m = 3$, including two permanent magnets, and two iron poles each. The horizontal air gap between the rectangular iron poles is filled by an array of equally spaced iron slots, which are allowed to move horizontally. Periodic boundary conditions link the top border with the bottom border, as indicated by the light red horizontal lines. Similarly, the light blue vertical lines indicate a periodic boundary condition linking the left border with the right border.

Figure 3.9 shows the geometry of the system used for this analysis, which represents a rotary magnetic structure. The angular coordinate, ϕ , corresponds to the horizontal axis, and the vertical coordinate, z , to the vertical axis. The radial direction is not considered in this model. Periodic boundary conditions connect the left border with the right border, and the

top with the bottom, as it is highlighted by the light blue and light red lines shown in the figure. The structure is composed by $N_m = 3$ independent magnetic circuits, each including two vertically magnetized permanent magnet blocks and two iron cores. An array of $N_s = 11$ equally spaced iron slots partially occupies the air gap of the magnetic circuits. All the slots belong to the same part, and move rigidly with respect to each other. The rotation of the slots with respect to the magnets is represented in figure 3.9 as an horizontal shift, as indicated by the white horizontal arrow. The angle spanned by each slot is indicated by W_s , and can assume values in the interval $[0, \Delta\phi_s = 2\pi/N_s]$. Similarly, the angle spanned by each magnet satisfies the relation: $W_m \in [0, \Delta\phi_m = 2\pi/N_m]$.

The magnetic behaviour of this system has been analysed using the magnetic circuit model. The circuit diagram includes different leakage paths, whose reluctances have been calculated using the methods described in the previous section. As explained in [76], the torque can be calculated from the dependence of the *coenergy* W' on the rotation angle θ . The mathematical procedure described in [76] for systems including permanent magnets, involves the addition of a fictitious excitation current I in the magnetic system. The value of fictitious current which would reduce the magnetic flux Φ_m to zero is used in the calculation, and will be denoted by I_0 :

$$I_0 : \Phi_m(I_0) = 0 \quad (3.25)$$

The coenergy is thus expressed in terms of I_0 :

$$W' = \int_{I_0}^0 \Phi(I) dI \quad (3.26)$$

The torque $T^{(k)}$ between each magnetic circuit and the part containing the slots is finally calculated as the derivative of the coenergy with respect to the rotation angle θ :

$$T^{(k)}(\theta) = \frac{\partial W'}{\partial \theta} \quad (3.27)$$

The vector representing the torque is oriented in the z direction. For a single loop linear magnetic circuit the torque can be expressed in terms of the reluctance of the magnet, indicated by \mathcal{R}_m and the reluctance of the rest of the circuit, indicated by $\mathcal{R}_{\text{load}}$:

$$W' = \frac{1}{2} \left(\frac{B_r L_m}{\mu_m} \right)^2 \frac{1}{\mathcal{R}_m + \mathcal{R}_{\text{Load}}(\theta)} \quad (3.28)$$

Where L_m represents the vertical length of the magnets, μ_m their permeability, and B_r the remanence. It has to be stressed that, even though each of the three magnetic circuit is solved independently, the slots are not counted multiple times. Each circuit is only linked with the portions of slots which are closer than the middle point of its distance with the following circuit. For example the middle circuit its only linked with the portions of slots inside the blue shaded area. Clearly the dependence of T on θ is characterized by a periodic behaviour with period given by $\Delta\phi_s$. Since the three magnets are also assumed to be mechanically connected to each other, the total torque between these and the slots is obtained by summing the three independent contributions: $T_{\text{Tot}}(\theta) = \sum_{k=1}^3 T^{(k)}(\theta)$. In general the contributions from the different magnetic circuits can superimpose constructively or destructively, thus resulting in a signal with higher or lower amplitude, respectively. The amplitude of the total signal can in fact be used to quantify the total effect of the cogging torque. The order of magnitude of the

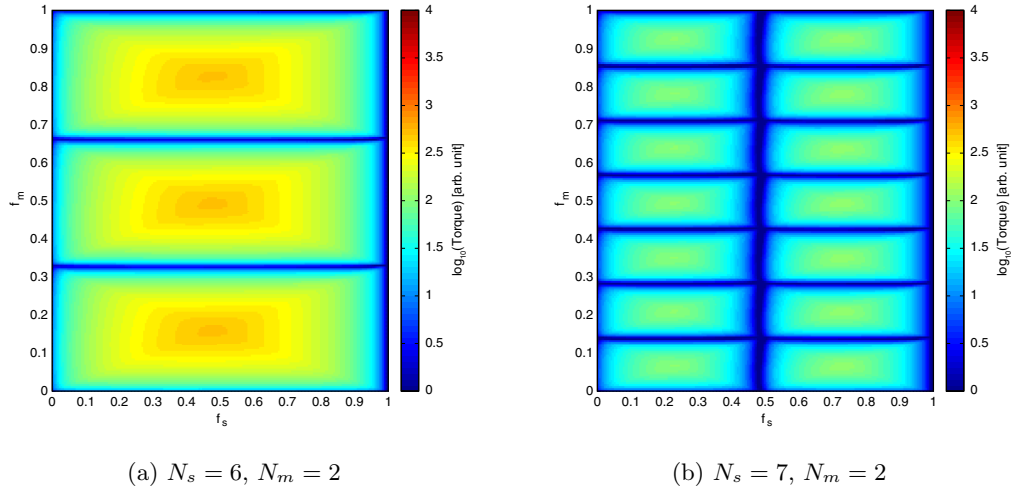


Fig. 3.10: Dependence of the order of magnitude of the cogging torque amplitude on the parameters f_s and f_m . These parameters represent respectively the angular sector spanned by each slot and each magnet, expressed as a function of the maximum available angles. Both the figures correspond to the case of two magnets, i. e.: $N_m = 2$. Figure 3.10a corresponds to $N_s = 6$, while figure 3.10b corresponds to the case $N_s = 7$. The figures show the existence of special values of f_s and f_m for which the torque is drastically reduced. The case of figure 3.10b presents more options, and the torque is generally lower. This is due to the fact that with $N_m = 2$ is convenient to have an odd number of slots.

cogging torque will be evaluated as the logarithm of the root mean square amplitude of the total signal $T_{\text{Tot}}(\theta)$.

Figures 3.10a and 3.10b show the dependence of the order of magnitude of the cogging torque on the angular sectors occupied by the magnets and the slots, expressed as $f_m = W_m/\Delta\phi_m$ and $f_s = W_s/\Delta\phi_s$, respectively. These results correspond to a geometry with only two magnetic circuits: $N_m = 2$. Figure 3.10a corresponds to the case $N_s = 6$, while figure 3.10b shows the case $N_s = 7$. As can be noticed the amplitude decreases at the borders $f_s = 0$ or $f_s = 1$, which corresponds to the disappearance of the angular dependence when the slots are either absent or fill the whole 2π angle. Similarly, the signal is zero for $f_m = 0$ or $f_m = 1$. The interesting feature of this graph is the presence of particular values of f_s and f_m leading to a very small torque amplitude. These values correspond to a perfectly destructive superposition between the torques associated with the two magnetic circuits. This indicates that the cogging torque can be reduced by finely tuning the angular sectors spanned by the magnets or the slots [50]. The case of an odd number of slot, i. e. figure 3.10b, allows more options, and the torque is generally lower. This is due to the fact that N_s and N_m are mutually prime. As mentioned in [50] and [49], it is advantageous to minimise the greatest common divisor between N_s and N_m .

We will now consider different combinations of these two values. In order to proceed systematically, for each pair (N_s, N_m) the results are evaluated on a grid of combinations of the relative angles f_s , and f_m . This grid spans the whole region $[0, 1] \times [0, 1]$, represented in figures 3.10a and 3.10b. The results for all the different points of the grid are then averaged to

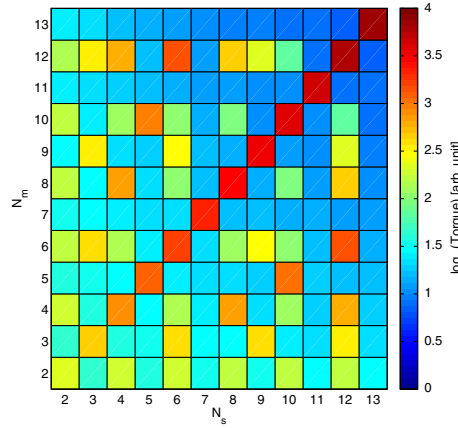


Fig. 3.11: Order of magnitude of the amplitude of the cogging torque for different combinations of number of magnets and number of slots. Each tile of this table corresponds to an average over different combinations of f_s and f_m . As can be noticed, the best result correspond to mutually prime numbers.

evaluate when a choice of (N_s, N_m) is better than another. This average is shown in figure 3.11 for different combinations of N_s and N_m , ranging from 2 to 13. As expected, the worst combinations are the ones where the greatest common divisor is large. The blue background giving a small torque corresponds to mutually prime numbers.

The simple model discussed in this section provides some insight in the causes leading to the emergence of cogging torque, and also suggest some possible solutions. The problem of eliminating this detrimental effect has been investigated extensively, and many approaches are available. One of the most frequently used solutions consists in skewing the permanent magnet blocks.

For rotary magnetocaloric devices the slots could represent different regenerators enclosing the magnetocaloric material. During the operation of the devices, the temperature of the magnetocaloric material inside a given regenerator varies with its angular position. The magnetic response of the magnetocaloric material is affected by its temperature, thus producing a net torque which includes a non-oscillating term. The power associated with this constant term is provided by the electric motor performing the rotation, and is the essential (unavoidable) power contribution entering in the expression of the COP of rotary magnetocaloric devices.

3.6 Boundaries and surface current

We have seen that the circuit analysis can include the effect of flux leakage across the lateral surfaces of the iron parts or the permanent magnets. Application of Ampère's law at the boundary between two different regions implies that as long as the free current is zero everywhere the tangential component of the field \mathbf{H} must be conserved across the surface. Denoting by $\hat{\mathbf{n}}$ the unit vector normal to the surface and by \mathbf{H}_1 and \mathbf{H}_2 the field on the two sides, the boundary condition is written as: $\hat{\mathbf{n}} \times (\mathbf{H}_1 - \mathbf{H}_2) = \mathbf{0}$. Because of the high permeability of the iron

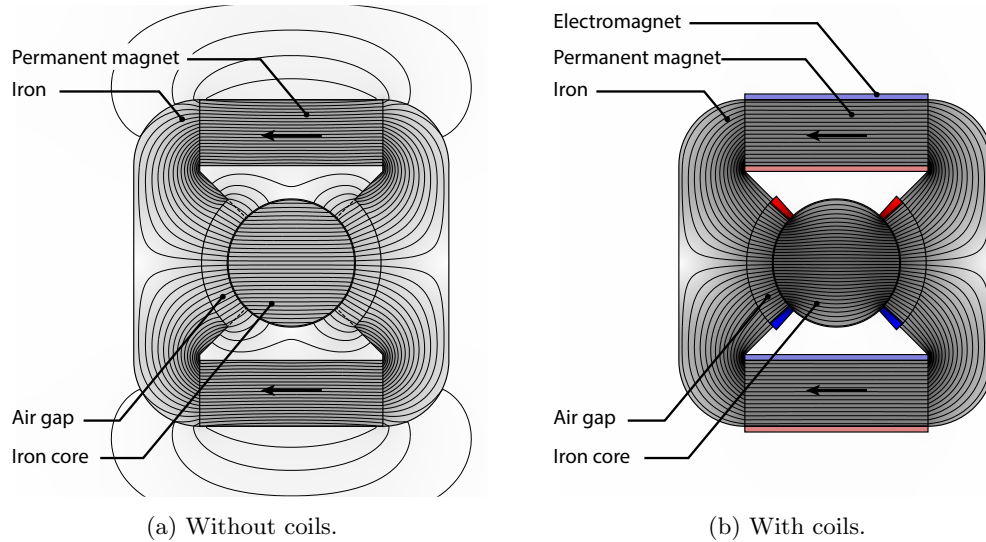


Fig. 3.12: Rotary device for room temperature magnetic refrigeration. The purpose of this comparison is to illustrate a possible way to completely eliminate the flux leakage across the lateral surfaces of the different components of the structure. This can be accomplished by strategically placing electromagnets at the external borders of the various parts. The current must be selected so that the tangential component of the magnetic field is conserved, which means that it is not necessary to include the coils at the borders of the iron parts. Figure 3.12a shows the simulation performed without coils, and thus exhibiting leakage, while figure 3.12b shows the effect of introducing the electromagnets.

parts, \mathbf{H} is very small inside these regions, and the circuit can quite realistically be considered insulated from the surrounding air. Inside the permanent magnets, whose permeability is often quite low, the field is given by $(\mathbf{B} - \mathbf{B}_r)/\mu$, implying that when \mathbf{B} is near to \mathbf{B}_r the error of not including the leakage is smaller. The greatest discrepancy is reasonably given by the lateral surfaces of the air gap, since assuming that the field suddenly becomes zero when crossing the imaginary line delimiting the air gap is of course unrealistic. If a free surface current is present on the separating surface, the boundary condition is modified as $\hat{\mathbf{n}} \times (\mathbf{H}_1 - \mathbf{H}_2) = \mathbf{K}$, where \mathbf{K} represents the free surface current density.

This suggests a practical way to achieve almost perfect insulation of the magnetic circuit. This can be accomplished by analysing the system with the magnetic circuit model, and then introducing the proper current densities which will correct the violation of the boundary conditions across the interfaces [83]. As example, we consider the magnetic structure shown in figure 3.12a. This system represents a rotary device for magnetic refrigeration. The magnetocaloric material is located in the air gap between the external structure, which includes the permanent magnets, and the central iron core. The purpose of this assembly is to create in the air gap alternating regions of low and high field intensity, each spanning an angle of 90° . The borders between the high and low field regions are represented in figure 3.12a as the four radial dashed lines. As can be seen from this result, calculated with the FEM method, the structure is far from being insulated from its surroundings. Moreover, a significant fraction of the total flux

leaks into the low field regions, thus decreasing the final performance of the device. Both these discrepancies between the FEM calculation and the idealized situation can be corrected by means of strategically placed coils. For what has been explained above, it is not necessary to place coils around the borders of the iron parts. As can be seen from figure 3.12b, the final result exhibits an almost perfect insulation. The out of the plane currents are indicated by in blue or red, corresponding to the two opposite directions. As expected, the currents at the borders of the high field regions are more intense than the currents at the lateral surfaces of the permanent magnets.

It must be stressed that, since the regenerators must be allowed to rotate inside the cylindrical air gap, the internal coils can only be located between two adjacent regenerator cassettes. This issue could be solved by including multiple copies of the coils. In a given moment the only active coils would be the ones that are closer to the borders between low and high field regions. The current being constant, the power consumed by the coils is inversely proportional to their cross section area. On the other hand, increasing the cross-section area of the coils would reduce the portion of the air gap that can be filled with magnetocaloric material. The angular sector spanned by each coil can be optimised to find the optimal thickness with respect to this trade-off.

Magnet design and optimisation

An optimisation algorithm maybe characterized by (a) the technique used to calculate the magnetic field for a given configuration, (b) the underlying assumptions about the magnetic behaviour of the materials in the system, (c) the possible restrictions to the class of objectives it can be applied to, (d) the extent of the search space that is considered, i.e., the possible allowed configurations, and finally (e) the optimisation strategy used to search for the optimal configuration among those allowed.

While a complete review of optimisation algorithms for magnet design is beyond the scope of this thesis, in this chapter we will analyse the general building blocks of optimisation methods, and define a framework to compare strengths and limits of different approaches. The optimisation methods described in the following chapters are discussed starting from the concepts introduced here.

4.1 Magneto-static equations

As mentioned in section 2.1, the field of magnetostatics is based on two fundamental equations. Gauss's law for magnetism:

$$\nabla \cdot \mathbf{B} = 0 \quad (4.1)$$

Ampère's law:

$$\nabla \times \mathbf{H} = \mathbf{J} \quad (4.2)$$

It is important to notice that for systems that are in the steady state regime, Ampère's law implies directly the following continuity equation:

$$\nabla \cdot \mathbf{J} = 0 \quad (4.3)$$

This is easily verified by applying the divergence operator to both sides of equation 4.2. Any current density field not obeying equation 4.3 would exhibit a corresponding variation of the electric charge density, therefore violating the steady state requirement that all the physical quantities are time independent.

Gauss's law for magnetism implies that the component of \mathbf{B} that is normal to the interface between two different materials is conserved across the interface. If the flux densities on the two sides of the surface are labelled by 1 and 2 respectively, and the unit vector normal to the surface is denoted by $\hat{\mathbf{n}}$, this continuity property is expressed as:

$$\hat{\mathbf{n}} \cdot (\mathbf{B}_2 - \mathbf{B}_1) = 0 \quad (4.4)$$

Ampère's law implies that the components of \mathbf{H} that are tangential to the interface are conserved. Denoting the surface current density flowing on the boundary surface by \mathbf{K} , and labelling the fields on the two sides by 1 and 2, the continuity property is expressed as:

$$\hat{\mathbf{n}} \times (\mathbf{H}_2 - \mathbf{H}_1) = \mathbf{K} \quad (4.5)$$

4.1.1 Scalar potential formulation

In absence of free currents Ampere's law reduces to $\nabla \times \mathbf{H} = \mathbf{0}$. This means that the magnetic field \mathbf{H} is an irrotational field and implies that is always possible to write it as gradient of a scalar potential, Φ , which is called *magnetic scalar potential*:

$$\mathbf{H} = -\nabla\Phi \quad (4.6)$$

If the magnetic scalar potential Φ is modified by adding a constant scalar constant Φ_0 , its gradient does not change and the corresponding magnetic field \mathbf{H} is the same. This transformation is called gauge transformation and is expressed by the following formula:

$$\Phi \rightarrow \Phi + \Phi_0 \quad (4.7)$$

The partial differential equation obeyed by Φ is derived by plugging the general constitutive relation, $\mathbf{B} = \mathbf{f}(\mathbf{H})$, into Gauss's law for magnetism:

$$\nabla \cdot \mathbf{f}(-\nabla\Phi) = 0 \quad (4.8)$$

Using the definition of magnetization \mathbf{M} , the equation can be formally simplified:

$$\nabla \cdot \nabla\Phi = \nabla \cdot \mathbf{M} \quad (4.9)$$

When the linear relation expressed by $\mathbf{B} = \mathbf{B}_r + \underline{\underline{\mu}}\mathbf{H}$ is considered, Gauss's law for magnetism leads to:

$$\nabla \cdot \left(\underline{\underline{\mu}} \nabla\Phi \right) = \nabla \cdot \mathbf{B}_r \quad (4.10)$$

Equation 4.9 leads to interpreting the quantity $\rho_M = -\nabla \cdot \mathbf{M}$ as an effective magnetic charge density. In fact, if the magnetization is known, equation 4.9 is Poisson's equation: $\nabla^2\Phi = -\rho_M$.

At the boundary between two materials the magnetization may be modeled as if it was discontinuous, leading to an effective magnetic charge surface density $\sigma_M = \hat{\mathbf{n}} \cdot \mathbf{M}$, where $\hat{\mathbf{n}}$ is the unit vector normal to the discontinuity surface at each point.

4.1.2 Vector potential formulation

Gauss's law for magnetism means that the magnetic flux density \mathbf{B} is solenoidal, and this implies that is always possible to write \mathbf{B} as the curl of a vector field, denoted by \mathbf{A} and called *magnetic vector potential*:

$$\mathbf{B} = \nabla \times \mathbf{A} \quad (4.11)$$

If the magnetic vector potential \mathbf{A} is modified by adding the gradient of a scalar field Λ , its curl does not change and the corresponding magnetic flux density \mathbf{B} is the same. This transformation is called gauge transformation and is expressed by the following formula:

$$\mathbf{A} \rightarrow \mathbf{A} + \nabla\Lambda \quad (4.12)$$

The freedom deriving from this family of possible transformations can be removed by imposing some additional condition on \mathbf{A} , an operation that is referred to as *gauge fixing*. An example of gauge condition is the Coulomb gauge, expressed by: $\nabla \cdot \mathbf{A} = 0$.

It is assumed that the general constitutive relation, $\mathbf{B} = \mathbf{f}(\mathbf{H})$, is invertible, and the inverse of the function \mathbf{f} is denoted by \mathbf{f}^{-1} . Ampere's law is then written in terms of the vector potential:

$$\nabla \times \mathbf{f}^{-1}(\nabla \times \mathbf{A}) = \mathbf{J} \quad (4.13)$$

Using the definition of magnetization \mathbf{M} , the equation can be formally simplified:

$$\frac{1}{\mu_0} \nabla \times \nabla \times \mathbf{A} = \mathbf{J} + \nabla \times \mathbf{M} \quad (4.14)$$

With the linear constitutive relation, $\mathbf{B} = \underline{\underline{\mu}} \mathbf{H} + \mathbf{B}_r$, equation 4.13 is written as:

$$\nabla \times \left((\underline{\underline{\mu}})^{-1} (\nabla \times (\mathbf{A})) \right) = \mathbf{J} + \nabla \times \left((\underline{\underline{\mu}})^{-1} \mathbf{B}_r \right) \quad (4.15)$$

The effective magnetic current density is defined as $\mathbf{J}_M = \nabla \times \mathbf{M}$. If the magnetization is known, equation 4.14 in the Coulomb gauge is the vector analogous of Poisson's equation: $\nabla^2 \mathbf{A} = -(\mathbf{J} + \mathbf{J}_M)$.

At the interface between two materials the effective magnetic surface current density is defined as $\mathbf{K}_M = -\hat{\mathbf{n}} \times \mathbf{M}$, where $\hat{\mathbf{n}}$ is the unit vector normal to the discontinuity surface at each point.

4.1.3 Boundary Conditions

The equations for Φ and \mathbf{A} admit a unique solution, once appropriate boundary conditions are fixed. For example it is considered Poisson's equation, $\nabla^2 \Phi = -\rho_M$, and the problem of solving this equation on the region of space delimited by a closed bounded surface S . The condition of specifying the value of Φ on all the points of the surface S is called Dirichlet boundary condition. The condition of specifying the value of the component of the gradient of Φ that is normal to the surface S is called Neumann boundary condition. It is possible to show that Poisson's equation admits a unique solution with Dirichlet or Neumann boundary conditions. Different conditions need to be introduced if the domain of the potentials is the whole space, for example imposing that the fields are square integrable vector functions implies that all the derivatives of the potentials vanish at infinity.

It is interesting to consider the boundary conditions that describe the magnetic behaviour at the boundary of a perfect magnetic conductor, or a perfect magnetic insulator.

Equation 4.5 implies that on the external side of the boundary S of a perfect magnetic conductor (infinite permeability), the field is normal to the surface: $\mathbf{H} \perp S$. This means $\Phi = \text{const.}$, since the gradient is normal to the level surfaces. In the vector potential formulation this condition is written $\hat{\mathbf{n}} \times \mathbf{H} = \hat{\mathbf{n}} \times \mathbf{f}^{-1}(\nabla \times \mathbf{A}) = \mathbf{0}$. The boundary condition for Φ implies that for an arbitrary magnetic system, it is possible to start with a closed surface characterized by $\Phi = \text{const.}$, and replace with perfect magnetic conductor all the material on one side of the surface without affecting the solution on the other side of the surface.

Equation 4.4 implies that on the external side of the boundary S with a perfect magnetic insulator (zero permeability), the flux density is parallel to the surface: $\mathbf{B} \parallel S$. This means $\mathbf{A} \times \hat{\mathbf{n}} = \mathbf{0}$, since a closed line integral of \mathbf{A} on the surface is equal to the flux of \mathbf{B} through the portion of the surface enclosed by the loop. In the scalar potential formulation this condition is written: $\hat{\mathbf{n}} \cdot \mathbf{B} = \hat{\mathbf{n}} \cdot \mathbf{f}(-\nabla \Phi) = 0$. The boundary condition for \mathbf{A} implies that for an arbitrary

magnetic system, it is possible to start with a closed surface characterized by $\mathbf{A} \times \hat{\mathbf{n}} = \mathbf{0}$, and replace with perfect magnetic insulator all the material on one side of the surface without affecting the solution on the other side of the surface.

4.2 Solving the equations

In section 4.1, the magnetic scalar potential and magnetic vector potential have been introduced, and the partial differential equations obeyed by these potential have been derived from the fundamental equations of magnetostatics. In section 4.2 we will focus on analytical and computational techniques that can be used to solve these partial differential equation.

4.2.1 Formal solution

The method of Green's function can be applied to derive the formal solutions to the equations of magnetostatics [75, 42]. It is considered a linear differential operator L acting on the scalar field Φ . The starting point is the following non-homogeneous linear equation for Φ , involving the scalar field ρ as constant term:

$$L[\Phi(\mathbf{x})] = \rho(\mathbf{x}) \quad (4.16)$$

The Green's function G for the linear operator L is defined as the function of \mathbf{x} and \mathbf{x}' , satisfying the following equation:

$$L[G(\mathbf{x}, \mathbf{x}')] = \delta^3(\mathbf{x} - \mathbf{x}') \quad (4.17)$$

The Green's function can be interpreted as the generalization to the infinite dimensional case of the matrix expansion of the operator L^{-1} . The formal solution of equation 4.16 can be written in terms of the Green's function G :

$$\Phi(\mathbf{x}) = \int d^3x' G(\mathbf{x}, \mathbf{x}') \rho(\mathbf{x}') \quad (4.18)$$

It is important to notice that the function G is not completely determined since it is defined by the differential equation 4.17. This additional freedom is removed by combining equation 4.16 with a set of boundary conditions.

If the magnetization is known, equation 4.9 is Poisson's equation with $-\rho_M$ as constant term. For the three dimensional Laplace operator $L = \nabla^2$ the Green function $G(\mathbf{x}, \mathbf{x}')$ given by:

$$G(\mathbf{x}, \mathbf{x}') = - \left(\frac{1}{4\pi} \right) \frac{1}{\|\mathbf{x} - \mathbf{x}'\|} \quad (4.19)$$

The formal solution for the magnetic scalar potential Φ is then given by:

$$\Phi(\mathbf{x}) = \left(\frac{1}{4\pi} \right) \int d^3x' \frac{\rho_M(\mathbf{x}')}{\|\mathbf{x} - \mathbf{x}'\|} \quad (4.20)$$

The solution can be expressed in operator notation as $\Phi = F_\rho^\Phi[\rho_M]$.

However, the magnetization \mathbf{M} is not always known in advance since in general it is dependent on the field \mathbf{H} . The same mathematical techniques can be applied to derive a formal solution to equation 4.10. In this case the differential operator L depends on the permeability

tensor field $\underline{\mu}(\mathbf{x})$ so the Green's function G is not known in general. However the linear constitutive relation $\mathbf{B} = \underline{\mu} \mathbf{H} + \mathbf{B}_r$ assumes that remanent flux density field $\mathbf{B}_r(\mathbf{x})$ is independent from \mathbf{H} and it is justified to use $\nabla \cdot \mathbf{B}_r$ as constant term of the differential equation 4.16. The solution for the magnetic scalar potential Φ can then be expressed in the integral form given by equation 4.18 which shows the linearity of Φ with respect to the source \mathbf{B}_r . Using $\mathbf{H} = -\nabla\Phi$ and the linear constitutive relation, it is possible to express the field and flux density generated by a given remanence in operator notation:

$$\mathbf{H} = \mathbf{F}_r^H[\mathbf{B}_r], \quad \text{and} \quad \mathbf{B} = \mathbf{F}_r^B[\mathbf{B}_r] \quad (4.21)$$

The operators \mathbf{F}_r^H and \mathbf{F}_r^B are both linear.

The Green's function approach can be used for the case of a vector differential equation such as:

$$\mathbf{L}[\mathbf{A}(\mathbf{x})] = \mathbf{J}(\mathbf{x}) \quad (4.22)$$

For this equation $\underline{G}(\mathbf{x}, \mathbf{x}')$ is in general a 3×3 matrix (rank-2 tensor) acting on the vector $\mathbf{J}(\mathbf{x}')$. The formal solution is:

$$\mathbf{A}(\mathbf{x}) = \int d^3x' \underline{G}(\mathbf{x}, \mathbf{x}') \mathbf{J}(\mathbf{x}') \quad (4.23)$$

The formal solution to equation 4.14 is:

$$\mathbf{A}(\mathbf{x}) = \left(\frac{\mu_0}{4\pi}\right) \int d^3x' \frac{\mathbf{J}(\mathbf{x}') + \mathbf{J}_M(\mathbf{x}')}{\|\mathbf{x} - \mathbf{x}'\|} \quad (4.24)$$

The solution is expressed in operator notation as: $\mathbf{A} = \mathbf{F}_J^A[\mathbf{J} + \mathbf{J}_M]$. The Biot-Savart law is obtained from equation 4.24 using $\mathbf{B} = \nabla \times \mathbf{A}$:

$$\mathbf{B}(\mathbf{x}) = \frac{\mu_0}{4\pi} \int d^3x' \frac{\left(\mathbf{J}(\mathbf{x}') + \mathbf{J}_M(\mathbf{x}')\right) \times (\mathbf{x} - \mathbf{x}')}{\|\mathbf{x} - \mathbf{x}'\|^3} \quad (4.25)$$

This solution is only useful if \mathbf{M} is known, i.e. when \mathbf{M} does not depend on \mathbf{H} . For the case of the linear constitutive relation equation 4.14 is replaced with equation 4.15. The Green's function for the differential operator appearing in the left-hand side of equation 4.15 is not known in general, but the source terms \mathbf{J} and \mathbf{B}_r are assumed to be independent from \mathbf{H} . It is possible to separate the field generated by the current term from the field generated by the remanence term and to write the formal solution in operator notation:

$$\mathbf{H} = \mathbf{F}_J^H[\mathbf{J}] + \mathbf{F}_r^H[\mathbf{B}_r], \quad \text{and} \quad \mathbf{B} = \mathbf{F}_J^B[\mathbf{J}] + \mathbf{F}_r^B[\mathbf{B}_r] \quad (4.26)$$

All the operators appearing in equation 4.26 are linear. This property is extremely useful for the purpose of magnet design and optimisation and is fulfilled as long as the linear relation $\mathbf{B} = \underline{\mu} \mathbf{H} + \mathbf{B}_r$ is assumed, with pre-determined permeability, $\underline{\mu}(\mathbf{x})$, and sources, $\mathbf{J}(\mathbf{x})$ and $\mathbf{B}_r(\mathbf{x})$.

In this case *the magnetic field generated by the different sources is the superposition of the fields generated by the individual sources.*

4.2.2 Analytically solvable geometries - Halbach cylinders

The geometry of some magnetic systems are very simple or highly symmetrical, which makes it possible to employ analytical approaches to derive the exact solution to the partial differential equations. We consider a system for which all the materials are characterized by a linear B - H relations. Let us start with equation 4.10 that is obeyed by the scalar potential Φ . As any linear non-homogeneous equation, the solution can be decomposed into the general solution of the homogeneous equation plus a particular solution of the non-homogeneous equation. A unique solution is then obtained by applying proper boundary conditions. Spectral methods can be used to get the general solution to the homogeneous equation.

For simplicity, we focus on a geometry that is subdivided into several regions and we assume that the permeability tensor is uniform over each of these regions. Since the permeability is piece-wise constant, in each region equation 4.10 reduces to Poisson's equation:

$$\nabla^2 \Phi = (\underline{\mu})^{-1} \nabla \cdot \mathbf{B}_r \quad (4.27)$$

The corresponding homogeneous equation is Laplace's equation: $\nabla^2 \Phi = 0$. The general solution of Laplace's equation for each region can be expanded as a linear combination of orthogonal eigenfunctions of the Laplace operator ∇^2 . The continuity equations 4.4 and 4.5 must be applied at each interface between two adjacent regions. These are expressed as equations involving the coefficients of expansion of Φ for the two regions. The unique solution for the whole geometry is then obtained by applying the boundary conditions at the external border of the domain of Φ .

Many of the examples that will be analysed in the following sections are parametrized by cylindrical coordinates ρ , ϕ and z . Moreover, if the geometry is invariant with respect to a translation in the z direction, the z coordinate is irrelevant. For these cases it is relevant to consider the general solution of Laplace's equation in polar coordinates ρ and ϕ . If the potential Φ is required to be continuous at any point, except possibly for the origin or infinity, the general solution is given by:

$$\Phi(\rho, \phi) = \Phi_0 + a_0 \log(\rho) + \sum_{n=1}^{+\infty} (c_n^{(\text{In})} \rho^n + c_n^{(\text{Out})} \rho^{-n}) \cos(n\phi) + \sum_{n=1}^{+\infty} (s_n^{(\text{In})} \rho^n + s_n^{(\text{Out})} \rho^{-n}) \sin(n\phi) \quad (4.28)$$

The constant term Φ_0 expresses the gauge freedom and does not have any physical consequence. The fields generated by the coefficients $c^{(\text{In})}$ and $s^{(\text{In})}$ are called interior cylindrical multipole fields and the fields generated by the coefficients $c^{(\text{Out})}$ and $s^{(\text{Out})}$ are called exterior cylindrical multipole fields.

It is possible to use these techniques to derive the solution for the Halbach cylinder geometry [91, 102], which is broadly used in magnetic systems for different applications [4, 93]. The geometry of this system can be modelled as an infinitely long hollow cylindrical shell, with internal radius denoted by R_I and external radius denoted by R_O . The permanent magnet material filling the region between these two radii is characterized by a linear B - H relation, with isotropic permeability μ . The remanent flux density field \mathbf{B}_r depends only on the angular coordinate ϕ according to the following equation:

$$\mathbf{B}_{r,p}(\rho, \phi) = B_r \left(\cos(p\phi) \hat{\mathbf{e}}_\rho + \sin(p\phi) \hat{\mathbf{e}}_\phi \right) \quad (4.29)$$

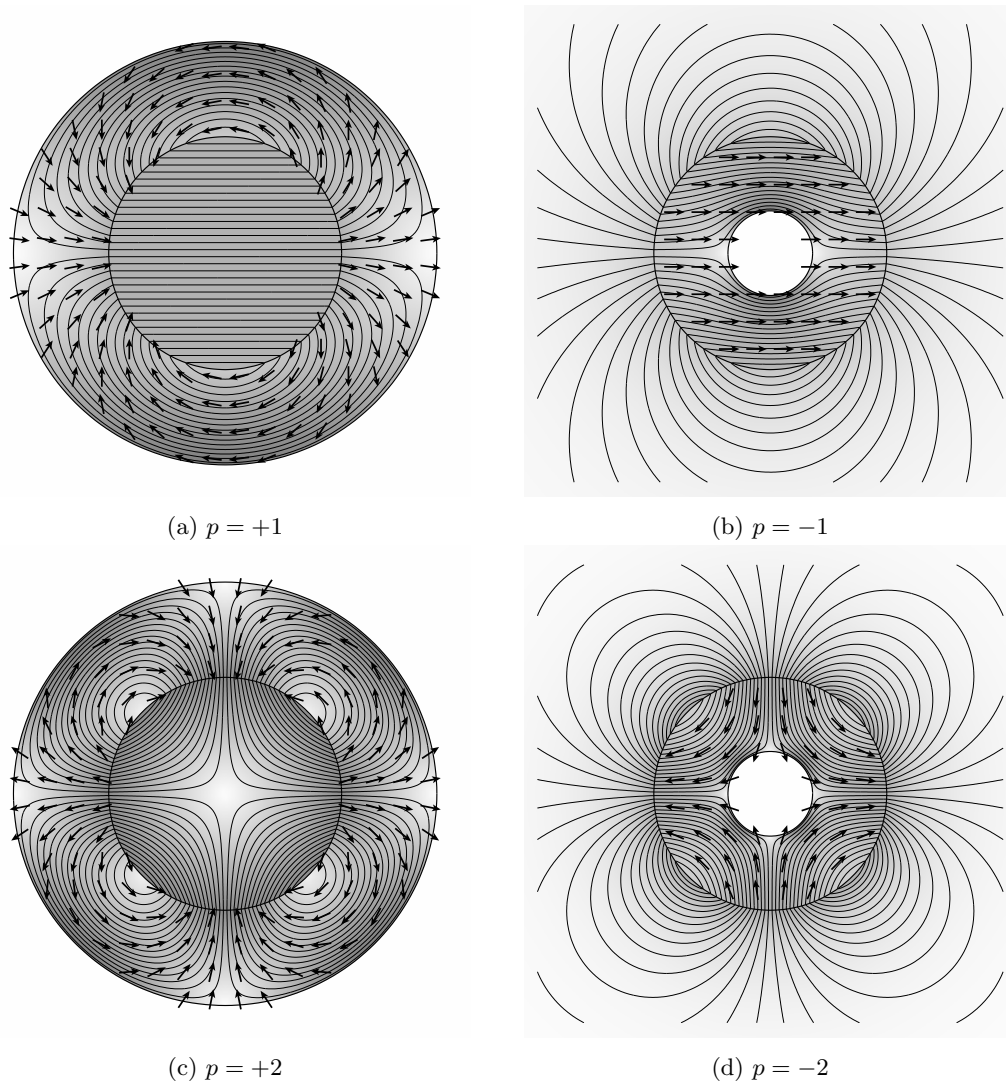


Fig. 4.1: Halbach cylinders corresponding to different values of p . The positive values of p correspond to self-insulated cylinders generating a field in their inner cavity, while the negative values correspond to cylinders generating the field in the external region. These ideal remanence distributions always generate a perfect multi-pole field, the cases $p = \pm 1$ corresponding to dipole fields, and $p = \pm 2$ to quadrupole fields. Increasing the ratio between external radius and internal radius, i.e. R_O/R_I , increases the intensity of the produced field.

The integer parameter denoted by p determines the multi-pole moment of the field generated by the magnetic structure. The exact solution can be determined also in presence of two cylindrical surfaces of perfect magnetic conductor with radii $R_c \leq R_I$ and $R_e \geq R_O$. When these cylinders are not present, and for the special case of a permanent magnet with $\mu = \mu_0$, the flux density

\mathbf{B} assumes a particularly simple expression:

$$\mathbf{B}_{p>0}^{(\text{In})}(\rho, \phi) = B_r f_p \rho^{p-1} \left(\cos(-p\phi) \hat{\mathbf{e}}_\rho + \sin(-p\phi) \hat{\mathbf{e}}_\phi \right) \quad (4.30)$$

$$\mathbf{B}_{p<0}^{(\text{Out})}(\rho, \phi) = B_r f_p \rho^{p-1} \left(\cos(-p\phi) \hat{\mathbf{e}}_\rho + \sin(-p\phi) \hat{\mathbf{e}}_\phi \right) \quad (4.31)$$

The notation $\mathbf{B}_{p>0}^{(\text{In})}$ is used to indicate the flux density generated by a cylinder with $p > 0$ in the region $\rho \leq R_I$, since the flux density is null in the region $\rho \geq R_O$. Similarly, $\mathbf{B}_{p<0}^{(\text{Out})}$ indicates the field generated by a cylinder with $p < 0$ in the region $\rho \geq R_O$, and the flux density is null in the region $\rho \leq R_I$. For $p = 0$ the flux density is null in both the regions. In all cases the solution does not exhibit singularities, since the norm of the flux density goes to zero in the limits $\rho \rightarrow 0$ and $\rho \rightarrow +\infty$. The scaling factor denoted by f_p is determined by p , R_I and R_O according to the following expressions:

$$f_{p>1} = \left(\frac{p}{p-1} \right) \left(1 - \left(\frac{R_I}{R_O} \right)^{+p-1} \right) \left(\frac{1}{R_I} \right)^{p-1} \quad (4.32)$$

$$f_{p<0} = \left(\frac{p}{p-1} \right) \left(1 - \left(\frac{R_I}{R_O} \right)^{-p+1} \right) \left(\frac{1}{R_O} \right)^{p-1} \quad (4.33)$$

$$f_{p=1} = \log \left(\frac{R_O}{R_I} \right) \quad (4.34)$$

The fact that the radii R_I and R_O affect the solution only by determining the multiplicative factor f_p , gives an analogous to the gravitational shell theorem: the field generated by a hollow cylinder with $p < 0$ in the external region is equivalent to the field of a point multi-pole placed in the origin. and the field in the internal region is zero. For cylinders with $p > 0$ the result is reversed: the field in the internal region is an internal multi-pole field and the field in the external region is zero.

It is very interesting to notice another symmetry exhibited by this geometry: the field generated by a cylinder with a given p is proportional to the remanence of the cylinder with opposite p :

$$\mathbf{B}_p \propto \mathbf{B}_{r, -p} \quad (4.35)$$

This can be also noticed by comparing the flux lines indicating \mathbf{B} in the left panels with the black arrows indicating \mathbf{B}_r in the right panels or vice versa.

The case of $p = 1$ is particularly relevant for the applications since the field inside the cylindrical bore in this configuration is perfectly uniform and its norm is given by $B_r \log(R_O/R_I)$, which means that in this ideal situation is possible to achieve a field with the desired magnitude by adjusting the ratio R_O/R_I .

4.2.3 Finite Element Method

When it is not possible to determine the solution the partial differential equations governing the potentials Φ or \mathbf{A} , we may resort to numerical techniques to calculate an approximate solution. As an example, it is considered the linear differential equation:

$$\mathbf{L}[\Phi] = -f \quad (4.36)$$

Where $\Phi \in L_2(\Omega)$ is a square integrable function defined over the domain Ω . The starting point [44] is expressing equation 4.36 in *weak form*, that is: requiring that the equation $(L\Phi, \Psi)_2 = -(f, \Psi)_2$ is satisfied for all the test functions Ψ belonging to a sufficiently large¹ functional space \mathcal{X} :

$$\int_{\Omega} d^3x \left(L[\Phi](\mathbf{x}) \right) \Psi(\mathbf{x}) + f(\mathbf{x}) \Psi(\mathbf{x}) = 0, \quad \forall \Psi \quad (4.37)$$

For the example of the Poisson's equation $\nabla^2\Phi = -f$ with the boundary condition that Φ is zero on the boundary of Ω , we can require that the test function Ψ is differentiable and also vanishes on the border of Ω . Application of Green's theorem gives:

$$\int_{\Omega} d^3x \left(\nabla^2\Phi(\mathbf{x}) \right) \Psi(\mathbf{x}) = - \int_{\Omega} d^3x \nabla\Phi(\mathbf{x}) \cdot \nabla\Psi(\mathbf{x}) \quad (4.38)$$

Which leads to the weak formulation of Poisson's equation:

$$\int_{\Omega} d^3x \nabla\Phi(\mathbf{x}) \cdot \nabla\Psi(\mathbf{x}) = \int_{\Omega} d^3x f(\mathbf{x}) \Psi(\mathbf{x}) \quad (4.39)$$

If the set of test functions $\psi_n(\mathbf{x})$ is an orthonormal basis for the Hilbert space $L_2(\Omega)$, then the functions Φ , and f , and the operator L can be expanded, according to the following expressions:

$$\Phi_n = (\Phi, \psi_n)_2 = \int_{\Omega} d^3x \Phi(\mathbf{x}) \psi_n(\mathbf{x}) \quad (4.40)$$

$$f_n = (f, \psi_n)_2 = \int_{\Omega} d^3x f(\mathbf{x}) \psi_n(\mathbf{x}) \quad (4.41)$$

$$L_{nm} = (L[\psi_m], \psi_n)_2 = \int_{\Omega} d^3x \left(L[\psi_m](\mathbf{x}) \right) \psi_n(\mathbf{x}) \quad (4.42)$$

Equation 4.37 can be written in terms of these coefficients:

$$\sum_m L_{nm} \Phi_m = -f_n, \quad \forall n \quad (4.43)$$

The matrix A is referred to as *stiffness matrix* and the column vector f as *force vector*, or load vector. Note that the stiffness matrix for the problem expressed by equation 4.39 is symmetric.

The basis ψ_n might be chosen with the purpose of simplifying the matrix equation 4.43. This is often the case when the set ψ_n is the set of eigenfunction of some Hermitian operator defined on $L_2(\Omega)$. Let us consider the case of the Poisson's equation on a rectangular domain Ω . Since the Fourier basis is the set of eigenfunctions of the Laplace operator itself, the matrix A is diagonal on this basis and equation 4.43 can be solved immediately simply by calculating the Fourier expansion of the source term f . This class of methods goes under the name of *spectral methods*.

Since the basis of the Hilbert space is in general composed by an infinite number of elements, the equation is not easy to handle except for special cases. For numerical computations it is convenient to consider a finite set of functions $\{\psi_n\}_{n=1,\dots,N}$, which allows us to approximate

¹The properties required for the space \mathcal{X} are described in [44].

the true solution Φ . Equation 4.43 can be projected on the vector subspace $\mathcal{X}^{(N)}$ spanned by the finite set $\{\psi_n\}$. This is called *Galerkin approximation*:

$$\sum_{m=1}^N L_{nm} \Phi_m^{(N)} = -f_n, \quad \text{for } n = 1, \dots, N \quad (4.44)$$

where $\Phi^{(N)}$ denotes the solution of the approximate equation. By subtracting equation 4.44 from equation 4.43 we notice that the only terms of the expansion of the error $\Delta = L[\Phi] - L[\Phi^{(N)}]$ are those for $n > N$. In other words: Δ is normal to $\mathcal{X}^{(N)}$.

It is possible to choose the finite set of functions $\{\psi_n\}$ such that each of the $\psi_n(\mathbf{x})$ has support only in a neighborhood of a point \mathbf{x}_n belonging to some discretisation of the domain Ω . This leads to the class of methods known as *finite element methods* (FEM).

Let us consider again the case of Φ vanishing on the border of Ω , but with the differential equation 4.10:

$$\nabla \cdot (\mu \nabla \Phi) = \nabla \cdot \mathbf{B}_r \quad (4.45)$$

corresponding to $L[\Phi] = \nabla \cdot (\mu \nabla \Phi)$ and $f = -\nabla \cdot \mathbf{B}_r$. The stiffness matrix L and the force vector f are then given by:

$$L_{nm} = - \int_{\Omega} d^3x \mu(\mathbf{x}) \nabla \psi_m(\mathbf{x}) \cdot \nabla \psi_n(\mathbf{x}) \quad (4.46)$$

$$f_n = - \int_{\Omega} d^3x (\nabla \cdot \mathbf{B}_r(\mathbf{x})) \psi_n(\mathbf{x}) \quad (4.47)$$

It is worth mentioning that stiffness matrix and the force vector are used in many topology optimisation procedures based on FEM simulations. It is considered an optimisation problem for which the objective functional \mathcal{S} can be expressed in terms Φ , which naturally covers all the functionals depending on the field. The geometrical arrangement of materials having different magnetic properties is controlled by a number of design variables ξ_i which could be, e.g., the value of a certain control field $\xi(\mathbf{x})$ at the point \mathbf{x}_i . The derivative of \mathcal{S} with respect to the design variables ξ_i is then calculated by:

$$\frac{d\mathcal{S}}{d\xi_i} = \sum_n \frac{\partial \mathcal{S}}{\partial \Phi_n} \frac{\partial \Phi_n}{\partial \xi_i} \quad (4.48)$$

Since the potential Φ satisfies $\sum_n L_{nm} \Phi_m = f_n$, the derivatives $\frac{\partial \Phi_m}{\partial \xi_i}$ can be expressed in terms of the inverse of the stiffness matrix, denoted by L^{-1} :

$$\frac{\partial \Phi_m}{\partial \xi_i} = (L^{-1})_{mn} \frac{df_n}{d\xi_i} + \left(\frac{dL^{-1}}{d\xi_i} \right)_{mn} f_n \quad (4.49)$$

If the design variable ξ_i does not affect the remanence \mathbf{B}_r then equation 4.47 implies that $\frac{df_n}{d\xi_i} = 0$. Similarly, if ξ_i does not affect the permeability μ then equation 4.46 implies that $\frac{dL^{-1}}{d\xi_i} = 0$. When the inverse of the stiffness matrix is known, it is possible to easily calculate the sensitivity of \mathcal{S} with respect to the design variable ξ_i . This calculation can be applied in iterative approaches such as sequential linear programming.

4.2.4 Validation

This section discusses strategies adopted to evaluate the accuracy and precision of the results of FEM simulations. As FEM simulations are used extensively in this thesis, it is important to be able to rely on the results calculated with this method. This means verifying that the numerical integration of the differential equations leads to the correct result, and that the mathematical model corresponding to these equations is a realistic description of the behaviour of a real magnetic system.

As mentioned in section 4.2.2, the analytical solution for the Halbach cylinder geometry is available also for the case of a permanent magnet material characterized by a general permeability μ . The solution can be calculated analytically even when an internal core and an external yoke of infinite permeability are introduced in systems at the radii $R_c \leq R_I$ and $R_e \geq R_O$, respectively. Many different cases have been considered and simulated with finite element methods. The results always exhibited a perfect agreement between the numerical simulation and the analytical calculations.

As long as the susceptibility is zero at any point, it is also straightforward to use analytical methods, e.g. equation 4.20, to calculate the field generated by a two-dimensional uniformly magnetized polygon of arbitrary shape, representing an infinitely long prism. Some examples of randomly generated polygonal prism have been simulated with finite element methods, showing again a perfect match with the theory.

These validations however, only prove that the finite element methods calculations are correct. The only way to evaluate if the mathematical model is a faithful description of the real magnetic system is by means of experimental validation. For this purpose, it is considered the rotary device for magnetic refrigeration previously developed by the magnetic refrigeration group of the Technical University of Denmark, represented in figure 1.2a. The three-dimensional model and the middle cross-section transversal to the z axis are shown in figure 4.2a and 4.2b, respectively. The geometry presents mirror symmetry with respect to all the planes x - y , y - z and z - x , passing by the central point, which is also the origin of the axes. In order to reveal the inner part of the system, one octant of the geometry is not displayed in figure 4.2a. The magnetic system is composed by two separate coaxial cylinders. The external cylinder includes 12 permanent magnet blocks, (NdFeB, grade N50), and two iron parts allowing a return path for the magnetic flux. The inner cylinder is an iron core which allows the flux from the left half, to the right half. The magnetocaloric material experiencing the field is collected in cassettes located in the air gap between the two cylinders. The cassettes, not included in this model, remain stationary with respect to the inner iron core, as the external cylinder rotates thus shifting the high field regions to different angular sectors of the air gap. The effect of the rotation is thus to cyclically vary the intensity of the field experienced by each cassette. The high field regions are the two angular sectors spanning an angle of 90° each, which are delimited in figure 4.2b by the radial dotted lines. As can be noticed from figure 4.2b, the magnetic circuit describing this system is the single loop realized by combining in series the two permanent magnets and the two air gaps corresponding to the left and right halves, respectively. The procedure leading to the design of this device and the values of some of the parameters describing its geometry are discussed in [103]. Many examples analyzed in this thesis consider a geometry inspired by this magnetic system, as the examples represented in figures 6.3b, 6.7a and 6.25a.

The magnetic system has been modelled with FEM simulation, by assuming that the per-

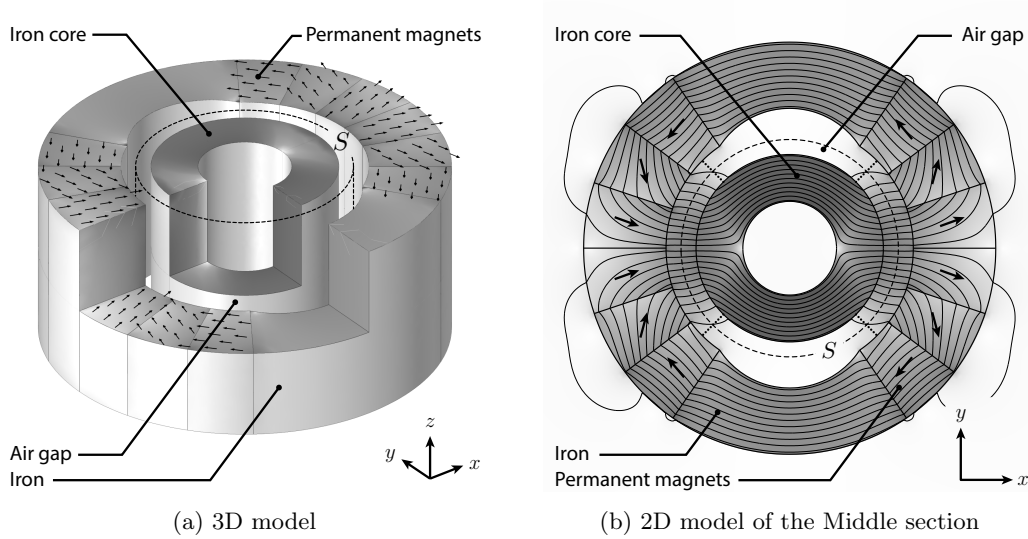


Fig. 4.2: Rotary device for room temperature magnetic refrigeration. The model corresponds to the prototype shown in figure 1.2a. Figure 4.2a shows the three-dimensional model, while 4.2b represents the middle section. The purpose of this system is to create a field inside the air gap characterized by two high field regions spanning an angle of 90° each, separated by two low field regions spanning the same angle. The borders between these regions are indicated in figure 4.2b by the radial dotted lines. The magnetic field of the prototype has been measured in different positions of the cylindrical surface S which corresponds to the middle radius of the air gap.

manent magnet material is characterized by the linear relation $\mathbf{B} = \mu\mathbf{H} + \mathbf{B}_r$ with $\mu = 1$ and $B_r = 1.4$ T. The iron parts have been modelled with the non-linear isotropic \mathbf{B} - \mathbf{H} relation included in the material library of the commercial software Comsol. The B - H curve is characterized by a magnetic saturation of around 2 T.

The magnetic field in the air gap has been measured in different angular and vertical positions of the cylindrical surface S indicated in figures 4.2a and 4.2b by the black dashed lines. This surface is coaxial with the geometry and its radius R_S corresponds to the middle radius of the air gap. The characterization has been performed using a three-axis Hall probe (Arepo s. r. o. AXIS-3) which measures each of the three components of field separately. The measurement spans the full 360° angle, and all the vertical positions from the bottom border to the top border of the magnetic structure, i.e. $z \in [-50 \text{ mm}, +50 \text{ mm}]$. The vertical grid is composed by 21 points spaced by 5 mm each, the angular grid is composed by 250 points for a total of $21 \times 250 = 5250$ data points. Figure 4.3a shows the results for one quarter of the air gap, corresponding to the angular sector $\phi \in [-90^\circ, +90^\circ]$ of the upper half of the air gap, i.e. $z \in [0 \text{ mm}, +50 \text{ mm}]$. The norm of the flux density, expressed in teslas, is plotted as function of ϕ for 6 different vertical positions. the experimental data is indicated by the dashed lines, and the FEM simulation is indicated by the solid lines. Figure 4.3b, shows the dependence on the z coordinate evaluated at the angular position $\phi = 0^\circ$. The results show a satisfactory agreement between the model and the measurement. In order to quantify the difference between the two

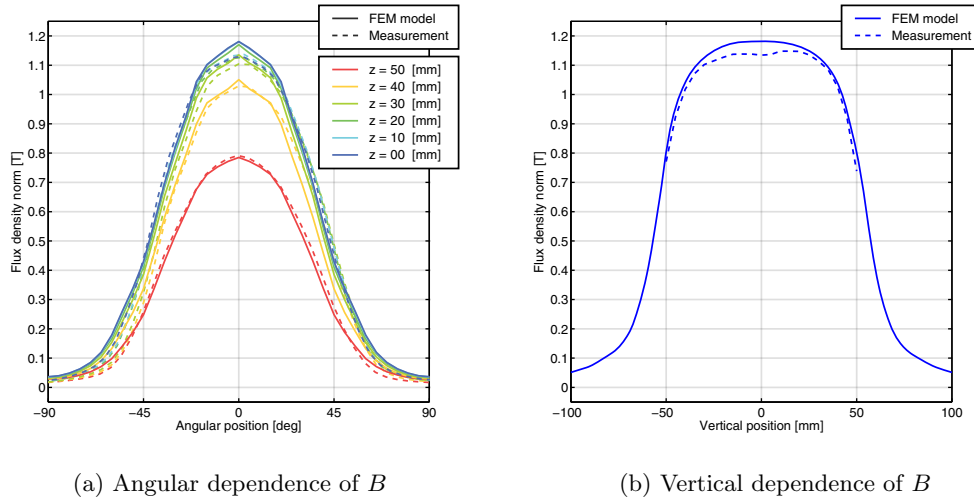


Fig. 4.3: 4.3a: the flux density \mathbf{B} in the air gap of the system shown in figure 4.2a is plotted as function of the angular position ϕ for different values of vertical position z . The results of the experimental measurement with a three-axes Hall probe are compared with the FEM calculation. The experimental data and the numerical calculations are represented as dashed lines and solid lines, respectively, while the color indicates the vertical position. 4.3b: vertical dependence of the flux density norm evaluated at $\phi = 0^\circ$. The comparison shows a good agreement between the two data sets.

data sets, it is considered the parameter Δ , defined as the average norm of the vector difference between the experimental data $\mathbf{B}^{\text{Exp.}}$ and the FEM data \mathbf{B}^{FEM} :

$$\Delta = \frac{\int_S dz d\phi \|\mathbf{B}^{\text{Exp.}}(z, \phi) - \mathbf{B}^{\text{FEM}}(z, \phi)\|}{\int_S dz d\phi} \quad (4.50)$$

Numerical evaluation of the integrals appearing in 4.50 over the 21×250 grid mentioned above leads to an average error of $\Delta = 0.064$ T, which is a reasonable accuracy for this case.

This difference might be due to different factors. One of the sources of error is the uncertainty on the values of ϕ and z corresponding to the experimental data-points. Because of engineering tolerances, the geometry of the real structure is not exactly identical to the geometry of the model. The model used to describe the magnetic behaviour is judged to be a realistic description of the real behaviour of the magnetic materials in the structure. However, the value of $\mu = 1$ used for the permeability of the permanent magnets might be slightly different than the real slope of the B - H curve around its working point, which is usually around 1.03 – 1.05 for typical Neodymium magnets. Moreover, as different parts of the magnets are experiencing different demagnetization fields, the working point of small areas of the geometry might be in the region of the B - H curve where the linear approximation is not a completely realistic description. Some of these effects are discussed in chapter 7. Small non-linear effects might also be present along the directions transversal to the easy axis of magnetization. Similarly, the real B - H curve of the iron parts of the structure might be slightly different from the one included in the material library. The FEM simulation introduces some numerical noise. This

is supposed to be a minor source of error, as the mesh underlying the simulation is extremely fine with respect to the complexity of the geometry, and the integration tolerances have been selected adequately. However, in the vicinity of sharp edges FEM simulations might be unstable with respect to mesh refinement, thus slightly overestimating the intensity of the field in the adjacent region. Besides being a source of numerical instability, sharp edges are also one of the differences between the geometry of the model and the real structure, as the edges are filleted during the manufacturing. Finally, the measurement itself is always affected by a certain degree of imprecision. Because of the precision and reliability of the equipment used for the measurement this is also presumed to have a relatively small on the total error.

Determining the relative contribution of all the potential sources of error mentioned above would require further investigations and measurements, going beyond the scope of this thesis. The difference between the experimental measurement and the simulation is small enough to rely on the other FEM results considered in this work.

4.3 Theorems

In this section we will derive different reciprocity theorems which are the foundations of the some of the optimisation methods presented in the following sections.

4.3.1 Remanence Reciprocity theorem

In order to formulate the reciprocity theorems[74], we need to start with a few assumptions:

- *Localized Fields*: we can always define a set Ω large enough such that every surface integral defined on the border $\partial\Omega$ will lead to a null value (normally Ω coincides with the whole space and the set $\partial\Omega$ is at infinite distance).
- *Steady State*: The time derivatives of \mathbf{B} and \mathbf{H} are both null.
- *No currents*: the current density \mathbf{J} is null everywhere. This implies that the magnetic field \mathbf{H} is *irrotational*, i.e.: can be expressed as the gradient of a scalar field: $\mathbf{H} = -\nabla\Phi$, referred to as magnetic scalar potential.
- *Linear materials*: the relation between \mathbf{B} and \mathbf{H} in every point of the space can be written as $\mathbf{B} = \mu\mathbf{H} + \mathbf{B}_r$, where the vector \mathbf{B}_r is referred to as remanent flux density. \mathbf{B}_r and μ can be function of the position \mathbf{x} both are independent from \mathbf{H} . This implies that \mathbf{M} can be written as $\mathbf{M} = \frac{1}{\mu_0}\mathbf{B}_r(\mathbf{x}) + \chi_m(\mathbf{x})\mathbf{H}$.

The flux density \mathbf{B} is a *solenoidal* vector field, and can always be expressed as the curl of a vector field denoted by \mathbf{A} and referred to as magnetic vector potential: $\mathbf{B} = \nabla \times \mathbf{A}$.

The first three assumptions are already enough to prove the following equation:

$$\int_{\Omega} d^3x \mathbf{H}_1 \cdot \mathbf{B}_2 = 0 \quad (4.51)$$

where \mathbf{H}_1 and \mathbf{B}_2 are any couples of magnetic field and magnetic flux density which satisfy all the requirements stated above. Expressing \mathbf{B}_2 as $\nabla \times \mathbf{A}$ and \mathbf{H}_1 as $-\nabla\Phi$, and integrating by parts:

$$\int_{\Omega} d^3x \mathbf{H}_1 \cdot \mathbf{B}_2 = \int_{\partial\Omega} \Phi ((\nabla \times \mathbf{A}) \cdot d\mathbf{S}) - \int_{\Omega} \Phi \nabla \cdot (\nabla \times \mathbf{A}) \quad (4.52)$$

The first integral on the right side vanishes because of the localized fields hypothesis, and the second integral vanishes since the divergence of a curl is always null. More in general: the integral over the whole space of the scalar product between an irrotational vector field \mathbf{H}_1 and a solenoidal vector field \mathbf{B}_2 is always null if the two vector fields are localized.

Using the definition of the magnetization \mathbf{M} , we can re-write \mathbf{H}_1 , as $\frac{1}{\mu_0}\mathbf{B}_1 - \mathbf{M}_1$. Together with equation 4.51 we get the *\mathbf{M} - \mathbf{B} reciprocity theorem*:

$$\int_{\Omega} d^3x \mathbf{M}_1(\mathbf{x}) \cdot \mathbf{B}_2(\mathbf{x}) = \int_{\Omega} d^3x \mathbf{M}_2(\mathbf{x}) \cdot \mathbf{B}_1(\mathbf{x}) \quad (4.53)$$

Similarly, using $\mathbf{B}_2 = \mu_0\mathbf{H}_2 + \mu_0\mathbf{M}_2$ together with equation 4.51 we get the *\mathbf{M} - \mathbf{H} reciprocity theorem*:

$$\int_{\Omega} d^3x \mathbf{M}_1(\mathbf{x}) \cdot \mathbf{H}_2(\mathbf{x}) = \int_{\Omega} d^3x \mathbf{M}_2(\mathbf{x}) \cdot \mathbf{H}_1(\mathbf{x}) \quad (4.54)$$

This result is not useful for magnet design as it is, since, except for hard magnets, we have no direct control over the magnetization. However, using the fourth hypothesis of linear materials and the additional hypothesis that the susceptibility $\chi_m(\mathbf{x})$ is the same for both the systems, we can replace \mathbf{M}_1 and \mathbf{M}_2 in equation 4.54 with $\mathbf{M}_i = \frac{1}{\mu_0}\mathbf{B}_{r_i}(\mathbf{x}) + \chi_m\mathbf{H}_i$, and we get to the *remanence reciprocity theorem*, that is at the core of powerful optimisation approaches that will be described in the following sections:

$$\int_{\Omega} d^3x \mathbf{B}_{r_1}(\mathbf{x}) \cdot \mathbf{H}_2(\mathbf{x}) = \int_{\Omega} d^3x \mathbf{B}_{r_2}(\mathbf{x}) \cdot \mathbf{H}_1(\mathbf{x}) \quad (4.55)$$

It can be noticed that the integration domain on each side of this equation can be reduced to the region in which the corresponding remanence is not null. Moreover, if the two magnet regions are disconnected, it is possible to replace \mathbf{H}_i with $\frac{1}{\mu}\mathbf{B}_i$ on both sides.

The theorem has been introduced for the isotropic case, for which the χ and μ are scalar numbers. However the reciprocity theorems expressed by equation 4.55 remains true even in the anisotropic case, as long as the susceptibility tensor is symmetric, that is: $\underline{\underline{\chi}} = \underline{\underline{\chi}}^T$.

It is insightful to express equation 4.55 in operator notation:

$$\int_{\Omega} d^3x_1 \mathbf{B}_{r_1} \cdot \mathbf{F}_r^H[\mathbf{B}_{r_2}] = \int_{\Omega} d^3x_2 \mathbf{B}_{r_2} \cdot \mathbf{F}_r^H[\mathbf{B}_{r_1}] \quad (4.56)$$

We can express the theorem in very simple terms, by saying that the operator \mathbf{F}_r^H is symmetric. Once it is expressed in this form that automatically excludes the field generated by any current that might be present in the systems, the no-currents assumption can be removed. This is a consequence of the linear materials assumption which implies that the field generated by the free currents is independent from the field generated by the magnetization currents.

4.3.2 Current reciprocity theorem

It is possible to derive another reciprocity theorem that is satisfied in presence of current densities \mathbf{J}_1 and \mathbf{J}_2 in the two systems. This is done by removing the third assumption from the bullet-point list of section 4.3.1. Starting from the integral over the set Ω of the product $\mathbf{H}_2 \cdot \mathbf{J}_1$, and replacing \mathbf{J}_1 with $\nabla \times \mathbf{H}_1$, we get to the following identity:

$$\int_{\Omega} d^3x \mathbf{H}_2(\mathbf{x}) \cdot \mathbf{J}_1(\mathbf{x}) = \int_{\Omega} d^3x \nabla \cdot \left(\mathbf{H}_2(\mathbf{x}) \times \mathbf{H}_1(\mathbf{x}) \right) + \mathbf{H}_1(\mathbf{x}) \cdot \left(\nabla \times \mathbf{H}_2(\mathbf{x}) \right) \quad (4.57)$$

The first term of the right-hand side is removed by applying the divergence theorem together with the localized fields hypothesis. If the quantity $\nabla \times \mathbf{H}_2$ is replaced with \mathbf{J}_2 , the equation leads to the *current reciprocity theorem*:

$$\int_{\Omega} d^3x \mathbf{H}_1 \cdot \mathbf{J}_2 = \int_{\Omega} d^3x \mathbf{H}_2 \cdot \mathbf{J}_1 \quad (4.58)$$

This theorem can be written in operator notation:

$$\int_{\Omega} d^3x \mathbf{F}_J^H[\mathbf{J}_1] \cdot \mathbf{J}_2 = \int_{\Omega} d^3x \mathbf{F}_J^H[\mathbf{J}_2] \cdot \mathbf{J}_1 \quad (4.59)$$

This theorem is satisfied even if the permeability fields of the systems 1 and 2 are not the same. It is important to notice an important difference between equation 4.58 and equation 4.55: in order for the current reciprocity theorem to be satisfied, the current densities \mathbf{J}_1 and \mathbf{J}_2 must be solenoidal fields as they must comply with Ampere's law. The theorem expressed by equation 4.55 on the other hand does not require to formulate any additional conditions on the remanences \mathbf{B}_{r1} and \mathbf{B}_{r2} .

4.4 Objectives

The general formulation of the optimisation problems that are approached in sections 5 and 6, is expressed by objective functionals \mathcal{S} that are defined in terms of the magnetic field \mathbf{H} :

$$\mathcal{S}[\mathbf{H}] \rightarrow \mathbb{R} \quad (4.60)$$

The objective usually depends only on the characteristics of the magnetic field over some limited region of space which is referred to as working area. This region of space, which might also not be simply connected, will also be called *air gap* and denoted by R_g . The region occupied by the parts of the magnetic system that are being optimised is referred to as *design area*, and denoted by R_m .

It is important to point out that formulating the optimisation problem with equation 4.60, and assuming the equations of magnetostatics as physical model, means that the interactions due to other physical mechanisms are not considered. Some of the most relevant effects with respect to the analysis of magnetic structures are electrical and thermal conductivity, particularly for what concerns eddy currents inside the soft magnetic materials and temperature stability of permanent magnets. The mechanical behaviour of the materials in the systems is also important, because of the forces due to the magnetic interaction between different parts. The analysis of the interdependence between these effects is generally carried out with numerical methods.

4.4.1 Linear Objectives

An important class of optimisation objectives is expressed by linear objective functionals \mathcal{L} , satisfying the following property:

$$\mathcal{L}[\alpha_1 \mathbf{H}_1 + \alpha_2 \mathbf{H}_2] = \alpha_1 \mathcal{L}[\mathbf{H}_1] + \alpha_2 \mathcal{L}[\mathbf{H}_2] \quad (4.61)$$

The optimisation of linear objective functionals has a central role in the following chapters. In particular, we will focus on objective functionals expressed in integral form:

$$\mathcal{L}[\mathbf{H}] = \int_{\Omega} d^3x \mathbf{H}(\mathbf{x}) \cdot \mathbf{u}(\mathbf{x}) \quad (4.62)$$

The vector field \mathbf{u} can be interpreted as an *objective vector field*, since maximizing \mathcal{L} with respect to the direction of \mathbf{H} is equivalent to maximizing the alignment with \mathbf{u} . The contributions to the value of a linear functional from the field in different points are independent. Moreover, the result does not depend on the value of \mathbf{H} in the points where $\mathbf{u} = \mathbf{0}$. For example, the objective of maximizing the x component of the field, averaged over a certain region R_g , is expressed by an objective vector field \mathbf{u} that is equal to $\hat{\mathbf{e}}_x$ inside R_g , and null outside. The integration domain can thus be reduced to the region R_g .

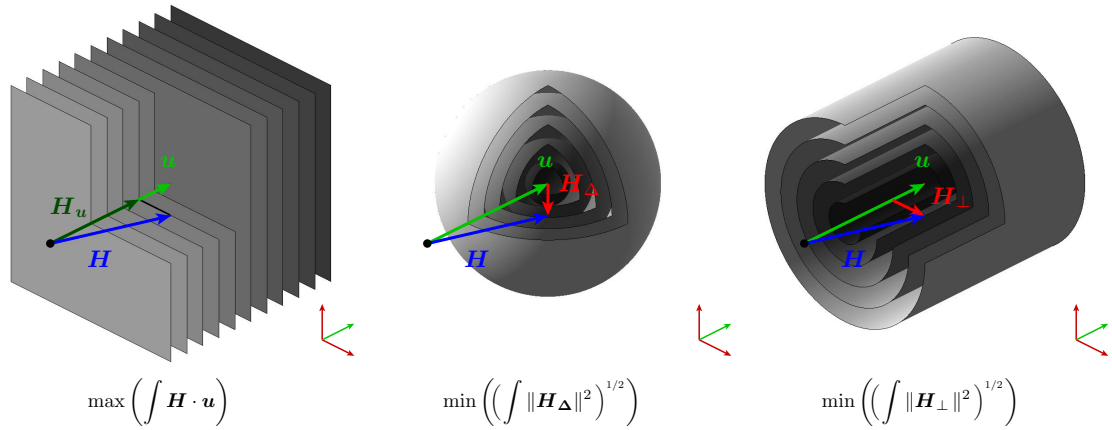


Fig. 4.4: Symbolic representation of the objective functionals defined in equations 4.62, 4.66 and 4.70, shown in the left, middle and right panels, respectively. The three directions represent the first three components of the expansion of the magnetic field over a basis of orthogonal functions. It is assumed that the first function of the basis coincides with the desired field \mathbf{u} , the remaining terms representing the field distortion. The three directions are indicated by the small vector diagram on the bottom-right corner of each panel: the green arrow corresponds to \mathbf{u} . Each of the grey surfaces represents magnetic field distributions that would lead to the same value of the objective. Darker shades indicate better configurations with respect to the optimisation problem. The black point represents the zero field, and the light green and blue arrows represent \mathbf{u} and \mathbf{H} , respectively. In the middle and right panel the bright red arrows represent the component of the field penalizing the objective.

As long as \mathbf{u} is allowed to be a generalized function of \mathbf{x} , any functional obeying equation 4.61 can be expressed in the integral form of equation 4.62. For example the functional expressing the x derivative of the x component of \mathbf{H} in the point $\mathbf{x} = \mathbf{0}$ corresponds to the following integral form:

$$\mathcal{L}[\mathbf{H}] = \left(\frac{\partial H_x}{\partial x} \right)_{\mathbf{x}=\mathbf{0}} = \int_{\Omega} d^3x \mathbf{H}(\mathbf{x}) \cdot \frac{d}{dx} \left(\delta^3(-\mathbf{x}) \right) \hat{\mathbf{e}}_x \quad (4.63)$$

It is interesting to consider the case when \mathbf{u} is a physically realizable magnetic field satisfying $\nabla \times \mathbf{u} = \mathbf{0}$. It is assumed that the field \mathbf{H} can be expanded over a set of orthonormal functions,

and that the field \mathbf{u} is, after normalization, the first element of this basis. Because of the orthogonality between these functions, only the first component of the expansion has an effect on the value of the functional \mathcal{L} defined in equation 4.62. This is symbolically represented in the left panel of figure 4.4. The three orthogonal directions indicate the first three components of the expansion of \mathbf{H} over the basis, the remaining terms of the expansion are not considered. The direction of first component, proportional to \mathbf{u} , is indicated by the green arrow in the diagram located on the bottom-right corner, while the second and third components are indicated by the red arrows. Each of the grey planes represents a surface corresponding to field distributions giving the same value of \mathcal{L} , darker shades indicating higher values. The black dot represents the null field, while the field \mathbf{H} and its projection on \mathbf{u} are represented by the blue arrow and dark green arrow, respectively. This diagram symbolically represents the fact that linear functionals correspond to the problem of maximizing the intensity along the desired direction. The deviation of the field from the distribution \mathbf{u} has no effect. In the next section we will consider another class of optimisation functionals which describe the problem of minimizing the field distortions.

It is worth to mention here another important property which may characterise an objective functional, namely p -homogeneity with respect to the field. This property is expressed by the following equation:

$$\mathcal{S}[\alpha \mathbf{H}] = \alpha^p \mathcal{S}[\mathbf{H}] \quad (4.64)$$

For this objectives the scaling of the solution with respect to the global factor α is known, thus simplifying the optimisation procedure. The particular case of quadratic functionals, corresponding to the case $p = 2$, is particularly relevant, as forces due to the magnetic interactions are expressed by this class of functionals [72, 91]. The integral form is given by the following expression:

$$\mathcal{S}[\mathbf{H}] = \int_{\Omega} d^3x \int_{\Omega} d^3x' \mathbf{H}(\mathbf{x}) \cdot \underline{\underline{A}}(\mathbf{x}, \mathbf{x}') \mathbf{H}(\mathbf{x}') \quad (4.65)$$

Where $\underline{\underline{A}}$ denotes a linear transformation which depends on \mathbf{x} and \mathbf{x}' . As can be noticed the integrand in equation 4.65 depends simultaneously on the magnetic field at two different locations \mathbf{x} and \mathbf{x}' .

4.4.2 Magnetic Inverse problem

In some studies the procedure of designing a magnetic structure is formulated as an inverse problem [79, 81]. The magnetic inverse problem consists in finding a distribution of sources generating a field \mathbf{H} equal to a given vector field \mathbf{u} . This optimisation problem is also relevant for measuring techniques concerning detection and characterization of magnetizable bodies [78]. A relaxed version of the inverse problem consists in minimizing the norm of the difference between \mathbf{H} and \mathbf{u} , evaluated as:

$$\mathcal{D}[\mathbf{H}] = \left(\int_{\Omega} d^3x \|\mathbf{H}(\mathbf{x}) - \mathbf{u}(\mathbf{x})\|^2 \right)^{1/2} \quad (4.66)$$

The target field $\mathbf{u}(\mathbf{x})$ can be any physically consistent field such as, e.g., a perfectly uniform field or a perfect quadrupole field. If we are only interested in the characteristics of the field inside a particular region R_g , the integration domain can again be reduced to this region. The middle panel of figure 4.4 represents this class of objectives using the same symbolic visualization

employed for linear functionals. The objective field \mathbf{u} , the magnetic field \mathbf{H} , and the difference $\mathbf{H}_\Delta = \mathbf{H} - \mathbf{u}$ are represented by the green, blue and red arrows, respectively. Each of the grey surfaces represents magnetic field distributions that would lead to the same value of \mathcal{D} , darker shades corresponding in this case to *lower* values of \mathcal{D} , as the objective is to minimise the functional. It is apparent that the minimum attainable value is zero, and it is only given by the case $\mathbf{H} = \mathbf{u}$. However, there might be different distributions of magnetization generating the same field in the region R_g [79, 86]. As pointed out in [44], usually the more well-posed is a forward problem, the more ill-posed is the corresponding inverse problem, and this concept also applies to the magnetic forward and inverse problems.

The objective functional expressed by equation 4.66 is not homogeneous with respect to the field \mathbf{H} , even though it is absolute homogeneous with respect to the vector difference \mathbf{H}_Δ . Removing the 1/2 exponent in the expression of Δ makes the functional quadratic with respect to \mathbf{H}_Δ , while representing a similar optimisation problem. This formulation, also called least square deviation criterion, may be advantageous for the implementation since gradient based methods can reduce the discrete version of this non-linear minimisation problem to a system of linear equations which can be solved with approaches of linear algebra [77, 78]. A similar optimisation problem is formulated by expanding the field into a series of orthogonal functions $\mathbf{H}_n(\mathbf{x})$, such as the fields generated by the different coefficients of the expansion cylindrical multipoles given in equation 4.28. This set of function must be a complete basis for the integration domain of the objective functional. The series expansion will be denoted by:

$$\mathbf{H}(\mathbf{x}) = \sum_n \mathbf{H}_n(\mathbf{x}) \quad (4.67)$$

Without loss of generality we can assume that the objective field \mathbf{u} is proportional to the first component of the expansion, i.e. \mathbf{H}_1 . The objective to minimize all of the components of the expansion except for $\mathbf{H}_1(\mathbf{x})$ is expressed by:

$$\mathcal{D}^*[\mathbf{H}] = \left(\int_{\Omega} d^3x \left\| \sum_{n \neq 1} \mathbf{H}_n(\mathbf{x}) \right\|^2 \right)^{1/2} \quad (4.68)$$

This expression shows the absolute homogeneity of \mathcal{D}^* with respect to \mathbf{H} :

$$\mathcal{D}^*[\alpha\mathbf{H}] = |\alpha| \mathcal{D}^*[\mathbf{H}] \quad (4.69)$$

The same functional can also be expressed in another form which highlights its similarity with the functional of equation 4.66:

$$\mathcal{D}^*[\mathbf{H}] = \left(\int_{\Omega} d^3x \|\mathbf{H}(\mathbf{x}) - \mathbf{H}_1(\mathbf{x})\|^2 \right)^{1/2} \quad (4.70)$$

This functional is illustrated in the right panel of figure 4.4, using the same symbolic visualization introduced above. The symbol \mathbf{H}_\perp represents the sum of the undesired components of the field, i.e. $\mathbf{H} - \mathbf{H}_1 = \sum_{k \neq 1} \mathbf{H}_k$. As suggested by a comparison between the middle panel and the right panel, the difference between \mathcal{D}^* and the functional of equation 4.66 is that \mathcal{D}^* does not penalize or favour a solution \mathbf{H} which is proportional everywhere to the target field \mathbf{u} , but has a different intensity. This functional is in this sense the opposite of a linear functional, as it tries to minimize the field distortion without rewarding the intensity of the desired component, while a linear functional rewards the intensity of the desired component without penalizing the field distortion.

Flux Sources Optimization

This chapter introduces the magnet optimisation techniques based on the formalism introduced in the previous section. The perspective adopted in this chapter consists in optimising the sources of the field, while keeping a fixed geometry. This means that the distribution of different materials in the geometry is assumed to be determined in advance. We will consider permanent magnet flux sources, electro magnets, and hybrid systems combining permanent magnets with electromagnets.

5.1 Pre-segmented systems

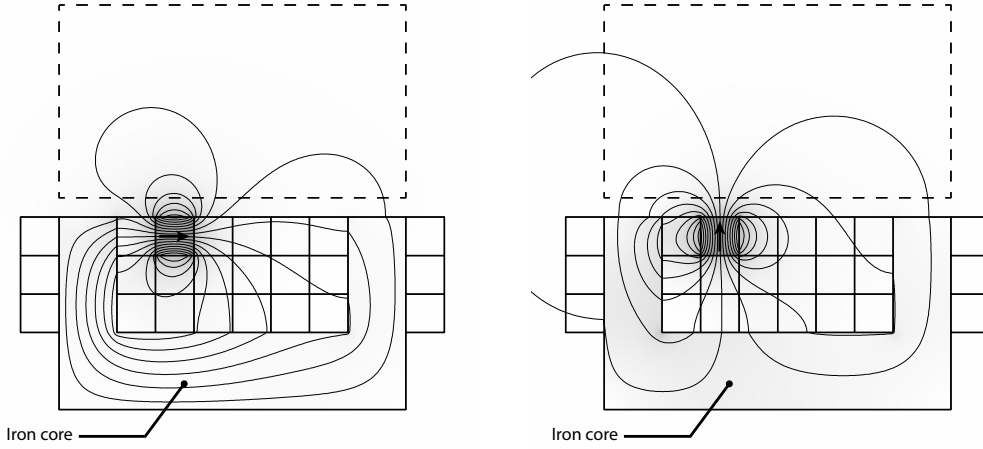
The topic of this section are magnetic system whose geometry is subdivided into a set of pre-determined coils and uniformly magnetized permanent magnets blocks of different shapes. The following section considers remanence distributions with a continuous spatial dependence. This section covers the results reported in the paper attached in section B.7.

5.1.1 Permanent magnet systems

Let us start by considering permanent magnet flux sources. The magnetic field distribution can be calculated using FEM analysis, even for very complex magnetic system. The search space corresponding to the problem of finding the optimal remanence direction for a finite set of uniformly magnetized blocks has a relatively low size. Many optimisation algorithms, however, require a large number of evaluations of the objective functional and each evaluation requires the solution of the magnetic field equations for the considered geometry. As mentioned, in some situations this can only be done by employing computationally expensive FEM calculations, and therefore many optimisation algorithms are infeasible. The method discussed in this section is based on the linearity of the magnetic field \mathbf{H} with respect to the remanent flux density \mathbf{B}_r producing it. As discussed in section 4.2.1, this property is only verified for system characterized by a linear magnetic behaviour.

It is considered a pre-determined geometry, and a permanent magnet that is divided into N uniformly magnetized segments. The n^{th} segment is then characterized by one remanence vector, denoted by \mathbf{B}_{rn} . The collection of all the N remanence vectors is simply denoted by $\mathbf{B}_r \equiv \{\mathbf{B}_{r1}, \dots, \mathbf{B}_{rN}\}$. The field generated by the n^{th} segment in any point of space is a linear combination of the x , y and z components of its remanence vector \mathbf{B}_{rn} . The total field $\mathbf{H} = \mathbf{F}_r^H[\mathbf{B}_r]$ is then given by the superposition of the individual fields generated by each segment.

The field generated by the n^{th} segment when its remanence is equal to the vector \mathbf{B}_{rn} , will be denoted by $\mathbf{F}_{rn}^H(\mathbf{B}_{rn})$. The use of round brackets instead of square brackets highlights the fact that the argument of \mathbf{F}_{rn}^H is not a vector field but a simple vector; the output of \mathbf{F}_{rn}^H is



(a) Field generated by the x component of \mathbf{B}_{r_n} (b) Field generated by the y component of \mathbf{B}_{r_n}

Fig. 5.1: Field generated by a magnet block included in a magnetic structure which contains a c-shaped iron core. The permeability distribution $\mu(\mathbf{x})$, determined by the arrangement of materials, affects the field generated by the magnet. Figures 5.1a and 5.1b show the field generated by the x and y component of the remanence, respectively. Since the magnetic behaviour is assumed to be linear, it is possible to apply the superposition principle.

a spatially dependent vector field. Applying the superposition property the total field \mathbf{H} is written as:

$$\mathbf{H} = \mathbf{F}_r^H[\mathbf{B}_r] = \sum_n^N B_{r_n x} \mathbf{F}_{r_n}^H(\hat{\mathbf{e}}_x) + B_{r_n y} \mathbf{F}_{r_n}^H(\hat{\mathbf{e}}_y) + B_{r_n z} \mathbf{F}_{r_n}^H(\hat{\mathbf{e}}_z) \quad (5.1)$$

The field generated by the n^{th} segment when the remanence is $\mathbf{B}_{r_n} = \hat{\mathbf{e}}_x$ can be calculated in advance, and similarly for the x , y , and z components of all the segments. Unless the permeability is equal to μ_0 everywhere, the field generated by a given segment is affected by the permeability field $\mu(\mathbf{x})$ in all the points of space and it is not always possible to compute it with analytical approaches. Figure 5.1 shows a two-dimensional example geometry. The field generated by the x and y components of the remanence of one of the segments is shown in figures 5.1a and 5.1b, respectively. It is interesting to notice how the presence of the c-shaped iron core affects the field generated by the square permanent magnet segment.

This concept has been implemented by performing the calculations using FEM techniques. For a three-dimensional system with N permanent magnet segments the pre-computation of the individual fields requires $3N$ FEM simulations. After performing these simulations it is possible to solve numerically the optimisation problem without the need for any additional simulation. This approach reduces the computational time for any optimisation algorithm that requires to simulate more than $3N$ different configurations.

It is considered the objective functional $\mathcal{S}[\mathbf{H}]$, defined in terms of the magnetic field \mathbf{H} . Once the pre-computations have been performed, the derivative of \mathcal{S} with respect to each of the independent components of the remanence of each segment is easily calculated. Since the

functional \mathcal{S} is non-linear, the derivative may depend on the point at which it is evaluated. In other words, the optimal direction of the remanence of a given segment is affected by the remanence of the other segments.

$$\frac{\partial \mathcal{S}}{\partial B_{rnx}}[\mathbf{B}_r] = \lim_{\varepsilon \rightarrow 0} \frac{\mathcal{S}[\mathbf{F}_r^H[\mathbf{B}_r] + \varepsilon \mathbf{F}_{rn}^H(\hat{\mathbf{e}}_x)]}{\varepsilon} \quad (5.2)$$

In practice it is possible to evaluate this quantity numerically by evaluating the finite difference corresponding to a small ε . Once all the derivatives have been numerically computed, it is possible to implement the following iterative optimisation scheme.

$$\mathbf{B}_{rn}^{(k)} = \mathbf{B}_{rn}^{(k-1)} + \gamma \frac{\partial \mathcal{S}}{\partial \mathbf{B}_{rn}}[\mathbf{B}_r^{(k-1)}] \quad (5.3)$$

This iterative algorithm is referred to as *gradient descent* [45] and consists into moving in the direction of the gradient of \mathcal{S} , i. e.: the direction giving the maximum rate of variation of \mathcal{S} . The small real parameter denoted by γ expresses the step size of each iteration. The approach has been implemented into a Matlab program which allows the user to choose between different optimisation algorithm besides gradient descent. In particular, it is possible to use the built-in optimisation functions based on simulated annealing, genetic algorithms and the NelderMead method. However, the gradient descent can some times prove more insightful as it brings a mental picture of the “energy landscape” underlying the optimisation problem.

In many magnet design problems it is desirable to determine in advance the norm of the remanence of each uniformly magnetized segment. Since the norm of the remanence is determined by the choice of material, this is equivalent to deciding the permanent magnet material of each segment. The optimisation algorithm is then modified by parametrizing each remanence vector and constraining the norm of each segment. For two dimensional geometries this is done by expressing each remanence vector in polar coordinates:

$$\mathbf{B}_{rn} = B_{rn} \left(\cos(\psi_n) \hat{\mathbf{e}}_x + \sin(\psi_n) \hat{\mathbf{e}}_y \right) \quad (5.4)$$

The norm and angle of the \mathbf{B}_{rn} are denoted by B_{rn} and ψ_n , respectively. The derivatives of \mathcal{S} with respect to all of the angles ψ_n are evaluated numerically, and the iterative optimisation scheme will affect only the angle of each remanence vector. In the following examples of optimisation problems the norm of the remanence is required to have the same value for all the segments.

As example of the interplay between geometry and objective functional, we consider the geometry of figures 5.2a and 5.2b, optimised respectively for field intensity in the x direction averaged over the air gap, and field uniformity. The two objectives depend only on the value of the field inside the circular air gap that is in the center of the magnetic system and is denoted by R_g . The geometry is identical for the two examples and is composed by a permanent magnet subdivided into $N = 16$ uniformly magnetized segments, and an external iron yoke, indicated in the figures. The only difference between the two examples is the objective functional of the optimisation problem. For the example of figure 5.2a the objective is to maximize the x component of the field averaged over the region R_g . This optimisation problem is then equivalent to maximizing the following linear functional:

$$\mathcal{L}[\mathbf{H}] = \int_{R_g} d^2x \mathbf{H}(\mathbf{x}) \cdot \hat{\mathbf{e}}_x \quad (5.5)$$

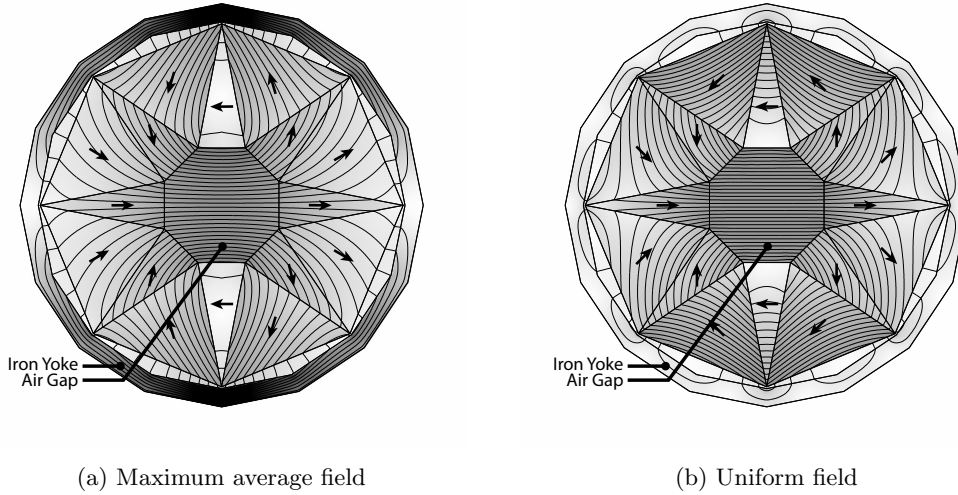


Fig. 5.2: Cylindrical Halbach array with an external iron yoke. The configuration shown in figure 5.2a has been optimised with respect to the x component of the field averaged over the central air gap. The configuration shown in figure 5.2b has been optimised for the quality of the field, with respect to a perfectly uniform field oriented in the x direction. Despite the presence of the yoke, this objective leads to the conventional Halbach cylinder solution given by equation 4.29.

For the example of figure 5.2b the goal is to obtain inside region R_g a magnetic field oriented in the x direction and as uniform as possible. This problem is formulated by the objective functional \mathcal{D}^* expressed by equation 4.70, with \mathbf{H}_1 being a uniform field in the x direction.

It is interesting to notice that the optimised configuration for the second problem is identical to the dipole Halbach cylinder, described by equation 4.29 with $p = 1$. The permanent magnet is self insulated and removing the iron yoke would change the solution only slightly: the magnetic flux density inside the iron yoke is minimal and is only due to the differences with respect to the ideal case. On the contrary, if the objective is to maximize the average field without rewarding its uniformity the optimised configuration is quite different from the Halbach case and the field inside the iron yoke is very intense. The remanences of the segments that are magnetized in the $\pm x$ directions are the same between the two examples, since the two axes of symmetry are present in both cases. The difference between the two configurations is only due to the slightly different orientation of the remanence of the remaining segments. The trade-off between field intensity and uniformity for this prototypical geometry will be investigated in more details in section 6.2.1.

5.1.2 Hybrid systems

The procedure outlined in the previous section does not change significantly when it is applied to the optimisation of hybrid magnetic systems which include electro-magnets combined with permanent magnets. This is due to the linearity of the field with respect to the sources that

generate it which is a consequence of assuming a linear B - H relation for all the materials in the system.

It must be kept in mind, however, that it is not possible to freely choose a current density field $\mathbf{J}(\mathbf{x})$ as it is done with the remanent flux density \mathbf{B}_r . The reason is that the current density must obey the continuity equation that is applied to steady-state magnetism: $\nabla \cdot \mathbf{J} = 0$. When formulating a three-dimensional optimisation problem for hybrid magnetic systems, it is only meaningful to search the optimal configuration among the physically acceptable solutions.

This can be done by decomposing the geometry into a set of M independent coils. The current density $\mathbf{J}_m(\mathbf{x})$ for any point \mathbf{x} inside the region occupied by the m^{th} coil is pre-determined and is consistent with the continuity equation. If the current density of the m^{th} coil is multiplied by the factor I_m , it will still be consistent with the continuity equation. The scale factor I_m determines the field generated by the coil in any point of space, which we will denote by $\mathbf{F}_{jm}^H(I_m)$. The optimisation problem is then to find the optimal set of currents $I = \{I_1, \dots, I_M\}$, with respect to the desired features of the field that they will generate. The field generated by each coil is affected by the permeability distribution $\mu(\mathbf{x})$, as it is schematically illustrated in figure 5.3a.

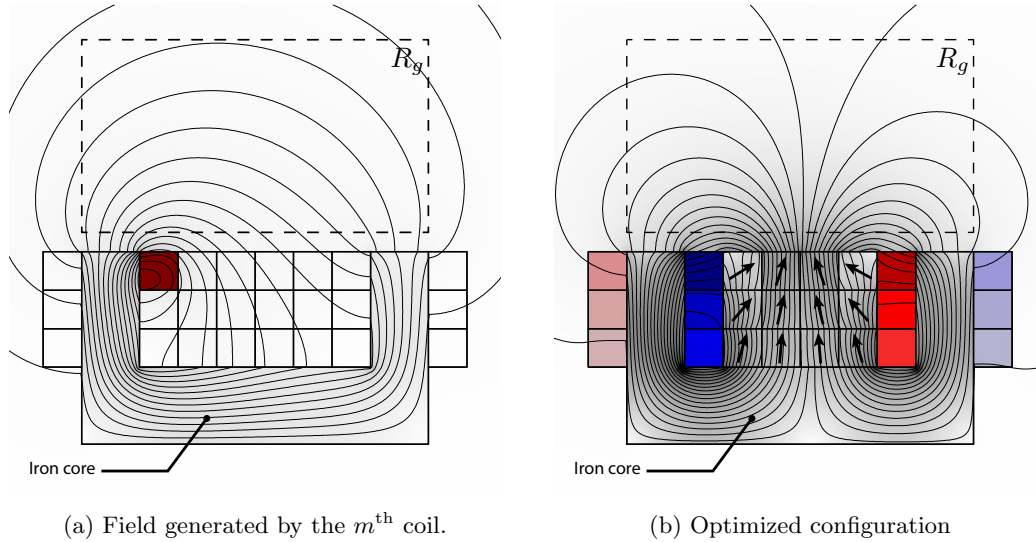


Fig. 5.3: 5.3a: field generated by a coil with square cross section. The field is affected by the presence of the c-shaped iron core shown in the figure. 5.3b: hybrid magnetic system optimised with respect to the gradient of the squared norm of the field averaged over the rectangular area delimited by the black dashed line shown in the figure.

As for permanent magnet based systems, the contributions to the total field due to the different sources are independent: it is possible to compute in advance the field generated by each coil and each component of the vectors \mathbf{B}_{rn} , and obtain the field for an arbitrary configuration by combining all the individual fields. For a two dimensional system the superposition is expressed as:

$$\mathbf{H} = \sum_n^N B_{rn x} \mathbf{F}_{rn}^H(\hat{e}_x) + B_{rn y} \mathbf{F}_{rn}^H(\hat{e}_y) + B_{rn z} \mathbf{F}_{rn}^H(\hat{e}_z) + \sum_m^M I_m \mathbf{F}_{jm}^H(1) \quad (5.6)$$

Following a procedure analogous to the one described in the previous section, the derivatives of the objective \mathcal{S} with respect to each current factor I_m is calculated at a given configuration. The currents and remanences are subsequently modified following an iterative optimisation algorithm. In many cases it is useful to apply a constraint on the total power $\mathcal{P}_J[I]$ dissipated by the coils because of the Joule effect:

$$\mathcal{P}_J[I] = \sum_m^M R_m^{\text{Eq.}} I_m^2 \quad (5.7)$$

The symbol $R_m^{\text{Eq.}}$ denotes the proportionality factor between the power dissipated by the m^{th} coil and the square of its current factor I_m . For the two dimensional examples that will be considered the shape and resistivity of each coil is the same, and this implies that the factors $R_m^{\text{Eq.}}$ are all equal.

The example shown in figure 5.3b is optimised to maximize the y component of the force experienced by magnetizable bodies when they are placed in the region R_g , enclosed by the black dashed line. Mathematically this is equivalent to maximizing the following functional [57]:

$$\mathcal{S}[\mathbf{H}] = - \int_{R_g} \hat{e}_y \cdot \nabla (\|\mathbf{H}\|^2) \quad (5.8)$$

The small asymmetry of the filed lines shown in the figure is due to the small numerical approximations inherent to the numerical implementation. However, the final configuration is evidently accomplishing the goal of maximising the gradient.

5.1.3 Linear Objectives

The procedure is particularly simple if the objective functional is linear. As was mentioned in section 4.4.1 any functional \mathcal{L} that is linear with respect to the field \mathbf{H} can be expressed as the integral over the whole space of the scalar product between \mathbf{H} and another vector field \mathbf{u} which will be referred to as objective vector field:

$$\mathcal{L}[\mathbf{H}] = \int d^3x \mathbf{H}(\mathbf{x}) \cdot \mathbf{u}(\mathbf{x}) \quad (5.9)$$

The linearity of \mathcal{L} can be used to simplify its expression, which for a two-dimensional hybrid system is written as:

$$\mathcal{L}[\mathbf{H}] = \sum_n^N B_{r_n x} \mathcal{L}[\mathbf{F}_{r_n}^H(\hat{e}_x)] + \sum_n^N B_{r_n y} \mathcal{L}[\mathbf{F}_{r_n}^H(\hat{e}_y)] + \sum_m^M I_m \mathcal{L}[\mathbf{F}_{j_m}^H(1)] \quad (5.10)$$

This expansion implies that the globally optimal solution can be determined directly, i. e.: without the need for an iterative algorithm. The remanences and current factors are given by:

$$B_{r_n} \propto \hat{e}_x \mathcal{L}[\mathbf{F}_{r_n}^H(\hat{e}_x)] + \hat{e}_y \mathcal{L}[\mathbf{F}_{r_n}^H(\hat{e}_y)] \quad (5.11)$$

$$I_m \propto \mathcal{L}[\mathbf{F}_{j_m}^H(1)] \quad (5.12)$$

Applying the constraints on $\|\mathbf{B}_{r_n}\|$ and $\sum_m^M R_m^{\text{Eq.}} I_m^2$ leaves only one possible solution, which is easily calculated through normalization.

As pointed out in [80], the reciprocity theorem has deep implications for the optimisation of linear objective functionals. Assuming that $\|\mathbf{B}_r\| = 1$, the expression of the optimal remanence of the n^{th} magnet block is given by:

$$\mathbf{B}_{r_n} = \hat{\mathbf{e}}_x \int d^3x \mathbf{F}_{r_n}^H(\hat{\mathbf{e}}_x) \cdot \mathbf{u}(\mathbf{x}) + \hat{\mathbf{e}}_y \int d^3x \mathbf{F}_{r_n}^H(\hat{\mathbf{e}}_y) \cdot \mathbf{u}(\mathbf{x}) \quad (5.13)$$

The integration domain could be reduced to the region where \mathbf{u} is not zero. It is possible to apply the reciprocity theorem expressed by equation 4.55, to modify the previous expression:

$$\mathbf{B}_{r_n} = \hat{\mathbf{e}}_x \int_{R^{(n)}} d^3x \hat{\mathbf{e}}_x \cdot \mathbf{F}_{r_n}^H[\mathbf{u}] + \hat{\mathbf{e}}_y \int_{R^{(n)}} d^3x \hat{\mathbf{e}}_y \cdot \mathbf{F}_{r_n}^H[\mathbf{u}] = \int_{R^{(n)}} d^3x \mathbf{F}_{r_n}^H[\mathbf{u}] \quad (5.14)$$

The new domain of integration is the region occupied by the n^{th} magnet block, which is denoted by $R^{(n)}$. The quantity $\mathbf{F}_{r_n}^H[\mathbf{u}]$ expresses the field generated by a magnet whose remanence is equal to $\mathbf{u}(\mathbf{x})$. The optimal orientation of the remanence of a magnet is then obtained by averaging $\mathbf{F}_{r_n}^H[\mathbf{u}]$ over the area occupied by the magnet. This correspondence will be investigated in section 5.2.2 in the context of optimisation of continuously varying remanence distributions. This symmetry cannot be applied to the optimisation of currents without involving the third dimension. Moreover, as stressed in section 4.3.2, the current reciprocity theorem would require the objective \mathbf{u} to be consistent with the continuity equation.

In some cases it is convenient to approach a non-linear optimisation problem by initially considering a suitable linear objective. The globally optimal configuration for the linear objective can be calculated directly and can be used as initial configuration for the iterative procedure. As long as the linear functional has been selected to closely represent the original non-linear objective, the convergence will be facilitated.

5.1.4 Illustrative examples

As examples of applications of the techniques introduced in the previous section we consider the magnetic systems shown in figure 5.4. The geometry of figure 5.4a represents a quadrupole magnet composed by triangular prismatic blocks. The system also includes an external iron yoke, and a set of coils located between the permanent magnets and the air gap. The first step of the optimisation procedure has been to calculate the globally optimal solution with respect to a linear objective expressed in integral form. The objective vector field \mathbf{u} is a perfect quadrupole field located in the air gap. The second step of the optimisation procedure consists into applying the gradient descent scheme to the following non linear objective:

$$\mathcal{S}[\mathbf{H}] = \int_{R_g} \|\mathbf{H}(\mathbf{x}) - \mathbf{H}_Q(\mathbf{x})\|^2 \quad (5.15)$$

The symbol \mathbf{H}_Q denotes the quadrupole component of \mathbf{H} . As mentioned in section 4.4.2, this objective corresponds to the problem of minimising the field distortions with respect to the required distribution, without rewarding or penalizing its intensity. As can be seen from figure 5.4a, the current is zero for the four coils located at the angles $\phi = 45^\circ, 135^\circ, 225^\circ$ and 315° .

The second example, shown in figure 5.4b, represents a rotary device for magnetic refrigeration, and is analogous to the structure shown in figure 4.2. The air gap between the coils and the inner iron core is subdivided into two high field regions and two low field regions, spanning

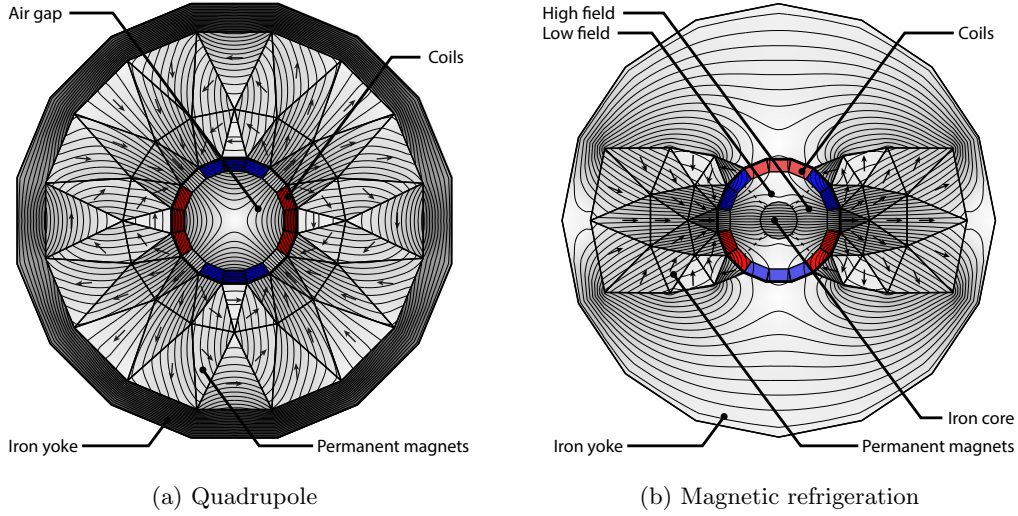


Fig. 5.4: Two examples of pre-segmented hybrid systems optimised with respect to non linear objectives. 5.4a: structure designed to create a quadrupole field inside the central cylindrical air gap. 5.4b: rotary magnetocaloric device analogous to the system represented in figure 4.2. In both cases, the starting configuration of the iterative optimisation scheme is the optimal solution of a suitable linear problem.

an angle of 90° each. The union of the two high field regions is denoted by R_{High} . The objective vector field describing the preliminary linear optimisation step is zero everywhere, except for the set R_{High} . On this domain \mathbf{u} is defined by: $\mathbf{u} = \text{sign}(x)\hat{\mathbf{e}}_\rho$. The symbol $\hat{\mathbf{e}}_\rho$ represents the unit vector oriented in the radial direction. The non-linear objective is represented by the following functional, linked to the cooling power provided by the device [101, 102]:

$$\mathcal{S}[\mathbf{H}] = \int_{R_{\text{High}}} \|\mathbf{H}(\mathbf{x})\|^{2/3} - \int_{R_{\text{Low}}} \|\mathbf{H}(\mathbf{x})\|^{2/3} \quad (5.16)$$

As can be seen from figure 5.4b, the final configuration manages to create a field with the desired features, i. e.: alternating angular sectors of high and low field intensity.

5.1.5 Cylinders segmentations

In this section, a systematic comparison between different ways to segment the Halbach cylinder geometry is presented. It is assumed that the permeability μ is equal to μ_0 everywhere, which is a good approximation for many modern permanent magnet materials. It is considered the case of the Halbach cylinder designed to create a uniform field inside the cavity, corresponding to the case $p = 1$. The four different segmentations shown in figure 5.5 are compared by calculating the x component of the magnetic flux field averaged over the cylindrical air gap R_g . This is equivalent to the following linear objective functional:

$$\mathcal{S}[\mathbf{H}] = \int_{R_g} d^3x \mathbf{H} \cdot \hat{\mathbf{e}}_x \quad (5.17)$$

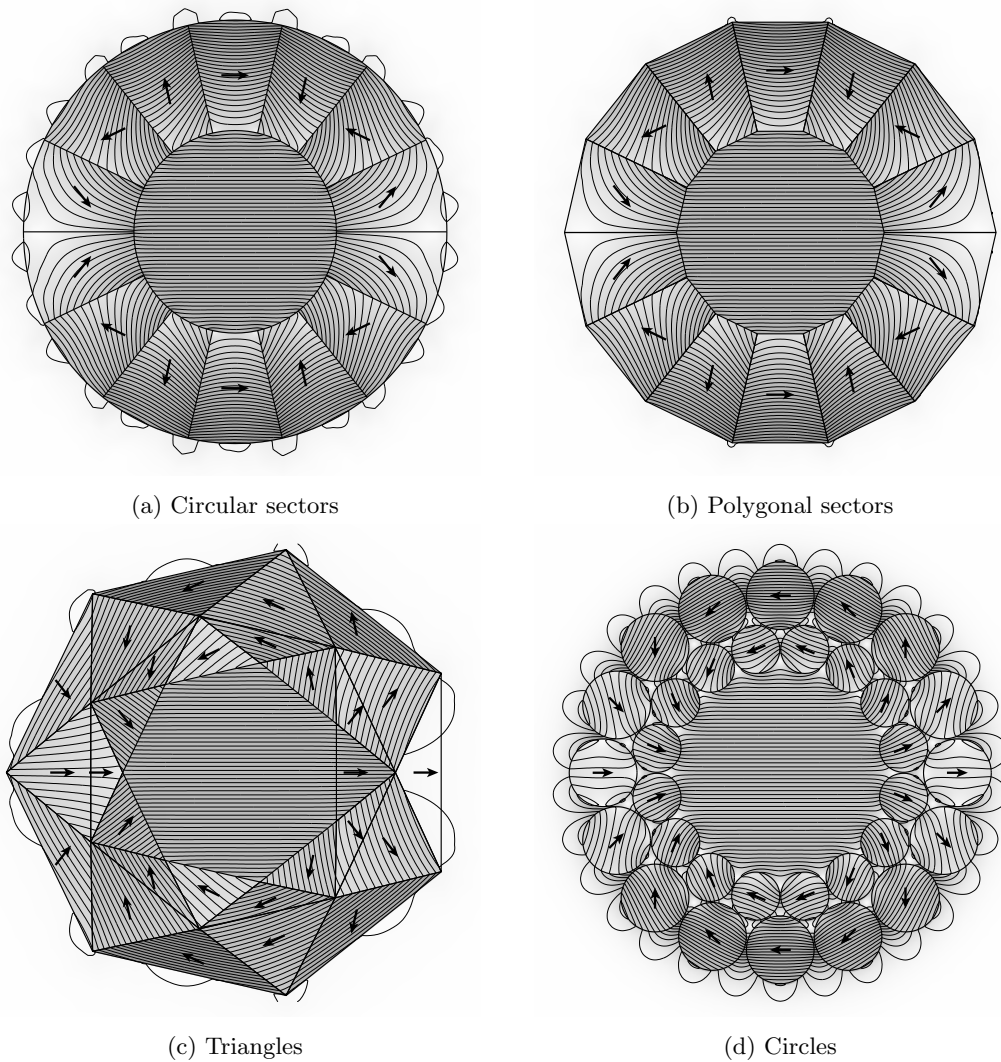


Fig. 5.5: Four possible ways to segment the Halbach cylinder geometry. The different segmentations present peculiar advantages and disadvantages which are addressed in the text.

The remanence is normalized, uniform inside each of the segments and its direction is determined by maximizing the objective functional \mathcal{S} using the approach introduced in section 5.1.3. All the considered shapes of segments are symmetrical with respect to the radial line passing by their center. Denoting by ϕ_k the angular coordinate of the center of the k^{th} segment, the optimal direction of the remanence is given by $2\phi_k$. This can be verified by checking the solution reported in equation 4.31 for the case $p = 1$. The four families of segmentations have different advantages and disadvantages:

- The most common way to subdivide this geometry is the segmentation into identical

sectors, as the one shown in figure 5.5a. As will be shown in this section, and will be proved rigorously in section 6.4.1, this is the subdivision method that maximizes \mathcal{S} for a given volume and a given number of segments N_{Segments} .

- Another possibility, shown in figure 5.5b, is to use pieces with trapezoidal cross-section. Since all the faces of each segment are flat polygons this might be advantageous from the point of view of the manufacturing costs.
- A similar argument applies to the segmentation into pieces with triangular cross section. This family of possible segmentation will be parametrized by the number of radial layers, denoted by N_r , and the number of segments for each radial layer, denoted by N_ϕ . The case of figure 5.5c corresponds to the case $N_r = 2$ and $N_\phi = 14$, i. e.: $N_{\text{Segments}} = 2 \times 14 = 28$ pieces in total.
- The other possible option that is compared in this section is shown in figure 5.5d: it uses cylindrical rods with remanence vector transverse to the axis. This geometry presents the unique advantage that it is possible to modify the field even after assembling the magnetic system [93, 90]. This is done by rotating each rod around its axis to reach the desired configuration. Using this method it is possible to switch between, e. g., the zero field and any of the multipole fields given by other values of p . As in the case of triangular prism, the total number of pieces is $N_{\text{Segments}} = N_r \times N_\phi$.

For the cases of circular-segments polygonal-segments and triangles the inner radius and the magnet volume can be decided independently. For the case of circles, however, the inner radius together with N_r and N_ϕ automatically determines the magnet volume because of the close-packing condition.

In order to compare the different configurations the value of the objective functional introduced in equation 5.17 is modified by dividing by the cavity volume V_g , to obtain the average field. The average is then normalized by the (uniform) field H^{Ideal} generated by an ideal Halbach cylinder with the same inner radius, R_I , and the same volume of permanent magnet:

$$\mathcal{S} \rightarrow \frac{\mu_0 \int_{R_g} d^3x \mathbf{H} \cdot \hat{\mathbf{e}}_x}{V_g H^{\text{Ideal}}} \quad (5.18)$$

The inner radius R_I is always given by the largest circle that can be inscribed in the cavity. For the cases of figures 5.5b and 5.5c the central circle is tangent to the inner sides of the polygons delimiting the cavity.

The normalized flux density is plotted in figure 5.6a as a function of the total number of segments N_{Segments} . For the cases of the circles and triangles the tick lines correspond to configurations having the same number of radial layers, which is indicated in the graph. The thin lines connect configurations having the same number of segments for each layer. For the case of circular sectors the average field $\langle \mathbf{H} \rangle$ can be calculated analytically, and is given by [65]:

$$\langle \mathbf{H} \rangle = H^{\text{Ideal}} \frac{N_{\text{Segments}} \sin(2\pi/N_{\text{Segments}})}{2\pi} \quad (5.19)$$

This relation corresponds to the thick grey line shown in the figure. As can be noticed, the green line, corresponding to the FEM calculation of the same geometry, is perfectly overlapped with the theoretical prediction. The field generated by the polygonal sectors is almost as intense as

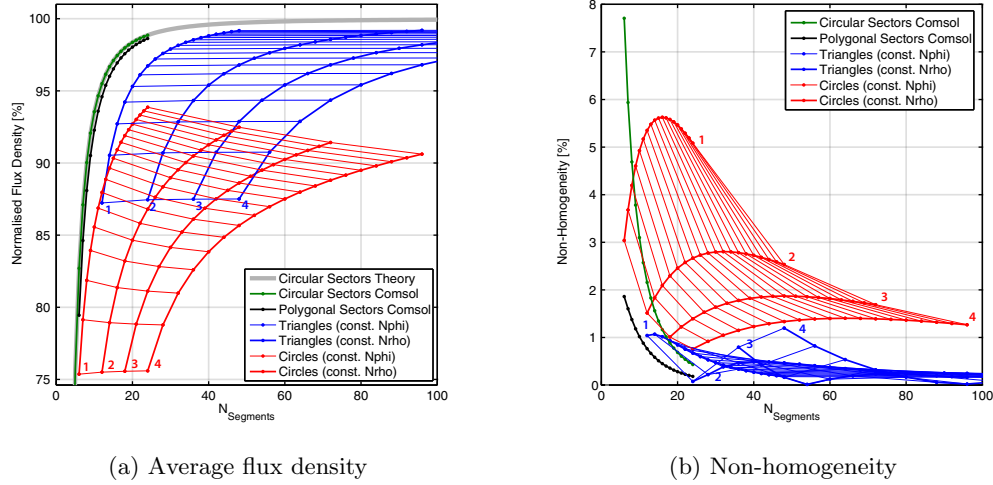


Fig. 5.6: Quantitative comparison of the different segmentations. 5.6a: average x component of the field normalized by the field generated by an ideal Halbach cylinder having the same volume. 5.6b: deviation from a perfectly uniform field, quantified by the parameter Δ defined in equation 5.20. For the segmentations using triangles and circular rods, the thick lines connect configurations having the same number of radial layers, while the thin lines connect configurations having the same number of segments for each layer. Figure 5.6a also shows the theoretical prediction for the case of the circular sectors, which can be checked to be perfectly overlapped with the corresponding FEM calculation.

the field of the circular sectors, while the other two possibilities, i.e. circles and triangles, are significantly inferior. It can also be noticed that increasing the number of radial layers while keeping the total number of segments constant always leads to a lower average intensity. The segmentation based on circular rods produces the lowest intensity because of the inevitable gaps between the different rods. This configuration is mainly advantageous because of its ability to modify the field.

It is interesting to evaluate the deviation from a perfectly uniform field. The non-homogeneity of the flux density in the air gap, denoted by Δ , is evaluated as the average norm of the 'error' flux density divided by the average norm of the flux density.

$$\Delta = \frac{\langle (B_x - \langle B_x \rangle)^2 + (B_y - \langle B_y \rangle)^2 \rangle}{\langle B_x^2 + B_y^2 \rangle} \quad (5.20)$$

This expression is analogous to the objective functionals discussed in section 4.4.2. The dependence of Δ on N_{Segments} is shown in figure 5.6b, expressed in percentage. For what concerns the uniformity, the polygonal sectors give a better results than the circular sectors. As explained above, intensity and homogeneity are evaluated inside the circle that is tangent to the segments. This implies that for the case of polygonal sectors the radial separations between adjacent magnet segments are not directly in contact with the inner circle. Since the field distortion is higher in the vicinity of these separations, the homogeneity is better for the case of polygonal sectors. A similar argument applies to the case of the triangular segments. As

shown in [82] and [89], for the case of triangular magnets the radial coordinate separating the different layers can be chosen in a particular way which results in a perfectly uniform field. These kinds of structures will be discussed in section 6.4.4. However, for the cases studied in this section the radial separations between the different layers are logarithmically spaced.

The systematic comparison performed here for the case of the dipole Halbach cylinder can be extended to multi-pole cylinders by replacing \hat{e}_x in equation 5.17 with the multi-pole fields expressed by equation 4.30. The normalization condition is generalized the same way. It is also possible to evaluate the field quality by considering the family of functionals introduced in section 4.4.2.

5.2 Continuously varying remanence field

The focus of this section is the optimisation of continuously varying remanence distributions. It is assumed that the geometry is pre-determined. This also implies that the region where the remanence field is not zero will be decided in advance. The approach discussed here provides the starting point for the development of the geometry optimisation techniques discussed in the next chapter.

5.2.1 Abele's approach

Because of its relevance in connection with optimisation approached described in the following sections, we examine the framework introduced by Abele et al. in [86, 89], employing the notation adopted in the present work.

$$\mathcal{M} = \frac{\int_{R_g} d^3x \|\mathbf{B}(\mathbf{x})\|^2}{\int_{R_m} d^3x \|\mathbf{B}_r(\mathbf{x})\|^2} \quad (5.21)$$

The inequality $\mathcal{M} \leq 1/4$, is always satisfied, and in [86] this is shown to be a consequence of the following inequality:

$$\underbrace{\frac{\mu_0}{2} \int_{R_g} d^3x \|\mathbf{H}(\mathbf{x})\|^2}_{U_{\text{ext}}} \leq \frac{1}{4} \underbrace{\frac{1}{2\mu} \int_{R_m} d^3x \|\mathbf{B}_r(\mathbf{x})\|^2}_{U_0} \quad (5.22)$$

Where U_{ext} is the energy associated with the field generated by the magnet outside of itself, and U_0 is the upper limit of the energy associated with the field generated by the magnet in the whole space.

The energy figure of merit \mathcal{M} can also be expressed in terms of the integral of energy product $(-\mathbf{B} \cdot \mathbf{H})$ over the permanent magnet region R_m :

$$\mathcal{M} = \frac{\mu_0 \int_{R_m} d^3x (-\mathbf{B} \cdot \mathbf{H})}{4\mu \int_{R_m} d^3x (-\mathbf{B} \cdot \mathbf{H})_{\text{max}}} \quad (5.23)$$

Where $(-\mathbf{B} \cdot \mathbf{H})_{\text{max}}$ denotes the maximum possible value of the energy product $(-\mathbf{B} \cdot \mathbf{H})$, given by:

$$(-\mathbf{B} \cdot \mathbf{H})_{\text{max}} = \frac{1}{4\mu} \|\mathbf{B}_r\|^2 \quad (5.24)$$

Maximizing the fraction of energy that associated with the field generated by magnet outside of itself, is thus equivalent to maximizing the integral of the energy product $(\mathbf{B} \cdot \mathbf{H})$.

Abele's optimisation approach assumes that the whole space is composed by two non-overlapping regions, denoted here by R_m and R_g . The region R_m is occupied by permanent magnet material. It is assumed that the permanent magnet obeys a linear relation $\mathbf{B} = \mu\mathbf{H} + \mathbf{B}_r$, where the permeability μ is uniform, but the remanence \mathbf{B}_r may vary both in norm and orientation. Inside R_g the permeability is equal to μ_0 , and the field is assumed by to be equal to a pre-determined distribution $\mathbf{H}_0(\mathbf{x})$. As none of the regions R_m and R_g is required to be a connected set, the border between R_m and R_g may be composed by many closed interfaces, denoted by ∂_i , which are disconnected from each other. The geometry may also include regions occupied by ferromagnetic material whose permeability is assumed to be infinite. In the limit of infinite permeability these regions are equivalent to infinitely thin hollow shells of infinite permeability filled with air. This means that they may be considered as part of R_g , with zero internal flux density. To fix the ideas let us consider the example of the Halbach cylinder geom-

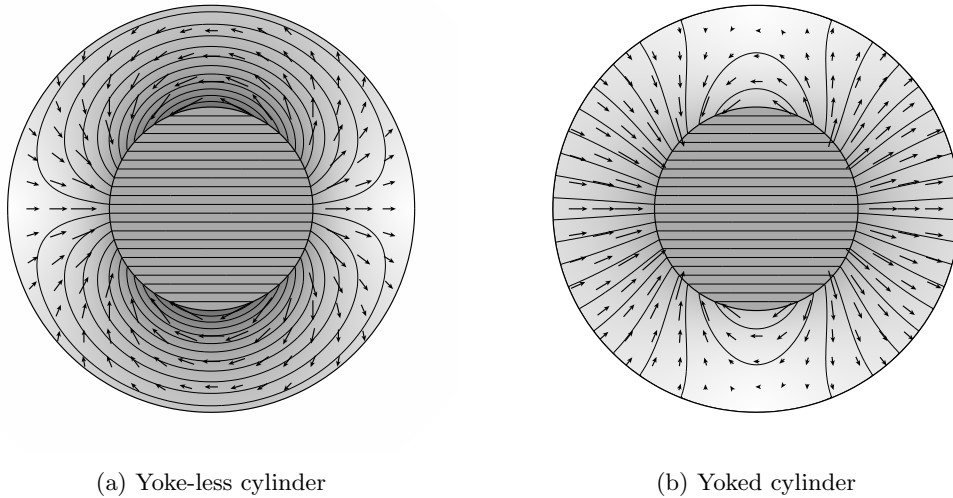


Fig. 5.7: Maximally efficient remanence field generating a uniform field in the central cylindrical cavity. Figure 5.7a shows the case of a cylinder without iron yoke. Except for the radial dependence of the norm of the remanence, this distribution is equivalent to the conventional Halbach cylinder. Figure 5.7b shows the case of a cylinder with an external iron yoke of infinite permeability. The optimal remanence distribution is different, but the air gap field is identical to the one of figure 5.7a.

etry with infinite length, parametrized with polar coordinates ρ and ϕ . The magnet region R_m extends between the internal radius R_I and the external radius R_O . The region R_g consists of the union between the two remaining disconnected regions: the internal cavity, with $\rho < R_I$ and the external region, with $\rho > R_O$. The field \mathbf{H}_0 inside the internal cavity is required to be equal to $H_0\hat{e}_x$, where \hat{e}_x denotes the unit vector of the \hat{e}_x coordinate. The field in the external region is required to be zero, which corresponds to a perfectly self-insulated magnetic system. Two possibilities are considered: the yoke-less case and the yoked case. In the yoked case an

infinitely thin ferromagnetic shell is introduced at the border $\rho = R_O$.

Among all the possible remanence distributions in R_m which are able to generate in R_g the required field \mathbf{H}_0 , the distribution referred to as *ideal remanence* is the one that maximizes the figure of merit \mathcal{M} . The ideal remanence is denoted by $\mathbf{B}_r^{\text{Id.}}$, and is constrained by a set of equations, formally derived in [86], which guarantees its optimality with respect to \mathcal{M} . These equations, together with the requirement that $\mathbf{B}_r^{\text{Id.}}$ generates \mathbf{H}_0 , completely determine $\mathbf{B}_r^{\text{Id.}}$. The ideal remanence is both solenoidal and irrotational:

$$\nabla \cdot \mathbf{B}_r^{\text{Id.}} = 0; \quad \nabla \times \mathbf{B}_r^{\text{Id.}} = \mathbf{0} \quad (5.25)$$

Being irrotational, the ideal remanence can always be defined in terms of a scalar potential $\Phi_r^{\text{Id.}}$:

$$\mathbf{B}_r^{\text{Id.}} = -\nabla \Phi_r^{\text{Id.}} \quad (5.26)$$

The requirement that $\mathbf{B}_r^{\text{Id.}}$ is also solenoidal implies that the potential $\Phi_r^{\text{Id.}}$ is harmonic, as it obeys Laplace's equation:

$$\nabla^2 \Phi_r^{\text{Id.}} = 0 \quad (5.27)$$

Additionally, the net magnetic charge on each border ∂_i separating R_m from R_g must be zero:

$$\int_{\partial_i} d^2x \mathbf{B}_r^{\text{Id.}} \cdot \hat{\mathbf{n}} = 0 \quad (5.28)$$

Finally, the ideal remanence is always normal to the borders between R_m and the regions occupied by ferromagnetic materials.

$$\mathbf{B}_r^{\text{Id.}} \times \hat{\mathbf{n}} = \mathbf{0} \quad (5.29)$$

This implies that the potential $\Phi_r^{\text{Id.}}$ is constant on each independent border separating R_m from the regions occupied by ferromagnetic material. The flux density $\mathbf{B}^{\text{Id.}}$ and magnetic field $\mathbf{H}^{\text{Id.}}$ associated with the ideal remanence $\mathbf{B}_r^{\text{Id.}}$, satisfy the following relation inside R_m :

$$\mathbf{B}^{\text{Id.}} = \mu \mathbf{H}^{\text{Id.}} + \mathbf{B}_r^{\text{Id.}} \quad (5.30)$$

As it is assumed that the permeability μ is constant over the region R_m , $\mathbf{B}^{\text{Id.}}$ and $\mathbf{H}^{\text{Id.}}$ are solenoidal and irrotational:

$$\begin{cases} \nabla \cdot \mathbf{B}^{\text{Id.}} = 0; & \nabla \times \mathbf{B}^{\text{Id.}} = \mathbf{0} \\ \nabla \cdot \mathbf{H}^{\text{Id.}} = 0; & \nabla \times \mathbf{H}^{\text{Id.}} = \mathbf{0} \end{cases} \quad (5.31)$$

As for $\mathbf{B}_r^{\text{Id.}}$, they can be defined in terms of scalar potentials:

$$\begin{cases} \mathbf{B}^{\text{Id.}} = -\nabla \Phi_B^{\text{Id.}} \\ \mathbf{H}^{\text{Id.}} = -\nabla \Phi_H^{\text{Id.}} \end{cases} \quad (5.32)$$

These potentials are also harmonic:

$$\nabla^2 \Phi_B^{\text{Id.}} = \nabla^2 \Phi_H^{\text{Id.}} = 0 \quad (5.33)$$

The problem is reduced to solving in the region R_m the two partial differential equations governing the potentials $\Phi_B^{\text{Id.}}$ and $\Phi_H^{\text{Id.}}$. The boundary conditions obeyed by the two potentials

at the borders ∂_i are determined from the field \mathbf{H}_0 inside R_g by imposing the conservation that the tangential component of $\mathbf{H}^{\text{Id.}}$ and the normal component of $\mathbf{B}^{\text{Id.}}$ across the interfaces ∂_i . The remaining degrees of freedom are removed by applying equations 5.28, and 5.29.

Since the flux density $\mathbf{B}^{\text{Id.}}$ is solenoidal everywhere, the flux through each of the closed borders δ_i is zero:

$$\int_{\partial_i} d^2x (\nabla \Phi_B^{\text{Id.}}) \cdot \hat{\mathbf{n}} = 0 \quad (5.34)$$

This also implies that equation 5.28 applies independently to $\mathbf{H}^{\text{Id.}}$:

$$\int_{\partial_i} d^2x (\nabla \Phi_H^{\text{Id.}}) \cdot \hat{\mathbf{n}} = 0 \quad (5.35)$$

The field $\mathbf{H}^{\text{Id.}}$, is always normal to the boundaries between R_m and the regions occupied by ferromagnetic material:

$$(\nabla \times \Phi_H^{\text{Id.}}) \times \hat{\mathbf{n}} = \mathbf{0} \quad (5.36)$$

This implies that equation 5.29 applies independently to $\mathbf{B}^{\text{Id.}}$:

$$(\nabla \times \Phi_B^{\text{Id.}}) \times \hat{\mathbf{n}} = \mathbf{0} \quad (5.37)$$

For the example of the Halbach cylinder we can calculate $\Phi_B^{\text{Id.}}$ and $\Phi_H^{\text{Id.}}$ starting from the most general form of continuous harmonic potential, given by equation 4.28, which we report here:

$$\Phi(\rho, \phi) = \Phi_0 + a_0 \log(\rho) + \sum_{n=1}^{+\infty} (c_n^{(\text{In})} \rho^n + c_n^{(\text{Out})} \rho^{-n}) \cos(n\phi) + \sum_{n=1}^{+\infty} (s_n^{(\text{In})} \rho^n + s_n^{(\text{Out})} \rho^{-n}) \sin(n\phi) \quad (5.38)$$

Using 5.32 the flux density $\mathbf{B}^{\text{Id.}}$ and the field $\mathbf{H}^{\text{Id.}}$ can then be expressed in terms of the coefficients of expansion appearing in 5.38. Application of equations 5.35 and 5.36 implies that the coefficient a_0 is zero for both $\Phi_B^{\text{Id.}}$ and $\Phi_H^{\text{Id.}}$. For the yokeless case we just have to match the tangential component of \mathbf{H} and the radial component of \mathbf{B} with the required distributions at $\rho = R_I$ and $\rho = R_O$. This results in all the coefficients being zero, except for c_{+1} and c_{-1} . The continuity conditions at R_I and R_O are written for these two coefficients as a system of two linear equations which is easily solved, leading to the following expression for $\Phi_r^{\text{Id.}}$:

$$\Phi_r^{\text{Id.}} = H_0 \left(\frac{R_I^2}{R_O^2 - R_I^2} \right) \left[\mu_0 \left(\frac{R_O^2}{\rho} + \rho \right) + \mu \left(\frac{R_O^2}{\rho} - \rho \right) \right] \cos(\phi) \quad (5.39)$$

For the yoked case the procedure is similar, except for the fact that the condition on the radial component of $\mathbf{B}^{\text{Id.}}$ at R_O is replaced with the condition that $\Phi_B^{\text{Id.}}$ is constant at $\rho = R_O$. As mentioned above, this means that $\mathbf{B}^{\text{Id.}}$ is normal to the boundaries of R_m with the regions filled with ferromagnetic material. The expression for $\Phi_r^{\text{Id.}}$, for the yoked case is:

$$\Phi_r^{\text{Id.}} = H_0 \left(\frac{R_O^2}{\rho} - \rho \right) \left[\mu_0 \left(\frac{R_I^2}{R_O^2 + R_I^2} \right) + \mu \left(\frac{R_I^2}{R_O^2 - R_I^2} \right) \right] \cos(\phi) \quad (5.40)$$

The study presented in [86] derives an important theorem concerning the geometry of the regions occupied by ferromagnetic material. If the field \mathbf{H}_0 is zero inside a certain subset R_g^0 of R_g , than completely insulating R_g^0 from R_m with ferromagnetic material will lead to the greatest

possible value of \mathcal{M} . Therefore self-insulated magnetic structures are more energetically efficient when they are fully yoked. Moreover, as mentioned in [86, 85, 84], the level surfaces of the magnetic scalar potential are efficiently used as separating interface between permanent magnet and soft magnetic material with $\mu \rightarrow \infty$. This idea, which ultimately is consequence of the invariance properties discussed in section 4.1.3, will be exploited extensively in this thesis. In particular, section 6.2 discusses the link between this concept and the reciprocity theorem.

5.2.2 The virtual magnet method

The connection between the reciprocity theorem and linear objective functionals has been introduced in section 5.1.3. This formalism derived from this theorem is readily applied to smoothly varying remanence distributions. As long as the permeability tensor is symmetric and is the same in any point for system 1 and 2, the theorem can be expressed as:

$$\int d^3x \mathbf{B}_{r1}(\mathbf{x}) \cdot \mathbf{H}_2(\mathbf{x}) = \int d^3x \mathbf{B}_{r2}(\mathbf{x}) \cdot \mathbf{H}_1(\mathbf{x}) \quad (5.41)$$

The reciprocity theorem can be used to solve magnet design problems by considering an empty air gap, and by aligning the remanence everywhere with the field generated by a *virtual* magnet placed in this air gap. When expressed in integral form a linear functional is written as:

$$\mathcal{S}[\mathbf{H}_1] = \int d^3x \mathbf{H}_1(\mathbf{x}) \cdot \mathbf{u}(\mathbf{x}) \quad (5.42)$$

where \mathbf{u} is an arbitrarily defined objective vector field. The integration domain can be reduced from the whole space to the region where the objective vector field \mathbf{u} is non-zero, denoted by R_g .

If the objective vector field \mathbf{u} is used as the remanent flux density \mathbf{B}_{r2} of a *virtual* magnet, equation 5.41 implies that \mathcal{S} is also equal to:

$$\mathcal{S}[\mathbf{B}_{r1}] = \int d^3x \mathbf{H}_2(\mathbf{x}) \cdot \mathbf{B}_{r1}(\mathbf{x}) \quad (5.43)$$

where \mathbf{H}_2 is the field generated by the virtual remanence \mathbf{B}_{r2} , and \mathbf{B}_{r1} is the remanent flux density of the real magnet, that is associated with the real field \mathbf{H}_1 . The functional \mathcal{S} has the dimensions of an energy. Again, the integration domain can be reduced to the region of space where the remanence of the real magnet is non-zero. This region, denoted by R_m and called the magnet design region, is assumed not to overlap with R_g . Equation (5.41) applies since R_m , (R_g), will be the only region in which \mathbf{B}_{r1} , (\mathbf{B}_{r2}), is not zero. The use of the reciprocity theorem for the optimisation of a magnetic system is schematically illustrated in figure 5.8.

The theorem provides the solution to the following problem: determine the optimal direction of the remanent flux density \mathbf{B}_{r1} in any point of the region R_m such that the field \mathbf{H}_1 generated by \mathbf{B}_{r1} maximizes the integral of Eq. (5.42). The answer is evidently: the optimal remanence \mathbf{B}_{r1} should be aligned in every point with the virtual field \mathbf{H}_2 generated by \mathbf{B}_{r2} . To illustrate this result we consider a simple example in which we wish to maximize the field in a given direction inside a cylindrical region with infinite length. This region will then be occupied by a virtual magnet with uniform remanent flux density. If the direction of the virtual remanence is transversal to the axis of the cylinder, for example in the positive x direction, the field generated

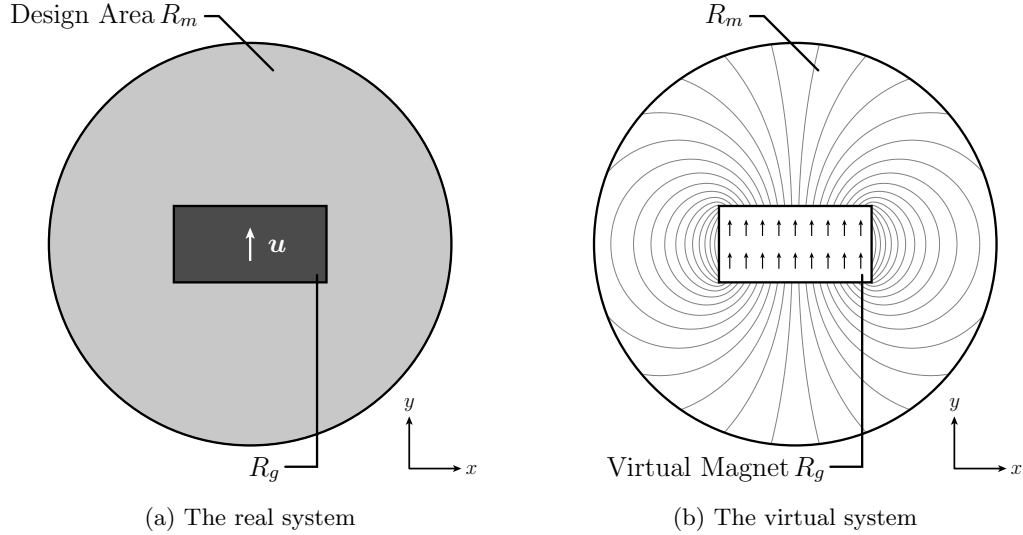


Fig. 5.8: 5.8a: The use of the reciprocity theorem for magnet optimisation is illustrated by considering a uniform objective field \mathbf{u} , oriented in the positive y direction and defined over the rectangular air gap R_g . 5.8b: The air gap R_g is filled with a virtual magnet, magnetized in the same direction of the objective vector field \mathbf{u} . The reciprocity theorem implies that the optimal remanence is aligned with the field generated by the virtual magnet in any point of the design area R_m . The flux lines of the virtual field \mathbf{H}_2 are shown in figure 5.8b.

by it will lead to the well-known Halbach cylinder solution[65], which in cylindrical coordinates is given by:

$$\mathbf{B}_{r1}(r, \phi) \propto \cos(2\phi) \hat{\mathbf{e}}_x + \sin(2\phi) \hat{\mathbf{e}}_y \quad (5.44)$$

This case of the Halbach cylinder case is discussed in detail in section 6.4.1.

For simplicity, most of the examples analysed in this thesis represent two dimensional geometries. This approximation is a realistic description of systems for which the length along one direction, e. g. z , is considerably larger than along the other two directions. It is also required that the characteristics of the system are constant along this direction. Almost all the methods present in this work are easily generalized to three-dimensional geometries. We will now consider two simple examples of applications of the virtual magnet method to three-dimensional systems. The geometry, shown in figure 5.9, consists in both cases of a spherical magnet with a central cavity of the shape of a rectangular box. The virtual remanence \mathbf{B}_{r1} is zero everywhere except for inside this cavity. One quarter of the spheres is not displayed in order to reveal the inside of the structure. For the case of figure 5.9a the virtual remanence is a uniform field oriented in the positive vertical direction. For the case of figure 5.9b the virtual remanence is given by a quadrupole field oriented in the x - z plane. The norm of the remanence is constant in both cases.

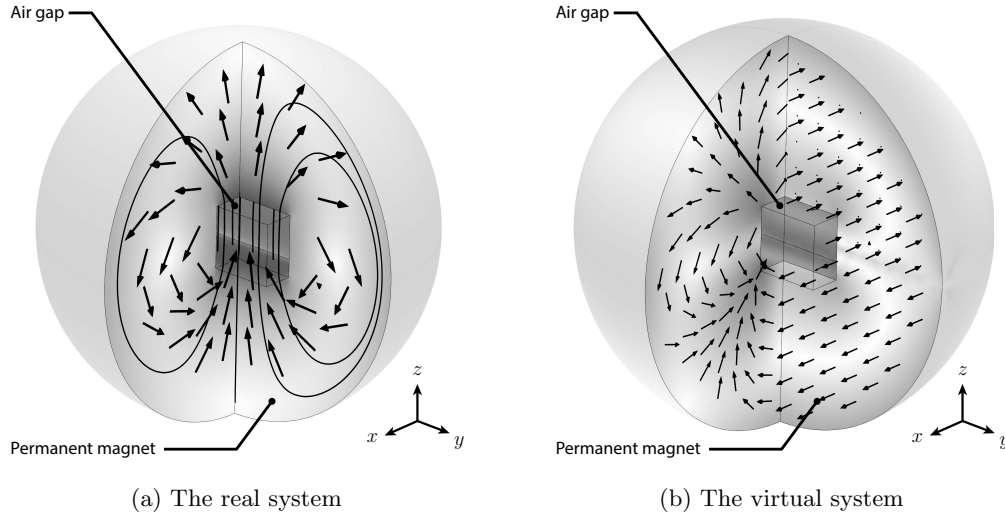


Fig. 5.9: Two examples of application of the virtual magnet method to three-dimensional geometries. In both cases, the permanent magnet region is a sphere with an air gap of the shape of a rectangular box. The objective of figure 5.9a is to generate inside the air gap a dipole field oriented in the z direction. The objective of figure 5.9b is to generate a quadrupole field oriented along the x - z plane.

5.2.3 Energy considerations

The virtual magnet method also suggests a practical technique for assembling systems composed of different pieces of permanent magnet. As it is explained in ref. [41] for the case of the Halbach cylinder geometry, if a permanent magnet, called the anchor, is temporarily placed in the central air gap region it will exercise a force on the surrounding pieces of permanent magnet which will automatically align them in the Halbach configuration. The central anchor magnet plays the same role in this case as the virtual magnet in the optimisation procedure presented here, and the value of \mathcal{S} corresponds to the mutual energy between the anchor magnet and the surrounding segments. This fabrication method can be extended to many different cases besides the Halbach cylinder geometry, as long as the forces resulting from the mutual interaction between the different magnet pieces are negligible compared to the force due to the anchor magnet .

Furthermore, by allowing configurations where the norm of the remanence is not uniform, the algorithm can provide solutions that are also maximally efficient, in the sense that they maximize the fraction of magnetic energy that the permanent magnet is able to generate outside of itself[86]. More specifically, among all of the possible remanence distributions \mathbf{B}_{r1} in R_m able to generate the same field \mathbf{B}_1 in R_g , the ideal remanence maximizes the figure of merit \mathcal{M} , introduced in section 5.2.1.

$$\mathcal{M} = \frac{\int_{R_g} d^3x \|\mathbf{B}_1(\mathbf{x})\|^2}{\int_{R_m} d^3x \|\mathbf{B}_{r1}(\mathbf{x})\|^2} \quad (5.45)$$

From the discussion of section 5.2.1, it is clear that the sufficient conditions for maximal energy

efficiency to occur are:

- The magnet design region R_m and the air gap region R_g are not overlapping.
- The union of R_g with R_m is equal to the whole space, except for the regions enclosed by material with infinite permeability
- Inside R_g the permeability is equal to μ_0
- Inside R_m the permeability μ is uniform
- The real remanent flux density is chosen to be not only aligned, but *proportional to* the virtual field \mathbf{H}_2 .

When the last two conditions are satisfied, the real remanent flux density is both solenoidal and irrotational, thus satisfying the ideal remanence equations of ref. [86]. When all the conditions above are satisfied the magnetic structure in R_m is maximally energy efficient.

5.2.4 Non-Linear Objectives

In this section we consider an iterative gradient based procedure which can be applied to non-linear objective functional. The method investigated here presents similarities with the algorithms discussed in [81], applied to the magnetic inverse problem expressed by the functional of equation 4.66. The technique described in this section can instead be applied to a general non linear objective. The approach is based on the reciprocity theorem, and applies to the optimisation of a smoothly varying remanence distribution $\mathbf{B}_r(\mathbf{x})$. However, the numerical implementation which employs FEM analysis, consists in optimising the expansion of $\mathbf{B}_r(\mathbf{x})$ on a discrete grid. For simplicity, we consider the case of two dimensional magnetic systems. The non-linear objective functional is denoted by \mathcal{S} . The value of \mathcal{S} is determined by the magnetic field distribution $\mathbf{H}(\mathbf{x})$ over a certain region R_g . We consider a very fine grid of points $\mathbf{x}_i \in R_g$, and the magnetic field $\mathbf{H}_i = \mathbf{H}(\mathbf{x}_i)$ in each of these points. The notation $\mathcal{S} = \mathcal{S}(\mathbf{H})$ will therefore be used to express the dependence of \mathcal{S} on all the vectors \mathbf{H}_i .

The procedure starts with a certain initial configuration, corresponding to the field values $\mathbf{H}_i^{(0)}$. The first step is consist in computing the linear approximation to \mathcal{S} , evaluated at the initial configuration $\mathbf{H}^{(0)}$. For a two-dimensional system this is written as:

$$\mathcal{S}(\mathbf{H}) \approx \mathcal{S}(\mathbf{H}^{(0)}) + \sum_i \left(\frac{\partial \mathcal{S}}{\partial H_{ix}} \right)_{\mathbf{H}^{(0)}} (H_{ix} - H_{ix}^{(0)}) + \sum_i \left(\frac{\partial \mathcal{S}}{\partial H_{iy}} \right)_{\mathbf{H}^{(0)}} (H_{iy} - H_{iy}^{(0)}) \quad (5.46)$$

It is convenient to write the previous expression in a more compact form:

$$\mathcal{S}(\mathbf{H}) \approx \mathcal{S}(\mathbf{H}^{(0)}) + \mathcal{L}_0(\mathbf{H}) - \mathcal{L}_0(\mathbf{H}^{(0)}) \quad (5.47)$$

The linear function \mathcal{L}_0 is defined as:

$$\mathcal{L}_0(\mathbf{H}) = \sum_i \left(\frac{\partial \mathcal{S}}{\partial H_{ix}} \right)_{\mathbf{H}^{(0)}} (H_{ix}) + \sum_i \left(\frac{\partial \mathcal{S}}{\partial H_{iy}} \right)_{\mathbf{H}^{(0)}} (H_{iy}) \quad (5.48)$$

It is convenient to introduce the vectors $\mathbf{u}_i^{(0)}$, defined by:

$$u_{ix}^{(0)} = \left(\frac{\partial \mathcal{S}}{\partial H_{ix}} \right)_{\mathbf{H}^{(0)}} \quad \text{and} \quad u_{iy}^{(0)} = \left(\frac{\partial \mathcal{S}}{\partial H_{iy}} \right)_{\mathbf{H}^{(0)}} \quad (5.49)$$

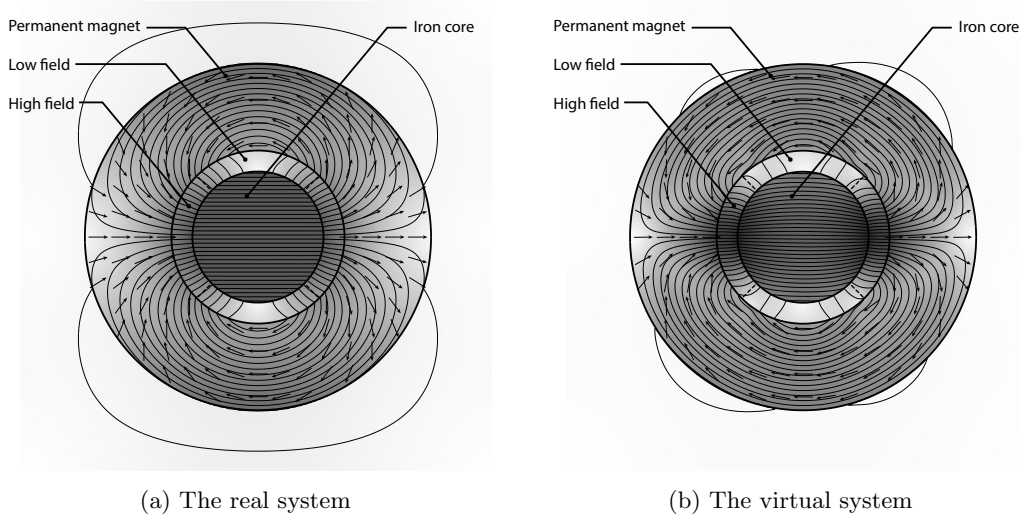


Fig. 5.10: : rotary device for magnetic refrigeration, analogous to the system shown in figure 4.2. The objective is expressed by the functional of equation 5.54. The optimisation is performed with an iterative procedure. Figures 5.10a and 5.10b show the initial and final configurations, respectively. As desirable, the air gap field intensity increased in the high field regions and decreased in the low field regions.

The linear function \mathcal{L}_0 can thus be written as

$$\mathcal{L}_0(\mathbf{H}) = \sum_i \mathbf{u}_i^{(0)} \cdot \mathbf{H}_i \quad (5.50)$$

If the gradient descent method was applied to the field itself, instead of the remanence, it would result in the following iterative scheme:

$$\mathbf{H}^{(k)} = \mathbf{H}^{(k-1)} + \gamma \mathbf{u}^{(k-1)} \quad (5.51)$$

The small parameter γ controls the step size, and its sign determines if the iteration will converge towards maxima or minima. However, the purpose of the procedure is to optimise \mathcal{S} with respect to the remanence \mathbf{B}_r which generates the magnetic field \mathbf{H} .

We can now use the reciprocity theorem to express \mathcal{L}_0 in terms of the remanence field \mathbf{B}_r :

$$\mathcal{L}_0(\mathbf{H}) = \sum_i \mathbf{u}_i^{(0)} \cdot \mathbf{H}_i \rightarrow \int_{R_g} \mathbf{u}^{(0)} \cdot \mathbf{H} = \int_{R_m} \mathbf{v}^{(0)} \cdot \mathbf{B}_r \quad (5.52)$$

The vector field $\mathbf{v}^{(0)}(\mathbf{x})$ is the magnetic field that would be generated if $\mathbf{u}^{(0)}$ was used as remanence of a virtual magnet. In the numerical implementation this vector field is defined on the same grid as \mathbf{H} and \mathbf{u} . Having calculated the vectors \mathbf{v}_i , we can apply the following iterative scheme on \mathbf{B}_r :

$$\mathbf{B}_r^{(k)} = \mathbf{B}_r^{(k-1)} + \gamma \mathbf{v}^{(k-1)} \quad (5.53)$$

Thanks to the reciprocity theorem this procedure only requires two FEM computations for each step of the iteration: one to calculate the field $\mathbf{H}^{(k)}$ generated by the remanence $\mathbf{B}_r^{(k)}$, and one to calculate the virtual field $\mathbf{v}^{(k)}$ generated by the virtual remanence $\mathbf{u}^{(k)}$.

In reality, many of the objectives of practical interest are p -homogeneous with respect to the field for some exponent p . This implies that the iterative procedure would never stop, leading to higher and higher values of the norm of the remanence (if $p > 1$), or smaller and smaller values (if $p < 1$). Moreover, it is often more interesting to consider remanence distributions with constant norm B_r . The homogeneity of \mathcal{S} allows us to rule out the norm of the remanence from our procedure, and apply the iteration to modify the orientation ψ of the remanence at each point. The homogeneity guarantees that the optimal distribution $\psi(\mathbf{x})$ does not depend on B_r .

As illustrative example we consider a rotary device for magnetic refrigeration. The geometry is analogous to the system shown in figure 4.2. The optimisation problem is to maximise the non linear objective functional \mathcal{S} expressed by:

$$\mathcal{S}[\mathbf{H}] = \frac{1}{V_{\text{High}}} \int_{R_{\text{High}}} d^3x \|\mu_0 \mathbf{H}(\mathbf{x})\|^{2/3} - \frac{1}{V_{\text{Low}}} \int_{R_{\text{Low}}} d^3x \|\mu_0 \mathbf{H}(\mathbf{x})\|^{2/3} \quad (5.54)$$

Here R_{High} and R_{Low} denote the high and low field regions respectively. As was introduced in section 3.3 this functional is related to the cooling power provided by the device. The starting configuration is given by the remanence distribution of the Halbach cylinder with $p = 1$, which is shown in figure 5.10a. As can be noticed, because of the central iron yoke, this system is not perfectly self insulated. The final configuration is shown in 5.10b. The largest deviation of the final remanence distribution with respect to the initial one, is observed in the proximity of the borders between the high and low field regions. The field simultaneously increases in the high field region and decreases in the low field region. Moreover, the whole structure is better insulated from its surroundings. Quantitatively, the value of the objective increases by 20%.

Geometry Optimization

The topic of this chapter is the introduction of techniques that allow us to optimise the geometry of magnetic systems, i.e.: subdividing the magnetic systems into regions occupied by materials with different magnetic properties. This problem presents more challenges than the one approached in the previous section. We will start by considering the implications of the reciprocity theorem with respect to this problem. As mentioned in section 5.2.2, this framework can only be applied under two main limitations: the linearity of the objective functional with respect to the magnetic field, and the linearity of the \mathbf{B} - \mathbf{H} relations describing the magnetic behaviour at each point.

We will see that starting with these somehow restrictive assumptions pays off, as will allow us to derive several interesting results. Besides their immediate relevance concerning magnet optimisation problems directly described by a linear functional, these results provide insight about general properties of magnetic systems.

The objective functional \mathcal{S} will always be expressed in terms of the virtual field \mathbf{H}_2 , as in equation 5.43:

$$\mathcal{S}[\mathbf{B}_{r1}] = \int_{R_m} d^3x \mathbf{H}_2(\mathbf{x}) \cdot \mathbf{B}_{r1}(\mathbf{x}) \quad (6.1)$$

6.1 Air-magnet border

We now consider the external border of the magnet. An important observation regarding Eq. (5.43) is that the different pieces of magnet contribute independently to the value of the objective functional \mathcal{S} : the optimal direction of the remanence in each point remains the same regardless of how the remanence has been chosen elsewhere. The independence is a consequence of the fact that \mathbf{H}_1 is linear with respect to \mathbf{B}_{r1} , and \mathcal{S} is linear with respect to \mathbf{B}_{r1} . Moreover, once \mathbf{B}_{r1} has been aligned to \mathbf{H}_2 at a point \mathbf{x} , the integrand of equation 5.43 becomes $\|\mathbf{H}_2(\mathbf{x})\| \|\mathbf{B}_{r1}(\mathbf{x})\| \geq 0$. This means that the contribution from that point of the magnet to the value of \mathcal{S} is proportional to the norm of the virtual field which can thus be interpreted as a weight factor of the corresponding site in the magnet design area [80]. This fact can be used to predict the optimal border between hard magnets and air.

As is explained in section 4.3.1, in order for Eq.(5.41) to be true, the magnetic susceptibility χ_m must be the same for the real and the virtual system, implying that it is not possible to determine the optimal susceptibility field, i.e. the optimal distribution of materials. However, if the susceptibility of the permanent magnet material is zero, as is approximately true for, e.g., rare-earth hard magnets, we are not forced to decide in advance which areas of the magnet design region are to be filled with magnet and which areas are to be filled with air. Instead, we can determine the optimal border between magnet and air using the amount of available permanent magnet material V_m as a constraint.

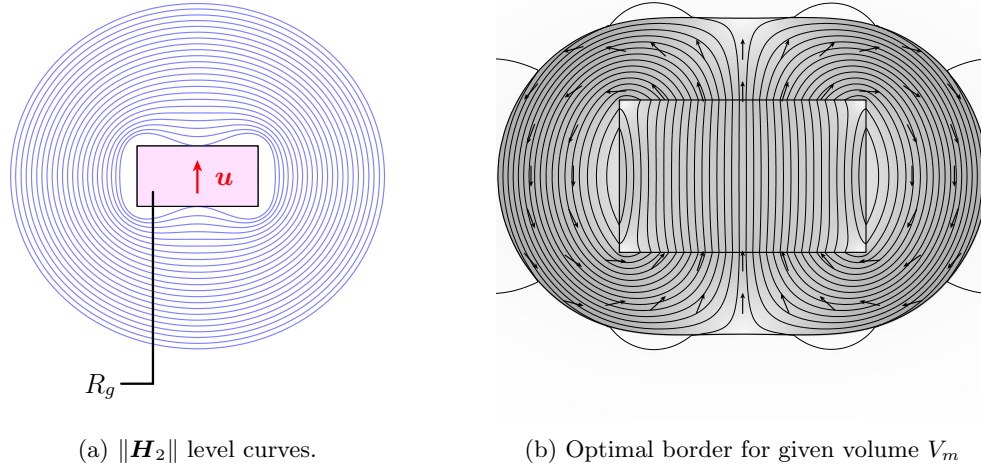


Fig. 6.1: Illustration of the technique to determine the optimal border between permanent magnet and air. The idea is illustrated for the example of a two-dimensional system designed to maximize the y component of the field averaged over the internal rectangular cavity. 6.1a: the virtual magnet is shown as the pink shaded area and its remanence is indicated by the red arrow. The blue curves are levels of $\|\mathbf{H}_2\|$ which, for a permanent magnet with $\chi_m = 0$, are the optimal borders between magnet and air. 6.1b: FEM simulation of the real system. One of the $\|\mathbf{H}_2\|$ level curves have been selected as border, thus determining the total volume of permanent magnet of the real system.

As the contribution to the value of \mathcal{S} from a point of the design region is equal to $H_2 = \|\mathbf{H}_2\|$, it is better to utilize the permanent magnet material in areas where the norm of the virtual field \mathbf{H}_2 is larger. This implies that the optimal borders between hard magnet and air are given by the level surfaces of the scalar field $H_2(\mathbf{x})$.

Figure 6.1 illustrates this approach for the case of a two-dimensional system designed to maximize the y component of the field averaged over the internal rectangular cavity. Figure 6.1a shows the virtual system and some level curves of $\|\mathbf{H}_2\|$. Figure 6.1b shows the FEM simulation of the real system corresponding to one of the possible borders. As this choice determines the amount of permanent magnet present in the real system, the selection of the border can match a given constraint on the magnet volume.

For the case of the Halbach cylinder with $p = 1$ the norm H_2 of the virtual field \mathbf{H}_2 depends only on the radial coordinates, and is proportional to $1/r^2$. This implies that the optimal external border of the magnet is always a cylindrical surface which is co-axial with the inner cylindrical cavity. It is insightful to consider in this respect the general expression of a continuous harmonic scalar potential expressed in polar coordinates, reported in equation 4.28. If we consider the field generated outside of itself by a two-dimensional permanent magnet which occupies a bounded subset of the x - y plane, the requirement that the field vanishes at infinity implies that the coefficients of the expansion corresponding to positive powers of ρ must be zero, as well as the coefficient of the $\log(\rho)$ term. Since, among the terms with negative

powers of ρ , the higher multipole terms vanish more quickly than the lower multipole terms, far enough from the magnet the behaviour is dominated by the lowest external multipole term, which is denoted by n_0 . As long as the other terms can be neglected the levels of the norm H_2 of the field of the virtual field are again given by cylindrical surfaces. Thus, far enough from a two-dimensional bounded virtual magnet the optimal borders are given by coaxial cylindrical surfaces, as can be noticed from figure 6.1a. Similarly, for three-dimensional systems the optimal borders become spherical surfaces having the same center. It is worth mentioning that in this limit, the improvement in the value of \mathcal{S} from increasing the magnet volume by dV_m is entirely determined by the order of the lowest multipole term n_0 .

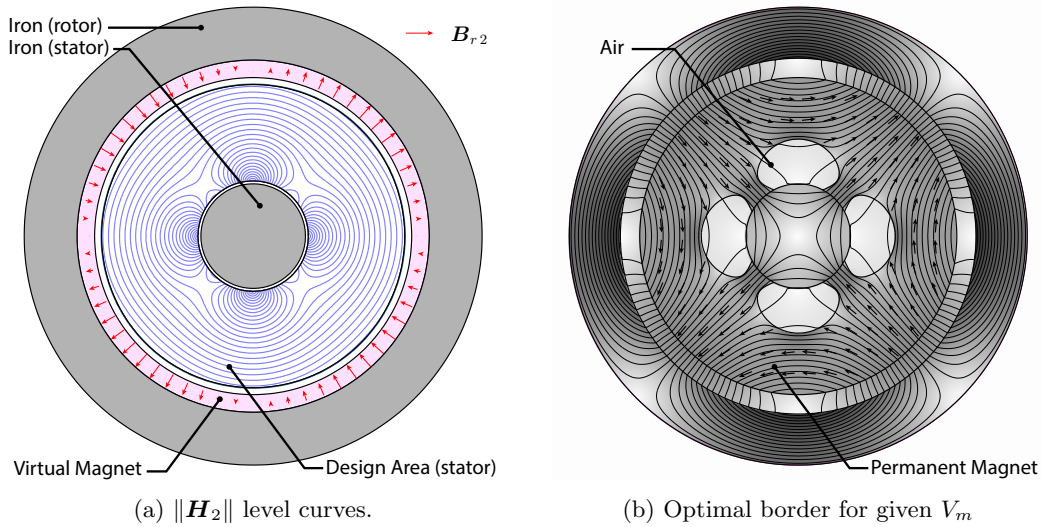


Fig. 6.2: Magnetic system designed to create a sinusoidal radial field in the air gap between stator and rotor. The virtual magnet indicated in figure 6.2a as a pink shaded area, and the virtual remanence is indicated by the red arrows. 6.2a: FEM simulation of the corresponding real magnetic system. It can be noticed that the virtual field is null in four points adjacent to the internal iron core. Since a constraint is applied on the total volume of permanent magnet, the regions surrounding these points are filled with air. The optimal shape of the border of these four regions is given by contours of $\|\mathbf{H}_2\|$. The segmentation of this geometry is shown in figure 6.24a.

Another interesting consequence of the results above concerns iron yokes, iron cores or similar soft magnetic structures, which are often present in magnetic assemblies. If the magnet design region R_m is adjacent to a region containing a material with very high permeability, e.g. iron, the virtual field \mathbf{H}_2 in R_m will be almost normal to the border between the magnet and the highly permeable material (it will be exactly normal in the limit $\mu \rightarrow \infty$). Thus, it is never optimal to have permanent magnet border an iron region and magnetized in a direction that is not normal to the border itself, as this would create a short-circuit for the flux lines to close without passing through the air gap region. Therefore, the optimal remanence is always normal to the border between magnet and iron. Figure 6.2 shows a magnetic system which includes an external iron yoke (rotor), and an internal iron core (stator). The magnet design

area is adjacent to the iron core, but is not adjacent to the inner border of the iron yoke. The virtual remanence $\mathbf{B}_{r,2}$, defined over the air gap between the yoke and the magnet area, is directed radially and depends sinusoidally on the angular coordinate ϕ . In polar coordinates the virtual remanence is expressed by: $\mathbf{B}_{r,2} = \sin(2\phi) \hat{e}_\rho$. This geometry is a simplified model for a permanent magnet electric motor with two poles, and will be discussed in more details in section 6.4.5. The virtual magnet is indicated in figure 6.2a as the pink shaded area and the virtual remanence is indicated by the red arrows. Figure 6.2b shows the FEM of the corresponding real system. As can be noticed from the figures, there are four points adjacent to the iron core where the virtual field is zero. This is an inevitable consequence of the fact that the virtual field “tries to be tangent” to the interface with the iron in those points. From the previous discussion it is evident that the efficiency, with respect to \mathcal{S} , of permanent magnet material placed in these points would be zero. Constraining the magnet volume to a smaller value than the total volume of the magnet design region, results in the exclusion of the regions adjacent to these points, as can be seen from figure 6.2b.

In many of the examples that will be presented in section 6.4 it is assumed that the susceptibility of the permanent magnet material is zero. However, it should be stressed that this requirement is only necessary for the purpose of determining the optimal border between magnet and air. All the remaining optimality results presented in this work remain true for any tensor permeability field $\underline{\underline{\mu}}(\mathbf{x})$ which is symmetric. Moreover, the susceptibility of most of modern rare earth based permanent magnets is in fact very close to zero.

6.2 Iron-magnet border

In this section we consider the problem of determining the border between permanent magnet and soft ferromagnetic material, such as iron. We assume that permeability of the soft ferromagnetic material is so high that it can practically be regarded as if it was infinite. This idealization, commonly used in the literature, is a surprisingly realistic description of many magnetic systems: it is often desirable to avoid magnetic saturation inside the ferromagnetic material, meaning that in the region of the B - H curve around the working point the permeability of these material exceeds by several order of magnitude the permeability of air and of permanent magnet materials. As we will see in section 7.2, as long as the iron parts are dimensioned correctly, the results of simulations performed with a more realistic model which also accounts for the non-linear behaviour are extremely close to the results obtained within the infinite-permeability approximation. The observations reported in section 4.1.3 provide the starting point to approach the problem of determining the border between permanent magnet and soft ferromagnetic material.

Let us consider the example two-dimensional magnetic system shown in figure 6.3. The geometry of the virtual system is illustrated in figure 6.3a. The purpose of this system is to create alternating high field and low field regions in the air gap between the internal iron core and the magnet design area, which is adjacent to the external iron yoke. This magnetic system which is a model for a rotary device for magnetic refrigeration, will be discussed in more details in section 6.4.6. The blue curves indicate levels of the virtual magnetic scalar potential Φ_2 . As mentioned in section 4.1.3 and discussed in [86], if the space on either side of one of those curves is filled with ferromagnetic material with infinite permeability, the solution on the other side of the curve would not change. From another point of view, the virtual field would remain

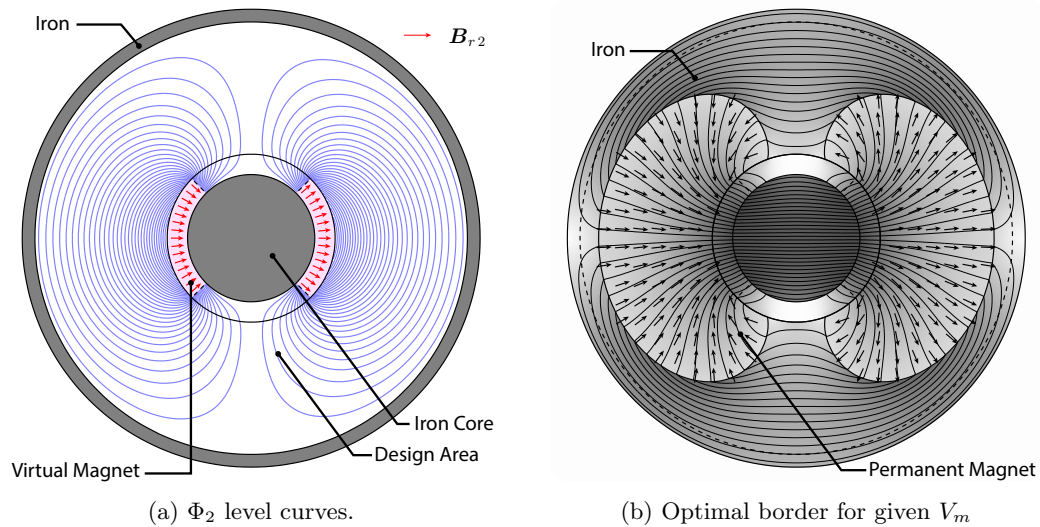


Fig. 6.3: Magnetic system designed to create alternating low and high field region in the air gap between the magnet design area and the central iron core. 6.3a: the virtual magnet is shown as the pink shaded area and its remanence is indicated by the red arrows. The blue lines indicate level curves of the virtual scalar potential Φ_2 . The part of the magnet design area outside of one pair of symmetrical level curves is filled with iron. Figure 6.3b shows the result of the FEM simulation of the corresponding real magnetic system. The segmentation of this geometry is shown in figure 6.25a.

normal to the border with iron, as we have seen to be optimal. For three-dimensional systems the levels of Φ_2 are surfaces, but the concept is the same. Even though the solution does not change on the side of the Φ_2 level that is not filled with ferromagnetic material, the portions of the air gap on the wrong side of the level curve would be modified as well. As the air gap is not part of the magnet design area, the resulting geometry would not anymore represent the original optimisation problem.

However, for this example we can use the same idea in an approximate way, and check if the final optimised configuration is satisfactory with respect to our original objective functional or, more in general, with respect to the purpose of the magnetic system. The approximation consists in filling with iron only the area between a Φ_2 level curve and the border of the magnet design area. The level curve can be selected to match a given constraint on the total magnet volume V_m . Figure 6.3b shows the result of the FEM simulation of the real system. It can be noticed that the resulting real flux density B_1 , indicated by the field lines, reproduces with a good approximation the virtual remanence, indicated in figure 6.3a by the red arrows.

It is worth mentioning that the external iron yoke that is present in the virtual system confines the Φ_2 level curves, thus affecting the resulting optimised configuration. The most external pair of contour curves is given by two adjacent semicircles having the same radius as the inner border of the yoke. This also shows that the last areas to be included in the permanent magnet region are the regions surrounding the highest and lowest points of the inner border of the yoke. As we approach these points the direction of the virtual field would become tangent

to the border itself, and therefore the norm of the virtual field goes to zero. This also indicates that the advantage of filling parts of the design area with iron instead of magnet is that the permanent magnet is only used close to the region where the objective vector field is not zero. The remaining gap is filled with iron, thus allowing a convenient path for the return flux lines to close. In general, as mentioned in section 5.2.1, the energy efficiency of a magnetic system is highest if the the parts of the geometry where the desired field is zero are insulated from the permanent magnet.

In practice, it is rarely useful to entirely fill with iron the space on one side of a Φ_2 level curve, as usually the curves are either unbounded or they invade the virtual magnet region, which is where we are interested in creating the field. Besides, there might be regions where the desired field is zero, but must remain accessible for practical reasons. This is the case of the low field regions of the air gap of the magnetic system of figure 6.3. However, as we will show with many realistic examples, applying the same idea in an approximate way produces results which, from many points of view, are superior to the corresponding “conventional” magnetic system. Moreover, similar concepts are already widely applied, as is mentioned in section 6.2.2.

It is also interesting to mention that a similar approach would allow to determine the borders of regions filled with perfect magnetic insulator, starting with surfaces characterized by $\mathbf{A} \times \hat{\mathbf{n}} = \mathbf{0}$. However, this perspective is less relevant for applications relating to non-superconducting magnetic systems, as the lowest permeability of room-temperature diamagnets is only very slightly smaller than μ_0 .

6.2.1 Yoked Halbach cylinders

We consider the application of the technique described above to the case of the Halbach cylinder with infinite length and $p = 1$. The purpose of the magnetic system is to create in the inner cylindrical cavity, whose radius is denoted by R_I , a uniform field oriented in the positive x direction. As in the illustrative example mentioned before, the geometry of the virtual system includes an iron yoke that is coaxial with the cylindrical cavity and its radius is denoted by R_O . The design area extends between the external border of the central cavity and the internal border of the iron yoke. Its cross section area is thus given by $V_{\text{Design}} = \pi(R_O^2 - R_I^2)$. Figure 6.4a shows the result of the FEM simulation of the optimised real system corresponding to the case where the magnet fills the whole design area, i.e. $V_m = V_{\text{Design}}$, and with external radius given by $R_O = 2.3R_I$.

The virtual field \mathbf{H}_2 is different with respect to the analogous yoke-less geometry. Moreover, the yoke confines the level curves of the virtual potential Φ_2 . Any of these curves can be used as border between permanent magnet and iron. Filling with iron the region outside one symmetrical pair of these curves reduces the volume of permanent magnet. For the example of figure 6.4b half of the volume of the design area has been filled with iron. One notices that in both the examples of figure 6.4 the field in the inner cavity is still quite homogeneous, although not perfectly as in the case of the yoke-less Halbach cylinder, shown figure 4.1a, or in the cases of the yoke-less and yoked cylinder optimised with Abele’s approach, shown in figure 5.7. The field distortion for the case of figure 6.4b is primarily located close to the equatorial region of the air gap, close to the intersections between the magnet-iron border and the border of the air gap. As we will show the advantage of these designs over the yoke-less Halbach cylinder is that the field is on average more intense when compared to a conventional cylinder having the same total volume of permanent magnet.

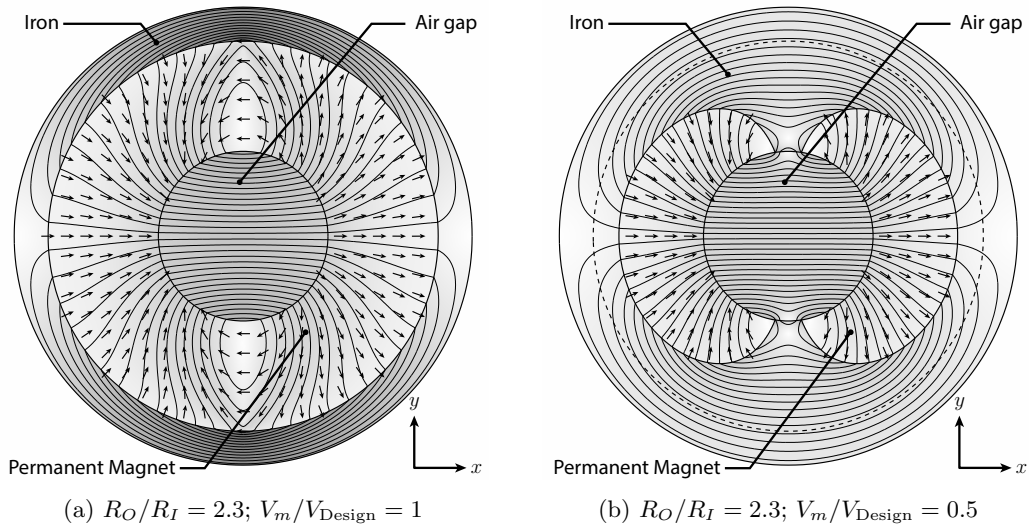


Fig. 6.4: Magnetic system optimised with respect to the x component of the field averaged over the inner cylindrical cavity, of radius R_I . For the example of figure 6.4a the design area between the inner cavity and the external iron yoke, with radius R_O , is entirely filled with permanent magnet. For the example of figure 6.4b half of the design area has been filled with iron. The border between magnet and iron has been selected among the level curves of the virtual potential Φ_2 to match this volume constraint.

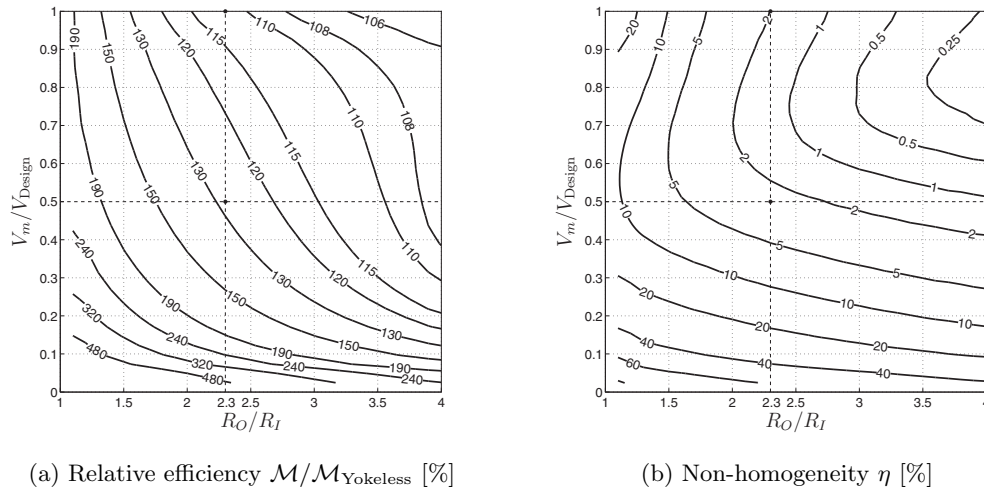


Fig. 6.5: Different combinations of magnet volume, expressed as V_m/V_{Design} and external radius, expressed as R_O/R_I . 6.5a: level curves of the efficiency figure of merit \mathcal{M} , normalized by the efficiency $\mathcal{M}_{\text{Yokeless}}$ of a yoke-less Halbach cylinder with the same volume. 6.5b: level curves of the inhomogeneity measure η .

We consider different combinations of magnet volume, expressed as V_m/V_{Design} and external radius, expressed as R_O/R_I . For each combination the value of the efficiency figure of merit \mathcal{M} is divided by the efficiency $\mathcal{M}_{\text{Yokeless}}$ of a yoke-less Halbach cylinder with the same volume. The external radius of a cylinder with the same volume depends on the volume fraction, and is given by:

$$R'_O = R_I \sqrt{\left(\frac{V_m}{V_{\text{Design}}}\right) \left(\left(\frac{R_O}{R_I}\right)^2 - 1\right) + 1} \quad (6.2)$$

The efficiency for the yoke-less Halbach cylinder is given by [94]:

$$\mathcal{M}_{\text{Yokeless}}(R'_O) = \frac{(\log(R'_O/R_I))^2}{(R'_O/R_I)^2 - 1} \quad (6.3)$$

The homogeneity of the field in the air gap is evaluated by the parameter η (see equation 4.68). The results are shown in figures 6.5a and 6.5b as level curves of $\mathcal{M}/\mathcal{M}_{\text{Yokeless}}$ and η , respectively. The labels indicating the level curves are expressed in percentage for both the quantities.

As can be noticed from figure 6.5a the normalized efficiency $\mathcal{M}/\mathcal{M}_{\text{Yokeless}}$ is always greater than 100 %. Even when the design area is entirely filled with permanent magnet, corresponding to $V_m/V_{\text{Design}} = 1$, the value of 100 % is only reached in the limit $R_O/R_I \rightarrow \infty$. The normalized efficiency increases as either R_O/R_I or V_m/V_{Design} are decreased. Unfortunately the inhomogeneity roughly exhibits the same behaviour, as can be seen from figure 6.5b. There is a trade-off between field quality and field strength, as the most homogeneous configurations are also the least efficient. At the end of the spectrum we find the traditional yoke-less Halbach cylinder which generates a perfectly homogeneous field, but is always less efficient than the yoked designs. The point at the intersection between the two thick dashed lines correspond to the example shown in figure 6.4b. The choice $R_O/R_I = 2.3$ is also extremely close to the optimal radius with respect to the efficiency of a yoke-less Halbach cylinder. The configurations with $R_O/R_I \geq 2.3$ and $V_m/V_{\text{Design}} \geq 0.5$ are mainly characterized by $\eta \leq 2$ %, which would be acceptable for many applications when the field homogeneity is not critical.

6.2.2 Multipoles pole-pieces

The practice of using the level surfaces of the scalar potential as shape of the iron parts of a magnetic system is not new [37, 38]. In fact, the shape of multi-pole elements commonly found as beam-focusing devices in particle accelerators is usually determined from the corresponding term of the expansion of the potential in internal cylindrical multi-poles given in equation 4.28. In cylindrical coordinates the potential is given by:

$$\Phi(\rho, \phi) = c_n^{(\text{In})} \rho^n \cos(n\phi) \quad (6.4)$$

The level curves of this potential may be parametrized by their minimum value of radius, denoted by ρ_0 :

$$\rho(\phi) = \rho_0 \left(\cos(n\phi) \right)^{-1/n} \quad (6.5)$$

Note that, since $n > 1$, the radius goes to infinity as $\cos(n\phi)$ goes to 0. This means that, as already noticed for other cases, one is forced to restrict to a finite portion of the level curves.

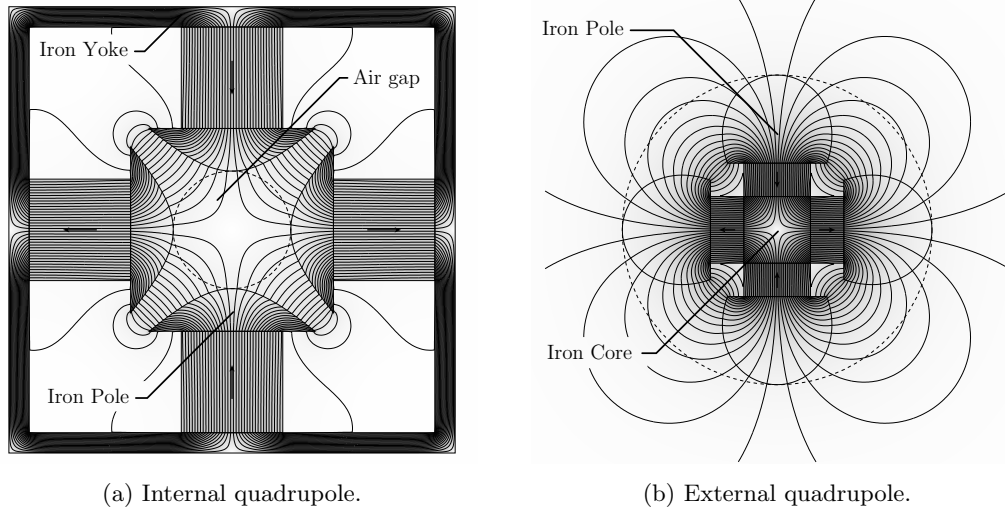


Fig. 6.6: Magnetic systems designed to create a quadrupole field. **6.6a**: the field is created in the internal region. **6.6a**: the field is created in the external region. In cases the shape of the iron poles is

Let us consider the two-dimensional example of figure 6.6a, which represents a magnetic system designed to create a quadrupole field in the central cylindrical area delimited by the dashed line. The shape of the iron parts adjacent to this region have been determined using equation 6.5 with $n = 2$. As $\phi \rightarrow \pm\pi/4$ or $\phi \rightarrow \pi \pm \pi/4$, the border of these parts would go to an infinite distance from the center, which is of course not realizable in practice. The only way to use this design concept is therefore to neglect the parts of the level curves which are further than a certain limit from the center, and to complete the magnetic circuit with the flux sources and the iron yoke which allows the flux lines to close. The flux sources may be permanent magnets, as in the example of figure 6.6a, electro-magnets or a combination of both. The quality of the field in the air gap increases as the volume of the iron poles increases. Moreover, the manufacturing of this kind of geometries is facilitated by the fact that the permanent magnets can be simple blocks with rectangular cross section. This is advantageous as the machining of soft ferromagnetic materials is generally less challenging than it is for, e.g., sintered Neodymium permanent magnet. The aspect ratio of the permanent magnet blocks can be optimised with respect to the air gap field intensity.

The main drawback of this design concept is that, since the intensity of the internal multipole fields increases with increasing distance from the center, we cannot avoid a large fraction of the magnetic energy to be stored in the field that is outside the cylindrical cavity. This means that from the point of view of field strength and energy efficiency this design concept is over-performed by yoked Halbach cylinder with the corresponding value of p .

Figure 6.6b shows a magnetic system designed following an analogous procedure, but having the purpose of creating a quadrupole field in the region outside the dashed line. Such a system could be applied, e.g., as element of a magnetic gear. The border of iron poles has the same expression given by equation 6.5, but with $n = -2$. The same strengths and weaknesses described for the system of figure 6.6a applies to the system of figure 6.6b.

6.2.3 Three dimensional designs

In this section we consider two examples of three-dimensional magnetic systems for magnetic refrigeration. The geometry of the systems is shown in figure 6.7.

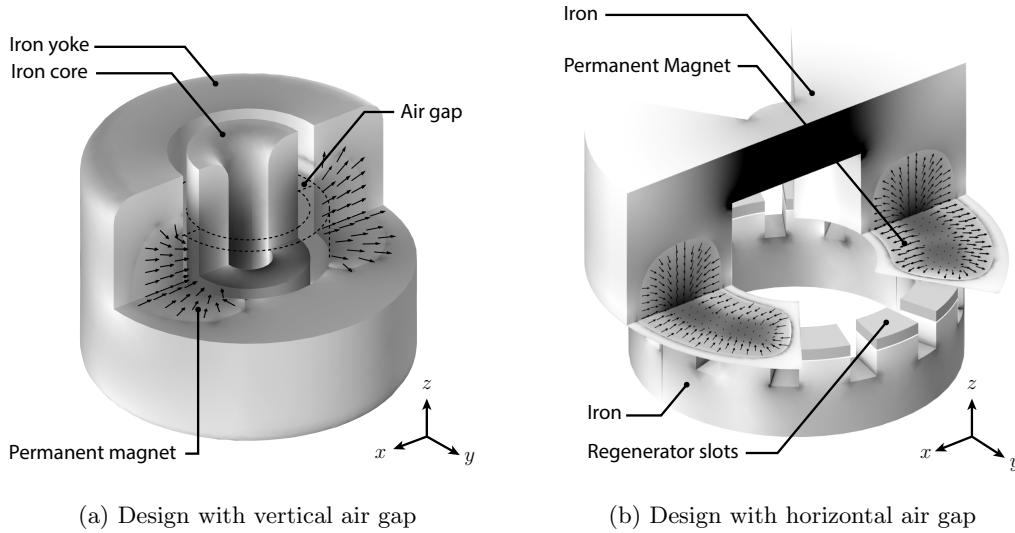


Fig. 6.7: Rotary devices for magnetic refrigeration. In both cases the permanent magnets are completely surrounded by iron, except for their border with the high field region. The surfaces separating magnet from iron coincides with a level surface of the virtual scalar potential Φ_2 . Topologically the two systems are equivalent. The principal difference is that for the case of figure 6.7a the air gap has the shape of a vertical pipe, while for the case of figure 6.7b the air gap, hosting the regenerator slots, has the shape of a disk. In both cases the axis of rotation is the z axis. The system of figure 6.7a is analogous to the device shown in figure 4.2.

In both cases the objective is to create a field with alternating intensity inside the magnetocaloric material. The magnetocaloric material is collected inside cassettes which rotate with respect to the part of the magnetic system that includes the magnet. For the geometry of figure 6.7a the magnet is incorporated in the external cylindrical part, while for the case of figure 6.7b is located in the top part. In both cases there is another part of the geometry composed by iron, which has the purpose of allowing the flux lines to close from the left side to the right side. For the case of figure 6.7a this part is the central iron core, while for the case of figure 6.7b it is the bottom part. In both cases the magnetocaloric material is located in the air gap between the part incorporating the permanent magnet and the other iron part. The difference is that for the case of figure 6.7b the bottom iron part is also moving with respect to the permanent magnet, while in the system of figure 6.7a it makes no difference, since the central iron core is rotationally symmetrical. The air gap has the shape of a pipe for the system of figure 6.7a and the shape of a disk for the system of figure 6.7b. For the case of figure 6.7a the magnetocaloric material is only located in the region delimited by the dashed line, while for the case of figure 6.7b is located in the regions labelled as regenerator slots. In both cases there are two high field regions, spanning an angle of 90° each, alternated by two low field regions, also spanning an angle of 90° each.

The magnetic systems have been optimised with the virtual magnet method. The virtual magnets are located in the high field regions of the air gap, and the virtual remanence $\mathbf{B}_{r,1}$ is directed radially for the case of figure 6.7a and vertically for the case of figure 6.7b. In both cases the virtual remanence of a point of the left half has opposite direction with respect to the remanence of the symmetrical point of the right half. This means that the magnetic circuit describing these systems is a single loop, where the two magnets and the two air gaps from the left and right side are all connected in series, and alternated by iron parts. The remanence of the real system is normalized and aligned at any point with the virtual field. The geometry of the virtual system also includes iron shells at the borders of the magnet design regions, which have the purpose of confining the level surfaces of the virtual potential Φ_2 . The border between the permanent magnet and the iron has been determined by selecting the symmetrical pair of contour surfaces of Φ_2 matching a given constraint on the total magnet volume V_m . The space enclosed between these surfaces and the iron shells delimiting the design regions is thus filled with iron.

These design concepts will be analysed in more details in sections 6.3.4, 6.4.6 and 6.4.7 by considering how to subdivide the permanent magnet into uniformly magnetized blocks.

6.3 Optimal Segmentation

In sections 5.2.2 we saw how the reciprocity theorem is the foundation of the virtual magnet method, which allows us to calculate the optimal spatial dependence of the remanence field $\mathbf{B}_{r,1}(\mathbf{x})$ with respect to a linear objective functional. In sections 6.1 and 6.2 we considered within the same framework the optimisation of the border of permanent magnet region. Real magnetic assemblies are realized by combining blocks of uniformly magnetized material.

In this section we investigate how the optimal remanence field $\mathbf{B}_{r,1}(\mathbf{x})$, calculated within the virtual magnet method, is the starting point to address the problem of how to design a segmented magnetic system whose segmentation is optimal with respect to a linear objective functional. Some of the following subsections reproduce the discussion reported in the paper attached in section B.3.

6.3.1 Segment-segment border

In this section we focus on the border between adjacent uniformly magnetized segments. For simplicity, the results will firstly be derived for a two-dimensional magnetic system. In section 6.3.2 we will see how the results presented in this section are generalised to three-dimensional systems.

We will show that an optimal segmentation of a two dimensional system consists of segments whose mutual borders are lines of constant direction of the virtual field. This we will do by showing that any segmentation which have a curve section $R(\psi)$ of constant ψ divided between two segments can always be replaced by a segmentation which assigns $R(\psi)$ completely to one segment and which is at least as good as the original segmentation.

We start with the objective functional \mathcal{S} , defined in equation 5.42 in terms of the field \mathbf{H}_1 , and expressed in terms of the remanence $\mathbf{B}_{r,1}$ as:

$$\mathcal{S}[\mathbf{H}_1] = \int d^2x \mathbf{B}_{r,1}(\mathbf{x}) \cdot \mathbf{H}_2(\mathbf{x}) \quad (6.6)$$

where \mathbf{H}_2 is the virtual field. The optimisation for the continuous case is immediate: we simply choose a remanence which in all points of the design region is aligned with \mathbf{H}_2 . Assuming that the remanence is constant in magnitude (and setting this magnitude equal to unity for convenience), we get the optimised value of the functional:

$$\mathcal{S}_{\text{Continuous}} = \int_{R_m} d^2x \|\mathbf{H}_2(\mathbf{x})\| \quad (6.7)$$

We now consider the segmentation of the design area R_m into N segments. We introduce the characteristic functions $\phi_n(\mathbf{x})$ that determine to which segment the point \mathbf{x} is assigned. They can only assume the values 0 or 1. If a given point \mathbf{x} is assigned to the k^{th} segment, $\phi_k(\mathbf{x}) = 1$ while $\phi_{n \neq k}(\mathbf{x}) = 0$. The objective functional \mathcal{S} corresponding to the segmentation $\{\phi_n\}$ is then given by:

$$\mathcal{S}[\{\phi_n\}] = \sum_{n=1}^N \mathbf{B}_{r_1}(n) \cdot \int d^2x \phi_n(\mathbf{x}) \mathbf{H}_2(\mathbf{x}), \quad (6.8)$$

since $\mathbf{B}_{r_1}(n)$ is constant on segment n . Now, the direction of the optimal remanence $\mathbf{B}_{r_1}^{\text{Opt}}(n)$ for the n^{th} segment is clearly aligned with $\int d^2x \phi_n(\mathbf{x}) \mathbf{H}_2(\mathbf{x})$. As before, we can then write \mathcal{S} as:

$$\mathcal{S}[\{\phi_n\}] = \sum_{n=1}^N \left\| \int d^2x \phi_n(\mathbf{x}) \mathbf{H}_2(\mathbf{x}) \right\|. \quad (6.9)$$

Thus, the problem of finding an optimal segmentation is equivalent to finding a set of characteristic functions $\{\phi_n\}$ which maximizes the value of \mathcal{S} in Eq. (6.8).

To proceed we make a change of integration variables. Let us assume for now that each set $R_m(\psi_a) = \{\mathbf{x} : \psi(\mathbf{x}) = \psi_a\} \cap R_m$, defined by a particular value of ψ_a , corresponds to a finite-length segment of a single curve of constant direction of the virtual field. In reality the same direction ψ can often be found in non contiguous parts of the geometry. We will exclude this scenario for now, and analyse this point in details in section 6.3.6. The curve segment $R_m(\psi_a)$ can be parametrized by some coordinate λ of finite range. We can then perform the coordinate transformation $\mathbf{x} \rightarrow (\psi, \lambda)$, as illustrated in figure 6.8a. One possible choice for λ is the curve length along $R_m(\psi)$ from the external border of the design area. It is possible to show that, if the permeability is uniform over the design area, the contour lines of ψ are also field lines of ∇H_2 . This implies that H_2 is monotonic along each $R_m(\psi)$ and is another possible choice for the parameter λ . We now write $\mathbf{H}_2(\mathbf{x})$ as $H_2(\mathbf{x}) \hat{\mathbf{e}}_\psi$, where $\hat{\mathbf{e}}_\psi = \cos(\psi) \hat{\mathbf{e}}_x + \sin(\psi) \hat{\mathbf{e}}_y$. We denote by $R'_m(\psi)$ the range of values of λ parametrising the set of points $R_m(\psi)$. Then the functional \mathcal{S} can be written as:

$$\mathcal{S} = \sum_{n=1}^N \left\| \int d\psi \hat{\mathbf{e}}_\psi \int_{R'_m(\psi)} d\lambda \phi_n(\mathbf{x}(\psi, \lambda)) H_2(\mathbf{x}(\psi, \lambda)) g(\psi, \lambda) \right\|, \quad (6.10)$$

where $g(\psi, \lambda)$ is the absolute value of the determinant of the Jacobian of this transformation. Let us now define $h(\psi)$ as the total contribution to \mathcal{S} from the set of points $R_m(\psi)$:

$$h(\psi) = \int_{R'_m(\psi)} d\lambda H_2(\psi, \lambda) g(\psi, \lambda) \quad (6.11)$$

We also define $h_n(\psi)$ as the amount of $h(\psi)$ that is assigned to the n^{th} segment:

$$h_n(\psi) = \int_{R'_m(\psi)} d\lambda \phi_n(\psi, \lambda) H_2(\psi, \lambda) g(\psi, \lambda) \quad (6.12)$$

Using the definition of the functions ϕ_n it can immediately be seen that $h_n(\psi) \geq 0$ for all n , and that the following relation holds for all ψ :

$$\sum_{n=1}^N h_n(\psi) = h(\psi) \quad (6.13)$$

The functional \mathcal{S} to be optimised can then be written as:

$$\mathcal{S}[\{\phi_n\}] = \sum_{n=1}^N \left\| \int d\psi h_n(\psi) \hat{e}_\psi \right\| \quad (6.14)$$

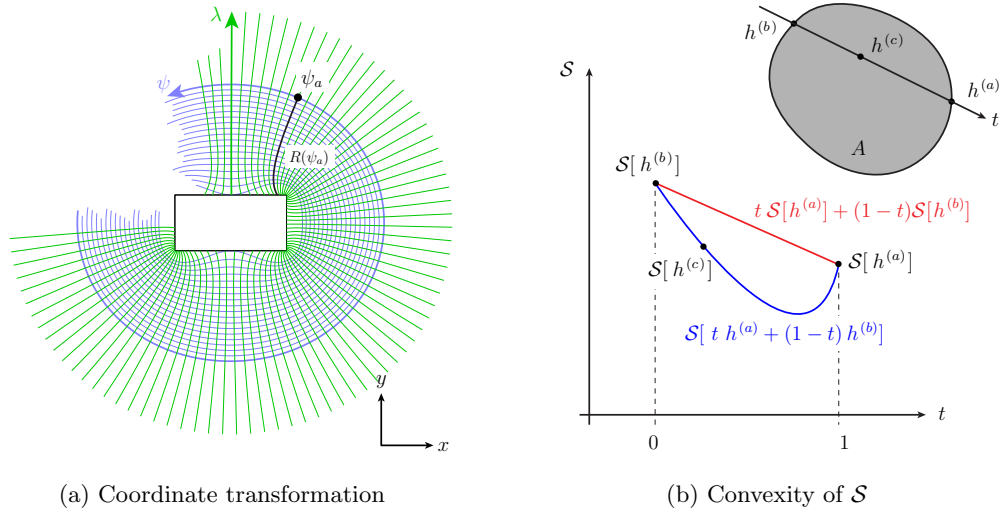


Fig. 6.8: **6.8a**: the coordinate transformation $\mathbf{x} \rightarrow (\psi, \lambda)$ is illustrated on an example geometry. **6.8b**: A convex set A and the value of the convex function \mathcal{S} over a line segment traced between two points, $h_n^{(a)}(\psi)$ and $h_n^{(b)}(\psi)$, belonging to the boundary of A . This illustrates that the either $\mathcal{S}[h^{(a)}]$ or $\mathcal{S}[h^{(b)}]$ is greater or equal to the value of \mathcal{S} for any other point on the line segment.

The only dependence of \mathcal{S} on ϕ_n is through the functions $h_n(\psi)$. Finding an optimal segmentation is then equivalent to finding a set of optimal functions $h_n(\psi)$. This makes the search space \mathcal{X} equal to the space of all the N -dimensional vector functions defined over the interval of the real axis spanned by the values of ψ , subject to the conditions of non-negativity and the sum rule expressed in 6.13. The sum between two elements $h^{(a)}$ and $h^{(b)}$ of \mathcal{X} is defined in the usual way:

$$\text{if } h^{(c)} = h^{(a)} + h^{(b)}, \text{ then } h_n^{(c)}(\psi) = h_n^{(a)}(\psi) + h_n^{(b)}(\psi), \quad \forall \psi, n \quad (6.15)$$

Similarly, multiplication of $h^{(a)}$ by the scalar c is defined through:

$$\text{if } h^{(c)} = c h^{(a)} \text{ then } h_n^{(c)}(\psi) = c h_n^{(a)}(\psi), \quad \forall \psi, n \quad (6.16)$$

These operations satisfy all the necessary properties that make \mathcal{X} a vector space.

We can show that the functional \mathcal{S} is convex with respect to $h_n(\psi)$. By definition, this means that if we consider two arbitrary vectors $h_n^{(a)}(\psi)$ and $h_n^{(b)}(\psi)$ and a scalar parameter $t \in [0, 1]$, the following property is always obeyed:

$$\mathcal{S}[t h^{(a)} + (1-t)h^{(b)}] \leq (t)\mathcal{S}[h^{(a)}] + (1-t)\mathcal{S}[h^{(b)}] \leq \max(\mathcal{S}[h^{(a)}], \mathcal{S}[h^{(b)}]) \quad (6.17)$$

This can be shown by considering each member of the summation over n appearing in Eq. (6.14) and applying the absolute homogeneity property of the norm and the triangle inequality.

We now restrict the search to a set $A \subset \mathcal{X}$ defined by the conditions of non-negativity and the sum rule of Eq. (6.13):

$$A = \left\{ h_n(\psi) : \underbrace{\sum_{n=1}^N h_n(\psi) = h(\psi)}_{\text{Equality}}, \underbrace{h_n(\psi) \geq 0}_{\text{Inequality}}, \quad \forall \psi \right\} \quad (6.18)$$

We observe that the set A is convex, since for any two points $h_n^{(a)}(\psi)$ and $h_n^{(b)}(\psi)$ belonging to the set and a value of $t \in [0, 1]$, all the points on the line segment $t h^{(a)} + (1-t)h^{(b)}$ also belong to the set.

Let us then consider a particular solution $h_n^{(c)}$ for which there is at least one value of ψ , denoted ψ' , for which $R_m(\psi')$ is subdivided between more than one segment. This means that there exists an n' for which $h_{n'}^{(c)}(\psi')$ is strictly between 0 and $h(\psi')$. We now define two additional points $h^{(a)}$ and $h^{(b)}$ which for $\psi \neq \psi'$ are equal to $h_n^{(c)}$. For $\psi = \psi'$ we set

$$h_{n'}^{(a)}(\psi') = 0; \quad h_{n \neq n'}^{(a)}(\psi') = h(\psi') \frac{h_n^{(c)}(\psi')}{\sum_{j \neq n'} h_j^{(c)}(\psi')} \quad (6.19)$$

and

$$h_{n'}^{(b)}(\psi') = h(\psi'); \quad h_{n \neq n'}^{(b)}(\psi') = 0. \quad (6.20)$$

Evidently the point $h^{(a)}$ corresponds to a segmentation identical to $h^{(c)}$ except that $R_m(\psi')$ is assigned entirely to the segment n' . Similarly, $h^{(b)}$ has nothing of $R_m(\psi')$ assigned to n' . The line segment $t h^{(a)} + (1-t)h^{(b)}$, for $t \in [0, 1]$, is entirely inside the set A , but for $t < 0$ or $t > 1$ we would be outside of A . The points $h^{(a)}$ and $h^{(b)}$ are thus on the boundary of A , and the original point $h^{(c)}$ is an interior point of the segment, corresponding to $t = h_{n'}^{(c)}(\psi')/h(\psi')$. Because of the convexity of \mathcal{S} , Eq. (6.17) is obeyed for all the points on the line segment. Moreover, $t\mathcal{S}[h^{(a)}] + (1-t)\mathcal{S}[h^{(b)}]$, which is the right-hand side of Eq. (6.17), is always smaller than or equal to its value at one of the end points, $h^{(a)}$ or $h^{(b)}$. This argument is illustrated in figure 6.8b and shows that either $h^{(a)}$ or $h^{(b)}$ gives a value of \mathcal{S} that is greater or equal to $\mathcal{S}[h^{(c)}]$. Therefore, for any solution in which the set $R_m(\psi')$ is partially assigned to the segment n' , there is a solution giving a greater or equal value of \mathcal{S} , for which $R_m(\psi')$ is either entirely assigned to the segment n' , or not at all.

Thus, it was shown that assigning each set $R_m(\psi)$ entirely to a single segment gives a value of \mathcal{S} which is equal to the maximum possible value achievable with N segments.

We are now left with the problem of determining how to assign each $R_m(\psi)$ to one of the N segments. However, until this point we never enforced that the segments should be connected regions. This requirement implies that each segment corresponds to a single interval $[\psi_{n-1}, \psi_n]$:

$$h_n(\psi) = h(\psi), \quad \forall \psi \in [\psi_{n-1}, \psi_n] \quad (6.21)$$

The border between the segments n and $n+1$ is thus given by the contour line $R_m(\psi_n)$, and the problem is reduced to the determination of the optimal splitting angles ψ_n . The approach described in section 6.3.5 will provide the answer to this problem.

6.3.2 Segment-segment border - three dimensional case

We will now consider how the results derived in the previous section generalize to three-dimensional systems. The change of variables for this case includes two orientation angles determining the direction of the virtual field \mathbf{H}_2 in the point \mathbf{x} . The azimuthal angle, denoted by ψ , and the inclination angle ϑ . The remaining degree of freedom is parametrized by the generic coordinate λ , which, as explained in the previous section, may be chosen in different ways. The virtual field \mathbf{H}_2 is then expressed as:

$$\mathbf{H}_2(\mathbf{x}) = H_2(\psi, \vartheta, \lambda) \left(\sin(\vartheta) \cos(\psi) \hat{\mathbf{e}}_x + \sin(\vartheta) \sin(\psi) \hat{\mathbf{e}}_y + \cos(\vartheta) \hat{\mathbf{e}}_z \right) = H_2(\psi, \vartheta, \lambda) \hat{\mathbf{e}}_{\psi \vartheta} \quad (6.22)$$

Where $\hat{\mathbf{e}}_{\psi \vartheta}$ denotes the unit vector whose direction is determined by ψ and ϑ . The set $R_m(\psi_a, \vartheta_a)$ is a curve segment of constant direction of the virtual field defined as:

$$R_m(\psi_a, \vartheta_a) = \{\mathbf{x} : \psi(\mathbf{x}) = \psi_a, \vartheta(\mathbf{x}) = \vartheta_a\} \cup R_m \quad (6.23)$$

The symbol $R'_m(\psi_a, \vartheta_a)$ will denote the range of values spanned by the coordinate λ parameterizing $R_m(\psi_a, \vartheta_a)$. The objective functional \mathcal{S} for the case of N segments can then be written as:

$$\mathcal{S} = \sum_{n=1}^N \left\| \int d\psi \int d\vartheta \hat{\mathbf{e}}_{\psi \vartheta} \int_{R'_m(\psi, \vartheta)} d\lambda \phi_n(\mathbf{x}(\psi, \vartheta, \lambda)) H_2(\mathbf{x}(\psi, \vartheta, \lambda)) g(\psi, \vartheta, \lambda) \right\|, \quad (6.24)$$

Where $g(\psi, \vartheta, \lambda)$ is the absolute value of the determinant of the Jacobian of the coordinate transformation, and $\phi_n(\mathbf{x}(\psi, \vartheta, \lambda))$ is the characteristic function of the set occupied by the n^{th} segment. Let us now define $h(\psi, \vartheta)$ as the total contribution to \mathcal{S} from the set $R_m(\psi, \vartheta)$:

$$h(\psi, \vartheta) = \int_{R'_m(\psi, \vartheta)} d\lambda H_2(\psi, \vartheta, \lambda) g(\psi, \vartheta, \lambda) \quad (6.25)$$

We also define $h_n(\psi, \vartheta)$ as the amount of $h(\psi, \vartheta)$ that is assigned to the n^{th} segment:

$$h_n(\psi, \vartheta) = \int_{R'_m(\psi, \vartheta)} d\lambda \phi_n(\psi, \vartheta, \lambda) H_2(\psi, \vartheta, \lambda) g(\psi, \vartheta, \lambda) \quad (6.26)$$

The functions h_n belong to the set A defined by:

$$A = \left\{ h_n(\psi, \vartheta) : \underbrace{\sum_{n=1}^N h_n(\psi, \vartheta)}_{\text{Equality}} = h(\psi, \vartheta), \quad \underbrace{h_n(\psi, \vartheta) \geq 0}_{\text{Inequality}}, \quad \forall \psi, \vartheta \right\} \quad (6.27)$$

As for the two-dimensional case, the only dependence of \mathcal{S} on ϕ_n is through the functions $h_n(\psi, \vartheta)$:

$$\mathcal{S}\{\{\phi_n\}\} = \sum_{n=1}^N \left\| \int d\psi d\vartheta h_n(\psi, \vartheta) \hat{e}_{\psi\vartheta} \right\| \quad (6.28)$$

Since the functional \mathcal{S} can be proven to be convex with respect to the functions $h_n(\psi, \vartheta)$, and the set A can be proven to be a convex set, the same argument employed in the previous section applies to the three-dimensional case. The elements of the boundary of A correspond to a value of \mathcal{S} that is at least equal to the value of any element in the interior of A . This implies that the segmentations for which each set $R_m(\psi, \vartheta)$ is entirely assigned to one of the segments correspond to a value of \mathcal{S} that is greater than or equal to the value of any other segmentation.

6.3.3 General coordinate transformation

We now consider a general framework to address the problem of segmenting a given permanent magnet region R_m by restricting the possible resulting configuration to a certain family of segmentations. This is an effective way to formalize the problem when there are reasons to prefer some segmentations over others. One reason could be to restrict to the family of segmentations that were shown to be optimal in sections 6.3.1 and 6.3.2. Other reasons may come from manufacturing considerations, since the shapes of the permanent magnet segments affect the realization cost of a magnetic assembly.

We start by introducing a coordinate transformation $\boldsymbol{\xi}(\mathbf{x})$ which we assume to be invertible and well-behaved inside R_m . The absolute value of the determinant of the Jacobian matrix of this transformation will be denoted by $g(\boldsymbol{\xi})$. Any set A of points \mathbf{x} is mapped into a corresponding set of points $\boldsymbol{\xi}$ which is denoted by A' . Introducing the vector field $\mathbf{H}'(\boldsymbol{\xi}) = \mathbf{H}_2(\mathbf{x}(\boldsymbol{\xi}))g(\boldsymbol{\xi})$ we have:

$$\int_A d^3x \mathbf{H}_2(\mathbf{x}) = \int_{A'} d^3\xi \mathbf{H}'(\boldsymbol{\xi}) \quad (6.29)$$

The optimisation of the geometry can be performed in the $\boldsymbol{\xi}$ space since the coordinate transformation was assumed to be bijective in R_m . The segmentation problem with respect to the three new parameters ξ_1 , ξ_2 and ξ_3 , is then to subdivide R'_m into a given number N of regions R'_k such that the following functional is maximized:

$$\mathcal{S}[\mathbf{H}] = \sum_k^N \left\| \int_{R'_k} d^3\xi \mathbf{H}'(\boldsymbol{\xi}) \right\| \quad (6.30)$$

As anticipated above, performing the coordinate transformation is useful when there is some reason to consider only a restricted family of segmentations which is naturally expressed in the new coordinate system $\boldsymbol{\xi}$. Let us suppose that we would like to prevent splittings along, e.g., the third coordinate ξ_3 . We can then calculate the following vector field \mathbf{h} :

$$\mathbf{h}(\xi_{1a}, \xi_{2a}) = \int_{R'_m(\xi_{1a}, \xi_{2a})} d\xi_3 \mathbf{H}'(\boldsymbol{\xi}) \quad (6.31)$$

where $R'_m(\xi_{1a}, \xi_{2a})$ denotes the intersection between R'_m and the set $R'(\xi_{1a}, \xi_{2a}) = \{\boldsymbol{\xi} : \xi_1 = \xi_{1a}, \xi_2 = \xi_{2a}\}$. We will denote by $R_m^{(1,2)}$ the set of all the points (ξ_1, ξ_2) for which $R'_m(\xi_1, \xi_2)$

is not empty. The problem with the two parameters ξ_1 and ξ_2 , is thus to find the subdivision of $R'_m{}^{(1,2)}$ in N regions R'_k such that the following functional is maximized:

$$\mathcal{S}[\mathbf{H}] = \sum_k^N \left\| \int_{R'_k} d\xi_1 d\xi_2 \mathbf{h}(\xi_1, \xi_2) \right\| \quad (6.32)$$

It can be noticed the similarity between the previous expression and equation 6.28.

Analogously, we could desire to avoid subdivisions along both the directions ξ_3 and ξ_2 , i.e. restricting to subdivisions along ξ_1 . Generalizing the same notation introduced for the two-parameters case we define the integral:

$$\mathbf{h}(\xi_{1a}) = \int_{R'_m(\xi_{1a})} d\xi_2 d\xi_3 \mathbf{H}'(\boldsymbol{\xi}) \quad (6.33)$$

Where the set $R'_m(\xi_{1a})$ is defined as the intersection $R'_m \cap (R'(\xi_{1a}) = \{\boldsymbol{\xi} : \xi_1 = \xi_{2a}\})$. It is also introduced $R'_m{}^{(1)}$ as the set of points ξ_1 for which the intersection $R'_m(\xi_1)$ is not empty. The problem with one parameter is then to subdivide the set $R'_m{}^{(1)}$ into N regions R'_k such that the following functional is maximized:

$$\mathcal{S}[\mathbf{H}] = \sum_k^N \left\| \int_{R'_k} d\xi_1 \mathbf{h}(\xi_1) \right\| \quad (6.34)$$

Again, it can be noticed the similarity between the previous expression and equation 6.14.

In section 6.3.4 it will be considered the two-parameters segmentation problem, by using as parameters the angles ψ , and ϑ , which determine the direction of the virtual field \mathbf{H}_2 . A numerical approach will be employed to address this problem, and the technique will be illustrated through different examples. In section 6.3.5 we will consider the one-parameter problem, and it will be shown how to determine the globally optimal solution to this problem. The solution can be determined with the desired degree of accuracy, as long as the parameter satisfies some properties which will be clearly stated.

6.3.4 Two-parameters segmentation

The scope of this section is to present a numerical heuristic approach which can be used to address the two-parameters segmentation problem.

The method is introduced with the illustrative example of the finite-length Halbach cylinder. The geometry is shown in figure 6.9. The purpose of the magnetic system is to maximize the x component of the field \mathbf{H}_1 , averaged over the central cylindrical cavity, of radius R_I , delimited by the two dashed lines located at $z = \pm z_0$. Since for many practical application is desirable that the cavity remains accessible, the design area does not occupy the regions above and below the air gap. The permanent magnet is delimited by the external curved surface, determined from the norm of the virtual field \mathbf{H}_2 as explained in section 6.1. For this example, the segmentation procedure will be applied to the first octant of the geometry and copied symmetrically to the remaining octants of the geometry.

Because of the results presented in section 6.3.2, we choose as parameters the two angles ψ , and ϑ . Other choices would be possible, but the optimality results derived in section 6.3.2

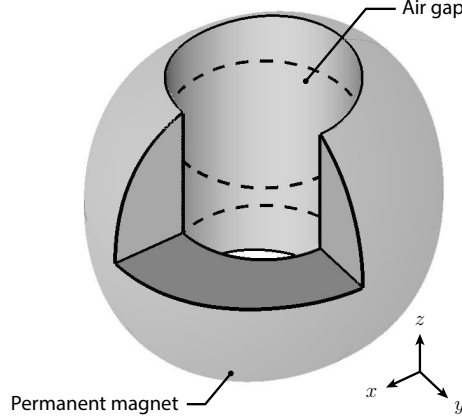


Fig. 6.9: Finite length Halbach cylinder. The purpose of this magnetic system is to maximize the x component of the field averaged over the central cylindrical cavity delimited by the two dashed lines. To allow access to the cavity, the magnet does not occupy the regions above and below the dashed lines. The external boundary of the permanent magnet is a level surface of the norm of the virtual field.

would not apply. Equation 6.32 is written in terms of ψ , and ϑ as:

$$\mathcal{S}[\mathbf{H}] = \sum_k^N \left\| \int_{R'_k} d\psi d\vartheta \mathbf{h}(\psi, \vartheta) \right\| \quad (6.35)$$

The symbol \mathbf{h} represents the three-dimensional vector parametrized by ψ , and ϑ , defined as:

$$\mathbf{h}(\psi, \vartheta) = \int_{R'_m(\psi, \vartheta)} d\lambda \mathbf{H}_2(\psi, \vartheta, \lambda) g(\psi, \vartheta, \lambda) \quad (6.36)$$

Where λ denotes the coordinate parametrising the remaining degree of freedom, and g denotes the absolute value of the Jacobian of the coordinate transformation. The symbol $R'_m(\psi_a, \vartheta_a)$ denotes the intersection between R'_m and the set $R'(\psi_a, \vartheta_a) = \{(\psi, \vartheta) : \psi = \psi_a, \vartheta = \vartheta_a\}$. In order to develop the procedure we just have to assume that each set $R'(\psi_a, \vartheta_a)$ is a single curve segment. This will ensure the invertibility properties assumed by this approach. The continuity properties are automatically satisfied because of the continuity of the virtual field \mathbf{H}_2 over R_m . These issues will be investigated in more details in section 6.3.6.

Figure 6.10 illustrates the coordinate transformation by showing with the use of the color gradient how the points of the $\psi - \vartheta$ plane, shown in figure 6.10a, are mapped into points on the external surface of the magnet, shown in figure 6.10b. The black lines indicates level curves of ψ or level curves of ϑ . The black dashed line shown in figure 6.10b delimits the region above the air gap, which does not belong to the design area R_m . The corresponding region of the $\psi - \vartheta$ plane is delimited by the dashed line shown in figure 6.10a, and does not belong to R'_m . The figures indicate that the invertibility property mentioned above is satisfied for any internal point. The only point of the $\psi - \vartheta$ which does not map into a single curve segment

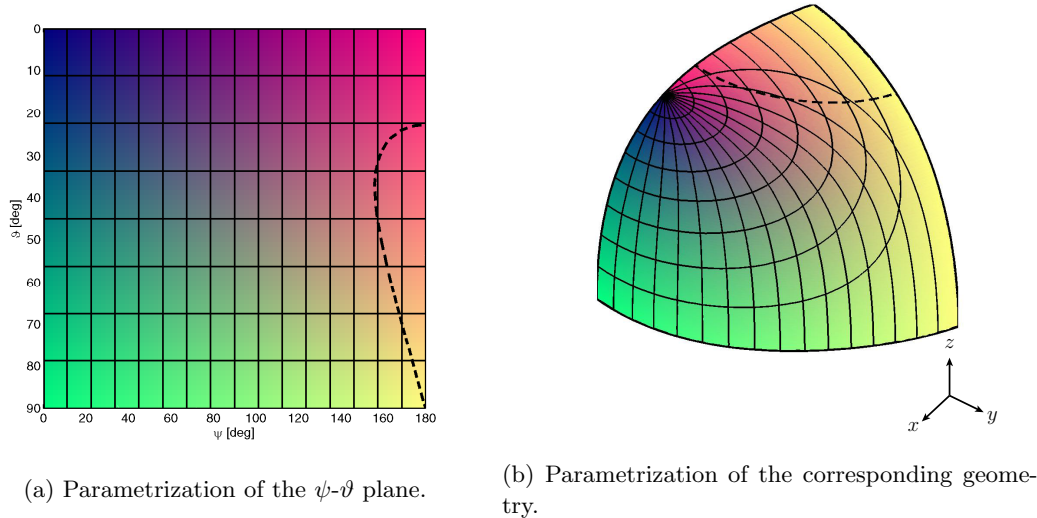


Fig. 6.10: The coordinate transformation is illustrated by showing the correspondence between points of the ψ - ϑ plane, shown in 6.10a, and points on the external boundary of the magnet, shown in 6.10b. Corresponding points are shaded with the same color. The solid lines indicate level curves of ψ or ϑ . The dashed line indicate in both panels the region outside the design area.

of the geometry is the point $\psi = 180^\circ$, $\vartheta = 90^\circ$. This orientation corresponds to the whole region characterized by $x = 0$. Since this issue is only limited to the region on the border of the considered design area, it does not prevent us from applying the optimisation procedure.

We will now examine the the numerical implementation of the two-parameters segmentation procedure, which is performed over a discrete grid on the ψ - ϑ plane, spaced by $\Delta\psi$ and $\Delta\vartheta$. The first step is the computation of the virtual field \mathbf{H}_2 corresponding to the linear optimisation problem. In general, this may require performing one FEM simulation of the virtual system. It is then necessary to calculate the quantity $\mathbf{h}(\psi, \vartheta)\Delta\psi\Delta\vartheta$. Numerically, this is done with the following expression:

$$\mathbf{h}(\psi, \vartheta)\Delta\psi\Delta\vartheta = \int_{\Delta R_m(\psi, \vartheta)} d^3x \mathbf{H}_2(\mathbf{x}) \quad (6.37)$$

Where the integration domain $\Delta R_m(\psi, \vartheta)$ is defined as:

$$\Delta R_m(\psi_a, \vartheta_a) = \{\mathbf{x} : \psi(\mathbf{x}) \in [\psi_a, \psi_a + \Delta\psi]; \vartheta(\mathbf{x}) \in [\vartheta_a, \vartheta_a + \Delta\vartheta]\} \cap R_m \quad (6.38)$$

The quantity $\mathbf{h}(\psi, \vartheta)\Delta\psi\Delta\vartheta$ will be denoted with the shorter expression $\Delta\mathbf{h}$. In the numerical implementation each subset R_k^l of the ψ - ϑ plane is identified by the set of grid elements belonging to the k^{th} segment.

Once $\Delta\mathbf{h}$ has been calculated on the whole grid, it is possible to evaluate \mathcal{S} for different possible segmentations. Since evaluating \mathcal{S} does not require to recompute either \mathbf{H}_2 or $\Delta\mathbf{h}$, each evaluation requires an extremely short computational time. It is therefore possible to employ even optimisation techniques requiring a large number of function evaluations, which would have otherwise been unfeasible.

We consider an iterative algorithm consisting into slightly modifying of the current configuration at each step of the iteration. The algorithm is greedy since the new configuration is accepted only if the value of \mathcal{S} increases with respect to the previous configuration. The algorithm is heuristic since each time a new configuration has to be generated from the previous one, one grid element element is selected at random among those on the boundary between two segments, i.e. adjacent to a grid element belonging to a different segment. This randomly selected grid element is then flipped into one of the adjacent segments.

We compare two different versions of the same approach. In both cases the starting configuration is generated by randomly assigning to one of the segment each grid element. In the first version of the algorithm, many randomly selected grid elements are simultaneously flipped during each step of the iteration, and the new configuration is accepted if and only if it is overall superior to the configuration at the beginning of the iteration step. The number of grid elements to be flipped at each step decreases as the iteration converges. The second version of the algorithm only allows one grid element to be flipped at each step of the iteration. The other difference is that the second algorithm starts with a coarse grid defined over the $\psi - \vartheta$ plane and cycles over the whole iteration several times. At each new cycle the grid is refined and the initial configuration is calculated from the last configuration of the previous cycle using nearest-neighbour interpolation.

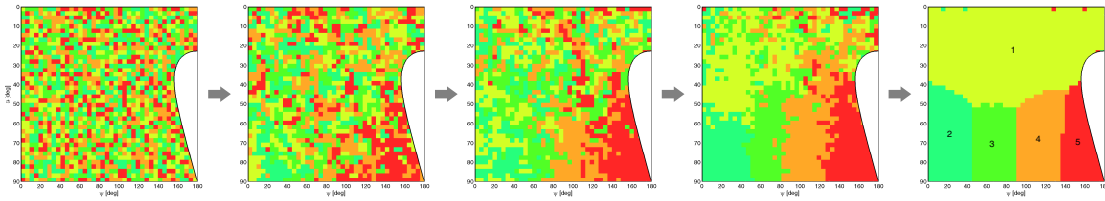


Fig. 6.11: Initial, final and three intermediate steps of the first version of the two-parameters optimisation algorithm. The different colours indicate the regions R'_k of the $\psi - \vartheta$ plane assigned to different segments.

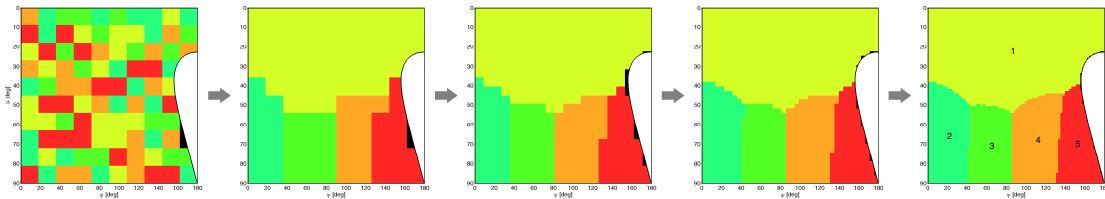


Fig. 6.12: Initial, final and three intermediate steps of the second version of the two-parameters optimisation algorithm. The different colours indicate the regions R'_k of the $\psi - \vartheta$ plane assigned to different segments.

We illustrate the results of the algorithms for the problem of segmenting the first octant of the geometry using 5 segments, i.e. $N_{\text{Segments}} = 5$. The results and some intermediate steps of the iterations are shown in figures 6.11 and 6.11 for the first and the second versions of the algorithm, respectively. The different colours represent regions assigned to the different

segments. In both cases the leftmost panel shows the initial configuration and the rightmost panel shows the final configuration. For the first algorithm shown in 6.11 the three middle panels represent intermediate steps of the iteration. For the second algorithm shown in 6.12 the three middle panels show the final configuration of each refinement cycle.

As can be seen from the figures, in both cases the different regions R'_k , initially randomly spread across the grid, agglomerate into simply connected sets. It is important to stress that this effect is a feature of the underlying optimisation problem. The only criteria to accept or reject a new configuration is whether the value of \mathcal{S} increases or not: the configurations with simply connected regions are not a priori preferred to other configurations. This is another evidence of the fact that it is not optimal to subdivide a region where the direction of \mathbf{H}_2 is almost uniform. It is also interesting to notice that both the algorithms converge to virtually the same result. Despite the fact that the initial configuration is randomly generated, and that the algorithms themselves are heuristic, the procedures almost invariably converge to the same final configuration. This can be interpreted as an indication that the procedure is able to determine the globally optimal solution.

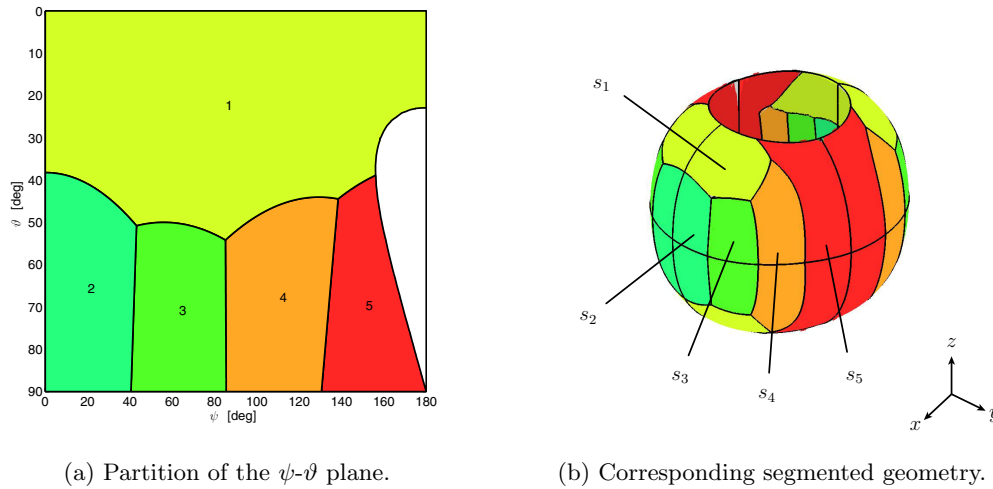


Fig. 6.13: Segmentation of one octant of the cylinder using $N_{\text{Segments}} = 5$. 6.13a: the partition of the ϑ - ψ plane and the curves fitted to the borders between adjacent regions. 6.13b: the optimally segmented octant of the geometry is mirrored to reconstruct the whole magnetic assembly.

The final optimised configuration is shown in figure 6.13. Figure 6.13a shows the partition of the ψ - ϑ plane. The black lines have been fitted to the border between different regions R'_k . The corresponding segmented geometry is shown in figure 6.13b. Even though the shape of the resulting segments may not be directly feasible for manufacturing, it would be possible to approximate the optimal segmentation using simplified shapes. Section 6.4.7 discusses an example of such a simplification, which might be advantageous for manufacturing purposes. Figure 6.14 shows the results of the algorithm for the same example geometry and different values of N_{Segments} . It can be noticed that the region adjacent to the border $x = 0$ is always occupied by a single segment, since ψ and ϑ are both constant over this boundary.

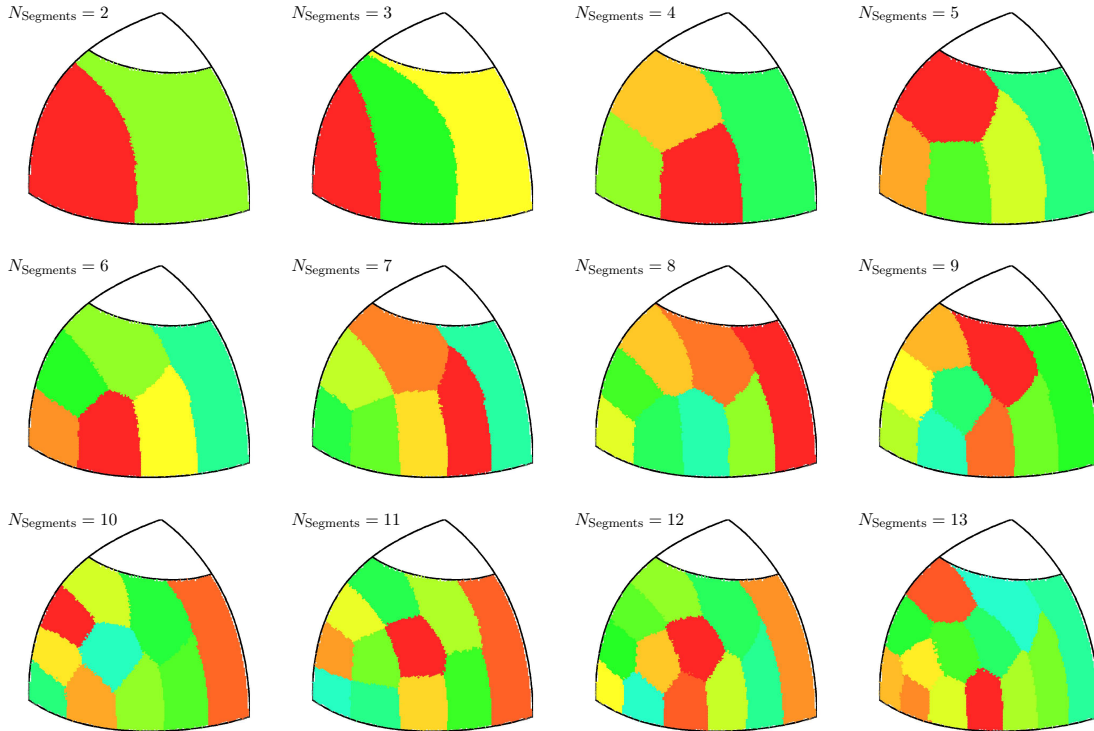
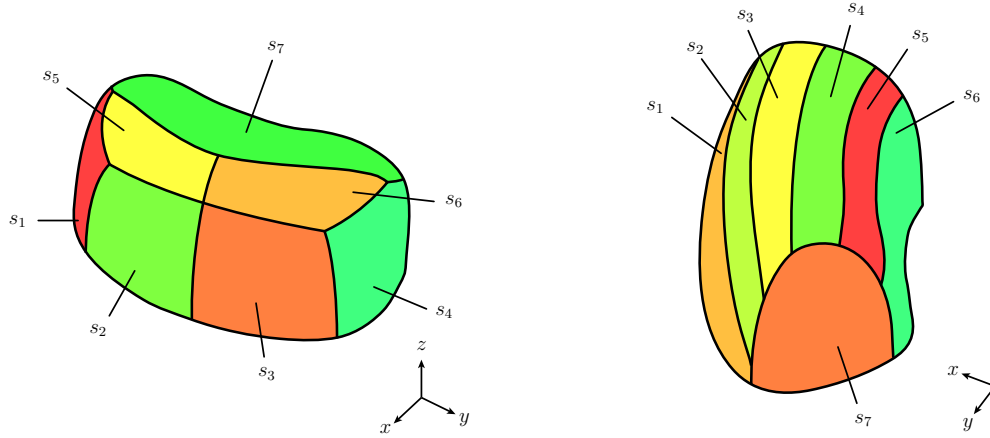


Fig. 6.14: Segmentation of one octant of the finite-length Halbach cylinder for different number values of the number of segments N_{Segments} .

As last examples of the two-parameter segmentation algorithm we consider the rotary magnetic systems for magnetic refrigeration described in section 6.2.3, shown in figure 6.15. In both cases, we consider the segmentation of the first quadrant of the $x - z$ plane of the geometry.

6.3.5 One-parameter segmentation

In this section we will show the one-parameter segmentation problem. Clearly the numerical approach employed for the two-parameters segmentation could also be used for the one-parameter case. However, since the one-parameter problem is considerably less challenging, it is possible to apply a mathematical approach which guarantees the global optimality of the solution within the desired degree of accuracy. For simplicity we will consider the procedure for two-dimensional systems, since the generalization to three-dimensional systems is straightforward. Because of the optimality results derived in section 6.3.1, we chose as parameter the azimuth angle ψ of the virtual field. Other choices may be considered, but the optimality results derived in section 6.3.1 would not apply. This maybe be advantageous for the purpose of reducing the manufacturing cost by limiting the shapes of the resulting segments to a family of predefined shapes which are feasible for the production. For now it will be assumed that the intersection between the magnet design area R_m with the set of points $R(\psi)$ corresponding to a specific



(a) Segmentation of the system shown in 6.7a. (b) Segmentation of the system shown in 6.7b.

Fig. 6.15: Segmentation of the first quadrant of the $x - z$ plane of the magnet area of the systems described in section 6.2.3. The segmentation corresponds for both geometries to the case $N_{\text{Segments}} = 7$. The geometry of figure 6.15b results in a larger number of subdivisions along the dimension spanned by the inclination angle ϑ .

value of ψ identifies a single curve segment, denoted by $R_m(\psi)$. This assumption, together with the fact that the virtual field \mathbf{H}_2 is continuous over R_m , guarantee the invertibility and continuity properties that are necessary to develop the segmentation procedure. The invertibility issues will be addressed in more details in section 6.3.6.

We now define the region $\mathcal{R}_{[\psi_0, \psi_1]}$ as the set of points \mathbf{x} in the magnet design area in which the orientation angle ψ of the virtual field \mathbf{H}_2 is in the interval $[\psi_0, \psi_1]$

$$\mathcal{R}_{[\psi_0, \psi_1]} = \{\mathbf{x} : \psi(\mathbf{H}_2(\mathbf{x})) \in [\psi_0, \psi_1]\} \cap R_m \quad (6.39)$$

The regions so defined satisfy: $\mathcal{R}_{[\psi_0, \psi_2]} = \mathcal{R}_{[\psi_0, \psi_1]} \cup \mathcal{R}_{[\psi_1, \psi_2]}$, for all $\psi_1 \in [\psi_0, \psi_2]$.

The integrated magnetic field vector associated with this region is

$$\mathcal{H}_{[\psi_0, \psi_1]} = \int_{\mathcal{R}_{[\psi_0, \psi_1]}} d^2x \mathbf{H}_2(\mathbf{x}) = \int_{\psi_0}^{\psi_1} d\psi h(\psi) \hat{\mathbf{e}}_\psi \quad (6.40)$$

with $h(\psi)$ defined in Eq. (6.11). The symbol \mathcal{H} denotes the integral of a field over a region of space. These vectors satisfy the property: $\mathcal{H}_{[\psi_0, \psi_2]} = \mathcal{H}_{[\psi_0, \psi_1]} + \mathcal{H}_{[\psi_1, \psi_2]}$, for all $\psi_1 \in [\psi_0, \psi_2]$.

Once a starting point ψ_0 has been fixed, it is possible to parametrize the vectors associated with the different regions, just using the value ψ of the ending point; the following notation will be used: $\mathcal{H}(\psi) = \mathcal{H}_{[\psi_0, \psi]}$. The velocity vector associated with this parametrized curve is denoted by $\mathbf{h}(\psi) = \frac{d}{d\psi} \mathcal{H}(\psi) = h(\psi) \hat{\mathbf{e}}_\psi$. In the general case \mathbf{h} is defined by equation 6.33.

An example geometry and the corresponding curve $\mathcal{H}(\psi)$ are shown in figure 6.16a and 6.16b, respectively.

In the continuous case the contribution to \mathcal{S} from the interval $[\psi_0, \psi_1]$ is equal to the length

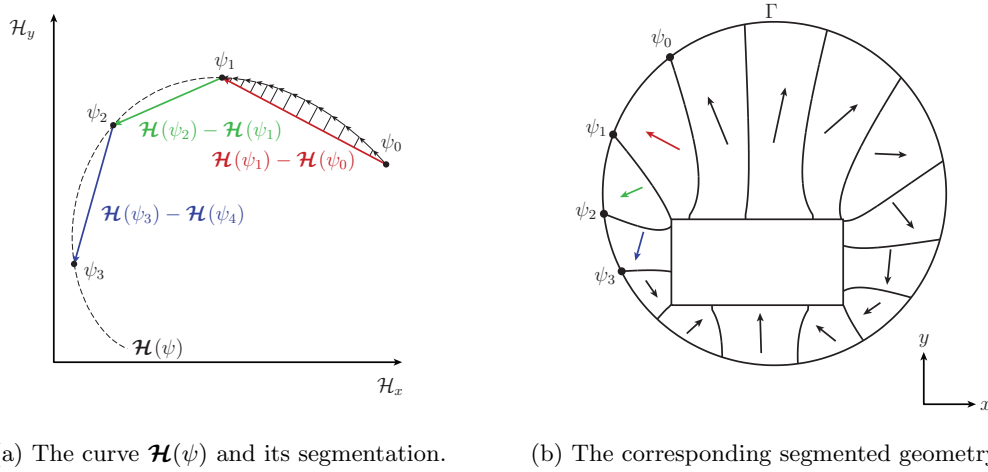


Fig. 6.16: In the continuous case the optimal remanence is normalized and aligned at any point with the virtual field. This implies that the value of \mathcal{S} is given by the length of the curve $\mathcal{H}(\psi)$. In the segmented case the contribution from a point belonging to a certain segment is proportional to the scalar product between the virtual field and the optimal remanence for that segment. This implies that the direction of the vector $\mathcal{H}(\psi_1) - \mathcal{H}(\psi_0)$ is also the optimal direction of the remanence, and its length is equal to the contribution from that segment to the total value of \mathcal{S}

of the corresponding arc of curve:

$$\mathcal{S}_{\text{Continuous}} = \int_{\mathcal{R}_{[\psi_0, \psi_1]}} d^2x \|\mathbf{H}_2(\mathbf{x})\| = \int_{\psi_0}^{\psi_1} d\psi \|\mathbf{h}(\psi)\| = \int_{\psi_0}^{\psi_1} d\psi h(\psi) \quad (6.41)$$

In the segmented case the contribution to \mathcal{S} is the length of the segment between the curve end points

$$\mathcal{S}_{\text{Segmented}} = \left\| \int_{\mathcal{R}_{[\psi_0, \psi_1]}} d^2x \mathbf{H}_2(\mathbf{x}) \right\| = \left\| \int_{\psi_0}^{\psi_1} d\psi \mathbf{h}(\psi) \right\| = \|\mathcal{H}(\psi_1) - \mathcal{H}(\psi_0)\| \quad (6.42)$$

When considering more than one segment the value of $\mathcal{S}_{\text{Segmented}}$ is given by the length of the polygonal line inscribed in $\mathcal{H}(\psi)$.

The problem of optimal segmentation is reduced to the problem of piecewise linear approximation of plane curves by perimeter optimisation.

The globally optimal solution for this problem can always be found by employing dynamic programming approach. This class of algorithms makes use of the optimal substructure exhibited by the problem, in order to reduce its computational complexity. An algorithm for the curve approximation problem can be found in [46]. It is interesting to examine the approach with the example curve $\mathcal{H}(\psi)$ given by the following expression:

$$\mathcal{H}(\psi) = \left((1/2) + (1/4) \cos(2\psi) \right) \left(\cos(4\psi) \hat{\mathbf{e}}_x + \sin(4\psi) \hat{\mathbf{e}}_y \right) + (4/5) \psi \hat{\mathbf{e}}_y \quad (6.43)$$

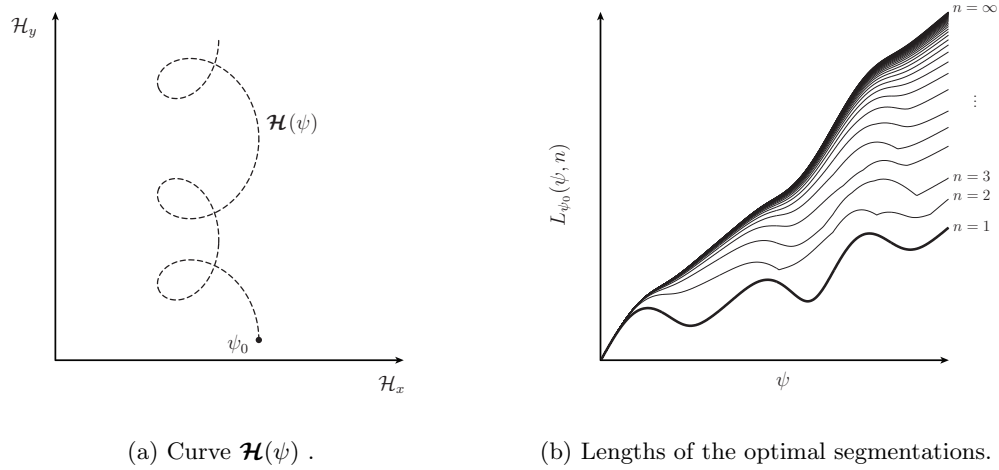


Fig. 6.17: 6.17a: graphs of the example curve $\mathcal{H}(\psi)$ defined in equation 6.43. 6.17b: lengths of the optimal segmentations using n segments, of the part of the curve going from the starting point ψ_0 to the point ψ . These functions, except for the cases $n = 1$ and $n \rightarrow \infty$, may exhibit discontinuities even when the original curve $\mathcal{H}(\psi)$ is continuous.

With ψ spanning the interval $[0, (3/2)\pi]$. The example curve is shown in figure 6.17a.

The distance between two points of the curve is by definition:

$$d(\psi_1, \psi_2) = \|\mathcal{H}(\psi_2) - \mathcal{H}(\psi_1)\| \quad (6.44)$$

The length ℓ of the segmentation with points ψ_0, \dots, ψ_N is given by:

$$\ell(\psi_0, \dots, \psi_N) = \sum_{n=0}^{N-1} d(\psi_n, \psi_{n+1}) \quad (6.45)$$

The function $L_{\psi_0}(\psi, N)$ is defined as the length of the optimal segmentation between ψ_0 and ψ that uses N segments. The symbols $\psi_{\psi_0}^{(n)}(\psi, N)$, with $n = 1, \dots, N - 1$ denote the optimal intermediate points of the same segmentation. The derivative of ℓ with respect to the each of the intermediate points ψ_n must be null when the segmentation is optimal. The concept at the base of the segmentation algorithm is based on the observation that, for an optimal segmentation, L must satisfy the following recursive relations:

$$\left\{ \begin{array}{l} L_{\psi_0}(\psi_1, 1) = d(\psi_0, \psi_1) \\ L_{\psi_0}(\psi_2, 2) = \max_{\psi_1} \left(L_{\psi_0}(\psi_1, 1) + d(\psi_1, \psi_2) \right) \\ L_{\psi_0}(\psi_3, 3) = \max_{\psi_2} \left(L_{\psi_0}(\psi_2, 2) + d(\psi_2, \psi_3) \right) \\ \vdots \\ L_{\psi_0}(\psi_N, N) = \max_{\psi_{N-1}} \left(L_{\psi_0}(\psi_{N-1}, N-1) + d(\psi_{N-1}, \psi_N) \right) \end{array} \right. \quad \begin{array}{l} \text{with } \psi_0 \leq \psi_1 \leq \psi_2 \\ \text{with } \psi_0 \leq \psi_2 \leq \psi_3 \\ \\ \text{with } \psi_0 \leq \psi_{N-1} \leq \psi_N \end{array} \quad (6.46)$$

The functions $L_{\psi_0}(\psi, n)$ are shown in figure 6.17b for the example curve of figure 6.17a. As the number of segments increases the length of the optimal segmentations converges asymptotically to the length of the original curve. The functions $L_{\psi_0}(\psi, n)$ can be calculated iteratively from $n = 1$ to $n = N$, as shown in equation 6.46. The calculation also gives the penultimate optimal points $\psi_{\psi_0}^{(n)}(\psi, n + 1)$ given recursively by:

$$\left\{ \begin{array}{ll} \psi_{\psi_0}^{(1)}(\psi_2, 2) = \operatorname{argmax}_{\psi_1} \left(L_{\psi_0}(\psi_1, 1) + d(\psi_1, \psi_2) \right) & \text{with } \psi_0 \leq \psi_1 \leq \psi_2 \\ \psi_{\psi_0}^{(2)}(\psi_3, 3) = \operatorname{argmax}_{\psi_2} \left(L_{\psi_0}(\psi_2, 2) + d(\psi_2, \psi_3) \right) & \text{with } \psi_0 \leq \psi_2 \leq \psi_3 \\ \vdots & \\ \psi_{\psi_0}^{(N-1)}(\psi_N, N) = \operatorname{argmax}_{\psi_{N-1}} \left(L_{\psi_0}(\psi_{N-1}, N-1) + d(\psi_{N-1}, \psi_N) \right) & \text{with } \psi_0 \leq \psi_{N-1} \leq \psi_N \end{array} \right. \quad (6.47)$$

Once the functions $\psi_{\psi_0}^{(n)}(\psi, n + 1)$ have been computed, they can be used in reverse order to find all the intermediate points for the original problem of segmenting the whole curve, i.e. between ψ_0 and ψ_N , using N segments. The penultimate point $\psi_{N-1} = \psi_{\psi_0}^{(N-1)}(\psi_N, N)$, which is already known, can be used as argument of the function $\psi_{\psi_0}^{(N-2)}(\psi, N - 1)$ to obtain the previous point. The remaining intermediate points are thus calculated with a reversed iteration until the first intermediate point.

As mentioned above, the derivative of the length ℓ of a generic segmentation with respect to the position of the intermediate splitting points must be null. However, even when the mathematical expression of the curve $\mathcal{H}(\psi)$ is available, it is rarely possible to solve analytically the equations leading to the stationary points of ℓ . In the practice the globally optimal solution of the discrete version of the same problem can quickly be computed numerically. The number of points used to discretise the curve should be much larger than the number of segments N . Since the original curve has been discretised, the resulting solution is an approximation of the true solution of the original analytical problem. The continuity of the virtual field \mathbf{H}_2 in R_m guarantees that we can exclude exotic cases, such as fractal curves. It is therefore possible to reach the desired degree of by increasing the number of points used to discretise the curve.

6.3.6 Invertibility issues and starting point

As mentioned in the previous sections, two fundamental properties need to be satisfied in order to apply the segmentation procedures: continuity and invertibility. We now consider the one-parameter segmentation procedure of a two-dimensional system. For this case the invertibility property means that each value of the parameter ψ identifies a single curve segment belonging to the design area R_m , and conversely each point of the design domain can be associated with one value of ψ . The continuity property means that if the distance between two values ψ_a and ψ_b goes to zero, then the distance between the corresponding curve segments in the design area goes to zero as well. The continuity property is automatically verified because of the continuity of the virtual field over R_m . The invertibility property requires more caution. Let us consider the example of the Halbach cylinder with infinite length and $p = 1$. As we perform *one* revolution around the cylindrical air gap, by increasing the angular coordinate ϕ from 0 to 2π , the virtual field \mathbf{H}_2 performs *two* revolutions. This means that each value of ψ corresponds to two separate contour lines in R_m matching that orientation of the virtual field. Instead

of using as parameter the value of ψ defined by $\psi = \text{atan}(H_{2y}/H_{2x})$, we can introduce the accumulated angle, which does not restart from 0 after reaching 2π . Since for this example the orientation of the virtual field is given by $\psi = 2\phi$, the accumulated angle spans the interval $[0, 4\pi]$. Introducing the accumulated angle allows us to circumvent the invertibility issues that would otherwise emerge for this example.

In order to define the accumulated angle for the general case, we consider a curve $\Gamma : t \in [0, 1] \rightarrow \mathbf{x}(t)$, and we assume that \mathbf{H}_2 is rotating counter-clockwise as we move along the curve. The purpose of Γ is to create a one-to-one correspondence between the level curves $R_m(\psi_n)$ and the continuous parameter $t \in [0, 1]$. The accumulated angle is defined for each t as the angle ψ which is obtained by shifting $\text{atan}(H_{2y}/H_{2x})$ by a number of complete revolutions, which is determined by requiring monotonicity and continuity. The monotonicity property means that $\frac{d}{dt}\psi(\mathbf{x}(t)) > 0, \forall t \in [0, 1]$. The continuity property means that if $t_a \rightarrow t_b$, then $\psi(t_a) \rightarrow \psi(t_b)$. If the curve Γ is closed, we also have the following continuity property across the starting point: if $t_a \rightarrow 0^+$ and $t_b \rightarrow 1^-$, then $\psi(t_b) - \psi(t_a) \rightarrow n2\pi$, where n is the number of revolutions performed by \mathbf{H}_2 from the first point $t = 0$ to the last point $t = 1$. The curve Γ can be constructed by starting from an arbitrary point and proceeding in a way such that each $R_m(\psi)$ is intersected once and only once. However, as long as ψ is monotonic, the result will be the same for all the choices of Γ . If we assume that the union of all the ψ contour lines passing by the points of the curve Γ is coincident with the whole design area, the definition of the accumulated angle ψ can be extended to any other point of design area that is not on Γ .

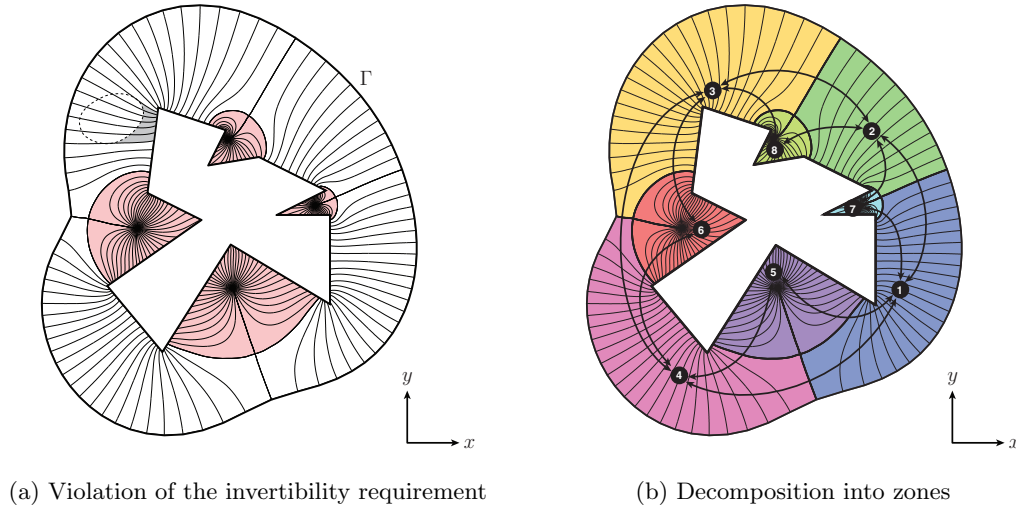


Fig. 6.18: 6.18a: example of a geometry for which the ψ contour lines passing by the curve Γ do not span the whole design area. As explained in section 6.3.6, the globally optimal segmentation cannot be determined by our method for this case. 6.18b: decomposition of the geometry into a network of connected zones. This decomposition can be used as starting point to address the segmentation problem for geometries presenting this issue.

As we have seen, the invertibility requirement implies that the union of all the ψ contour lines passing by the points of the curve Γ must fill the entire design area. This condition is not always verified. A counterexample is illustrated in figure 6.18a, where the curve Γ is coincident

with the external border of the design area, and represented by the thick black line. All the ψ contour lines are plotted inside the design area as thin black lines. As can be seen, none of the contour lines originating from the curve Γ are entering the pink shaded areas, and therefore the condition is not satisfied. Moreover, if the region enclosed by the dashed line is removed from the design area, the grey shaded region could not be reached by any of the contour lines passing by Γ .

Figure 6.18b shows a graph overlaying the illustration of the geometry. The graph describes how the different zones of the geometry are connected with each other. The zones are labelled from 1 to 8 and shaded with different colours. For a geometry not presenting these invertibility issues, such as the Halbach cylinder geometry, the graph would look like a single closed loop composed by one zone. The decomposition illustrated in figure 6.18b could provide the starting point to address the segmentation problem for this class of troublesome geometries. However, the globally optimal solution cannot be determined with the same method described in section 6.3.5.

Observing the different cases that were analysed during this work it seems reasonable to conjecture that these problems never occur for the case of a uniform objective field defined over a convex cavity, as long as the only hole of the design area is the cavity itself. However, while this condition is conjectured to be sufficient, it does not exhaust the class of design objectives for which the globally optimal segmentation can be determined using this approach.

If the curve Γ is closed, as it is in the Halbach example, the choice of the starting value ψ_0 could affect the value of \mathcal{S} : it is still possible to determine the dependence of \mathcal{S} on the starting point, and find the optimal value of ψ_0 . Once the curve $\mathcal{H}(\psi)$ is computed, this is not a computationally intensive procedure and can be performed as the last step of the optimisation. However, for the case of the Halbach cylinder with optimal external border all the starting points are equivalent. If the design area is not connected, each of the disconnected regions can be segmented independently using the same method.

The introduction of the accumulated angle helps solving similar invertibility issues that might emerge with the one-parameter segmentation procedure of three-dimensional systems. The construction of the accumulated angle is not useful with the two parameters procedure. Since the algorithms presented in section 6.3.4 do not enforce the connectedness of the resulting segments, two separated parts of the geometry corresponding to the same orientation of the virtual field would be always assigned to the same segment even though they separated in space. One possible approach to avoid these issues with the two-parameters segmentation is to subdivide the design area into zones where the invertibility condition is verified, and to segment these zones independently.

6.4 Examples

In this section we will consider various examples of magnetic structures optimised using the techniques introduced in the previous sections. Some of the following subsections reproduce the discussion reported in the paper attached in section B.4.

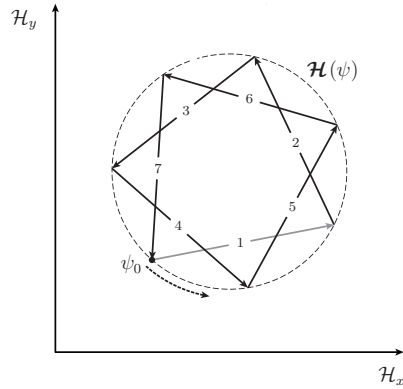
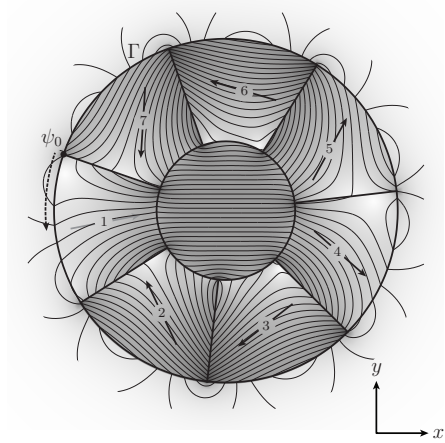
6.4.1 Halbach cylinder

We will now examine in detail the case of the Halbach cylinder, which we used as illustrative example in the previous sections.

We adopt cylindrical coordinates r and ϕ , and we denote the unit vectors in the radial and azimuthal directions by \hat{e}_r and \hat{e}_ϕ , respectively. The field \mathbf{H}_2 generated outside an infinitely long cylinder magnetized transversally to its axis is given by:

$$\mathbf{H}_2(r, \phi) = \frac{MR_I^2}{r^2} (\cos(\phi)\hat{e}_r + \sin(\phi)\hat{e}_\phi)$$

where the axis of the cylinder is in the z direction and the magnetization is in the x direction, R_I is the radius of the cylinder and M the norm of its magnetization. The solution is analogous to the field distribution given by equation 4.31 for the case $p = -1$. This uniformly magnetized cylinder is the virtual magnet for the Halbach case.

(a) Curve $\mathcal{H}(\psi)$ and segmentation.

(b) Corresponding segmented geometry

Fig. 6.19: Optimal segmentation of the Halbach cylinder geometry using 7 segments. Because of the symmetry the starting point, indicated in both the panels by a black circle, does not affect the value of the objective functional.

The norm of the virtual magnetic field, H_2 , is independent of ϕ , and the level curves of the norm are circles with their center in the origin. One of these circles is chosen as the external border. The points of the external border can be parametrised directly by the angle $\phi \in [0, 2\pi]$, and the orientation of the virtual field is described by the accumulated angle $\psi = 2\phi \in [0, 4\pi]$. The radius of the external border is denoted by R_O . The level curves of ψ are radial lines with constant ϕ . The vector $\mathcal{H}_{[\psi_0, \psi_1]}$ can be calculated explicitly:

$$\begin{aligned} \mathcal{H}_{[\psi_0, \psi_1]} &= \int_{R_{[\psi_0, \psi_1]}} d^2x \mathbf{H}_2(\mathbf{x}) = (MR_I^2) \int_{\psi_0/2}^{\psi_1/2} d\phi \left(\cos(\phi)\hat{e}_r + \sin(\phi)\hat{e}_\phi \right) \int_{R_I}^{R_O} dr \frac{1}{r} \\ &= (MR_I^2) \log\left(\frac{R_O}{R_I}\right) \left(\hat{e}_x \int_{\psi_0/2}^{\psi_1/2} d\phi \cos(2\phi) + \hat{e}_y \int_{\psi_0/2}^{\psi_1/2} d\phi \sin(2\phi) \right) \\ &= (MR_I^2) \log\left(\frac{R_O}{R_I}\right) \frac{1}{2} \left(\hat{e}_x (\sin(\psi_1) - \sin(\psi_0)) - \hat{e}_y (\cos(\psi_1) - \cos(\psi_0)) \right) \end{aligned}$$

Since $\psi \in [0, 4\pi]$, the curve $\mathcal{H}(\psi) = \mathcal{H}_{[\psi_0, \psi]}$ describes two revolutions around the point:

$$(\cos(\psi_0)\hat{e}_x + \sin(\psi_0)\hat{e}_y) (MR_I^2) \log(R_O/R_I) / 2$$

with radius $R_B = (MR_I^2) \log(R_O/R_I) / 2$. The initial point is in the origin: $\mathcal{H}(\psi_0) = \mathbf{0}$.

The length of this curve in the continuous case is equal to the value of \mathcal{S} and is given by $4\pi R_B$. Intuitively, since the curvature of the curve is constant, the best way to split it in N segments in order to maximize the length of the polygonal line, is to use identical segments. If this curve is segmented using N identical segments (for the two revolutions), each segment will span an angle of $(4\pi)/N$. The side s of a regular polygon with N sides inscribed in a polygon of radius R is equal to $s = 2R \sin(\pi/N)$. Considering the double revolution, the ratio between the length of the vector \mathcal{H} associated with each segment and the length of the corresponding curve arc is given by:

$$\frac{\mathcal{S}_N}{\mathcal{S}_{\text{Continuous}}} = \frac{N \sin(2\pi/N)}{2\pi} \quad (6.48)$$

which is the familiar formula for the segmented Halbach cylinder[65].

The $\mathcal{H}(\psi)$ curve and the geometry are shown in figures 6.19a and 6.19b for the case $N = 7$.

It is worth mentioning that the results of this section are also true for any multipole Halbach cylinder surrounded by air. This can be shown by considering the analytical expression of the field generated by a multipole Halbach cylinder[91]. If the virtual remanence is defined over an infinitely long cylindrical shell R_g and is expressed as $\mathbf{B}_{r,2}(r, \phi) = B_r(r) (\cos(+p\phi)\hat{e}_r + \sin(+p\phi)\hat{e}_\phi)$, then the optimal real remanence is oriented as $\cos(-p\phi)\hat{e}_r + \sin(-p\phi)\hat{e}_\phi$. The design area is adjacent to R_g and is located on the external side of R_g if $p < 0$ and on the internal side of R_g if $p > 0$. The optimal external border of the design area is always a cylinder which is coaxial with R_m . Moreover, the optimal boundaries between adjacent segments are given by radial surfaces, all separated by equal angles. The ratio between the value of \mathcal{S} in the segmented case and the value in the continuous case is still given by Eq. (6.48). In the continuous case the field generated \mathbf{H}_1 generated by the real remanence has exactly the same angular dependence as the virtual remanence:

$$\mathbf{H}_1 \propto r^{p-1} (\cos(+p\phi)\hat{e}_r + \sin(+p\phi)\hat{e}_\phi) \quad \text{for } p \neq 1 \quad (6.49)$$

The case analysed above of uniform field in the x direction is given by $p = -1$, and the region R_g is a cylinder instead of an hollow cylindrical shell.

6.4.2 Rectangular Cavity

A rectangular cavity is another example for which the equation of the virtual field is analytically solvable. In order to show the algorithm's results with an asymmetrical problem, a decentered circle is chosen as the external border of the design area, as visible in figure 6.20b.

The virtual remanence is uniform in the cavity in direction \hat{e}_y . The accumulated angle ψ spans an angle of 4π as in the previous example. This implies that the curve $\mathcal{H}(\psi) = \mathcal{H}_{[\psi_0, \psi]}$ can be extended indefinitely on both sides according to:

$$\mathcal{H}(\psi + n(4\pi)) = \mathcal{H}(\psi) + n \mathcal{H}_{[\psi_0, \psi_0 + 4\pi]}$$

where $\mathcal{H}_{[\psi_0, \psi_0 + 4\pi]}$ is the integral of the virtual field over the whole the design region. The curve $\mathcal{H}(\psi)$ is plotted in figure 6.20a over a period of 8π . Selecting a different starting point would

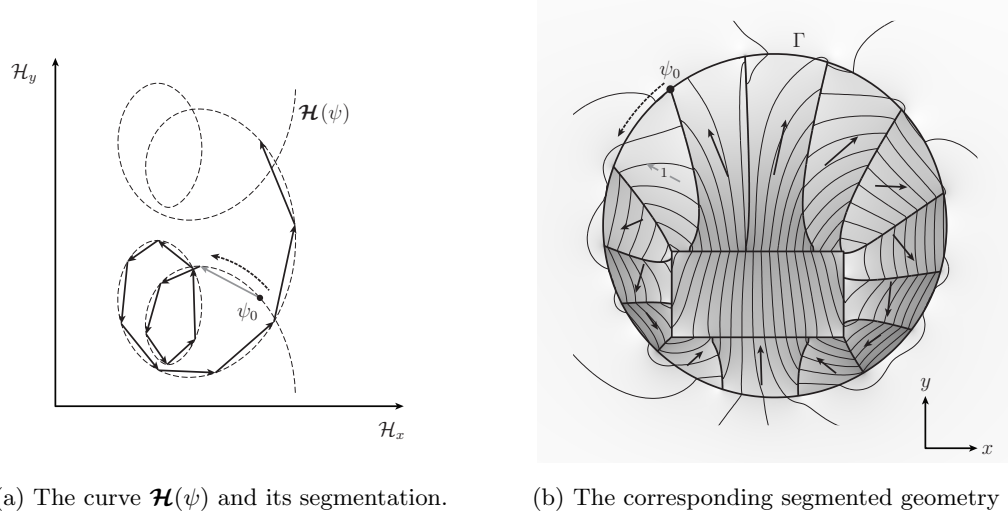


Fig. 6.20: Segmentation of a circular design region with a decentered rectangular cavity. The objective functional \mathcal{S} is the y component of the field integrated over the rectangular air gap. The curve $\mathcal{H}(\psi)$ and its optimal segmentation are shown in 6.20a as, respectively, a dashed curve and a collection of adjacent arrows. The arrows represent the optimal segmentation of the curve, their direction indicates the optimal direction of the remanence in each segment, and their length is proportional to the contribution to the value of \mathcal{S} from each segment. The norm of the remanence is the same for all the segments.

move the origin of the $(\mathcal{H}_x, \mathcal{H}_y)$ plane, indicated as a black circle, on different points of the curve $\mathcal{H}(\psi)$. Any interval $[\psi_0, \psi_0 + 4\pi]$ can be used for the segmentation, corresponding to the different starting points on the external border of the magnet. The point $\mathcal{H}(\psi_0)$ is indicated by the black circle in figure 6.20a, and corresponds to the point of the external border indicated in figure 6.20b. The vectors \mathcal{H} resulting from to the optimal segmentation are indicated as arrows in both the panels; the grey arrow indicates the direction of \mathcal{H} for the first segment.

6.4.3 Quadrupole magnet for beam focusing

Quadrupole magnets are used in the field of particle acceleration for the purpose of focusing beams of charged particles [35, 34]. The following virtual remanence, corresponding to a quadrupole field, is defined over the square cavity shown in figure 6.21a:

$$\mathbf{B}_{r,2} = y \hat{e}_x + x \hat{e}_y. \quad (6.50)$$

The magnet area is limited by the external circle visible in the figure. The radius of the circle is determined by the desired field intensity. The results of the FEM simulation for the optimally segmented system is shown in figure 6.21b. In order to evaluate the optimised magnetic system, we expand the field \mathbf{H}_1 in two components: a perfectly quadrupolar field $\mathbf{H}_Q(\mathbf{x})$, proportional to the virtual remanence $\mathbf{B}_{r,2}$ defined in equation 6.50, and the residual undesired component of the field, which we denote by $\mathbf{\Delta}(\mathbf{x})$:

$$\mathbf{H}_1(\mathbf{x}) = \mathbf{H}_Q(\mathbf{x}) + \mathbf{\Delta}(\mathbf{x}) \quad (6.51)$$

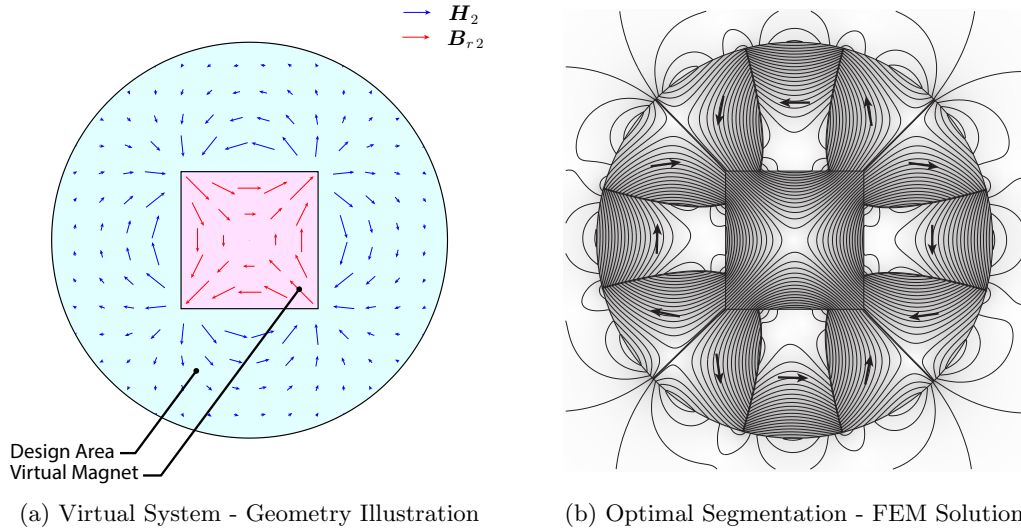


Fig. 6.21: Design of a quadrupole magnet with a square air gap and circular external border. The design is relevant for beam focusing applications in particle accelerator devices.

The field \mathbf{H}_Q is the second-order term of the interior cylindrical multipole expansion, and $\mathbf{\Delta}$ is the sum of all the remaining terms. The calculation of the normalized amplitudes of the two components shows that the field \mathbf{H}_1 is quadrupolar within a very good approximation:

$$c_Q = \left(\frac{\int_{\Omega} dS \|\mathbf{H}_Q(\mathbf{x})\|^2}{\int_{\Omega} dS \|\mathbf{H}_1(\mathbf{x})\|^2} \right)^{1/2} = 0.993 \quad (6.52)$$

$$c_{\Delta} = \left(\frac{\int_{\Omega} dS \|\mathbf{\Delta}(\mathbf{x})\|^2}{\int_{\Omega} dS \|\mathbf{H}_1(\mathbf{x})\|^2} \right)^{1/2} = 0.120 \quad (6.53)$$

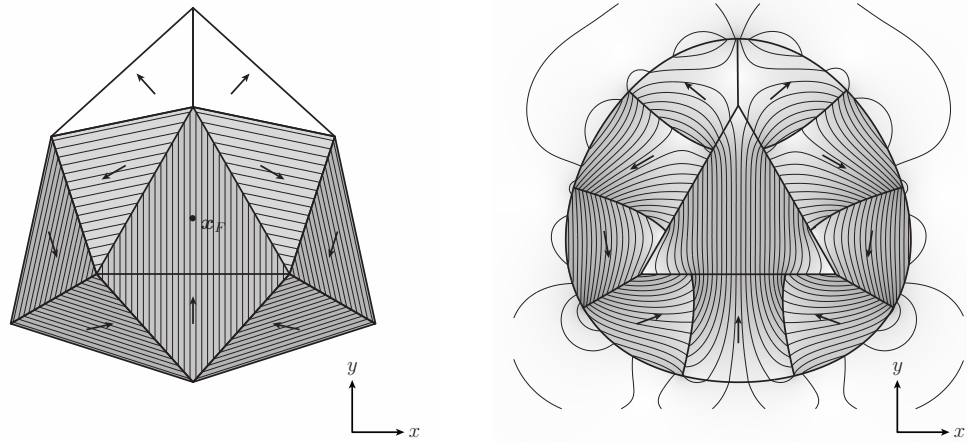
The integration domain Ω is the whole square cavity. Because of the normalization we have: $c_Q^2 + c_{\Delta}^2 = 0.986 + 0.014 = 1$.

The FEM calculation corresponding to the optimised configuration has been also performed for the case of permanent magnets with permeability given by $\mu = 1.05\mu_0$. With this computation the values of the coefficients change only slightly, thus giving: $c_Q = 0.992$ and $c_{\Delta} = 0.122$.

6.4.4 Comparison with uniform field magnets

It is instructive to compare the results of our method, which can also be applied to maximize the field along one direction averaged over a closed air gap, with another design approach which starts with the assumption that the field is perfectly homogeneous.

Abele et al. developed an elegant framework for the design of segmented magnetic systems which are able to generate a perfectly uniform field, \mathbf{H}_0 , inside a closed cavity and are perfectly self-insulated from the surrounding [87, 88, 89]. We consider the results in two-dimensional yokeless magnetic systems composed of a uniformly magnetized prism with triangular cross-sections. It is assumed that the permanent magnet material has zero susceptibility and that



(a) Segmented design that generates a uniform field. (b) Segmented design that maximizes the average field.

Fig. 6.22: Comparison between the two possible ways to segment the magnetic system designed to generate a field in the central triangular cavity and oriented in the y direction. Figure 6.22a shows the segmented system which create a perfectly uniform field inside the cavity. Figure 6.22b shows the segmentation determined using our method, which maximize the y component of the field averaged over the central cavity. The volume, V_m , of magnetic material is the same in the two cases. The arrows indicate the remanence inside each segment.

the norm, B_r , of the remanent flux density is constant. Any region of the system which is not occupied by magnet is occupied by air. It is interesting to notice the similarity between these structures and the segmentation shown in figure 5.5c.

The closed cavity is a polygon with Q sides, which may be irregular. A single layer structure in this framework must be composed of exactly $N = 3Q$ segments. Once the shape of the cavity has been fixed, the geometry of the structure is entirely determined by two decisions: the ratio, $K = H_0/B_r$, between the norm of the field inside the cavity and the norm of the remanence, and the position of a point \mathbf{x}_F inside the cavity in which the magnetic scalar potential is zero. The direction of \mathbf{H}_0 determines the direction of the remanence of each segment, but does not affect the geometry of the system. When the cavity is a regular polygon, the centre of the polygon is the position of \mathbf{x}_F which minimize the volume, V_m , of magnetic material, and leads to the highest efficiency. An example is shown in figure 6.22a: the cavity is an equilateral triangle, the field \mathbf{H}_0 is oriented in the y direction, and the point \mathbf{x}_F is in the center of the triangle.

This approach differs from the one presented in this paper since the resulting field is perfectly uniform, but the approach cannot be applied to any other objective, except the generation of a uniform dipole field. Moreover, there is a constraint on the number of segments and, for single layer structures, the volume of the magnet goes to infinity as H_0 goes to B_r . Since both are segmentation algorithms, it is interesting to compare the performance of the two approaches. This is best done by calculating the figure of merit \mathcal{M} , introduced in Eq. (5.45). We consider magnetic assemblies designed to generate a field in the y direction, therefore we

replace B_1 in the numerator of Eq. (5.45), with its y component. For the case of a uniform field this replacement has no effect, but it is a more realistic way to estimate the efficiency of our method, since the field is not perfectly uniform. It is also introduced the figure of merit η which characterizes the homogeneity of the field, and is zero for a uniform field:

$$\eta = \frac{\langle B_1^2 \rangle - \langle B_1 \rangle^2}{\langle B_1^2 \rangle} \quad (6.54)$$

The efficiency and uniformity with the two approaches are compared in figures 6.23a and 6.23b for different values of magnet volume, V_m , and for different shapes of the inner cavity: an equilateral triangle, $Q = 3$, and octagon, $Q = 8$, indicated by red and blue lines, respectively. We also consider a rectangular cavity, $Q = 4$, with a width that is double the height, indicated by the green lines. The results are plotted as a function of the ratio, V_m/V_g , between the volume of the magnet and the volume of the cavity, V_g . The dashed lines indicate uniform field magnets realized with $N = 3Q$ segments, and the dotted or solid lines indicate the magnets optimised for field average using our approach. Since within our framework it is possible to choose of the number of segments, we consider the cases $N = 3Q$ and $N = 2Q$, indicated by the solid lines and the dotted lines, respectively. The efficiency of the Halbach cylinder with continuously varying remanence is indicated in figure 6.23a by the black dash-dot line.

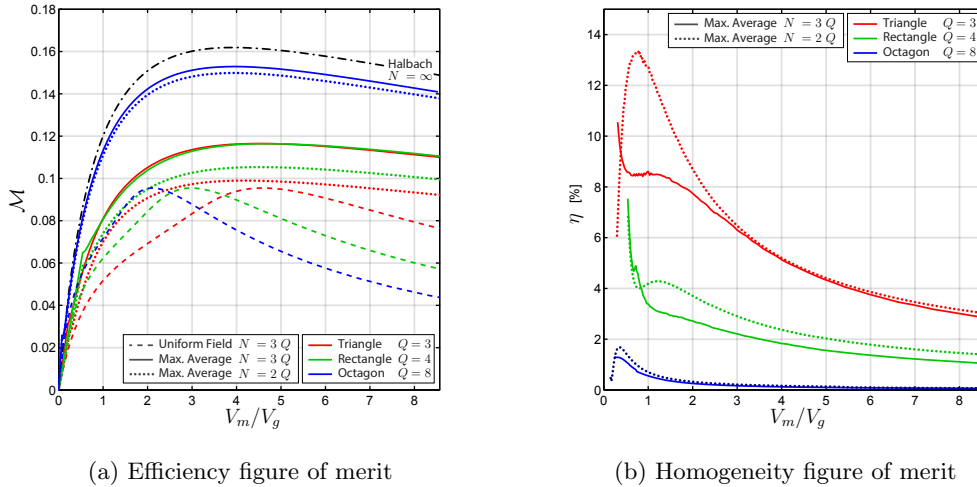


Fig. 6.23: Comparison between the performance of the two segmentation approaches for different shapes of the inner cavity. Figure 6.23a shows the value of the efficiency figure of merit \mathcal{M} and figure 6.23b shows the value of the homogeneity figure of merit η . In both panels the results are plotted as a function of the ratio V_m/V_g .

Even if \mathcal{M} is not equivalent to the objective functional \mathcal{S} of our optimisation approach, the results of this method are characterized by a high efficiency when compared to the uniform field designs, even with a smaller number of segments. The choice of a magnet volume higher than the optimal, which results in higher values of field, does not decrease the efficiency with our method as it does for single-layer uniform field magnets.

The uniformity figure of merit η is shown in figure 6.23b. The field is more uniform for the case of the rectangle than it is for the triangle, and even more uniform for the case of the octagon. In all cases the value of η is $\lesssim 5\%$ for magnet volumes above the maximum efficiency \mathcal{M} . The data points corresponding to very small magnet volumes are slightly affected by the numerical noise arising from the fact that the calculation of the curve $\mathcal{H}(\psi)$ is performed by a numerical integration. The estimation of the parameter η for small volumes is particularly affected by the noise and therefore a few data points have been omitted from figure 6.23b. The limit $V_m \rightarrow 0$ is also not very relevant for practical applications since $\mathcal{M} \rightarrow 0$.

6.4.5 Electric Motor

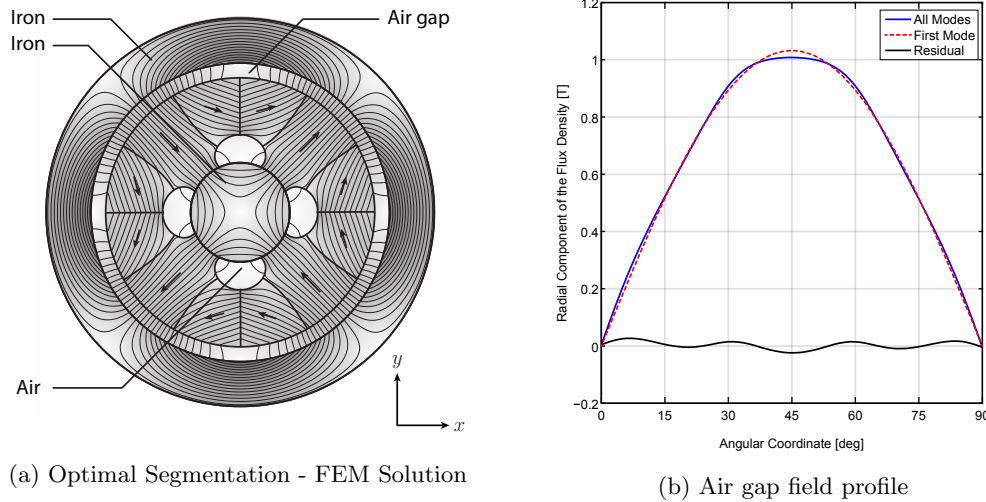


Fig. 6.24: 6.24a: magnetic system representing an electric motor with the purpose of creating a sinusoidal radial field in the air gap between the stator and the rotor. The solid blue line shown in figure 6.24b represents the angular dependence of the radial component of the flux density evaluated at the external border of the air gap. The red dashed line corresponds to the first mode of the Fourier expansion, and the solid black line represents the small deviation from a perfectly sinusoidal field.

In this section we consider an example of four-poles surface-mounted permanent magnet electric motor. The geometry of the systems, shown in figure 6.24a, is analogous to the structure shown in figure 6.2. The iron core of the stator is surrounded by permanent magnet material. A small air gap is present between the stator and the external iron ring of the rotor (the rotor's slots are not included in this model). The virtual magnet area is located in the air gap, where the following virtual remanence is defined, with the purpose of minimizing the detrimental higher harmonics[56]:

$$\mathbf{B}_{r,2} = \sin(2\phi) \hat{e}_\rho. \quad (6.55)$$

It is possible to apply a constraint on the total volume of permanent magnetic material.

The volume of magnetic material was arbitrarily set to 90% of the total volume of the design region. This volume constraint is used to determine the optimal border between magnet and air by considering the norm of the virtual field \mathbf{H}_2 , as explained in section 5.2.2. This results in the four holes adjacent to the iron core in the centre, which are visible in figure 6.24a.

The desired properties of the solution can be checked by expanding in Fourier series the radial component B_ρ of the flux density $\mathbf{B}_1 = \mu_0 \mathbf{H}_1$ in the air gap between the stator and the rotor, close to external yoke. This is plotted in figure 6.24b for one quadrant of the geometry, given by the following interval of the angular coordinate: $\phi \in [0^\circ, 90^\circ]$. The amplitude of the first harmonic is 0.9998 of the amplitude of the total signal, corresponding to 1.032 T. This implies that the total harmonic distortion, THD, is equal to 0.02. When the field is calculated taking into account the non-linear behaviour of iron, and by setting the permeability of the magnets to $\mu = 1.05$, the amplitude of the first harmonic decreases to 1.020 T, but remains 0.9998 of the amplitude of the total signal, and thus the THD does not change.

6.4.6 Magnetic refrigeration 1

Figure 6.25a shows the geometry of the virtual system for a rotary device for active magnetic refrigeration at room temperature. This structure is analogous to the system shown in figure 6.3.

The goal of this system is to maximise the difference between the field intensity in the low and high field regions, as it is desirable for this kind of devices[96]. For this purpose, the following virtual remanence is defined:

$$\mathbf{B}_{r2} = \text{sign}(x) \hat{e}_\rho \quad (6.56)$$

where x denotes the coordinate parametrizing the horizontal direction. As shown in figure 6.3a, the virtual remanence is only defined in the high field regions of the air gap, which are situated on the two sides of the iron core.

We apply a constraint on the total volume of magnet material, which is equal to 5 times the volume of the high field region. This ratio is comparable to other published designs of magnetic refrigeration devices[98].

As explained in section 5.2.2, we can convert an equipotential line of the virtual scalar potential Φ_2 into the external border between permanent magnet and soft magnetic material. The level curves corresponding to the volume constraint are the kidney shaped lines shown on both the sides of the air gap in figure 6.25a. After determining the boundary between magnet and iron, the outer border of the iron region can be determined arbitrarily, as long as magnetic saturation is avoided. We choose a circular external border which encloses the design area.

Figure 6.25a shows the result of the FEM calculation. The flux density norm averaged over the high field region is equal to 1.25 T and averaged over the low field region is 0.13 T, which is a satisfactory result with respect to other published magnetic refrigeration devices[96]. The norm of the flux density evaluated at the middle radial position of the air gap is plotted in figure 6.25b as function of the angular coordinate ϕ in the interval $\phi \in [-90^\circ, 90^\circ]$. It would be possible to further reduce the average norm in the low field region by employing non-linear optimisation techniques as the final step of the optimisation process. The FEM calculation has also been performed using the more realistic models for magnets and iron, as for the example of the previous section: the flux density norm averaged over the high field region decreases slightly to 1.23 T, while the low field region average remains 0.13 T.

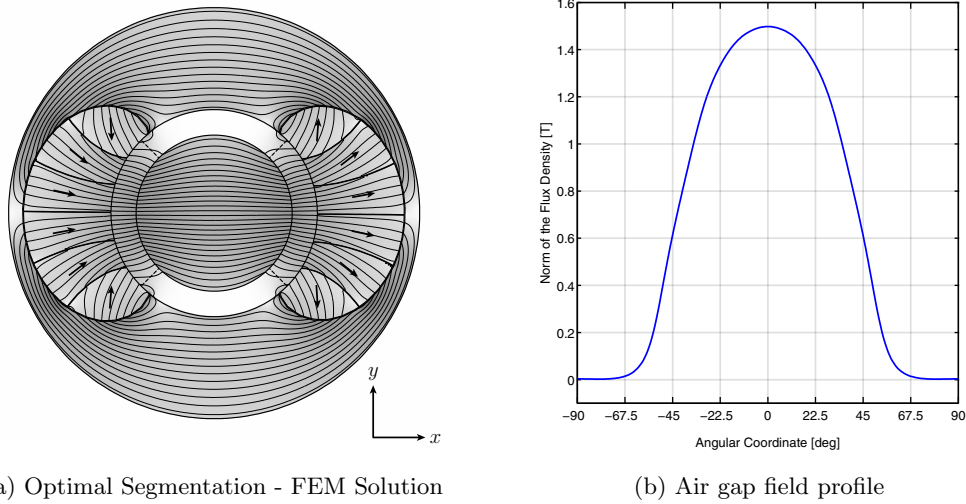


Fig. 6.25: 6.25a: rotary device for magnetic refrigeration, equivalent to the system shown in figure 6.3. The permanent magnet is segmented using $N = 12$ segments. Figure 6.25b shows the angular dependence of the norm of the flux density evaluated in the middle radial position of the air gap.

The same magnetic system has been optimised using different values of magnet volume V_m , while keeping all the other parameters fixed, and almost identical to the the case of figure 6.25a. This investigation covers the results presented in the paper attached in section B.8. The results are shown in figure 6.26 as function of the ratio V_m/V_{High} , where V_{High} denotes the volume of the high field region. The top panel shows the norm of the flux density averaged over the high field regions. The middle panel shows the quantity $\dot{q}_c = \langle \|\mathbf{B}\|^{2/3} \rangle_{\text{High}} - \langle \|\mathbf{B}\|^{2/3} \rangle_{\text{Low}}$, which is related to the cooling power provided by the device. The third panel represents the figure of merit Λ_{Cool} , defined by [98]:

$$\Lambda_{\text{Cool}} = \frac{V_{\text{High}}}{V_m} \left(\langle \|\mathbf{B}\|^{2/3} \rangle_{\text{High}} - \langle \|\mathbf{B}\|^{2/3} \rangle_{\text{Low}} \right) \quad (6.57)$$

As can be noticed from the figure, the rate of growth of $\langle \|\mathbf{B}\| \rangle_{\text{High}}$ decreases with V_m , and Λ_{Cool} is monotonically decreasing. However, compared with other published designs [96], this system achieves a rather high field using a relatively low amount of permanent magnet.

6.4.7 Magnetic refrigeration 2

As last example we consider the segmentation of the rotary magnetocaloric device shown in figure 6.7b. The permanent magnet region to be subdivided is enclosed by the upper iron part, and the interface between magnet and iron is given by a level surface of the virtual scalar potential Φ_2 . One of the two symmetrical level surfaces is shown in figure 6.27a. For manufacturing purposes it is generally convenient that the magnet segments have flat lateral surfaces, or at least shapes that can be extruded from a flat base.

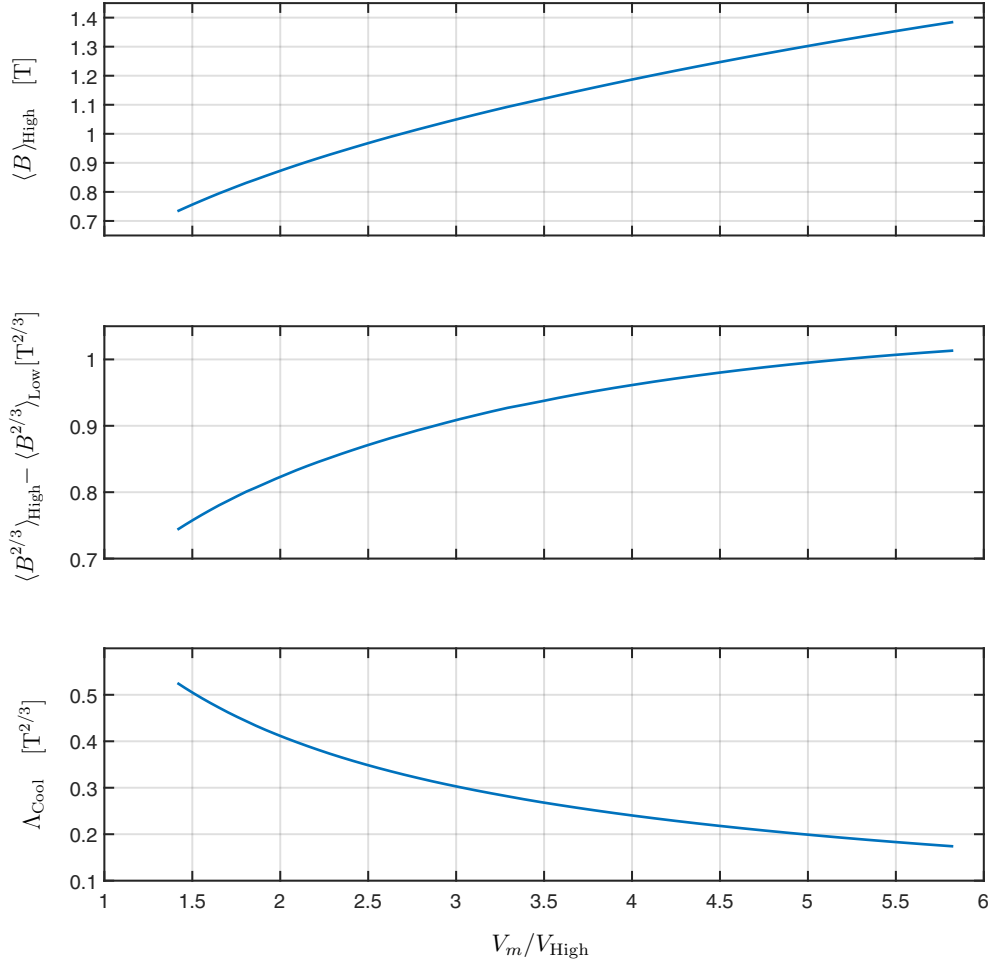
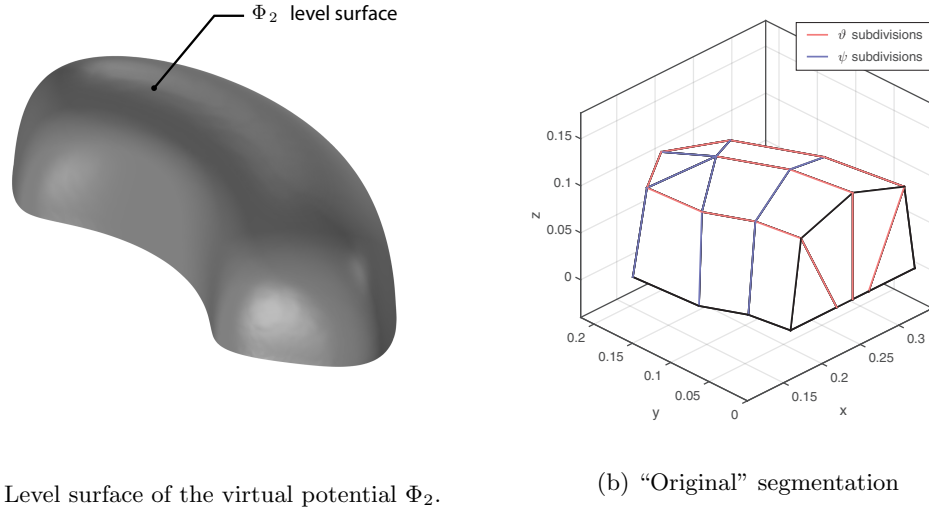


Fig. 6.26: the system shown in figure 6.25a has been optimised using different values of magnet volume V_m . The results are shown here as function of the ratio between V_m and the volume of the high field region. The top panel shows the norm of the flux density averaged over the high field region. The middle panel shows the parameter \dot{q}_c , whose expression is indicated in the vertical axis; \dot{q}_c is linked with the cooling power provided by the magnetocaloric device. The parameter Λ_{Cool} is the product between \dot{q}_c and the volume ratio V_{High}/V_m .

The challenge is to simplify the shapes of the magnet blocks, while allowing the subdivisions to reproduce the spatial distribution of the angles ψ and ϑ , describing the orientation of the virtual field \mathbf{H}_2 . The family of segmentations as the one shown in figure 6.27b are a good compromise between these two conflicting goals. It can be noticed that the external surface reproduces approximately the same shape of the Φ_2 level surfaces. The sections highlighted

(a) Level surface of the virtual potential Φ_2 .

(b) “Original” segmentation

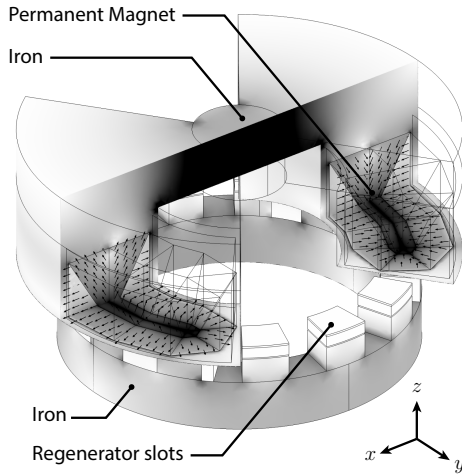
Fig. 6.27: Segmentation of the permanent magnet of the magnetocaloric device for the ENOVHEAT project. 6.27a: external surface of one of the two symmetrical magnets. This boundary is calculated as level surface of the virtual scalar potential Φ_2 . 6.27b: parametrized segmentation composed by segments having all flat faces. This segmentation approximately reproduces the spatial dependence of the orientation of the virtual field \mathbf{H}_2 . The subdivision highlighted by the light red lines correspond to the inclination angle ϑ , while the light blue lines correspond to the azimuthal angle ψ .

by the light red lines correspond to ϑ subdivisions, while the sections highlighted by the light blue lines correspond to ψ subdivisions. Since these flat faces are an approximation of the real behaviour, the orientation of \mathbf{H}_2 may change from different points of the same face.

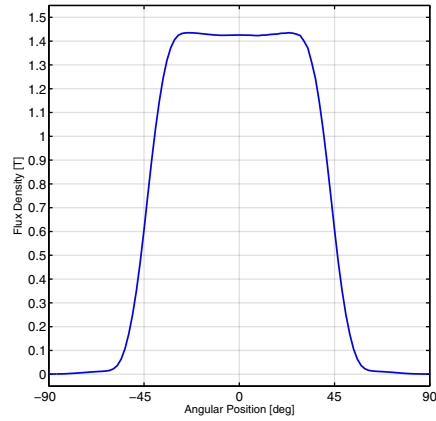
Thanks to the computational efficiency of the virtual magnet approach, it is possible to compare many different segmentation, without the need of performing too many slow FEM calculations. Appendix A.1 presents different segmentations obtained by further simplifications of the “original” segmentation shown in figure 6.27b. Different values of magnet volume are also considered. This systematic comparison resulted in the selection of a relatively simple solution, which is shown in figure 6.28a. This figure shows in fact the final design of the permanent magnet for the ENOVHEAT. A detailed description of the geometry is reported in appendix A.2.

The iron parts are still being analysed in details, and might be subject to small modifications. The FEM calculation have been performed using linear B - H relations: the permanent magnet corresponds to $\mu = 1.05\mu_0$ and $B_r = 1.4$ T, the iron has been modelled using $\mu = 1000\mu_0$. Chapter 7 discusses the effects of these approximations, and how to suggests how to predict and avoid some of the detrimental effects associated with non linear magnetic behaviour.

The final design includes 13 regenerator cassettes, which are connected to the bottom iron structure. Figure 6.28b shows the flux density experienced by a particular regenerator slot while the top and bottom parts are rotated. The angular sector shown in the figure corresponds to half of the rotation. The flux density has been averaged over the entire volume of the cassette.



(a) Geometry of the final segmentation



(b) Field profile

Fig. 6.28: 6.28a: final design of the permanent magnet of the ENOVHEAT prototype. The iron structures might still be subject to small modifications. The segmentation of the permanent magnet has been obtained by simplifying the segmentation shown in figure 6.27b. Figure 6.28b shows the flux density experienced by one of the regenerator slots, as the magnet rotates. The flux density has been averaged over the entire volume of the cassette. As can be noticed, the field remains relatively constant over the high field region. As desired, the field profile exhibits a quite sharp transition between the high and low field regions.

It has to be stressed that this simulation does not include the effect of the magnetocaloric material, which would be located in the regenerators. When it is in its ferromagnetic state the material would have a permeability greater than μ_0 , thus increasing the total flux across them. As can be noticed, the field profile exhibits several features which are desirable for this application. The high field region spans a wide angle, and the intensity of the field remains fairly constant over this angle. The transition between high and low field region is quite sharp, and the intensity of \mathbf{B} remains very small inside the low field region.

Non Linear effects

In this section we will consider the effects of non-linear magnetic behavior. A numerical approach based on FEM analysis will be used to investigate how the field generated by some example magnetic structures is altered by the non-linear behaviour. In particular, it will be discussed how the finite coercivity of permanent magnets and the finite saturation magnetization of the iron parts may decrease the performance of the magnetic structure. The effect of coercivity is particularly important when the goal is to generate an intense field. Some geometrical arrangements of magnets, such as the Halbach cylinder geometry, are theoretically able to produce fields of arbitrary intensity by increasing the total permanent magnet volume. In practice however, the finite coercivity of the material limits the maximum strength of the demagnetizing field that a point of the magnet can experience without undergoing non-linear demagnetization [47, 97, 48]. Very intense fields in the directions transversal to the remanence may also induce non-linear behaviour.

7.1 Finite Coercivity

This section mostly reproduces the discussion reported in the paper attached in section B.2. Following a similar procedure to the one described in ref. [6], the B - H relation is split into a relation for the direction perpendicular to the remanence vector, and a relation for the direction parallel to the remanence vector; the parallel B - H relation is assumed to be non-linear. The components of the field for parallel and perpendicular directions will be denoted by H_{\parallel} and H_{\perp} , respectively, and similarly for the flux density \mathbf{B} . The decomposition is illustrated in figure 7.1a for the Halbach cylinder geometry, which is used as illustrative example in the next section.

The B_{\parallel} - H_{\parallel} relation in the direction parallel to the remanence vector \mathbf{B}_r , is modelled with a piecewise linear function, parametrized by the values of the coercivity H_c , the relative permeability μ_r^{\parallel} and the remanence B_r . The piecewise relation is schematically illustrated in figure 7.1b together with some example load lines and the corresponding working points. The relation is expressed by the following equation:

$$\begin{cases} B_{\parallel} = \mu_0 \mu_r^{\parallel} H_{\parallel} + B_r & \text{for } H_{\parallel} > -H_c & \text{(linear region)} \\ B_{\parallel} = \mu_0 \mu_r^{\parallel} H_{\parallel} - B_r & \text{for } H_{\parallel} < -H_c & \text{(reversed linear region)} \end{cases} \quad (7.1)$$

The two regions are connected by the vertical line segment $H_{\parallel} = -H_c$. As all hard magnetic materials exhibit a B - H curve with a very steep slope around the knee point[10][12], this piecewise relation is a good approximation. In the direction perpendicular to the remanence, the relation remains linear $B_{\perp} = \mu_0 \mu_r^{\perp} H_{\perp}$, but with a permeability μ_r^{\perp} which may be different from μ_r^{\parallel} . The assumption of linear behaviour in the perpendicular direction holds as long

as the corresponding magnetic field component H_{\perp} remains below the anisotropy field of the material[5].

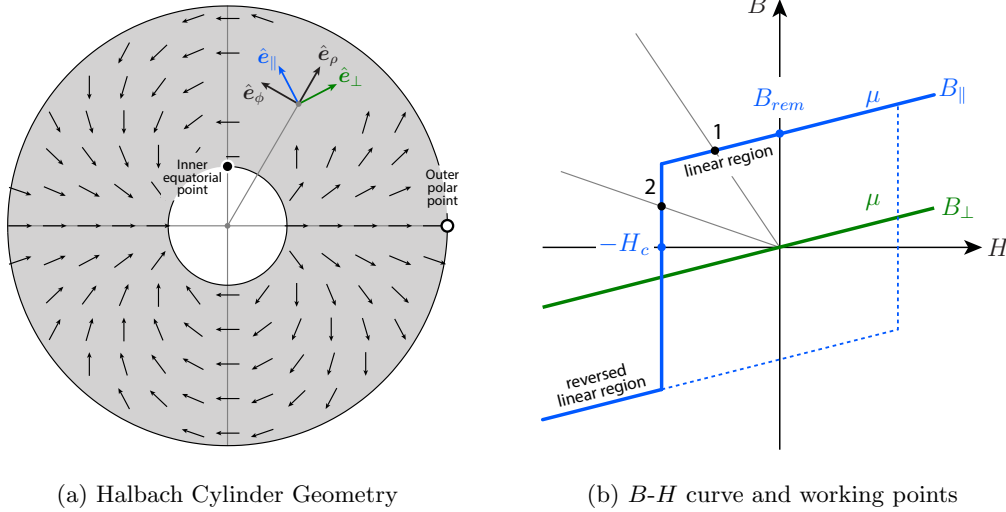


Fig. 7.1: (7.1a): Illustration of the Halbach cylinder geometry: the remanence is plotted as black arrows. The unit vectors \hat{e}_r , \hat{e}_ϕ , \hat{e}_\parallel and \hat{e}_\perp are shown for a particular point. (7.1b): Illustration of the B - H curve and the different categories of working points. The working point labelled by 1 lies on the linear region of the B_{\parallel} - H_{\parallel} curve, while the working point labelled by 2 intercepts the curve after the knee-point.

7.1.1 Halbach cylinder

We will examine the demagnetization effects emerging from the simple model introduced above, using the Halbach cylinder geometry as example. Let us consider the illustrative example shown in figure 7.2, corresponding to the proportion between inner radius and outer radius given by: $R_O/R_I = 3.7$. The results shown in figure 7.2b corresponds to $\mu_{\parallel} = \mu_{\perp} = \mu_0$, $B_r = 1.4$ T, and $H_c = 315$ kA/m, or $\mu_0 H_c \approx 0.4$ T. The results shown in figure 7.2a has the same parameters, but the calculation has been performed with a linear B_{\parallel} - H_{\parallel} relation, corresponding to the limit $H_c \rightarrow \infty$. The non-linear demagnetization has a dramatic effect with this choice of parameters. As can be observed from figure 7.2b, wide regions of the geometry are demagnetized, resulting in an air gap flux density which has roughly half of the intensity predicted by the linear model. The field in the bore is also considerably non-homogeneous for this case.

It is interesting to consider the volumetric distribution of working points, calculated as the fraction of magnet volume characterized by a value of H_{\parallel} or B_{\parallel} below a certain threshold value. The same calculation can be performed for the direction perpendicular to the remanence vector. The results of this analysis are shown in figure 7.3. The top-left panel shows the B - H curves for the parallel and perpendicular directions, plotted as blue and green solid lines, respectively. The linear B_{\parallel} - H_{\parallel} for the linear model is indicated by the dashed blue line. The top-right and bottom-left panels show the volumetric distribution of working points for B and H , respectively.

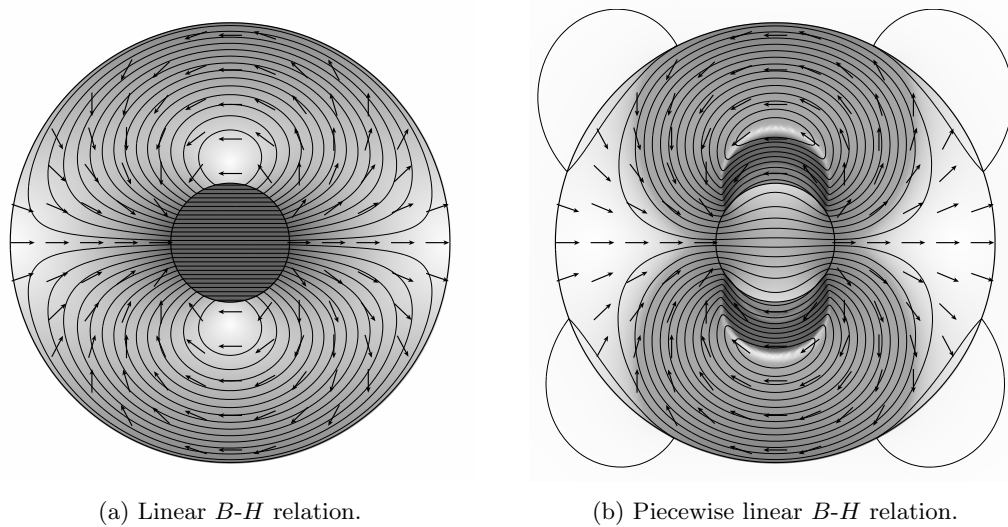


Fig. 7.2: The effect of the coercivity on the field generated by the Halbach cylinder. The result shown in figure 7.2a corresponds to the calculation performed with a linear B_{\parallel} - H_{\parallel} relation, while the results of figure 7.2b corresponds to the piecewise linear relation with $\mu_0 H_c \approx -0.4$ T. Large areas of the geometry of figure 7.2b are demagnetized, thus leading a considerably non-homogeneous air gap field, which has half the of the expected intensity on average.

The fraction of magnet volume above the threshold is indicated in percentage. The B and H axes are respectively aligned with the vertical and horizontal axes of the top-left panel. The values of H and B corresponding to the knee-point are highlighted by the black dashed lines, located at $H = -H_c \approx -0.4$ T and $B = B_r - \mu H_c \approx 1$ T. The volumetric distribution for the case of the piecewise-linear relation presents a special behaviour around the knee-point. A more realistic B - H curve with a smoother knee-point would mitigate these discontinuities but the general behaviour would remain similar.

The bottom-right panel shows the spatial dependence of the parallel component of the flux density. The colormap is aligned with the vertical axis of the top-right panel, to highlight the correspondence between points of the geometry and the working point on the B_{\parallel} - H_{\parallel} curve. The dashed lines indicate a working point exactly on the knee-point of the B_{\parallel} - H_{\parallel} curve, and delimit the blue shaded region from the partially demagnetized red shaded regions. The field in the direction transverse to the remanence has symmetric behaviour, and mostly remains below 1 T, as can be seen from the blue lines of the top-right and bottom-left panels.

As explained in ref. [94], it is possible to start from the linear B - H relation, $\mathbf{B} = \mu \mathbf{H} + \mathbf{B}_r$, and use the analytical solution of \mathbf{H} in any point of the magnet, to predict if the material will be demagnetized in some regions of the geometry. The analytical solution is reported in ref. [91]. Demagnetization occurs in a point when the linear B_{\parallel} - H_{\parallel} relation is not a good approximation; this can be expressed by the condition $H_{\parallel} \leq -H_c$. We included the case $H_{\parallel} = -H_c$ because in this case, using the piecewise relation with a vertical line segment for $H_{\parallel} = -H_c$ would result in a working point in the non-linear region of the curve, as the one labeled by 2 in figure 7.1b.

There are two points in the magnet geometry in which the demagnetization will occur first;

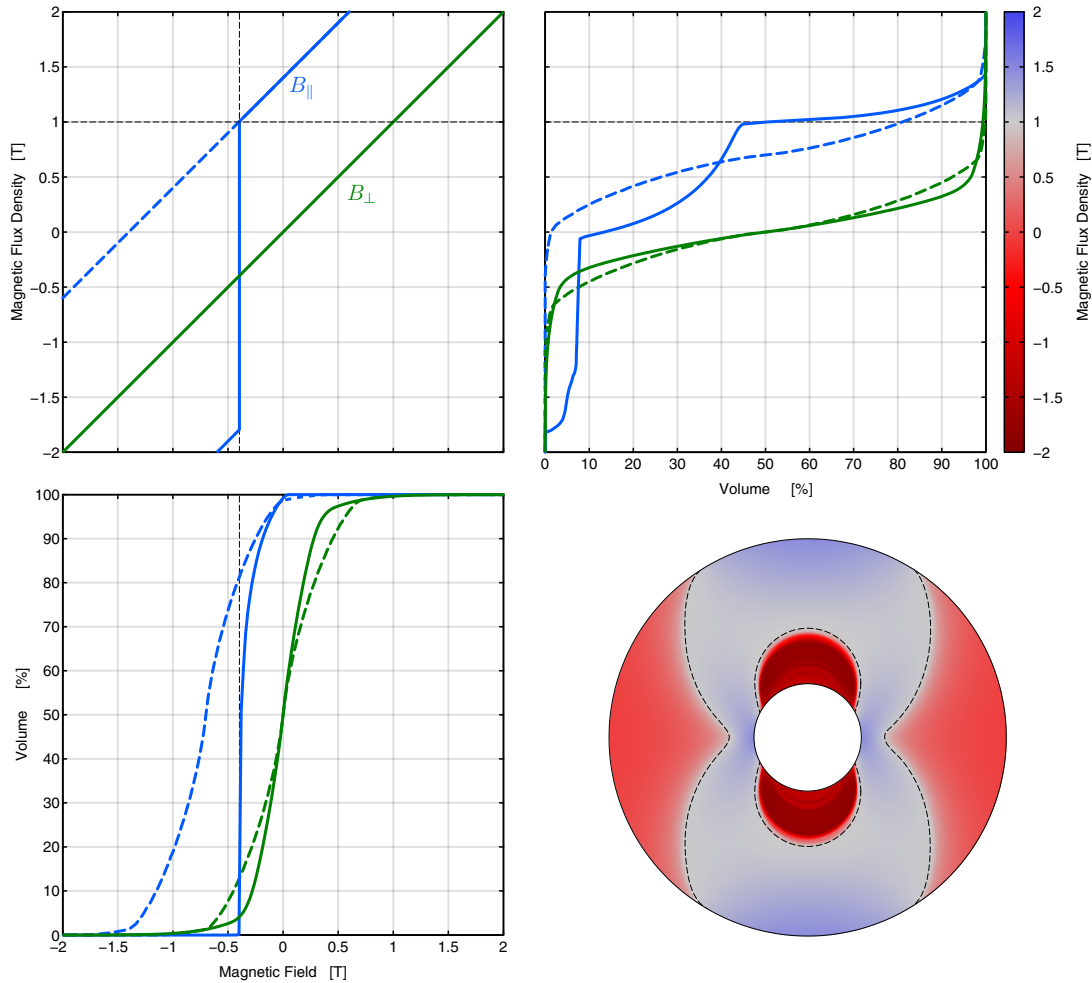


Fig. 7.3: The volumetric distribution of working points for the example shown in figure 7.2. The results of the non-linear calculation are indicated as solid lines, and the results of the linear model with dashed lines. The blue curves indicate the direction parallel to the remanence and the green curves the normal direction. The top-left panel shows the B - H curves, while the top-right and bottom-left panels show the volumetric distributions for B and H , respectively. The bottom-right panel shows the spatial dependence of B_{\parallel} using the colormap aligned with the vertical axis of the top-right panel.

if demagnetization is not occurring in any of these points, then it is not occurring in any other point of the magnet. The first point is the inner equatorial point ($r = R_I, \phi = \pi/2$), indicated in figure 7.1a as a black circle. The second point is the outer polar point ($r = R_O, \phi = 0$), indicated in figure 7.1a as a white circle. There are two independent conditions for demagnetization to occur at these points and for the case $\mu_r = 1$, the conditions are expressed respectively by the

following inequalities for H_c :

$$\text{Equatorial demagnetization: } \mu_0 H_c \leq B_r \log \left(\frac{R_O}{R_I} \right) \quad (7.2)$$

$$\text{Polar demagnetization: } \mu_0 H_c \leq B_r \quad (7.3)$$

It can be noticed that the condition for equatorial demagnetization involves B_r and the ratio between R_O and R_I , while the condition for polar demagnetization only involves B_r . The two equations can be directly derived from the boundary conditions from \mathbf{H} and \mathbf{B} at the border between two different materials. For the inner equatorial point the component of \mathbf{H} which is parallel to the border of the internal cylinder is conserved across the interface. For the outer polar point the component of \mathbf{B} which is normal to the border of the external cylinder is conserved across the interface. In both cases the conserved component is parallel to the remanence. At the inner equatorial point the value of H_{\parallel} is then equal to $-(B_r/\mu_0) \log(R_O/R_I)$. At the outer polar point the value of B_{\parallel} is equal to 0. These values of H_{\parallel} and B_{\parallel} lead to the conditions of equations 7.2 and 7.3.

The same procedure can be generalized to a general value of relative permeability μ_r , starting from the analytical expression of H_{\parallel} inside the magnet and applying the equation $H_{\parallel} \leq -H_c$ in the two critical points. The conditions cannot be written in closed form for H_c , but it is possible to solve the equations numerically and the results are shown in figure 2 from the paper attached in section B.2. The demagnetization conditions will be used to compare with the results of the finite element method simulations with a piecewise B - H curve. The air gap flux density for the linear case can be calculated for a general value of relative permeability μ_r . The linear model predict a uniform air gap flux density given by [91]:

$$\mathbf{B}^{(\text{Theory})} = \left(\frac{\mu_r - 1}{\mu_r + 1} R_O^{-2} - \frac{\mu_r + 1}{\mu_r - 1} R_I^{-2} \right)^{-1} \left(\frac{\mu_r + 1}{\mu_r - 1} - 1 \right) R_I^{-2} B_r \log \left(\frac{R_I}{R_O} \right) \hat{\mathbf{e}}_x \quad (7.4)$$

We will now consider the results for a set of four prototypical magnetic materials: two different grades of NdFeB magnets and two grades of Alnico magnets. The B - H curves of the materials are parametrized, according to equation 7.1, using the values reported in the data-sheets of commercial suppliers of magnetic materials. In particular, the parameters for the NdFeB magnets are derived from ref. [10] and the parameters for the Alnico magnets are derived from ref. [12]. The values of the parameters used for the simulations are listed in table 7.1:

	B_{rem} [T]	H_c [MA/m]	$\mu_0 H_c / B_{rem}$	μ_r
N48	1.41	1.027	0.92	1.04
N38	1.25	2.347	2.36	1.03
Alnico 5	1.25	0.051	0.05	3.7
Alnico 8H	0.74	0.151	0.25	2.0

Table 7.1: Parameters of the permanent magnetic materials

The resulting B - H curves and M - H curves are shown in figure 7.4b, respectively as solid lines and dashed lines.

We simulated different values of R_O/R_I and compared the results with the two demagnetization conditions introduced above. For each simulation we calculate the average flux density

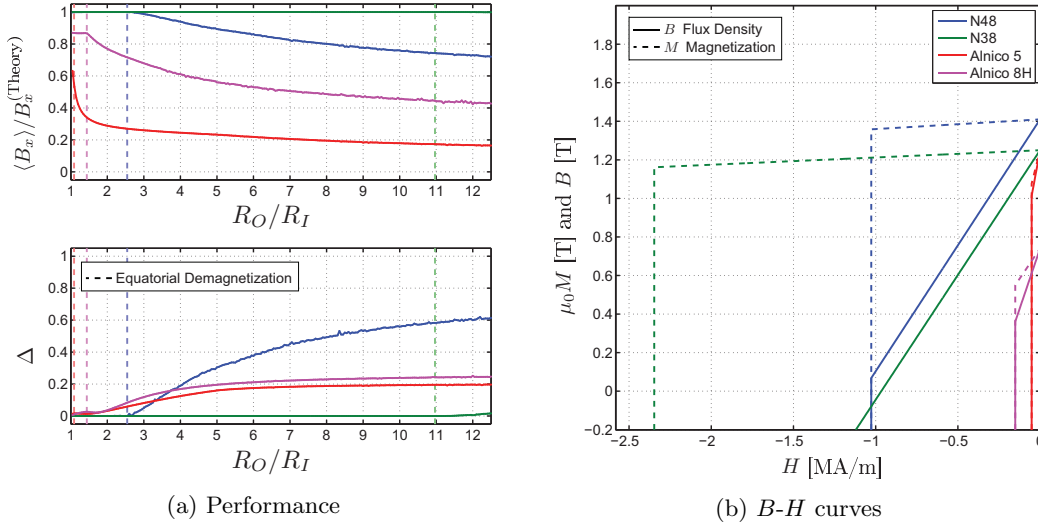


Fig. 7.4: Results of the simulations for the four materials corresponding to the B - H curves and M - H curves represented in figure 7.4b respectively as solid lines and dashed lines. The curves are determined by the set of parameters listed in table 2.1. Figure 7.4a indicates the results of simulations corresponding to different values of R_O/R_I , as visible on the horizontal axis of each panel. The top panel shows the value of the x component of \mathbf{B} averaged over the air gap region and normalized by the value predicted by the analytical solution of equation 7.4. The bottom panel shows the value of the indicator Δ of non-homogeneity, defined in equation 7.5.

\mathbf{B} inside the air gap region, denoted by $\langle \mathbf{B} \rangle$. The average air gap flux density in the x direction is compared with the analytical solution $B_x^{(\text{Theory})}$ of equation 7.4. The results are then expressed as the ratio $\langle B_x \rangle / B_x^{(\text{Theory})}$.

We also want to quantify how much the field fails to be homogeneous, and we will use the estimator Δ , evaluated as the average norm of the difference in flux density divided by the average norm of the flux density:

$$\Delta = \frac{\langle (B_x - \langle B_x \rangle)^2 + (B_y - \langle B_y \rangle)^2 \rangle}{\langle B_x^2 + B_y^2 \rangle} \quad (7.5)$$

The values of $\langle B_x \rangle / B_x^{(\text{Theory})}$ and Δ , for the different materials and different R_O/R_I ratios, are plotted respectively in the top panel and bottom panel of figure 7.4a. As can be noticed, the performance of the materials compared to the theoretical prediction will only decrease as R_O/R_I increases. This can be observed as a decrease of $\langle B_x \rangle / B_x^{(\text{Theory})}$ and an increase of Δ . For the two Alnico materials outer polar demagnetization occurs for all the values of R_O/R_I , and the performance is worse than the theoretical prediction even for small radii. This effect is to a smaller extent present also for N38. The vertical dashed lines in both the left panels indicate the critical value of R_O/R_I corresponding to the condition for inner equatorial

demagnetization. As this phenomenon occurs, the performance decreases both in the average and homogeneity of the air gap flux density.

All the materials, except N38, are demagnetized at the outer polar point for all values of R_O/R_I . However, N48 is only slightly demagnetized compared to the two Alnico materials. For this reason only for Alnico the value of $\langle B_x \rangle / B_x^{(\text{Theory})}$ is appreciably smaller than 1 even in the limit $R_O/R_I \rightarrow 1$. The polar demagnetization effect is very small for the case of N48, and the value of $\langle B_x \rangle / B_x^{(\text{Theory})}$ is very close to 1 for small values of R_O/R_I . For the case of N38 the polar demagnetization effect does not occur at all.

A more drastic effect is caused by the inner equatorial demagnetization. The critical value of R_O/R_I for which this phenomenon occurs for each material is indicated in figure 7.4a as vertical dashed lines. As equatorial demagnetization occurs, the performance decreases both in the average and homogeneity of the air gap flux density, as can be seen in both the panels. For the case of N38, these effects are very small for the simulated range of R_O/R_I .

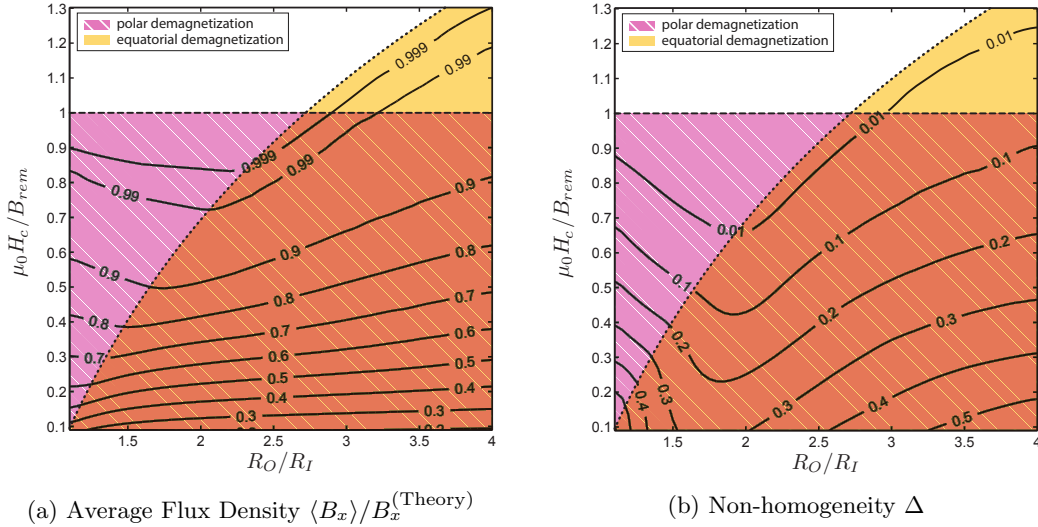


Fig. 7.5: (7.5a): ratio $\langle B_x \rangle / B_x^{(\text{Theory})}$ of the flux density in the air gap with respect to the ideal case. (7.5b): value of the estimator Δ of the non-homogeneity of the field in the air gap (see equation 7.5). The contour lines indicate for the left and right panels respectively the value of $\langle B_x \rangle / B_x^{(\text{Theory})}$ and Δ . The dotted black line represents the conditions for inner equatorial demagnetization expressed in equation 7.2, and the dashed black line corresponds to the outer polar demagnetization expressed in equation 7.3. The two lines delimit the orange and pink shaded regions, respectively. These conditions are calculated for the case $\mu_r^{\parallel} = \mu_r^{\perp} = 1$.

For these simulations we assumed that the relative permeability of each of the four materials has the same value for the parallel and perpendicular component. We will now consider also the effect of anisotropy, by setting the relative permeabilities for the parallel and perpendicular directions μ_r^{\parallel} and μ_r^{\perp} respectively equal to 1.05 and to 1.16[5]. Our simulations revealed that the results of the anisotropic simulations are quantitatively very similar to the results for the case of isotropic permeability.

To proceed systematically we simulate the system for different values of $\mu_0 H_c / B_{rem}$ and of R_O / R_I . These results are plotted in figure 7.5 as a function of R_O / R_I . The contour lines with their labels correspond to the value of $\langle B_x \rangle / B_x^{(\text{Theory})}$ for figure 7.5a and to the value of Δ for figure 7.5b. The value of $B_x^{(\text{Theory})}$ corresponds to the isotropic case with $\mu_r^\parallel = \mu_r^\perp = 1.05$. The two conditions for equatorial and polar demagnetization, expressed by equations 7.2 and 7.3, are indicated by the dotted and dashed black lines respectively. Even though these conditions correspond to the case $\mu = \mu_0$, they reproduce quite well the behaviour for the slightly anisotropic permeability field introduced above. The pink shaded region patterned with oblique lines correspond to occurrence of polar demagnetization. Similarly the orange shaded region corresponds to the equatorial demagnetization.

As expected, only above inside the white region, where none of the demagnetization conditions are met, is the magnet able to reproduce the theoretical flux density both for intensity and homogeneity. The phenomenon of equatorial demagnetization produces a more drastic effect in the performance of the Halbach cylinder with respect to the polar demagnetization. Moreover, it can be noticed that in the region $\mu_0 H_c / B_{rem} < 1$ for which polar demagnetization occurs, the value of $\langle B_x \rangle / B_x^{(\text{Theory})}$ is initially increasing as R_O / R_I increases from 1 to the critical value corresponding to the equatorial demagnetization. For the uniformity the optimal value of R_O / R_I , corresponding to minimum Δ , is even larger.

For each combination of values of R_O / R_I , corresponding to the horizontal axis, and of $\mu_0 H / B_{rem}$, corresponding to the vertical axis, we calculate fraction of the total magnet volume in which the H_\parallel component of the magnetic field is strictly larger than $-H_c$, indicated by the contour lines with their labels. This is equivalent to the fraction of volume for which the working points lie in the linear region of the $B_\parallel - H_\parallel$ curve. We compare the results performed with a piecewise $B-H$ relation, plotted in figure 7.6b, with simulations performed with a linear $B-H$ relation with $\mu_r^\parallel = \mu_r^\perp = 1$, plotted in figure 7.6a.

As expected from the results shown in figure 7.5, the linear and the piecewise model give the same result in the region in which the material is not demagnetized. This can be noticed by the fact that the region delimited by the dashed lines is in both cases above the contour line labelled by 0.99. However, outside this region of the graphs the two models give different results: the linear model indicates a volumetric distribution of working points symmetrically distributed around the middle value $\mu_0 H / B_{rem} = 1/2$; the piecewise model indicates a greater extension of the demagnetized volume, resulting in the reduced performance observed before.

These results, and in particular figure 7.6a, can be used to determine how much of the expensive material with high value of H_c can be replaced by a cheaper material with a low value of H_c without affecting the performance respect to the theoretical prediction. This is done by selecting the areas of the magnet in which the working point does not leave the linear region of the $B_\parallel - H_\parallel$ curve. The amount can be estimated by examining the vertical line corresponding to the desired value of R_O / R_I and observing the fraction of material that is able to work properly, given its coercivity. The coercivity of a NdFeB material, particularly at high temperatures, may be increased by adding dysprosium to the composition during the fabrication processes. Because of the elevated cost of dysprosium, materials with high coercivity are generally more expensive than materials with lower coercivity [2, 18, 17]. For this reason a method for indicating where the materials with low coercivity can be used without affecting the performance will result in an overall reduction in the cost of the materials.

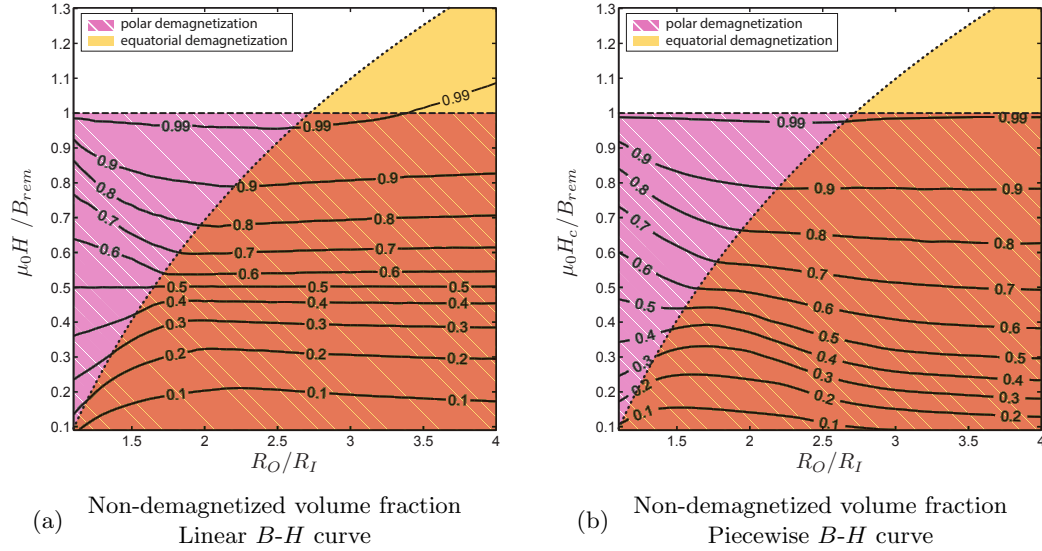


Fig. 7.6: Fraction of magnet in which the working point in the parallel direction lies above the values indicated on the magnetic field axis. The contour lines indicate the fraction with respect to the total magnet volume, as indicated by the labels. (7.6a) shows the simulations performed with the linear B - H relation, (7.6b) shows the simulations performed with the piecewise B_{\parallel} - H_{\parallel} curve corresponding to the coercivity that has the same value of the magnetic field indicated on the vertical axis. The dotted black line represents the conditions for inner equatorial demagnetization expressed in equation 7.2, and the dashed black line corresponds to the outer polar demagnetization expressed in equation 7.3. These conditions are calculated for the case $\mu_r^{\parallel} = \mu_r^{\perp} = 1$.

7.1.2 Magnetic refrigeration

As practical three-dimensional example of application of the approach discussed in the previous section, we consider the magnetic structure examined in section 6.4.7. The FEM computation have been performed with a linear model. For the permanent magnets the permeability has the same value for the parallel and perpendicular direction, given by $\mu = 1.05\mu_0$. The remanence has been set to 1.4 and the permeability of the iron parts is set to $\mu_{\text{Iron}} = 1000\mu_0$.

Since the permanent magnet region is segmented into uniformly magnetized blocks, we consider the volumetric distribution independently for the different kinds blocks mentioned in section A.2. The individual cumulative distributions with respect to the total magnet volume in percentage are plotted in figure 7.1.2. As can be noticed, the different kinds of segments are interested by the non-linear demagnetization effect in different measure. The segments labelled by E, are also indicated in figure 7.7b, are subject to stronger demagnetizing fields. We examine the possibility of realizing the magnetic structure with two different grades of Nd-Fe-B magnets with the same remanence. The first grade is N50, characterized by an intrinsic coercivity of 875 kA/m, i.e. $\mu_0 H_c \approx 1.1$ T. The second grade is N50M, and its intrinsic coercivity is 1080 kA/m, i.e. $\mu_0 H_c \approx 1.36$ T. Figure 7.7b only shows the fraction of the volume which would

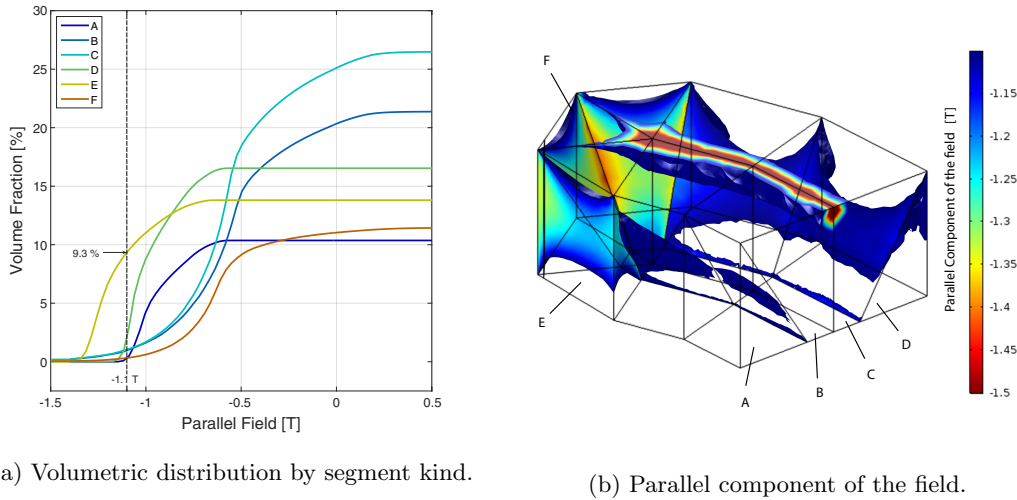


Fig. 7.7: 7.1.2: Fraction of the total magnet volume, expressed in percentage, experiencing a parallel field below the threshold indicated by the horizontal axis. The different curves corresponds to the different kinds of segments indicated in the legend. 7.7b: the parallel component of the field is indicated by the color for one quarter of the permanent magnet. Warmer shades indicate stronger demagnetizing fields. The figure only shows the fraction of the volume where H_{\parallel} is below -1.1 T, which corresponds to the intrinsic coercivity of N50.

experience a demagnetizing field above the intrinsic coercivity of N50, which is also indicated in figure by the vertical black dashed line. The parallel component of the field is represented in figure 7.7b using different colours, warmer shades corresponding to stronger demagnetizing fields, as indicated by the colorbar.

A closer inspection of the results reveals that around 14.1% of the total magnet volume is below -1.1 T, and the segments E alone are responsible for around 2/3 of this volume, corresponding to $(2/3) \times 14.1 = 9.3\%$ of the total magnet volume. The remaining fraction of magnet with $H_{\parallel} \leq -1.1$ T, is split among the other kinds of segments, and is 4.8% of the total magnet volume. Based on this analysis it was decided to use the grade N50M for the segments E, and the grade N50 for other segments. It is expected that this strategy should avoid most of the non-linear effects, thus achieving almost the same performance expected from the linear FEM calculation.

7.2 Iron Saturation

In these section we will focus on the non linear effects associated with soft ferromagnetic materials. Generally it is desirable to avoid these effects, since they would decrease the total flux across a magnetic structure. In order to separate the contribution due to soft magnetic materials from the other non linear effects, for the example present in this section the magnetic behaviour of the permanent magnet has been modelled with a linear relation.

Some of the examples presented in section 6.4 have been simulated using both the linear and

the non-linear model for the magnetic behaviour of the iron parts. As mentioned, the magnetic fields predicted by the two calculations are in all cases extremely similar to each other. This is a sign that the iron parts have been dimensioned correctly with respect to the magnetic flux across them. It is interesting to consider an example of magnetic system for which the iron yoke is under-dimensioned. As illustrative case, we consider the geometry of the magnetic refrigeration device examined in section 6.4.6. The external iron yoke has been reduced in order to make apparent the effect of non linear saturation. Figure 7.8a shows the result of the FEM computation performed within the linear approximation with $\mu = 1000\mu_0$, while figure 7.8b corresponds to the non-linear case, calculated using the non-linear $B-H$ relation included in the COMSOL model library.

As can be noticed from the figure, the realistic calculation leads to an air gap field, which is generally less intense, and with a slightly different distribution. The most noticeable effect is probably the flux leakage across the external surfaces of the structure: when saturation is included in the model the yoke is not able to bear the entirety of the flux generated by the permanent magnets. Quantitatively, the realistic model results in a average high field which is 16% lower than the average calculated from the linear model, while the average low field is 30% higher. The value of the parameter Λ_{Cool} , defined in equation 6.57, is thus 22.3% lower than what expected from the linear calculation.

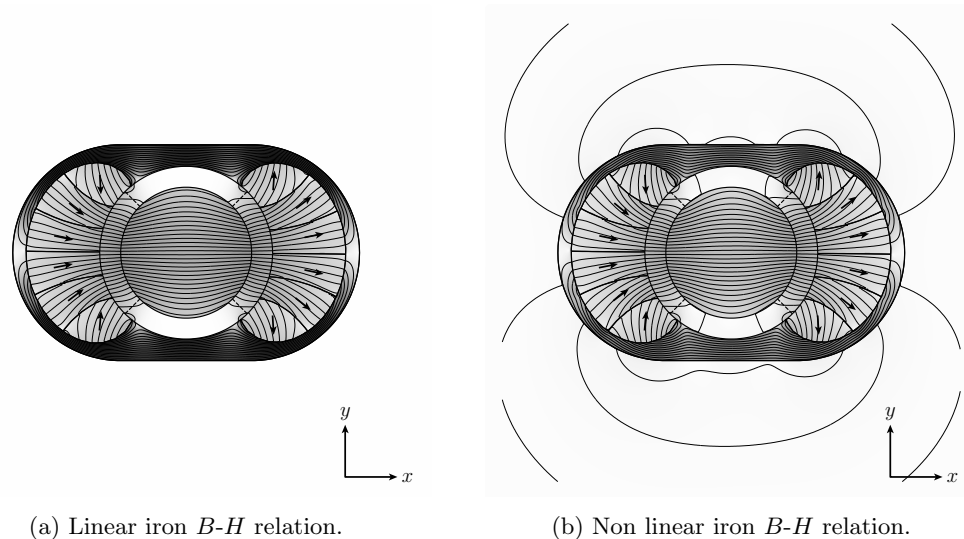


Fig. 7.8: System obtained from the structure discussed in section 6.4.6 by reducing the external iron yoke with the purpose of highlighting the effect of magnetic saturation. 7.8a: computation performed with a linear $B-H$ relation. 7.8b: computation performed by modelling the behaviour of the iron parts with the non-linear $B-H$ curve included in the COMSOL material library. With this geometry the two models produce a remarkable difference, which highlights the fact that the iron yoke is under-dimensioned.

We will now consider the case shown in figure 7.9 calculated using the non linear $B-H$ relation. The external iron yoke has been expanded, with the purpose of completely avoiding the possibility of magnetic saturation inside this part. As can be noticed, the air gap field

distribution closely resembles the distribution of figure 7.8a. Also the insulation from the external region is achieved with the same degree of accuracy predicted by the linear model. In fact, the high field is on average 2% greater than it is for the linear model, and the value of Λ_{Cool} is 1% greater.

We introduce the parameter Δ^{Sat} , which quantifies the difference between the linear calculation, for the case shown in figure 7.8a, with the non-linear results shown in 7.8b and 7.9. Δ^{Sat} is defined as:

$$\Delta^{\text{Sat}}[\mathbf{B}] = \left(\frac{\int_{R_g} d^2x \|\mathbf{B}(\mathbf{x}) - \mathbf{B}^{\text{Lin.}}(\mathbf{x})\|^2}{\int_{R_g} d^2x \|\mathbf{B}^{\text{Lin.}}(\mathbf{x})\|^2} \right)^{1/2} \quad (7.6)$$

Here the integration domain extends to the whole air gap region R_g . For the reduced yoke we have $\Delta_1 = 0.1784$, which expresses a significant difference. For the case shown in figure 7.9 we have $\Delta_2 = 0.0316$, indicating that the linear model would be a sufficiently realistic description of this geometry.

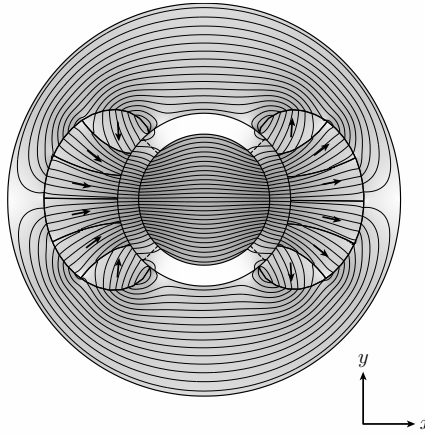


Fig. 7.9: The iron yoke has been expanded to suppress the non-linear effects almost completely. This calculation, which takes into account the non-linear magnetic behaviour of the iron parts, generates an air gap field which is almost identical to the case shown in figure 7.8a.

Since the saturation issues for this example occurred inside the external yoke, it has been possible to easily avoid these effect by resizing the saturated part. However, if the problems had occurred in the central iron core, this straightforward solution would not have been possible, and it would have been necessary to apply more drastic modifications to the geometry. When the purpose is to avoid the non linear effects, the calculations can often be performed within a linear model, while making sure that the flux density inside the highly permeable parts remains safely below their saturation magnetization $\mu_0 M_s$.

Conclusions

8.1 Discussion of the results

The goal of this thesis was to develop different schemes to design and optimise magnetic structures. The general strategy adopted in this work is to address the simplest and most fundamental problems and examine their implications before investigating more general and complex cases. The various optimisation approaches are illustrated with different examples of magnet design problems. In this section the findings of this work will be discussed with an emphasis on how they relate to previous studies, how they are original, and what is their relevance for the scientific community.

A central role is played by optimisation problems characterized by the two following properties:

- magnetic systems exhibiting a linear magnetic behaviour
- objective functionals which are linear with respect to the field

The connection between this family of optimisation problems and the reciprocity theorem has been explored in this work from many different perspectives.

The problem of optimising the flux sources in a system whose geometry is pre-determined has been considered before, and generally presents less challenges than geometry optimisation problems. Its relevance comes also from the simplicity of its implementation. The analysis presented in section 5.1.2 also considers the optimisation of hybrid systems including permanent magnets combined with electro-magnets, with a constraint on the total power dissipated by the electro-magnets. The link between the reciprocity theorem and the optimisation of pre-segmented permanent-magnet systems with respect to a linear objective functional has been considered [80]. In section 5.1.3 was shown that the presence of electro-magnets in the system does not actually modify the optimal orientation of the remanence vectors of the permanent magnet blocks. Moreover, it was shown that for linear objective functionals, the globally optimal current distribution among a set of pre-determined coils in a hybrid system obeys equations which are similar in form to the equations obeyed by the optimal remanence vectors. It was also illustrated that when the optimisation with respect to non-linear objective functionals is performed employing gradient-based methods, the convergence is greatly facilitated by selecting as starting configuration the globally optimal solution of a linear optimisation problem. Often the expression of the non-linear objective functional immediately suggests which linear objective would be suitable for this preliminary step of the optimisation procedure.

It is often insightful to consider a smoothly varying remanence field. The optimality results derived in [86] address the problem of determining the maximally energy efficient remanence distribution which generates a given field. The problem investigated in this thesis presents similarities and differences with these results. The procedure presented in section 5.2.2, and

considered in [80], provides a remanence distribution which maximises an arbitrary linear objective functional. Because of its relevance to real magnetic systems, this thesis focuses primarily on the case of remanence distributions with constant norm. It is also possible to consider an arbitrary permeability distribution, as long as it is pre-determined. The underlying link between these two different perspectives is investigated in section 5.2.3. In [81] the reciprocity theorem is employed within an iterative procedure in order to minimise the non-linear functional representing the magnetic inverse problem. The iterative procedure derived in section 5.2.4 is more general, as can be applied to an arbitrary non-linear objective functional.

Chapter 6 explores the implications of the reciprocity theorem with respect to the problem of optimising the geometry of the magnetic system. It has already been observed that the reciprocity theorem provides a way to calculate the contribution from a specific point of the magnet to the value of a linear objective functional [80]. However, it was not stressed how this calculation immediately yields the optimal border between air and permanent magnet material with zero susceptibility. This method is discussed in section 6.1. The border between permanent magnet and soft magnetic material has been investigated in [86]. The procedure of determining the shapes of iron poles from the level surfaces of the scalar potential is generally known [38]. The perspective adopted in section 6.2 is to investigate this aspect in connection with the reciprocity theorem. As was illustrated with different examples, considering only the portion of level surface that is inside the magnet design area can lead to satisfactory results. Since in all the cases the total magnet volume can be constrained to an arbitrary value, optimising the external border of the permanent magnet is equivalent to minimising the volume of permanent magnet necessary to obtain the same value of the objective functional.

Section 6.3 addresses the question of how a magnetic system is best subdivided into uniformly magnetized blocks such that a given linear objective is maximised. Once again, the reciprocity theorem provides the starting point to answer this question. As was shown in sections 6.3.1 and 6.3.2, within this formalism the only relevant quantity is the orientation of the virtual field and is therefore not convenient to subdivide a region if the direction of the virtual field does not vary. This optimality sufficient condition considerably reduces the complexity of the optimisation problem. In particular, section 6.3.5 presents an analytical approach to find the global solution for the case of segmentations depending on one parameter [105, 106]. This is accomplished by drawing an equivalence between this problem and the approximation of a continuous curve by an inscribed segmented curve with maximal perimeter. The curve approximation problem can then easily be solved employing dynamic programming. In section 6.4.4, the results of this approach are compared with the segmented structures discussed in [87, 89], which generate a perfectly uniform. The comparison reveals that the method introduced in this thesis leads to higher efficiency, even though the field is not perfectly homogeneous. The analytical procedure based on the curve approximation does not apply to the case of segmentations depending on two parameters. Section 6.3.4 investigates a heuristic approach to this problem. Even though optimality is not guaranteed with the same level of confidence given by an analytical derivation, the results provide a strong indication that the globally optimal solution has been found for all the considered examples.

All the optimisation approaches described in chapters 5 and 6 have been derived under the assumption of linear magnetic response. Chapter 7 presents a numerical approach to model some of the effects caused by non-linear magnetic behaviours. It is worth mentioning that non-linear magnetic phenomena are often detrimental, and their occurrence can also be predicted by linear calculations [94]. A non-linear simulation is only necessary for the purpose of determining

the effects of the non-linear behaviour. The non-linearity associated with the finite coercivity of permanent magnet materials have been examined in detail for the Halbach cylinder geometry in section 7.1.1. The analytical solution for the linear regime is available for this geometry, and the results of the non-linear simulations are consistent with the analytical prediction as long as the working point remains within the region where the linear approximation is justified [104].

The Halbach cylinder geometry has been investigated in this thesis from different viewpoints. The relevance of this geometry for the applications is revealed by the huge number of scientific publications on this subject. Thanks to the reciprocity theorem this geometry have been shown to be the globally optimal solution of the underlying linear optimisation problem. In this sense, the procedures developed in this thesis generalise the results to an arbitrary linear objective and an arbitrary geometry. When an iron yoke is introduced at the external border of the magnet region the optimal configuration changes. This aspect was already investigated in [86, 95]. Section 6.2.1 systematically analyses the possibility of replacing an arbitrary fraction of the magnet volume with soft magnetic material. The results show a trade-off between field intensity and field homogeneity. The selection of the best configuration can thus be based on the relative importance between these two factors. Section 5.1.5 compares different segmentations of the same geometry, characterized by different advantages and disadvantages. In section 6.4.1 the segmentation into identical angular sectors is shown to be optimal with respect to the linear objective. Section 6.3.4 considers the geometry optimisation of a three dimensional Halbach cylinder of finite length. As mentioned above, the non-linear effects caused by finite coercivity has been examined in section 7.1.1.

Several examples illustrate how the optimisation approaches are applied to systems for room temperature magnetic refrigeration. The process leading to the design of the prototype for the ENOVHEAT project is examined in greater detail. Several other examples from different fields demonstrate the flexibility of the approaches. In particular, it is investigated the generation of cylindrical multi-pole fields which are fundamental for many applications.

The results presented in this thesis provide an effective way to solve optimisation problems in magnetostatics. Being mainly based on analytical derivations, these methods are easy to implement, computationally efficient, and reliable. The possibility of applying these approaches in combination with finite element methods allows one to apply them to a vast class of geometries and optimisation problems. Moreover, because of the relevance of linear functionals from a theoretical perspective, the optimality results derived for this case provide a deeper understanding of many optimisation problems.

8.2 Outlook

Scientific research is driven by questions rather than answers. Luckily there is usually no shortage of questions, since the process of seeking for answers usually results in opening up new questions. This work is not an exception. The focus of this section is on the limitations of the procedures presented in this thesis, and how future investigations could further develop this work.

It must be stressed that is not even always possible to reduce a given optimisation problem to a functional depending solely on the magnetic field. As the magnetic field itself is never the ultimate goal of a magnetic system, a more realistic analysis should include the influence of the field with respect to the specific purpose of the device of which the magnetic system is part of. Often this means modelling the interplay between different physical mechanisms, e.g. thermal conduction. It is rarely possible to apply analytical approaches to the optimisation of systems modelled with this degree of complexity. The methods discussed in this thesis are developed starting from the assumption that magneto-static system can be simulated independently, and that the objective is only affected by the magnetic field.

As has been stressed along the course of this work, most of the optimality results have been derived under the premise that the magnetic behaviour is described by a linear $\mathbf{B}\text{-}\mathbf{H}$ relation. Even though chapter 7 illustrates how to predict the non-linear effects and possibly how to avoid them, the question of how the different optimisation procedures could be modified to account for the non-linear behaviour remains unanswered. Since the superposition of the fields generated by different sources is not verified for this case, it seems unlikely that it would be possible to apply analytical geometry optimisation techniques when the magnetic behaviour is non-linear.

Non-linear objective functionals have been investigated to some extent. The problem of optimising the flux sources with respect to a non-linear functional has been considered here for pre-segmented structures or smoothly varying remanence distribution. It would be interesting to investigate the generalization of the geometry optimisation results presented in chapter 6 to the case of non-linear objectives. The optimality results derived in sections 6.3.1 and 6.3.2 are based on the convexity of the related optimisation functional with respect to its arguments. These derivations do not extend to a general non-linear functional. However, numerical techniques could be examined for this purpose. Another unsolved problem that could be approached with numerical methods is the determination of the optimal border between materials with arbitrary magnetic susceptibility. A promising strategy could be to combine topology optimisation techniques with the methods based on the reciprocity theorems.

It would be worth to investigate in greater depth the link between maximal energy efficiency and optimality with respect to a linear functional, and define in which situations the two approaches lead to the same result. This would be equivalent to determining in which conditions the field generated by the configuration maximising a linear functional reproduces exactly the desired field.

As stressed in [80], linear objective functionals include linear differential operators. The virtual magnet method would be modified by allowing the virtual remanence to be a generalized functions, e.g. derivative of the Dirac delta function. It would be interesting to consider examples of optimisation problems expressed by linear differential operators, and apply the procedures described in chapter 6 to these examples.

It has been mentioned that for the case of the Halbach cylinder with infinite length, the

globally optimal segmentation can be determined analytically. Future studies could address the problem of finding three-dimensional geometries for which is possible to find analytically the globally optimal two-parameters segmentation. The ideal Halbach sphere would be the most natural candidate for the first investigations.

Magnetic systems designed to generate multipole fields are relevant for many applications. This thesis considered different design concepts of multipole magnets combining permanent magnets, air and soft magnetic material. Some concepts privilege the field intensity while other privilege the field quality. A systematic comparative study of the different possibilities would be pertinent to different applications. While many examples in this thesis focus on cylindrical geometries, it would also be interesting to apply the different design concepts to the realization of linear arrays, producing a one sided flux, and compare the results systematically.




Overall, the relevance of the work of this thesis is also demonstrated by its vast potential for future studies.







Appendices

A.1 Segmentations of the ENOVHEAT prototype

This appendix presents the result of the comparison between different segmentations of the permanent magnets of the ENOVHEAT prototype. The geometry of the prototype is shown in figure 6.7b. The starting configuration, denoted as “original”, is shown in figure 6.27b. The other possibilities are obtained by further simplifications of this initial option. The purpose is to reduce the complexity of the permanent magnet segments and of the iron structure enclosing them. Permanent magnet blocks of different shapes are generally realised by machining rectangular blocks whose remanence vector is normal to one of the faces. For this reason we will also consider the possibility of approximating the optimal direction of B_r of each block by making either parallel or normal to one of the faces. Because of this expedient one of the faces of the final machined segments coincides with one of the original faces of the rectangular block, thus simplifying the manufacturing procedure. We will refer to this approximated segmentation with the label “Approx. B_r ”. As will be stressed from case to case, approximating the remanence in this way might produce pairs of adjacent segments having the same remanence direction. In this situation the two segments can be merged, thus reducing the total number of blocks.

Some of the possible segmentations considered in this comparative study are shown in figure A.1, and labelled by the corresponding names:

- *Original Segmentation*: characterised by 14 segments for each magnet quarter, for a total of 6 unique different shapes (). This diagram shows a trapezoidal magnet quarter divided into six segments of various shapes, with red arrows indicating the remanence direction.
- *Original Segmentation - Approximate B_r* : for this configuration the remanence of each block is constrained to be perfectly normal to the interface separating magnet and iron (). This diagram shows a trapezoidal magnet quarter divided into six segments, all with remanence vectors pointing vertically upwards.
- *Shaved on the top*: obtained from the original segmentation by removing the top convex part (). The number of segments is the same, but the shape of the iron structure is simpler. This diagram shows a trapezoidal magnet quarter with a flat top, divided into six segments.
- *Shaved on the top - Approximate B_r* : when the remanence of the previous segmentation is approximated, the number of segments reduces more than it does for the original segmentation. The maximum reduction leads to $7 + 1/2$ segments for each quarter. However, requiring that the shape of the resulting segments remains relatively simple, results in a reduction to 12 segments for each quarter with 5 unique shapes.

- *Double-Shaved*: obtained from the shaved segmentation by converting the lateral faces into vertical planes, i. e. parallel to the z axis. The number of segments is the same as in the original segmentation, but shape of the iron structure surrounding the magnets is even simpler than it is for the previous case ().
- *Double-Shaved - Approximate B_r* : the reduction in the number of segments due to the approximation of the remanence vectors is the same as for the previous segmentation ().
- *Double-Shaved - Approximate B_r (2)*: for this case the approximation of the remanence direction is performed in a different way. Since this configuration has been selected for the final design of the ENOVHEAT prototype, it will be described in details in the next section.
- *Triangular Grid*: for this case there are 14 segments for each quarter, for a total of 10 unique shapes. The shape of the iron structure is simpler than in the case of the “Double-Shaved” configuration (). The different points correspond to different proportions of the total magnet design region.
- *Triangular Grid - Approximate B_r* : this configuration is only composed by pyramidal or prismatic segments having triangular base. For this case the number of segments can be reduced to 10 segments for each quarter and 7 unique shapes ().
- *Simple Grid*: the external shape is the same kind of the triangular grid, but all the blocks have the same shape (). Different proportions of the total magnet design region have been considered. Moreover, different number of segments have been considered, i. e.: 8, 12, 16, 18, 20 or 24 segments for each quarter. The results will only be shown for the best combination of subdivisions along each dimension among those having the same total number of segments.
- *Single Block*: the various segmentations have also been compared with a simple magnetic system composed by one block for each half (). In this case only the top face of the block is connected with the iron structure, as doing otherwise would create a short-circuit for the field lines. Different proportions of the single block have been considered.

The result of this comparison is shown in figure A.2. Different amounts of magnet volume V_m are considered: the results will be presented as function of the ratio between V_m and the volume of the high field region. The top panel shows the norm of the flux density averaged over the high field region. The middle and bottom panels shows respectively the parameters \hat{q}_c and Λ_{Cool} introduced in section 6.4.6. Figure A.2 is a zoomed-in version of the same plot showing only the best configurations. All the simulations correspond to the same value of internal radius $R_I = 21$ cm. The permanent magnet has been simulated using the parameters: $\mu = 1.05\mu_0$ and remanence $B_r = 1.4$ T.

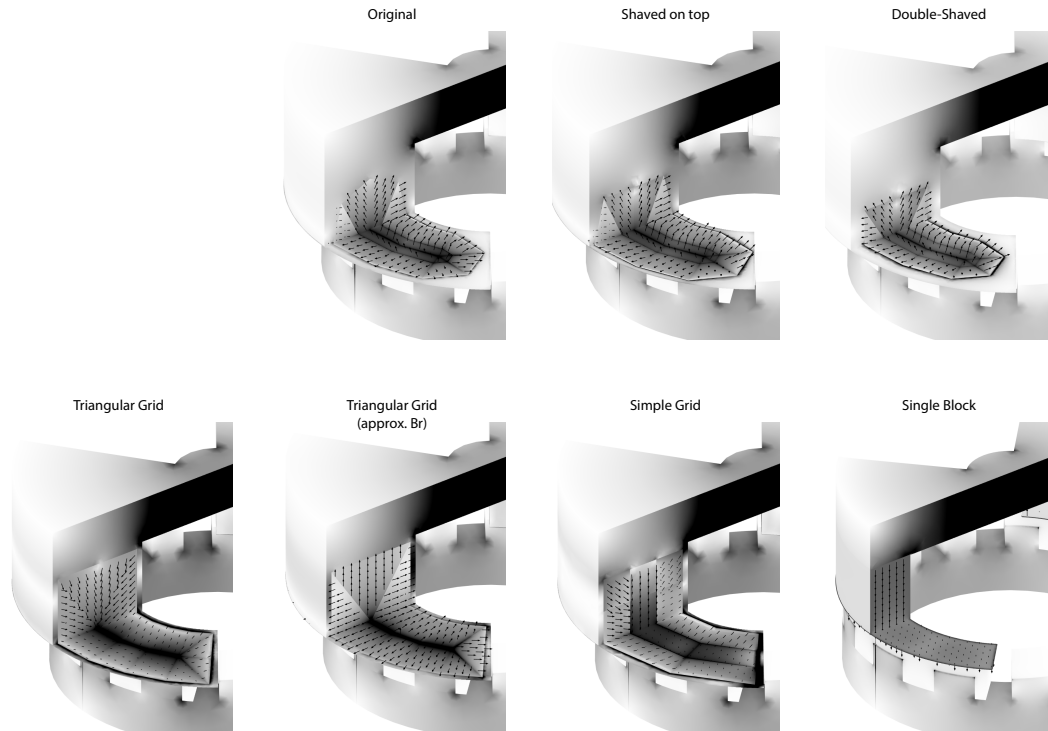


Fig. A.1: Illustration of different possible ways to segment the permanent magnet of the ENOVHEAT prototype, shown in figure 6.7b. These configurations are obtained by further simplifications of the original segmentation. The purpose of this analysis is to compare the performance of segmentations presenting less manufacturing challenges. The result of this study is shown in figures A.2 and A.3.

The configuration with a single block has a significantly lower performance. For the original segmentation, approximating the remanence vectors as explained above leads to a slightly higher \dot{q}_c than the original vectors. This is due to the fact that the optimisation have been performed with respect to the a linear objective functional. The “shaved on top” segmentation has almost exactly the same performance when the remanence vectors are not approximated. With the approximate remanence the performance decreases slightly, but the number of segments can be reduced. The “double-shaved” segmentation exhibits a good performance. However, with the original way of approximating the remanence, the performance decreases quite significantly. The new way of approximating the remanence, labelled as “Approx. B_r (2)”, is able to achieve almost the same performance of the original approximation. This option has been selected for the final design of ENOVHEAT prototype. In particular, the final configuration corresponds to the red diamond shown in figure A.3. The triangular grid and simple grid give a comparable result for what concerns $\langle B \rangle_{\text{High}}$. However, the other two parameters shown in the middle and bottom panels indicate a worst performance. The generally lower values with respect to the results shown in figure 6.26, are due to differences inherent to the design concept.

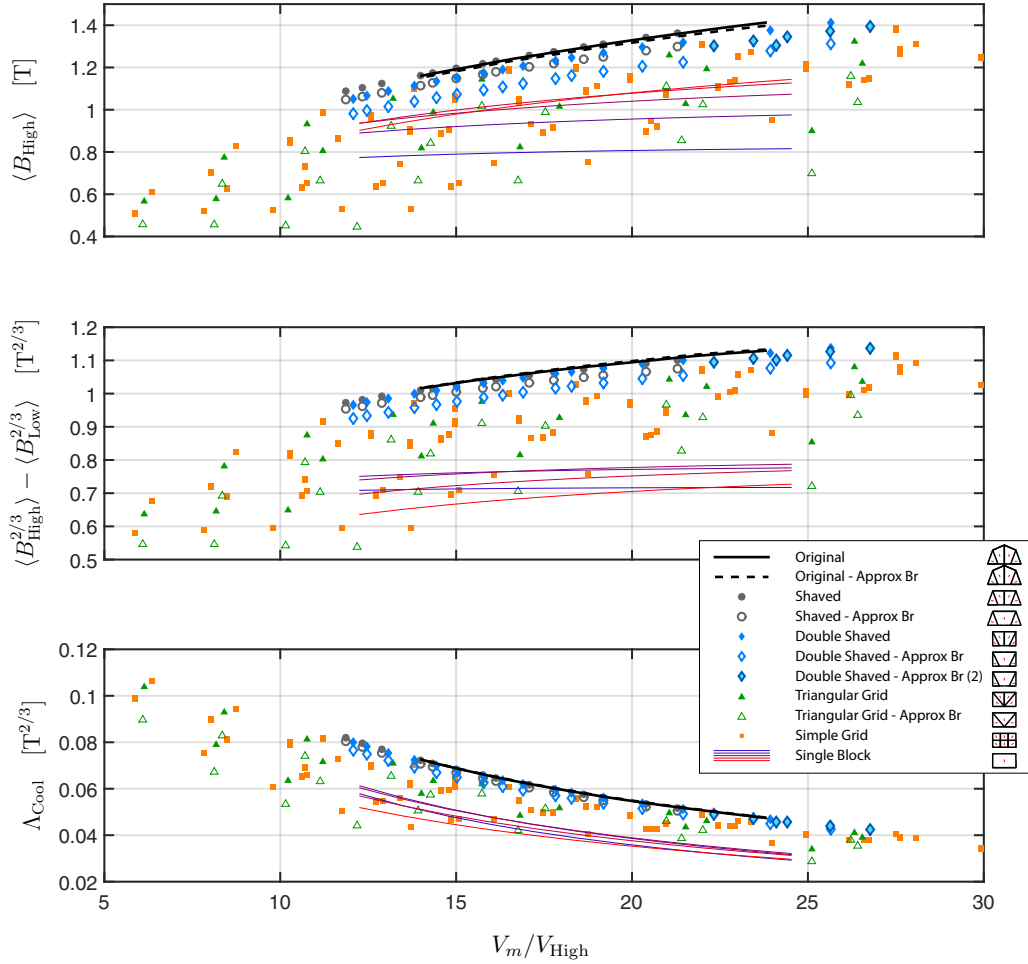


Fig. A.2: Comparison of the different segmentations plotted as function of the ratio between the magnet volume and the volume of the high field region. The top panel shows the norm of the flux density averaged over the high field region. The middle and bottom panels show respectively the parameters \dot{q}_c and Λ_{Cool} , introduced in section 6.4.6. These parameters are linked to the cooling power provided by the device. Figure A.3 shows a portion of these data, including the most relevant results.

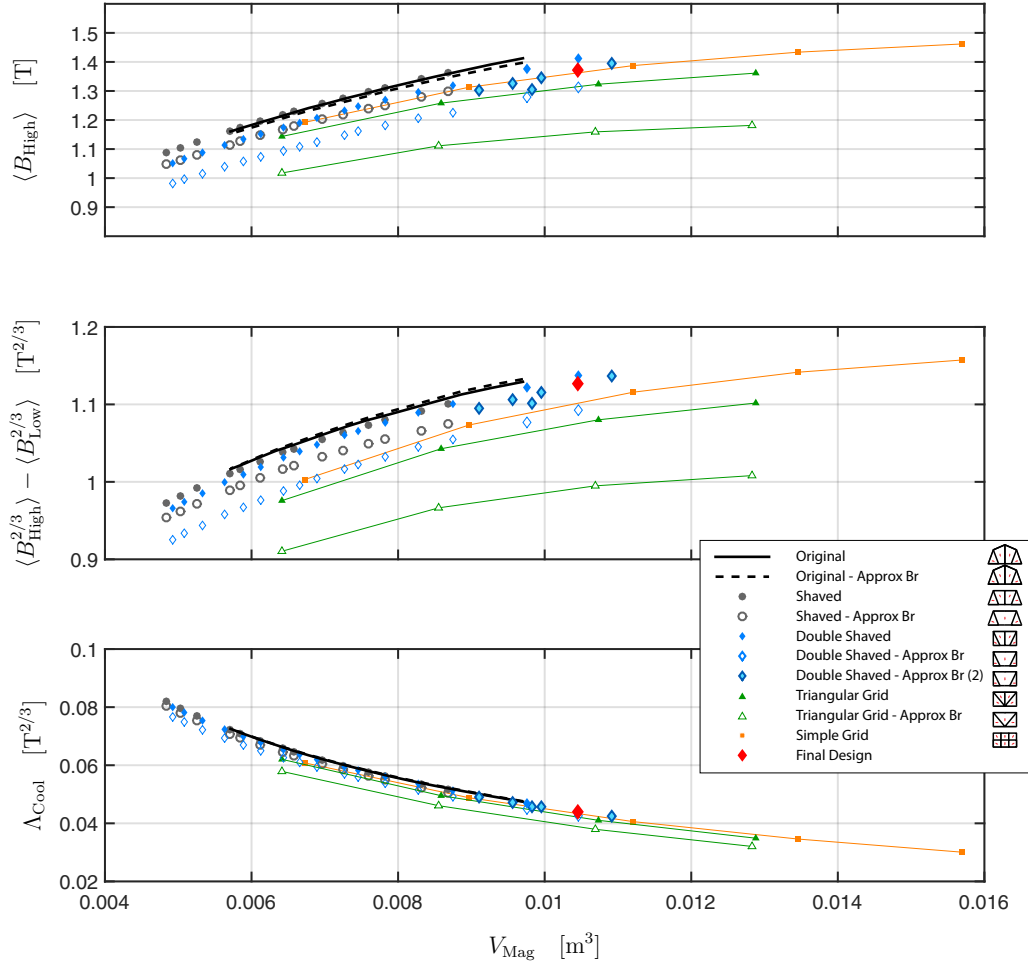


Fig. A.3: enlarged portion of the graphs shown in figure A.2. Only the most relevant segmentations are shown. The configuration indicated by the red diamond, belonging to the family labelled as “Double Shaved - Approx B_r (2)”, has been selected for the final design of the ENOVHEAT prototype. The geometry of this configuration is described in details in appendix A.2.

A.2 Final design

In this appendix the final design of the permanent magnet for the ENOVHEAT prototype is described in details.

The magnet is composed by two identical halves: the *left half* and the *right half*, as illustrated in figure A.4. The left half is obtained from the right half by reflecting it across the plane $x = 0$: the left half is on the side $x < 0$ and the right half on the side $x > 0$. Moreover, each half is symmetrical with respect to a reflection across the plane $y = 0$. The rotational axis of the device is the line $(x = 0, y = 0)$.

Each of the two halves is surrounded by iron on all sides, except for the bottom surface. All the lateral faces of the boundary between magnet and iron are vertical, and the top and bottom faces are horizontal. The external shape of each half is thus a prism oriented along the z axis, with irregular polygonal base.

In total the magnet is composed by 56 segments, selected among 6 different segment shapes. These unique shapes are labeled by the letters A, B, C, D, E, and F.

Each magnet half can be thought as being composed by different groups of segments, as illustrated in figure A.5: one *middle group* and two *side groups*.

The middle group is composed up by 4 identical slices, as illustrated in figure A.6: each of which is made from 4 segments: A, B, C and D. Thus there 4×2 copies of each of the shapes A, B,C and D, as indicated in table A.1.

Each side group is composed by 3 identical slices, each of which is made from 2 segments, as illustrated in figure A.7: E and F. Thus there are 3×4 copies of each of the shapes E and F, as indicated in table A.1.

The magnet segments are composed by Sintered Neodymium. The segments A,B,C,D and F are composed by the grade N50, while the segments E are composed by the grade **N50M**. The number of copies for each segment shape and the Neodymium grade are reported in table A.1. The labels of the different segments shapes are also indicated in figure A.8.

Segment Label	Number of copies	Neodymium Grade
Segment A	8	N50
Segment B	8	N50
Segment C	8	N50
Segment D	8	N50
Segment E	12	N50M
Segment F	12	N50

Table A.1: Segments numbers and grades.

The geometry of the magnet is completely determined by the 6 fundamental parameters reported in table A.2.

The axis of construction of the right half is translated with respect to the axis of rotation of the device, by a distance x_c in the negative x direction. The center of construction of the left half is translated symmetrically. This is illustrated in figure A.9, where this distance have been exaggerated for clarity.

The parametrization is illustrated in figure A.10. Each slice of the middle group of the

R_R	=	245.69	mm
R_I	=	20.80	mm
R_O	=	74.17	mm
z_{Top}	=	92.30	mm
x_C	=	5.57	mm
α_{Tot}	=	33.758346	deg

Table A.2: The 6 fundamental parameters.

right half spans an angle of $\alpha_{\text{Tot}}/2$ traced from the center of construction $x = -x_c$, $y = 0$, and symmetrically for the left half. Each slice of the side groups spans an angle of 60 deg. The height of each segment is given by z_{Top} . The other parameters affect the geometry as illustrated in the figure.

The magnetization vectors are indicated in figure A.10 as red arrows. The magnetization vector of the segments A, D, and E, is normal to the interface between these segments and the external iron. The z component of the magnetization is thus zero for these segments. The magnetization vector of the segments B, C, and F is parallel to their border with the segments A, D, and E, respectively. If the z component of the magnetization vectors of the segments B, C, and F is neglected, these vectors would have the same orientation as the adjacent segments A, D, and E, respectively.

The magnetization vectors of the left half have the opposite direction with respect to the symmetrical segment of the right half. In other words: the magnetization vectors of the right half are all pointing “inward”, and the vectors of the left half are pointing “outward”, as illustrated in figure A.10. Figure A.11 shows the top and side views of all the different segment shapes, each segment oriented along its axis of symmetry.

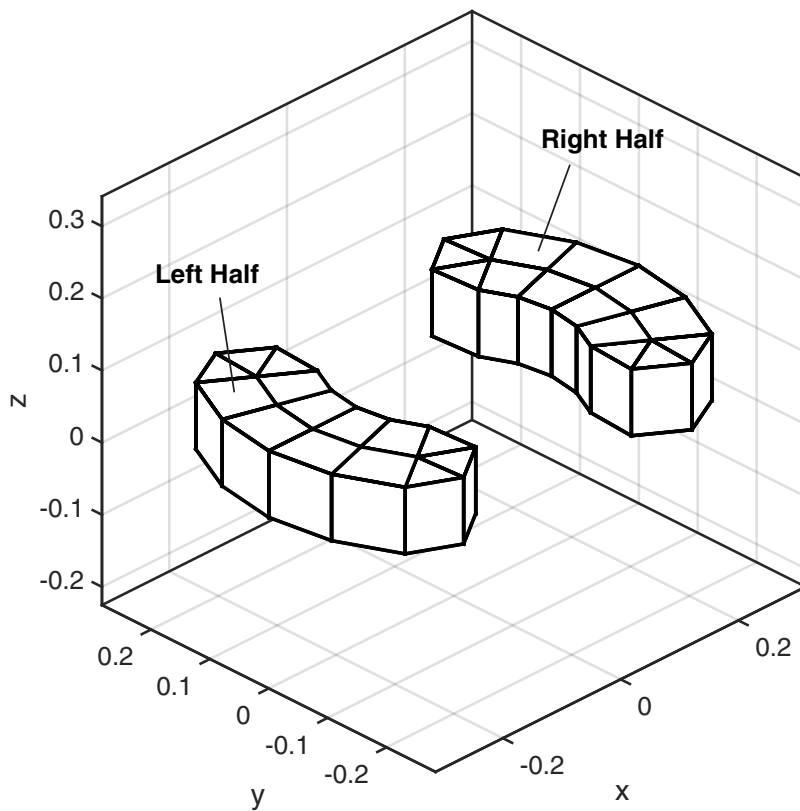
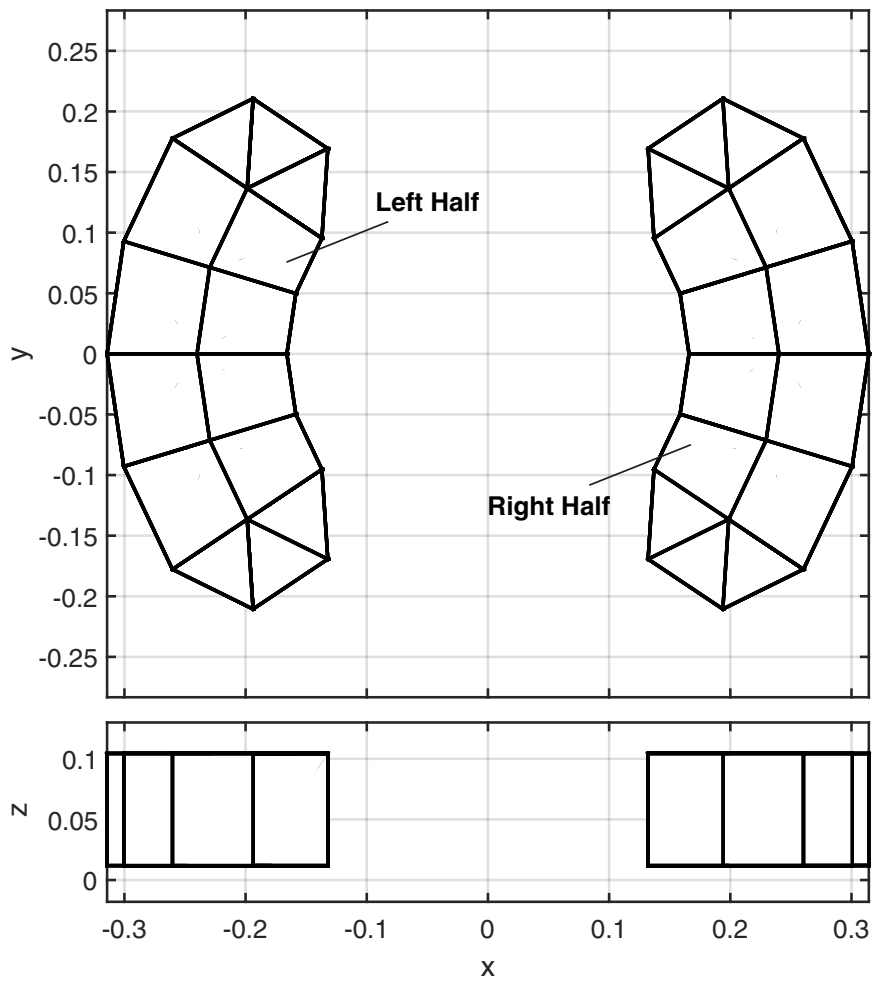


Fig. A.4: The two halves of the magnet.

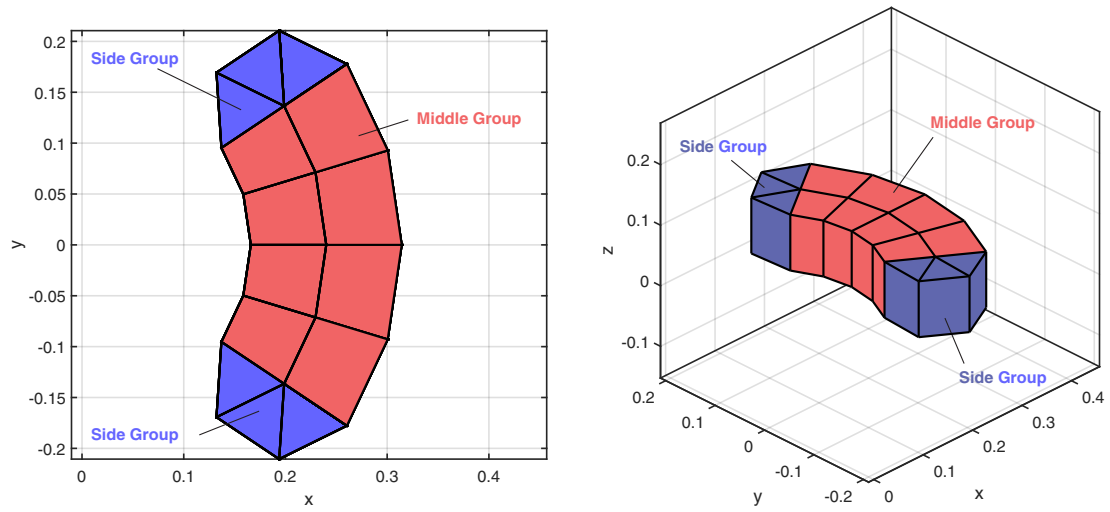


Fig. A.5: Middle and side groups of the right half.

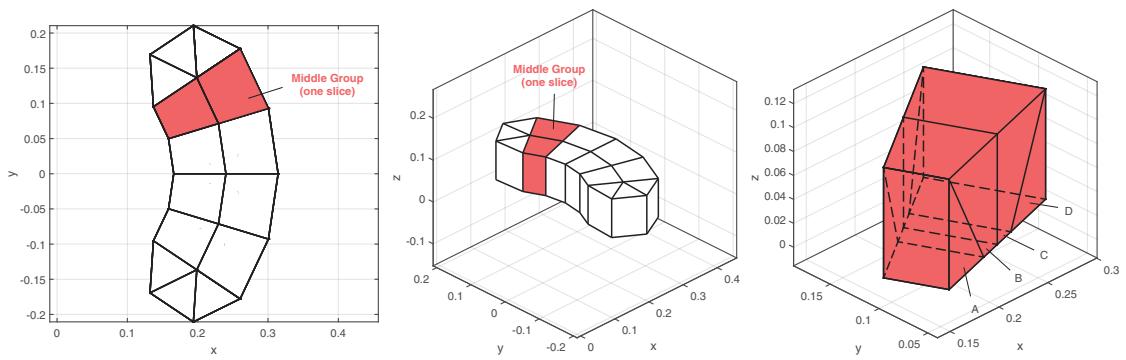


Fig. A.6: Middle group

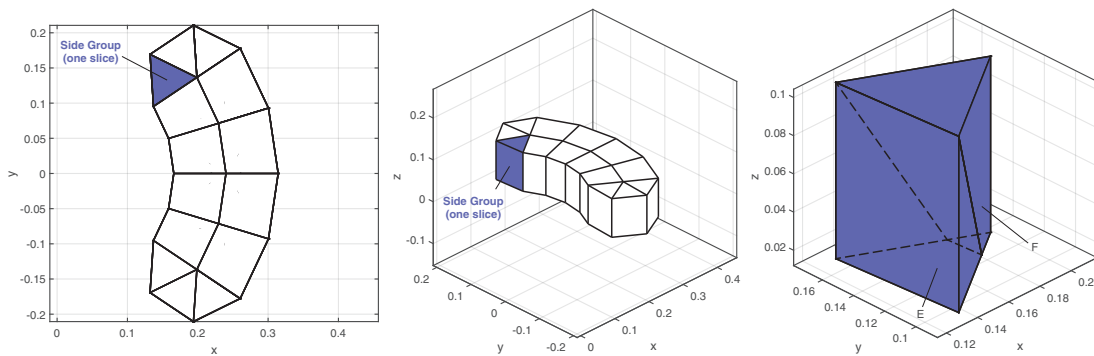


Fig. A.7: Side group

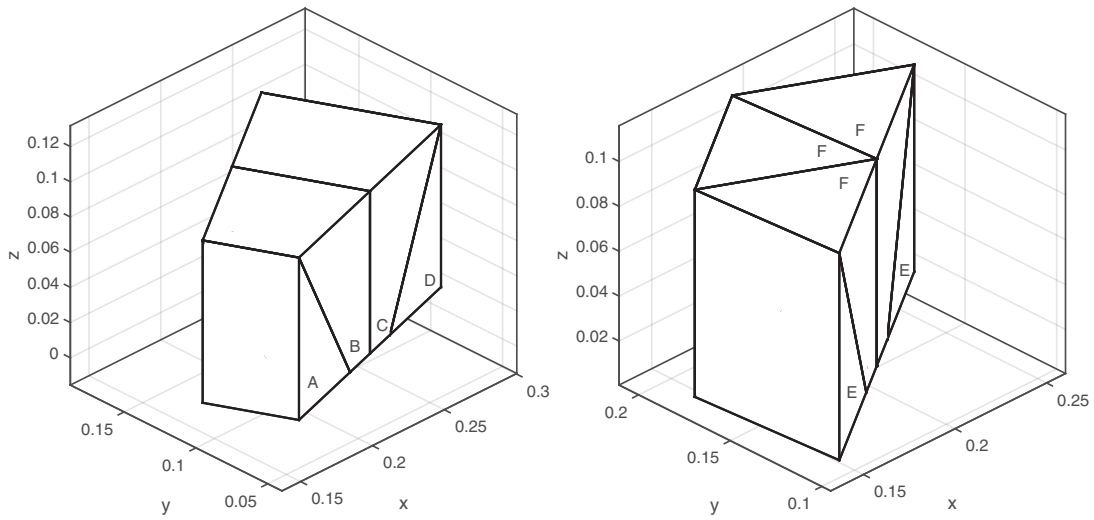


Fig. A.8: Segment labels.

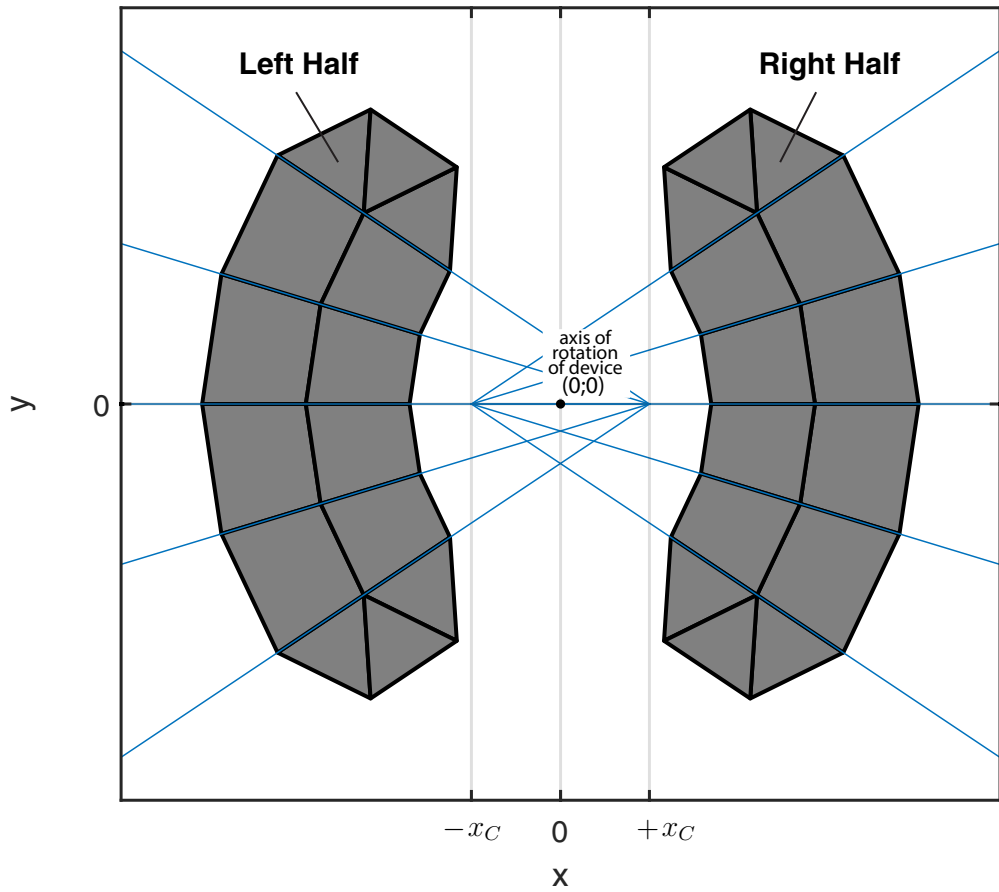


Fig. A.9: Centers of construction of each half.

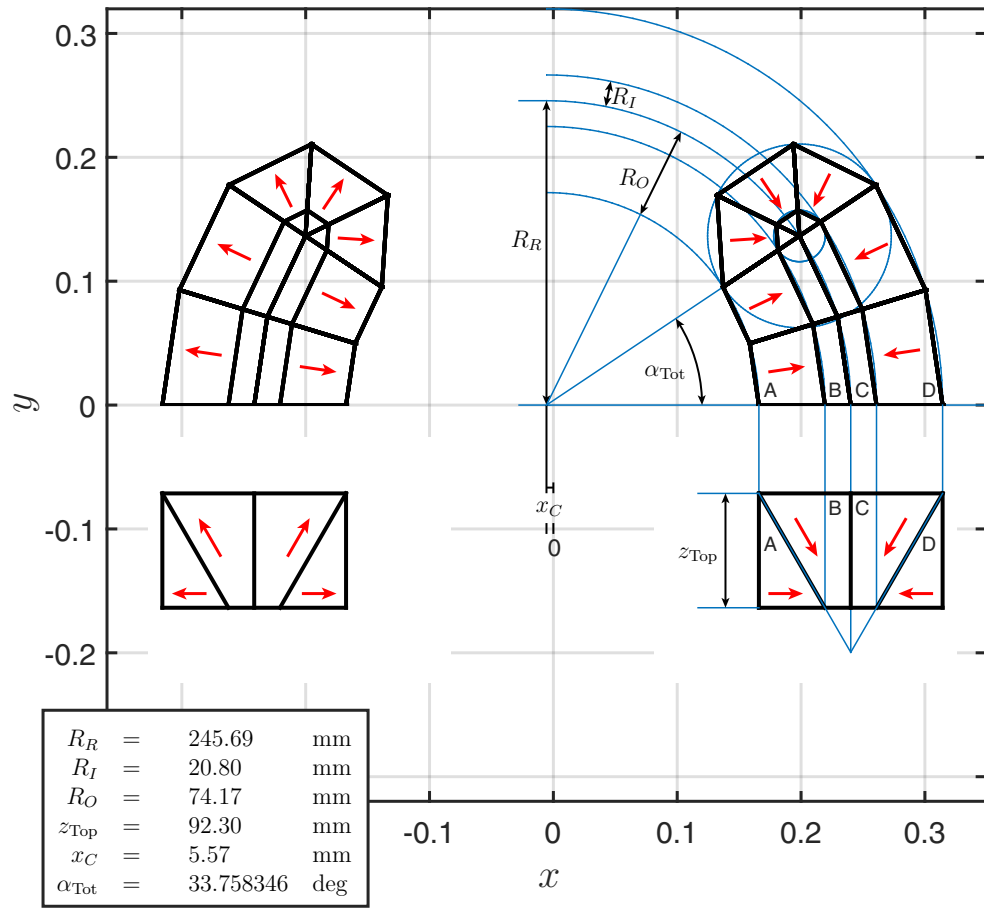


Fig. A.10: Geometry parametrization

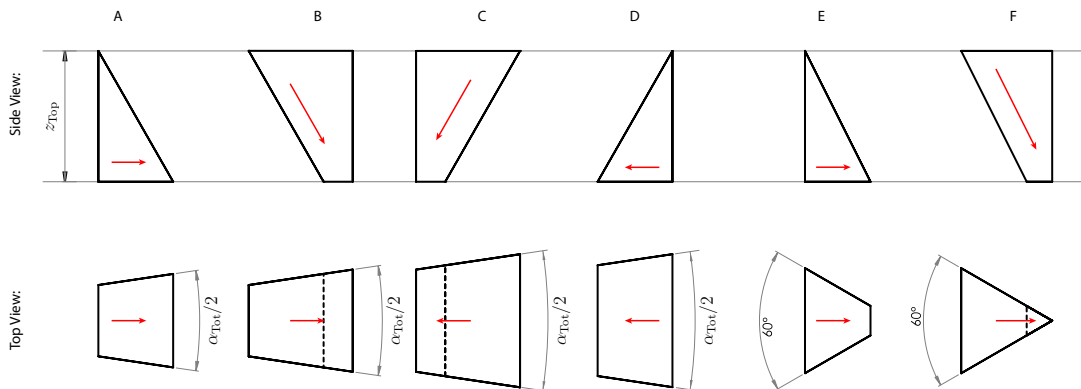


Fig. A.11: Individual segments projections.

APPENDIX B

Published or submitted papers

B.1 Design and experimental tests of a rotary active magnetic regenerator prototype

D. Eriksen, K. Engelbrecht, C. R. H. Bahl, R. Bjørk, K. K. Nielsen, A. R. Insinga and N. Pryds

International Journal of Refrigeration 58, 14-21, (2015).



ELSEVIER

Available online at www.sciencedirect.com

ScienceDirect

journal homepage: www.elsevier.com/locate/ijrefrig

Design and experimental tests of a rotary active magnetic regenerator prototype



CrossMark

D. Eriksen^{*}, K. Engelbrecht, C.R.H. Bahl, R. Bjørk, K.K. Nielsen,
A.R. Insinga, N. Pryds

Department of Energy Conversion and Storage, Technical University of Denmark, Frederiksborgvej 399,
4000 Roskilde, Denmark

ARTICLE INFO

Article history:

Received 6 January 2015

Received in revised form

29 April 2015

Accepted 10 May 2015

Available online 20 May 2015

Keywords:

Magnetic refrigeration

Design

Model

Efficiency

Experimental

ABSTRACT

A rotary active magnetic regenerator (AMR) prototype with efficiency and compact design as focus points has been designed and built. The main objective is to demonstrate improved efficiency for rotary devices by reducing heat leaks from the environment and parasitic mechanical work losses while optimizing the utilization of the magnetized volume. Heat transfer calculations combined with 1D AMR modeling have revealed the necessity for an insulating air gap between magnet and regenerator when designing for high efficiency. 2D finite difference AMR modeling capturing the interplay between heat transfer fluid flow and an inhomogeneous time-varying magnetic field in the individual regenerator beds has been used in the design process. For one operating point a COP of 3.1 at a temperature span of 10.2 K and a cooling power of 103 W were measured. Major issues limiting the performance have been identified and improvements are outlined for future work.

© 2015 Elsevier Ltd and IIR. All rights reserved.

Conception et essais expérimentaux d'un prototype de régénérateur rotatif magnétique actif

Mots clés : Froid magnétique ; Conception ; Modèle ; Efficacité ; Expérimentale

1. Introduction

Magnetic refrigeration is a promising alternative to conventional vapor compression technology. It is based on the magnetocaloric effect in ferromagnetic materials, hereafter referred to as magnetocaloric materials (MCM). As a consequence of this effect, the temperature of an MCM will, under adiabatic conditions, change as a response to a change in an

applied magnetic field, such that the temperature will increase when the field is increased and vice versa. The effect, which is most pronounced in the vicinity of the Curie temperature of the material, can be utilized in heating or cooling devices; see e.g. [Smith et al. \(2012\)](#). In 1982 Barclay demonstrated a cooling device based on a concept where the MCM itself was used to regenerate heat which was transported between a cold and a hot reservoir via a heat transfer fluid; see [Barclay, \(1982\)](#). Since then this principle, known as the active

^{*} Corresponding author.

E-mail address: daer@dtu.dk (D. Eriksen).
<http://dx.doi.org/10.1016/j.ijrefrig.2015.05.004>

0140-7007/© 2015 Elsevier Ltd and IIR. All rights reserved.

Nomenclature			
<i>Acronyms</i>			
AMR	active magnetic regenerator	m_s	mass of MCM in a bed (kg)
COP	coefficient of performance	\dot{Q}	cooling power (W)
GFRE	glass fiber reinforced epoxy	\dot{Q}_{Loss}	total heat loss (W)
HHEX	hot heat exchanger	T	temperature (K)
MCM	magnetocaloric material	T_C	cold side temperature (K)
		T_H	hot side temperature (K)
		T_∞	ambient temperature (K)
		ΔT	temperature span (K)
		\dot{V}	volumetric flow rate ($m^3 s^{-1}$)
<i>Symbols</i>		\dot{W}	work input (W)
B	magnetic flux density (T)	\dot{W}_{mag}	magnetic work (W)
c_f	fluid heat capacity ($J kg K^{-1}$)	\dot{W}_{pump}	pump work (W)
c_s	MCM heat capacity ($J kg K^{-1}$)	ϕ	utilization factor (–)
f	AMR operating frequency (Hz)		
m_f	mass of fluid flowing through a bed during one blow period (kg)		

magnetic regenerator (AMR) cycle, has been used in an increasing number of devices with the aim of making magnetic refrigeration near room temperature a competitive alternative to conventional vapor compression technology. For a more comprehensive description of the AMR cycle; see Engelbrecht et al. (2012). In general, magnetic refrigeration has the advantage of not using gaseous refrigerants. The absence of a compressor opens the possibility of silent operation. Furthermore, some of the losses associated with vapor compression are avoided, which may lead to a higher efficiency. Already in 1998, COPs above 6 were obtained at cooling powers exceeding 500 W, see Zimm et al. (1998). However, this device used a liquid helium cooled superconducting 5 T magnet and the power used for the magnet itself was not included in the COP calculation. Superconducting magnet AMRs are not economically viable with the present technology. Over the years, permanent magnets have been used in an increasing number of published devices; see e.g. Bjørk et al. (2010a) and it seems that devices based on rotary concepts with permanent magnets have a good potential for high performance; see e.g. Yu et al. (2010).

A design with a rotary magnet structure and regenerator with reciprocating flow provided by a displacer has produced high temperature spans, e.g. a temperature span of 29 K has been achieved by Tura and Rowe (2011). Recently, a temperature span of 33 K was demonstrated for an improved version of the same device; see Arnold et al. (2014). In other devices, a compartmentalized regenerator and a magnet system are mechanically rotated relative to each other. The flow system in these devices is of major importance. By applying valve systems to control the heat transfer fluid flow, it is possible to achieve a continuous flow circuit driven by a pump to transport heat to and from the regenerator while ensuring a reciprocating flow in the regenerator compartments; see eg. Tusek et al. (2010), Engelbrecht et al. (2012) and Jacobs et al. (2014). By carefully balancing magnetic forces and fluid flow, a smooth and efficient operation may be obtained. However, during each AMR cycle, the work performed on the regenerator is negative during magnetization and positive during demagnetization. In order to obtain efficient operation which is comparable to numerical AMR model predictions, the work performed by the regenerator during magnetization

has to be utilized. In a multi bed rotary AMR configuration, such as the one presented in this paper and the earlier device presented by Engelbrecht et al. (2012), this is done by always having beds moving into the magnetic field, thus contributing to the driving torque, while others are moving out. However, a poorly mechanically and magnetically balanced configuration will result in large torque fluctuations and drive train losses. How to achieve an optimum configuration in this regard is not well understood. With the presented device, an improved drivechain is realized by minimizing the thickness of the walls separating the regenerator beds in order to obtain a more even distribution of MCM and hence a more smooth driving torque. Furthermore, an odd number of regenerator beds are combined with a two pole magnet in order to avoid magnetic equilibrium positions during rotation.

Although much work has been conducted over the years to improve the efficiency of the devices, there are still significant technical challenges that need to be overcome. Recently, it was shown that care should be taken to reduce a number of parasitic losses associated with the overall COP of an AMR system; see Lozano et al. (2013). In this paper we report a compact new regenerator design, bringing these losses down. In the process, detailed numerical AMR modeling has been used as a design tool to address heat loss issues and the inhomogeneous magnetic field in regenerator compartments.

2. System design

The AMR device consisting of a regenerator, a magnet and a flow control system is shown in Fig. 1. For the device presented here, the MCM is confined in a cylindrical regenerator which is divided into eleven compartments. The regenerator is fixed on the outside of an iron core that is a part of the magnet system. The core consists of laminated plates of iron and glass fiber reinforced epoxy (GFRE) in order to minimize losses due to eddy currents and thermal conduction in the axial direction. On the upper and lower sides of the regenerator, valve arrangements ensure reciprocating flow of the heat transfer fluid in the regenerator compartments and a continuous, unidirectional flow in the external flow circuit. Special

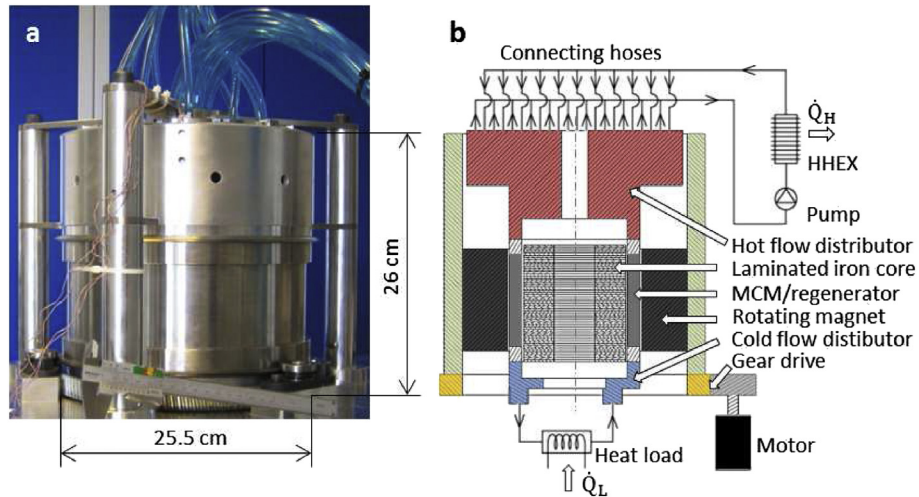


Fig. 1 – (a) Photo and overall dimensions of the AMR device. (b) Simplified cross section and diagram with external components.

care has been taken to reduce losses on the cold lower side of the regenerator. The outer magnet ring, which is the only rotating part of the device, is situated on the outside of the regenerator and mounted concentrically with the iron core. The structure is rotated at an AMR frequency which can be varied between zero to approximately 4 Hz. The rotating outer part not being mechanically connected to a central shaft enables simple connection between the flow distribution system mounted above the regenerator and the external flow circuit. On the hot top side of the device, hoses supply fluid in and out of 11 regenerator beds timed with the rotation of the magnet. The timing of the flow is ensured by poppet valves in the flow distributor. These valves are actuated by cam rings rotating along with the magnet. A detailed description of the flow system will be available in Eriksen et al. (2015). The excess heat in the hotter outgoing fluid is rejected in the hot heat exchanger (HHEX), before going back into the regenerator. On the cold side, the fluid goes through an electrical heater, simulating a heat load.

2.1. Magnet system

A cross section of the magnet, iron core and regenerator is shown in Fig. 2a. The magnet consists of a number of blocks of permanent NdFeB magnets, magnetized in the indicated directions. In combination with flux-conducting iron yokes and an iron core, the structure forms a Halbach-like array with two high field and two low field regions in the gap where the regenerator is situated. These regions will be swept over the regenerator as the magnet rotates.

The 12 pieces of permanent NdFeB magnet, grade N50, have a total volume of 1.5 L. The flux density in the gap between iron core and magnet was measured using a three-axis Hall probe (Arepoc s. r. o. AXIS-3) as a function of radius, length and azimuthal angle. There is a good agreement between modeled and measured flux density; see Fig. 2. However, modeling has also shown that a higher flux density may be obtained if the insulation between the iron discs in the core is reduced to a minimum. The calculations reveal a potential

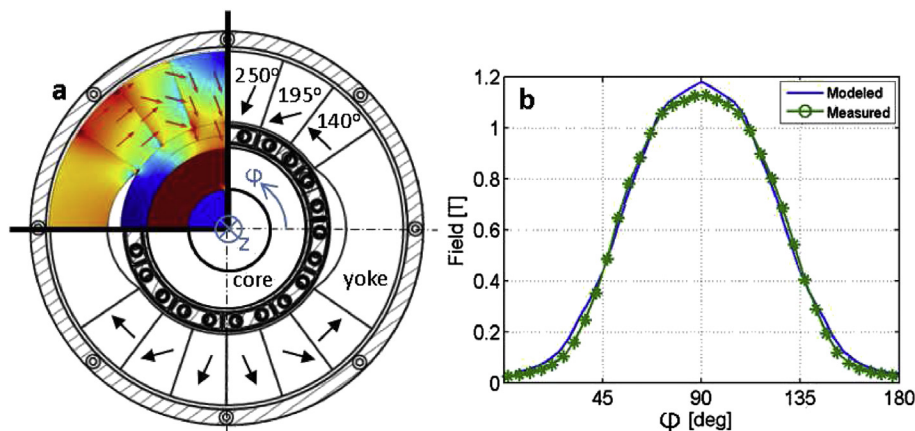


Fig. 2 – (a) Rotating magnet system consisting of 12 NdFeB blocks connected by iron yokes. In the middle: stationary iron core and regenerator in the gap. (b) Measured and modeled field.

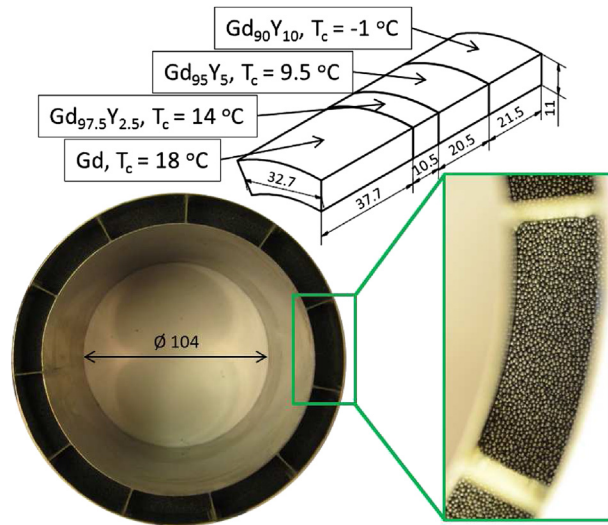


Fig. 3 – Regenerator divided into 11 compartments, filled with spheres of Gd and different compositions of $Gd_{100-x}Y_x$. The drawing shows the Curie temperature of each layer in a compartment. All sizes are in mm.

to increase the maximum flux density from the current 1.13 T–1.4 T. This is considered for future work.

2.2. Regenerator

A photograph showing the regenerator filled with spheres of Gd and three different compositions of $Gd_{100-x}Y_x$ from Santoku Corp. (Japan) is shown in Fig. 3. These materials are arranged such that they will operate near their respective Curie temperatures. The diameter of the spheres is between 500 μm and 600 μm for the Gd and between 300 μm and 500 μm for the $Gd_{100-x}Y_x$ compounds. As the magnitude of the magnetic flux density decreases near the ends of the 100 mm long magnet, only the central 90 mm is utilized as AMR. The total mass of MCM is 1.7 kg. The regenerator housing consists of two concentric non-magnetic stainless steel cylinders, grade 304, with a thickness of 0.5 mm. The walls separating the 11 regenerator beds are made from 0.5 mm thick GFRE plates. This material was chosen to avoid eddy currents while ensuring sufficient mechanical stability.

After packing the regenerator with MCM spheres, it was closed at the ends with PVC/PA parts with stainless steel wire mesh screens facing the MCM and holes for flow system connections. The dimensions of the housing material inside the magnet were minimized using the commercially available finite element software Comsol Multiphysics for strength calculations, taking expected temperature and pressure gradients into account. This was done to optimize the volume available for MCM in the magnetized volume. Furthermore, minimizing the thickness of the walls separating the regenerator compartments gives a more consistent magnetization of the regenerator and enables a smooth driving torque as the magnet is rotated.

3. Modeling used as design tool

This section describes the use of numerical modeling as a tool for addressing both heat losses and the effects of having an inhomogeneous magnetic field in the regenerator compartments. The modeling has been used for the design and dimensioning of the presented prototype. However, the issues addressed are inherent to the considered type of rotary devices.

The modeling is based on a 1D numerical AMR model solving coupled governing equations based on energy balances for the MCM and heat transfer fluid respectively. The model takes property data for these materials, given fluid flow and applied magnetic field as functions of time during the cycle and a given temperature span and cycle frequency as inputs. The main outputs are the hot and cold heat flows and the input power. The model was originally validated experimentally against an AMR prototype described by Zimm et al. (2006), see Engelbrecht (2008). The model that is used to capture spatial variations in magnetization in a regenerator bed solves the same governing equations in 2D as described below. This model was based on previous passive 2D porous bed regenerator modeling described in Nielsen et al. (2013).

3.1. Parasitic heat loss through regenerator housing

Special attention has been given to the heat leakage between the regenerator and the magnet/iron core as earlier work has identified this as an important issue limiting the system

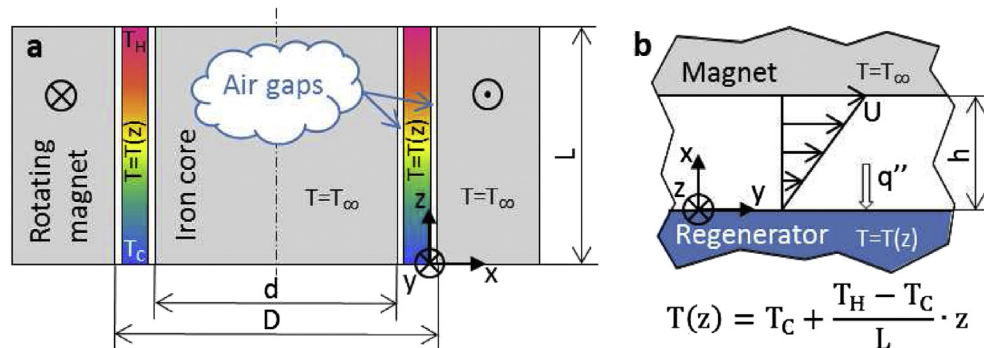


Fig. 4 – (a) Regenerator with temperature gradient situated between iron core and rotating outer magnet. (b) Air gap between regenerator and rotating magnet at a given z . Forced convection with linear velocity profile between 0 and U and heat flux, q'' , into the regenerator.

performance; see [Lozano et al. \(2013\)](#). The situation is illustrated in [Fig. 4](#). Between the regenerator housing and the rotating outer magnet is an air gap. The magnet, having a large thermal mass and good thermal transport properties, is considered to be at the ambient temperature, T_∞ , and the regenerator wall is considered to have a linear temperature gradient between T_C and T_H in the z -direction. The heat transfer through the regenerator housing due to both forced and natural convection has been considered. The rotation of the magnet will create a friction driven air flow in the gap, which is treated as a Couette flow; see e.g. [Incropera and DeWitt \(1996\)](#). This simple case of forced convection has an analytical solution revealing that the heat flux in the radial direction consists of only two terms: viscous dissipation in the air and conduction driven by the temperature difference between regenerator and magnet.

For the rotational speeds relevant for the present application, it is found that the viscous dissipation may be neglected. Furthermore, the natural convection was modeled with a simple finite element model made in Comsol Multiphysics. Based on this it has been concluded, that for an air gap of up to a few mm, the heat transfer is still dominated by conduction. Furthermore, the natural convection may be limited by physical barriers to the axial flow. Therefore, only the heat transfer by conduction is considered in the following, both for the gap between regenerator and rotating outer magnet and for the equally wide gap between gap between regenerator and iron core. Since the present device design was focused on efficiency, estimates of the influence of how the conduction based loss influences the COP have been made, based on the geometry shown in [Fig. 4](#), with $d = 100$ mm, $D = 132$ mm and $L = 90$ mm. It was assumed that the regenerator housing consisted of stainless steel with a thickness of 0.5 mm. For simplicity, it was assumed that the hot end of the regenerator was at the ambient temperature of 30°C and that the cold end was at 0°C . In this situation, all the heat flux is going into the regenerator from the magnet and the iron core, which was not considered to be laminated in this case. Then, the total heat flux into the inside and outside of the regenerator was integrated over its length, giving a total heat loss, \dot{Q}_{Loss} . The cooling power, \dot{Q} , produced by the device and the work input, \dot{W} , which consists of both magnetic work, \dot{W}_{mag} and pump work, \dot{W}_{pump} , i.e.

$$\dot{W} = \dot{W}_{\text{mag}} + \dot{W}_{\text{pump}}, \quad (1)$$

was calculated using the 1D numerical AMR model described above, see also [Engelbrecht and Bahl \(2010\)](#), assuming a varying flow rate and an AMR operational frequency of 0.75 Hz. The COP was then evaluated as:

$$\text{COP} = \frac{\dot{Q}}{\dot{W}}. \quad (2)$$

Next, as a rough estimate, the calculated loss was simply subtracted from the cooling power when calculating the COP with losses, COP_L :

$$\text{COP}_L = \frac{\dot{Q} - \dot{Q}_{\text{Loss}}}{\dot{W}}. \quad (3)$$

Results from these calculations are shown in [Fig. 5a](#), where the flow rate is increased from 4.2 L min^{-1} , corresponding to a utilization of $\phi = 0.4$, until the cooling power reaches zero. Here, the utilization is defined as

$$\phi = \frac{m_f c_f}{m_s c_s}, \quad (4)$$

where m_f is the mass of fluid flowing through a bed during a blow period, m_s is the mass of MCM in a bed and $c_f = 4200 \text{ J kg}^{-1} \text{ K}^{-1}$ and $c_s = 300 \text{ J kg}^{-1} \text{ K}^{-1}$ are the heat capacities of the fluid and MCM respectively. In each case, the cooling powers plotted in [Fig. 5a](#) reach their maximum values at approximately $\phi = 0.8$. It is clear that, without the loss term included, the regenerators with the smaller air gaps and hence higher masses perform better in most cases, both in terms of cooling power and COP. However, when the utilizations become low, higher COPs can be achieved with larger air gaps. This is considered to be an effect of smaller air gaps giving larger cross sectional areas, which leads to increased axial heat conduction losses. This is captured directly by the AMR model. The figure furthermore shows, that when the heat losses through the regenerator walls are included, the COPs of the smaller air gaps become significantly decreased. Therefore, when designing for high COP, it will be desirable to have a certain air gap, which in this case is larger than 1 mm, even though it slightly decreases the maximum cooling power. In [Fig. 5b](#) the COP is plotted as a function of the air gap for different

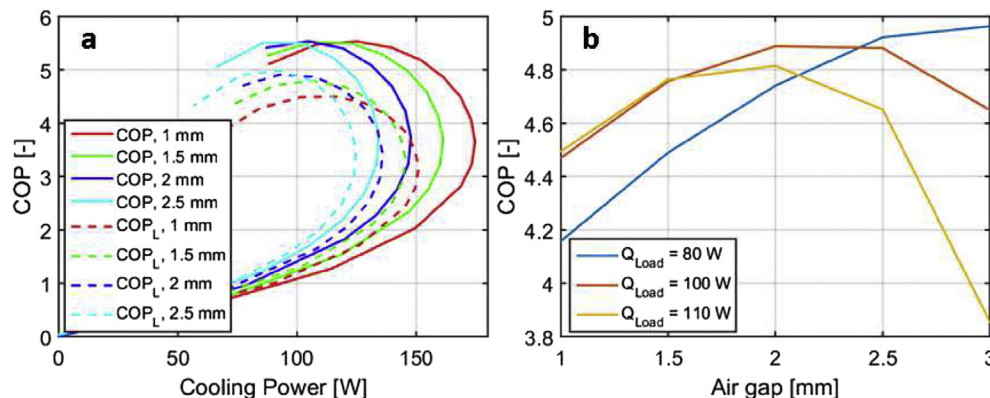


Fig. 5 – (a) Modeled COP and cooling power with varying flow rate. Different thicknesses of air gap, with and without losses included in the COP calculation. (b) Highest COP from the same data set at fixed cooling powers plotted as a function of air gap.

cooling powers. Based on these considerations, an air gap of 2 mm was chosen in the present case. Such a tradeoff between insulating air gap and the amount of MCM in the magnet is inherent to this type of rotary AMR devices. Having a clearance between rotating and stationary components furthermore has the advantage of reducing the demands for manufacturing tolerances.

3.2. Inhomogeneous magnetic field and 2D AMR modeling

The field in a regenerator bed is inhomogeneous, meaning that the MCM experiences an applied field that varies with the azimuthal direction. This makes it non-trivial to optimize the flow rate of the heat transfer fluid during the cycle because the entire bed experiences the same fluid flow rate. To address this issue, a finite difference AMR model, based on previous work by Nielsen et al. (2013), was developed that resolves the regenerator in both the z and ϕ directions indicated in Fig. 2. This 2D model has been used as a design tool to iterate between different combinations of magnet design, regenerator design and flow profile (flow rate versus rotation) design. In this process, different magnetic field profiles have been developed and investigated, using the iterative finite element based methodology described in Bjørk et al. (2010b, 2011). This has been done in combination with a variety of regenerator and flow profile designs modeled with the 2D AMR model. The investigated flow profiles are trapezoidal, meaning that they consist of full flow periods, no flow periods and linear ramps. This combined modeling approach has been used as a tool to design the present prototype and the methodology will be described in further detail in future works.

Once the inner and outer dimensions of the magnet and regenerator were fixed, the number of beds was varied in the 2D AMR model; see Fig. 6. It is a clear result that having more beds is desirable, although not from a practical standpoint because many beds require smaller dimensions, more valves and more intricate assembly. The number of beds was chosen to be eleven as a compromise in the present case. This number

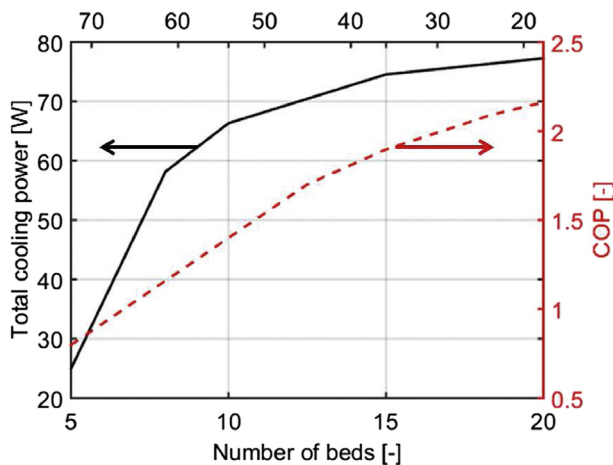


Fig. 6 – Cooling power and COP versus number of beds and resulting width of the individual regenerator compartments. The utilization is 0.4.

was also chosen not to be a multiple of the number of magnetic poles to improve mechanical efficiency.

4. Interfacing

Adjustable operational parameters and instrumental readings are handled by a dedicated LabView PC program, allowing the control of operational frequency and heater power. Data were acquired using a National Instruments system (cDAQ-971). The fluid flow rate is regulated manually by needle valves. The hot side temperature is controlled by a recirculating cooler (Julabo FL4003) connected to the hot counter flow heat exchanger. The inlet and outlet temperatures on the hot and cold sides of the regenerators are measured by type K thermocouples and the fluid flow rate is measured by a magnetic inductive flow sensor (Omega FMG71). Furthermore, a portable flow meter (Omega Microflow FTB322D) can be inserted on the connecting hoses indicated in Fig. 1 to measure the actual flow in any of the eleven regenerator beds.

5. Experimental results

AMR experiments have been conducted with the hot side temperature held constant around 18 °C. A series of experiments at an AMR frequency of 0.75 Hz and a fluid flow rate of 3 L min⁻¹ resulted in the cooling curve shown in Fig. 7. The indicated COP values are calculated according to Eqs. (1) and (2) with \dot{Q} being the power supplied to the heater providing the cooling load. \dot{W}_{mag} is taken as the power supplied to the motor and \dot{W}_{pump} is evaluated as the measured fluid flow rate times the total pressure drop over the regenerator. Thus, the efficiency of the pump itself is the only parameter which was not included in the COP. The current pump is over dimensioned in order to be able to cover a wide range of pressure drops and flow rates for experimental purposes. Demineralized water with 5% ethylene glycol based automotive antifreeze was used as heat transfer fluid. Measured as a fraction of the Carnot efficiency, the best result is obtained at a temperature span of 10.2 K at a cooling load of 102.8 W. In this case

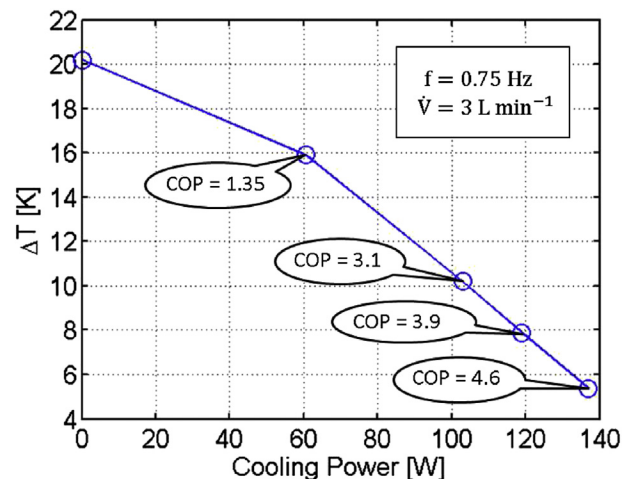


Fig. 7 – Cooling curve with corresponding COP values. The utilization was 0.3.

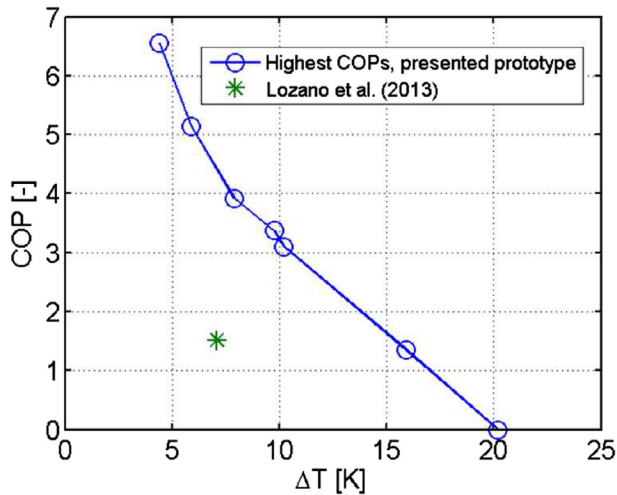


Fig. 8 – COP versus temperature span showing significant improvement compared to rotary prototype previously presented by DTU.

the COP of 3.1 is 11.3% of the Carnot Efficiency. The highest COP values obtained so far at different temperatures are plotted in Fig. 8, where a significant improvement compared to the first rotary DTU prototype is also shown, see Lozano et al. (2013). Beside the minimized parasitic losses, the driving torque fluctuations are greatly reduced, hence drive train losses are also reduced as described above. So far the device has only been operated at very modest conditions, especially in terms of flow rate and pressure drop, in order to avoid possible mechanical overloading of the regenerator.

The actual flow rates in some of the regenerator compartments have been measured as a function of magnet rotation angle using the portable flow meter. The result of such a measurement can be seen in Fig. 9, where also the expected flow profile is indicated together with the magnet profile. It is clear, that there is a significant discrepancy between the expected and measured flow rates, indicating that adjustments to the flow system are needed. Already, the system has shown

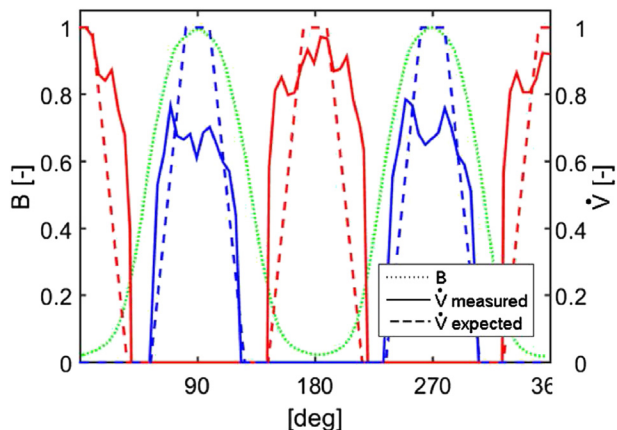


Fig. 9 – Normalized magnet and measured flow profiles in one of the eleven regenerator compartments. Red indicates hot to cold and blue indicates cold to hot blow. (For interpretation of the references to colour in this figure legend, the reader is referred to the web version of this article.)

strong responses to such adjustments. It is evident that, for the bed measured in this case, the total flow is less in the cold to hot direction than in the hot to cold direction. This is hypothesized by the authors to be due to the way different beds with somewhat different flow resistances are connected during operation. This flow balancing issue might also be an important factor limiting the achieved temperature spans, which are quite modest compared to what could be expected from the present staggered regenerator using materials with four different Curie temperatures as described in the introduction.

The potential for getting a higher magnetic field with a different iron core as mentioned above combined with adjustments to the flow system indicate a good potential for improved results in the future.

6. Conclusion

A rotary AMR prototype has been designed and built. The focus has been on enhanced performance in terms of efficiency and compact design at temperature spans and cooling powers relevant for commercial applications. During the design process, heat transfer calculations combined with 1D AMR modeling have revealed that there will be a trade-off between the amount of MCM and insulating air gap between magnet and regenerator in rotary prototypes when designing for high COP. Furthermore, 2D AMR modeling has proven to be an important tool for the design of AMR device configurations where the magnetic field varies as a function of rotation angle. Experimental results from the presented prototype have shown promising results, including a temperature span of 10.2 K at a cooling load of 103 W and a COP of 3.1. A potential for obtaining a higher magnetic field and the need for improving the balancing of heat transfer fluid flow have been identified and significant improvements of system performance are expected in the future.

Acknowledgments

The authors would like to acknowledge the technical support from A. Bijedic and J. Geyti. C. R. H. Bahl and A. R. Insinga acknowledge the ENOVHEAT project which is funded by Innovation Fund Denmark (contract no 12-132673).

REFERENCES

- Arnold, D.S., Tura, A., Ruebsaat-Trott, A., Rowe, A., 2014. Design improvements of permanent magnetic active magnetic refrigerator. *Int. J. Refrigeration* 37, 99–105.
- Barclay, J.A., 1982. Use of a ferrofluid as a heat exchange fluid in a magnetic refrigerator. *J. Appl. Phys.* 53, 2887–2894.
- Björk, R., Bahl, C.R.H., Smith, A., Pryds, N., 2010a. Review and comparison of magnet designs for magnetic refrigeration. *Int. J. Refrigeration* 33, 437–448.
- Björk, R., Bahl, C.R.H., Smith, A., Christensen, D.V., Pryds, N., 2010b. An optimized magnet for magnetic refrigeration. *J. Magn. Magn. Mater.* 232, 3324–3328.

- Björk, R., Bahl, C.R.H., Smith, A., Pryds, N., 2011. Improving magnet designs with high and low field regions. *IEEE Trans. Magn.* 47, 1687–1692.
- Engelbrecht, K., 2008. A Numerical Model of an Active Magnetic Regenerator Refrigerator with Experimental Validation (PhD thesis). University of Wisconsin Madison.
- Engelbrecht, K., Bahl, C., 2010. Evaluating the effect of magnetocaloric properties on magnetic refrigeration performance. *J. Appl. Phys.* 108, 123918.
- Engelbrecht, K., Eriksen, D., Bahl, C.R.H., Björk, R., Geyti, J., Lozano, J.A., Nielsen, K.K., Saxild, F., Smith, A., Pryds, N., 2012. Experimental results for a novel rotary active magnetic regenerator. *Int. J. Refrigeration* 35, 1498–1505.
- Eriksen, D., Engelbrecht, K., Bahl, C. R. H., 2015. An active magnetic regenerator device. European Patent Application 14154015.3.
- Incropera, F.P., DeWitt, D.P., 1996. *Introduction to Heat Transfer*. John Wiley & Sons, ISBN 0-471-30458-1.
- Jacobs, S., Auringer, J., Boeder, A., Chell, J., Komorowski, L., Leonard, J., Russek, S., Zimm, C., 2014. The performance of a large-scale rotary magnetic refrigerator. *Int. J. Refrigeration* 37, 84–91.
- Lozano, J.A., Engelbrecht, K., Bahl, C.R.H., Nielsen, K.K., Eriksen, D., Olsen, U.L., Barbosa Jr., J.R., Smith, A., Prata, T., Pryds, N., 2013. Performance analysis of a rotary active magnetic refrigerator. *Appl. Energy* 111, 669–680.
- Nielsen, K.K., Nellis, G.F., Klein, S.A., 2013. Numerical modeling of the impact of regenerator housing on the determination of Nusselt numbers. *Int. J. Heat. Mass Transf.* 65, 552–560.
- Smith, A., Bahl, C.R.H., Björk, R., Engelbrecht, K., Nielsen, K.K., Pryds, N., 2012. Materials challenges for high performance magnetocaloric refrigeration devices. *Adv. Energy Mater.* 2, 1288–1318.
- Tura, A., Rowe, A., 2011. Permanent magnet magnetic refrigerator design and experimental characterization. *Int. J. Refrigeration* 34, 628–639.
- Tusek, J., Zupan, S., Sarlah, A., Prebil, I., Poredos, A., 2010. Development of a rotary magnetic refrigerator. *Int. J. Refrigeration* 33, 294–300.
- Yu, B., Liu, M., Egolf, P.W., Kitanovski, A., 2010. A review of magnetic refrigerator and heat pump prototypes built before the year 2010. *Int. J. Refrigeration* 33, 1029–1060.
- Zimm, C., Jastrab, A., Sternberg, V., Pecharsky, V., Gschneidner Jr., K., Osborne, M., Anderson, I., 1998. Description and performance of a near room temperature magnetic refrigerator. *Adv. Cryog. Eng.* 43, 1759–1766.
- Zimm, C., Boeder, A., Chell, J., Sternberg, A., Fujita, A., Fujieda, S., Fukamichi, K., 2006. Design and performance of a permanent magnet rotary refrigerator. *Int. J. Refrigeration* 29 (8), 1302–1306.

B.2 Performance of Halbach magnet arrays with finite coercivity

A. R. Insinga, C. R. H. Bahl, R. Bjørk and A. Smith

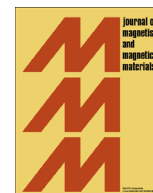
Journal of Magnetism and Magnetic Materials 407, 369-376, (2016).



ELSEVIER

Contents lists available at ScienceDirect

Journal of Magnetism and Magnetic Materials

journal homepage: www.elsevier.com/locate/jmmm

Performance of Halbach magnet arrays with finite coercivity



A.R. Insinga*, C.R.H. Bahl, R. Bjørk, A. Smith

Department of Energy Conversion and Storage, Technical University of Denmark – DTU, Frederiksborgvej 399, DK-4000 Roskilde, Denmark

ARTICLE INFO

Article history:

Received 7 May 2015

Received in revised form

11 December 2015

Accepted 23 January 2016

Available online 2 February 2016

Keywords:

Halbach cylinders

Magnetic field

Permanent magnet flux sources

Coercivity

ABSTRACT

A numerical method to study the effect of finite coercivity on the Halbach cylinder geometry is presented. Despite the fact that the analytical solution available for this geometry does not set any limit to the maximum air gap flux density achievable, in real life the non-linear response of the magnetic material and the fact that the coercivity is not infinite will limit the attainable field. The presented method is able to predict when and where demagnetization will occur, and these predictions are compared with the analytical solution for the case of infinite coercivity. However, the approach presented here also allows quantification of the decrease in flux density and homogeneity for a partially demagnetized magnet. Moreover, the problem of how to realize a Halbach cylinder geometry using a mix of materials with different coercivities without altering the overall performance is addressed. Being based on a numerical approach, the presented method can be employed to analyze the demagnetization effects due to coercivity for any geometry, even when the analytical solution is not available.

© 2016 Elsevier B.V. All rights reserved.

1. Introduction

The generation of high magnetic fields is a problem which is relevant for many technological and scientific areas. Until the 1960s, the highest magnetic field obtainable from permanent magnet sources was extremely limited. Two breakthrough discoveries drastically changed this scenario.

The first was the discovery of a new family of permanent magnet materials based on rare earth elements. The development of this class of magnetic materials started in the 1960s and is still a field of intense research. Among rare earth magnets, the most frequently encountered are samarium cobalt and neodymium iron boron (NdFeB) magnets, which can reach remanent flux densities as high as 1.48 T [1,2].

The second breakthrough was the invention in 1973 of a novel geometric arrangement of permanent magnet blocks [3], with many desirable characteristics. This arrangement, later known as the Halbach cylinder [4], is able to produce a homogeneous magnetic flux density over an arbitrarily large cylindrical air gap region. The norm of the flux density generated inside the air gap can exceed the value of the remanence and, if enough magnetic material is used, there is no theoretical limit to the maximum field achievable with this geometry. Finally, the magnetic system is perfectly self-insulated, i.e. the magnetic flux lines cannot escape from the external surface of the magnet.

With these new powerful tools available, the range of applications of permanent magnets has extended to fields which were traditionally the exclusive domains of electromagnets. Variations of Halbach-type designs have been used in NMR spectroscopy [5–7], cyclotrons [8], electric motors and actuators [9], generators [9], magnetic levitation [9], magnetic refrigeration [10,11] and many other industrial and scientific applications [9]. At the same time, the quest for generating high fields with permanent magnet flux sources has attracted more and more attention in the scientific community [12,13]. Since assuming infinite coercivity sets no limit to the highest magnetic field obtainable with the Halbach configuration, this problem may look trivial.

However, in real life the field is limited by the coercivity of the magnetic material used to realize the geometry [10]. If the demagnetizing field becomes too large, the magnetization can be locally reversed and the structure may not be able to generate the field predicted by the theory [12]. This effect is mainly due to the non-linear behaviour of the magnetic material for too strong demagnetizing fields. To avoid this problem, magnetic systems designers aiming at creating high magnetic fields must use special design precautions [12], and carefully select materials with high coercivities [13].

Even so, it is not possible to go above a certain limit without demagnetizing the material and it is worth investigating this problem systematically. The questions of *when* this phenomenon is going to occur for the Halbach geometry, and *where* in the system geometry it is expected to happen first, have been answered using an analytical approach [14]. Since the analytical

* Corresponding author.

E-mail address: aroin@dtu.dk (A.R. Insinga).

solution is only available for the linear response of the material, it is not possible to use the analytical techniques to predict *what* will happen when the material is demagnetized, that is: when the linear model fails to describe the magnetic material properly.

In this work, we employ a numerical technique based on finite element simulations to simulate the non-linear response of the material and quantify the decrease in the performance for a partially demagnetized magnet. The results are compared with the results of the analytical predictions given in ref. [14]. We also analyse the limitations of readily available magnetic materials using the properties of these as given by the manufacturers. Moreover, we describe a method to realize the Halbach cylinder geometry using a mix of different magnetic materials, in a way that the performance will not decrease. As the materials with higher coercivity are usually also the most expensive, a technique that only uses them in the parts of the geometry where they are really needed may considerably reduce the cost of the Halbach system. Work on identifying new hard magnetic materials with different coercivities is ongoing [15].

2. Methods

In the modeling of NdFeB magnetic assemblies it is common [4,14,16] to approximate the B – H curve of the magnet with a linear relation with respect to the $H=0$ point:

$$\mathbf{B} = \mu_0 \mu_r \mathbf{H} + \mathbf{B}_{\text{rem}} \tag{1}$$

This relation also assumes that the magnetization dynamics is independent in each spatial direction and reduces to $B_{\perp} = \mu_0 \mu_r H_{\perp}$ in directions perpendicular to the easy axis of magnetization.

Real magnetic materials are characterized by a more complex B – H relation and in some cases the difference with respect to the linear approximation may play an important role.

2.1. Geometry

We consider the relevant case of the Halbach cylinder, designed to create a homogeneous field inside its inner bore. The geometry is described by the following remanence field [16], expressed in

polar coordinates r and ϕ :

$$\mathbf{B}_{\text{rem}}(r, \phi) = B_{\text{rem}} \cos(\phi) \hat{\mathbf{e}}_r + B_{\text{rem}} \sin(\phi) \hat{\mathbf{e}}_{\phi} \tag{2}$$

where $\hat{\mathbf{e}}_r$ and $\hat{\mathbf{e}}_{\phi}$ denote the radial and tangential unit vectors in a given point, respectively.

As is common in the literature, the z direction will not be considered: this corresponds to considering a cylinder of infinite length. This approximation is justified for the calculation of \mathbf{H} and \mathbf{B} as long as the length is much greater than the external radius R_O , i.e. as long as the end effects are negligible [7,17,18].

The remanence is therefore a vector field of constant norm equal to B_{rem} ; the corresponding unit vector will be denoted by $\hat{\mathbf{e}}_{\parallel} = \cos(\phi) \hat{\mathbf{e}}_r + \sin(\phi) \hat{\mathbf{e}}_{\phi}$, and the components \mathbf{B} and \mathbf{H} along this direction will be denoted by B_{\parallel} and H_{\parallel} , respectively. The unit vector in the direction normal to the remanence and to $\hat{\mathbf{e}}_z$ is denoted by $\hat{\mathbf{e}}_{\perp} = \sin(\phi) \hat{\mathbf{e}}_r - \cos(\phi) \hat{\mathbf{e}}_{\phi}$. This is illustrated in Fig. 1a.

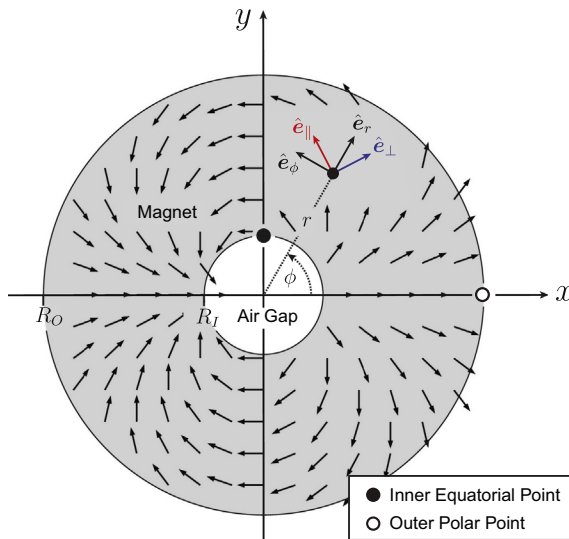
This geometry can be analytically solved [16] and the uniform flux density inside the air gap is given by:

$$\mathbf{B}^{(\text{Theory})} = \left(\frac{\mu_r - 1}{\mu_r + 1} R_O^2 - \frac{\mu_r + 1}{\mu_r - 1} R_I^2 \right)^{-1} \left(\frac{\mu_r + 1}{\mu_r - 1} - 1 \right) R_I^2 B_{\text{rem}} \log \left(\frac{R_I}{R_O} \right) \hat{\mathbf{e}}_x \tag{3}$$

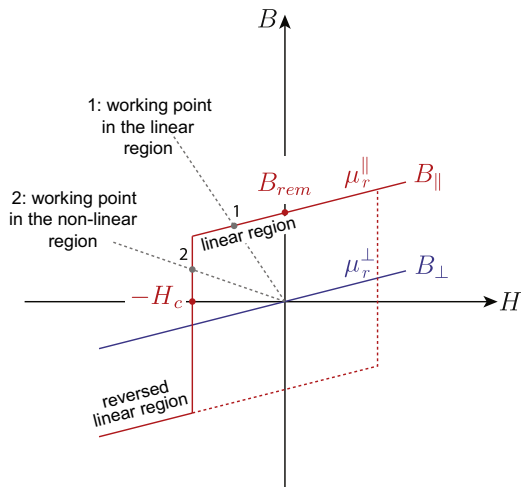
where R_O and R_I are the external and internal radii of the cylinder, $\hat{\mathbf{e}}_x$ is the unit vector in the x direction, and μ_r is the relative permeability of the material. For the case $\mu_r = 1$ the expression reduces to the well-known Halbach equation:

$$\mathbf{B}^{(\text{Theory})} = B_{\text{rem}} \log \left(\frac{R_O}{R_I} \right) \hat{\mathbf{e}}_x \tag{4}$$

These relations imply that, with a sufficiently large R_O/R_I ratio, it is possible to obtain an arbitrarily large field. In reality, however, the fact that all magnets have a finite coercivity results in a lower value of flux density for large R_O/R_I values. If the external radius is much larger than the internal radius, the magnetic material is not able to perform as predicted by the linear B – H relation in some critical regions of the magnet. The effect is that the direction of magnetization is reversed, creating an alternative path for the flux density that does not pass through the air gap. This effect will result in a reduction of the air gap flux density with respect to the theoretical prediction. Another negative effect is a decrease in the homogeneity of the field in the bore.



(a) Halbach Cylinder Geometry



(b) B – H curve and working points

Fig. 1. (1a) Illustration of the Halbach cylinder geometry: the remanence is plotted as black arrows. The unit vectors $\hat{\mathbf{e}}_r$, $\hat{\mathbf{e}}_{\phi}$, $\hat{\mathbf{e}}_{\parallel}$ and $\hat{\mathbf{e}}_{\perp}$ are shown for a particular point. (1b): Illustration of the B – H curve and the different categories of working points.

2.2. Parameterization of B–H curve

To investigate these effects we performed a numerical simulation with the finite element method using the commercial softwares Comsol Multiphysics [19] and Matlab [20]. A Comsol model has been run with a B–H relation which also includes the effect of finite coercivity H_c .

Following a similar procedure to the one described in ref. [21], the B–H relation is split into a relation for the direction perpendicular to the remanence vector, and a relation for the direction parallel to the remanence vector; the parallel B–H relation is assumed to be non-linear.

The B_{\parallel} – H_{\parallel} relation in the direction parallel to the remanence vector \mathbf{B}_{rem} , is modelled with a piecewise linear function, parametrized by the values of the coercivity H_c , the relative permeability μ_r^{\parallel} and the remanence B_{rem} . The piecewise relation is schematically illustrated in Fig. 1b together with some example load lines and the corresponding working points [11]. The relation is expressed by the following equation:

$$\begin{cases} B_{\parallel} = \mu_0 \mu_r^{\parallel} H_{\parallel} + B_{\text{rem}} & \text{for } H_{\parallel} > -H_c \quad (\text{linear region}) \\ B_{\parallel} = \mu_0 \mu_r^{\parallel} H_{\parallel} - B_{\text{rem}} & \text{for } H_{\parallel} < -H_c \quad (\text{reversed linear region}) \end{cases} \quad (5)$$

The two regions are connected by the vertical line segment $H_{\parallel} = -H_c$. As all hard magnetic materials exhibit a B–H curve with a very steep slope around the knee point [1,22], this piecewise relation is a good approximation. In the direction perpendicular to the remanence, the relation remains linear $B_{\perp} = \mu_0 \mu_r^{\perp} H_{\perp}$, but with a permeability μ_r^{\perp} which may be different from μ_r^{\parallel} . The assumption of linear behavior in the perpendicular direction holds as long as the corresponding magnetic field component H_{\perp} remains below the anisotropy field of the material [23].

We simulated only a particular choice of internal radius, R_i , and remanence, B_{rem} . The results are then extended to more general cases by considering the scaling of the solution. For this reason the results will be shown as function of the ratio R_o/R_i and of the quantity $\mu_0 H_c/B_{\text{rem}}$.

2.3. Demagnetization conditions

As explained in ref. [14], it is possible to start from the linear B–H relation of Eq. (1) and use the analytical solution of \mathbf{H} in any point of the magnet to predict if the material will be demagnetized in some regions of the geometry. The analytical solution is reported in ref. [16].

Demagnetization occurs in a point when the linear B_{\parallel} – H_{\parallel} relation is not a good approximation; this can be expressed by the condition $H_{\parallel} \leq -H_c$. We included the case $H_{\parallel} = -H_c$ because in this case, using the piecewise relation with a vertical line segment for $H_{\parallel} = -H_c$ would result in a working point in the non-linear region of the curve, as the one labeled by 2 in Fig. 1b.

There are two points in the magnet geometry in which the demagnetization will occur first; if demagnetization is not occurring in any of these points, then it is not occurring in any other point of the magnet. The first point is the inner equatorial point ($r = R_i$, $\phi = \pi/2$), indicated in Fig. 1a as a black circle. The second point is the outer polar point ($r = R_o$, $\phi = 0$), indicated in Fig. 1a as a white circle. There are two independent conditions for demagnetization to occur at these points; for the case $\mu_r = 1$, the conditions are expressed by the following inequalities for H_c :

$$\text{Equatorial demagnetization: } \mu_0 H_c \leq B_{\text{rem}} \log\left(\frac{R_o}{R_i}\right) \quad (6)$$

$$\text{Polar demagnetization: } \mu_0 H_c \leq B_{\text{rem}} \quad (7)$$

It can be noticed that the condition for equatorial demagnetization involves B_{rem} and the ratio between R_o and R_i , while the

condition for polar demagnetization only involves B_{rem} . The two equations can be directly derived from the boundary conditions from \mathbf{H} and \mathbf{B} at the border between two different materials. For the inner equatorial point the component of \mathbf{H} which is parallel to the border of the internal cylinder is conserved across the interface. For the outer polar point the component of \mathbf{B} which is normal to the border of the external cylinder is conserved across the interface. In both cases the conserved component is parallel to the remanence. At the inner equatorial point the value of H_{\parallel} is then equal to $-(B_{\text{rem}}/\mu_0) \log(R_o/R_i)$. At the outer polar point the value of B_{\parallel} is equal to 0. These values of H_{\parallel} and B_{\parallel} lead to the conditions of Eqs. (6) and (7).

The same procedure can be generalized to a general value of relative permeability μ_r , starting from the analytical expression of H_{\parallel} inside the magnet and applying the equation $H_{\parallel} \leq -H_c$ in the two critical points. The conditions cannot be written in closed form for H_c , but it is possible to solve the equations numerically and the results are shown in Fig. 2. Fig. 2a corresponds to the condition for equatorial demagnetization and Fig. 2b to the condition for polar demagnetization. It can be noticed how, as $\mu_r \rightarrow 1$, Fig. 2b indicates the condition $\mu_0 H_c/B_{\text{rem}} \rightarrow 1$, which is independent of R_o/R_i , consistent with Eq. (7). As μ_r increases from 1, the condition for polar demagnetization exhibits a small dependence on R_o/R_i .

These demagnetization conditions will be used in the present paper to compare with the results of the finite element method simulations with a piecewise linear B–H curve.

3. Results

3.1. Realistic magnets

In this section we will address the following question: *how would the field intensity and homogeneity change if we tried to realize the two dimensional Halbach cylinder with a material with a finite coercivity?* We start by considering the results for a set of four prototypical magnetic materials: two different grades of NdFeB magnets and two grades of Alnico magnets. The B–H curves of the materials are parameterized, according to Eq. (5), using the values reported in the data-sheets of commercial suppliers of magnetic materials. In particular, the parameters for the NdFeB magnets are derived from ref. [1] and the parameters for the Alnico magnets are derived from ref. [22]. The values of the parameters used for the simulations are listed in Table 1.

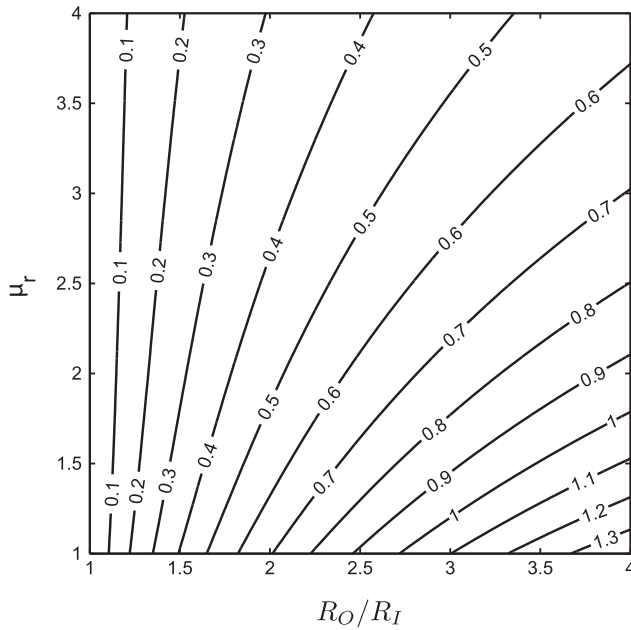
The resulting B–H curves and M–H curves are shown in Fig. 3b, respectively as solid lines and dashed lines.

We simulated different values of R_o/R_i and compared the results with the two demagnetization conditions introduced in Section 2.3. For each simulation we calculate the average flux density \mathbf{B} inside the air gap region, denoted by $\langle \mathbf{B} \rangle$. The average air gap flux density in the x direction is compared with the analytical solution $B_x^{\text{(Theory)}}$ of Eq. (3). The results are then expressed as the ratio $\langle B_x \rangle/B_x^{\text{(Theory)}}$.

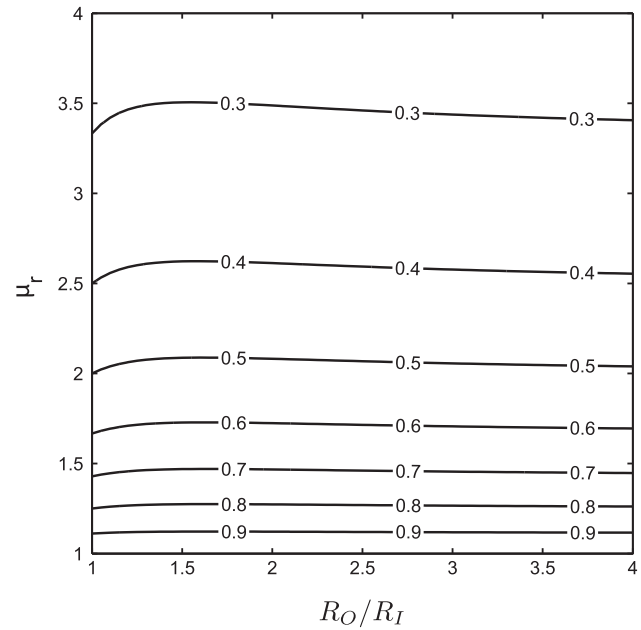
We also want to quantify how much the field fails to be homogeneous, and we will use the estimator Δ , evaluated as the average norm of the difference in flux density divided by the average norm of the flux density:

$$\Delta = \frac{\langle (B_x - \langle B_x \rangle)^2 + (B_y - \langle B_y \rangle)^2 \rangle}{\langle B_x^2 + B_y^2 \rangle} \quad (8)$$

The values of $\langle B_x \rangle/B_x^{\text{(Theory)}}$ and Δ , for the different materials and different R_o/R_i ratios, are plotted in the top panel and bottom panel of Fig. 3a respectively. As can be noticed, the performance of the materials compared to the theoretical prediction will only



(a) Inner Equatorial Point - Demagnetization



(b) Outer Polar Point - Demagnetization

Fig. 2. (2a) and (2b) represent respectively the demagnetization conditions for the inner equatorial point ($r = R_I$, $\phi = \pi/2$), indicated in Fig. 1a as a black circle, and the outer polar point ($r = R_O$, $\phi = 0$), indicated in Fig. 1a as a white circle. The horizontal axis of both the panels indicates the ratio between radii R_O/R_I . The vertical axis indicates the relative permeability μ_r . The contour lines, indicate a value of magnetic field multiplied by μ_0/B_{rem} . If the coercivity is smaller than or equal to this value demagnetization will occur. These panels represent the generalization to a general permeability $\mu_r \neq 1$ of Eqs. (6) and (7) respectively.

Table 1
Parameters of the permanent magnetic materials.

Material	B_{rem} [T]	H_c [MA/m]	$\mu_0 H_c / B_{rem}$	μ_r
N48	1.41	1.027	0.92	1.04
N38	1.25	2.347	2.36	1.03
Alnico 5	1.25	0.051	0.05	3.7
Alnico 8H	0.74	0.151	0.25	2.0

decrease as R_O/R_I increases. This can be observed as a decrease of $\langle B_x \rangle / B_x^{(Theoretical)}$ and an increase of Δ . For the two Alnico materials outer polar demagnetization occurs for all the values of R_O/R_I , and the performance is worse than the theoretical prediction even for small radii. This effect is to a smaller extent present also for N48. The vertical dashed lines in both the left panels indicate the critical value of R_O/R_I corresponding to the condition for inner equatorial demagnetization. As this phenomenon occurs, the performance decreases both in the average and homogeneity of the air gap flux density.

All the materials, except N38, are demagnetized at the outer polar point for all values of R_O/R_I . However, N48 is only slightly demagnetized compared to the two Alnico materials. For this reason only for Alnico the value of $\langle B_x \rangle / B_x^{(Theoretical)}$ is appreciably smaller than 1 even in the limit $R_O/R_I \rightarrow 1$. The polar demagnetization effect is very small for the case of N48, and the value of $\langle B_x \rangle / B_x^{(Theoretical)}$ is very close to 1 for small values of R_O/R_I . For the case of N38 the polar demagnetization effect does not occur at all.

A more drastic effect is caused by the inner equatorial demagnetization. The critical value of R_O/R_I for which this phenomenon occurs for each material is indicated in Fig. 3a as vertical dashed lines. As equatorial demagnetization occurs, the performance decreases both in the average and homogeneity of the air gap flux density, as can be seen in both the panels. For the case of N38, these effects are very small for the simulated range of R_O/R_I .

For these simulations we assumed that the relative permeability of each of the four materials has the same value for the parallel and perpendicular component. We also consider the effect of anisotropy, by setting the relative permeabilities for the parallel and perpendicular directions μ_r^{\parallel} and μ_r^{\perp} equal to 1.05 and 1.16, respectively [23]. Our simulations reveal that the results of the anisotropic simulations are quantitatively very similar to the results for the case of isotropic permeability.

To proceed systematically we simulate the system for different values of $\mu_0 H_c / B_{rem}$ and of R_O/R_I . These results are plotted in Fig. 4 as a function of R_O/R_I . The contour lines with their labels correspond to the value of $\langle B_x \rangle / B_x^{(Theoretical)}$ for Fig. 4a and to the value of Δ for Fig. 4b. The value of $B_x^{(Theoretical)}$ corresponds to the isotropic case with $\mu_r^{\parallel} = \mu_r^{\perp} = 1.05$. The two conditions for equatorial and polar demagnetization, expressed by Eqs. (6) and (7), are indicated by dashed lines as indicated in the legend.

As expected, only above the dashed black lines in the regions where none of the demagnetization conditions are met, is the magnet able to reproduce the theoretical flux density both for intensity and homogeneity. The phenomenon of equatorial demagnetization produces a more drastic effect in the performance of the Halbach cylinder with respect to the polar demagnetization. Moreover, it can be noticed that in the region $\mu_0 H_c / B_{rem} < 1$ for which polar demagnetization occurs, the value of $\langle B_x \rangle / B_x^{(Theoretical)}$ is initially increasing as R_O/R_I increases from 1 to the critical value corresponding to the equatorial demagnetization. For the uniformity the optimal value of R_O/R_I , corresponding to minimum Δ , is even larger.

3.2. Multi-material magnets

In this section we will address the following questions: *is it possible to realize the Halbach geometry using a set of materials with the same remanence but different coercivities? How much or how*

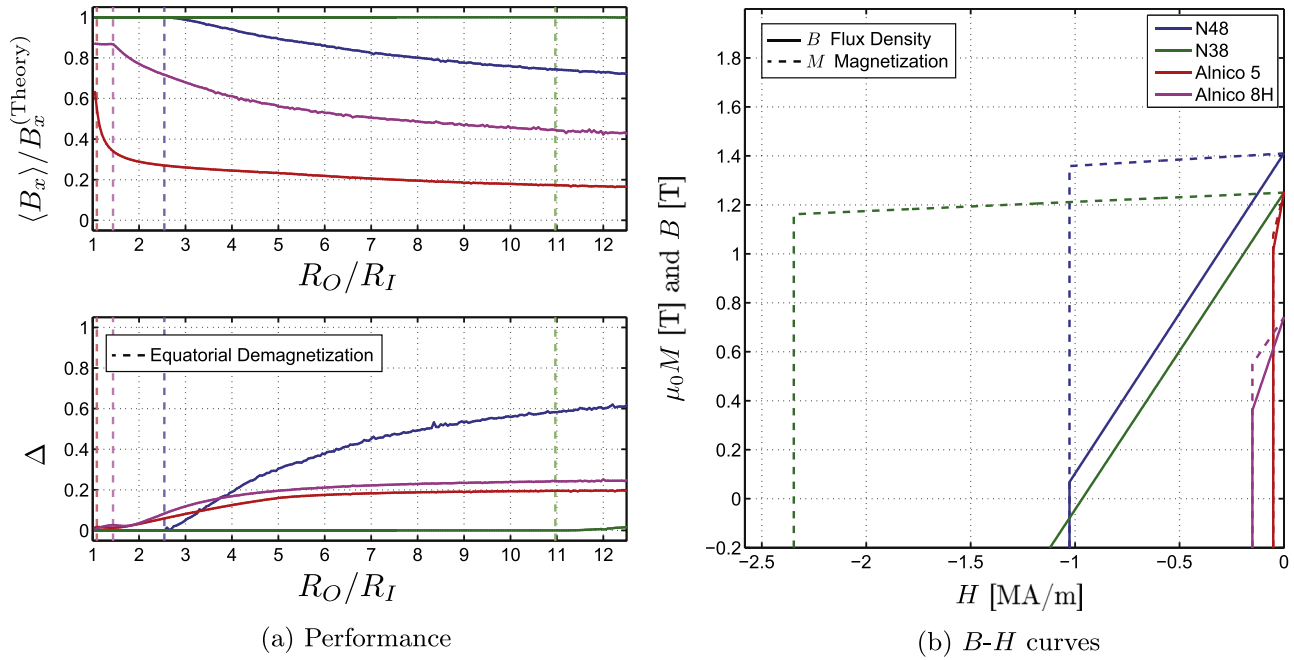


Fig. 3. Results of the simulations for the four materials corresponding to the B - H curves and M - H curves represented in Fig. 3b respectively as solid lines and dashed lines. The curves are determined by the set of parameters listed in Table 1. Fig. 3a indicates the results of simulations corresponding to different values of R_O/R_I , as visible on the horizontal axis of each panel. The top panel shows the value of the x component of B averaged over the air gap region and normalized by the value predicted by the analytical solution of Eq. (3). The bottom panel shows the value of the indicator Δ of non-homogeneity, defined in Eq. (8).

little of each material can be used? In which regions of the geometry it is possible to use a given material in the optimal way?

To investigate this topic we calculate the volumetric distribution of working points. Let us consider the illustrative example of Fig. 5, for a particular choice of geometry, $R_O/R_I = 3.3$, and for a material with the choice of parameters $\mu_r = 1$, $H_c = 0.65$ MA/m ($\mu_0 H_c = 0.82$ T), and $B_{rem} = 1.4$ T. With this choice of parameters the magnetic assembly is partially demagnetized. Fig. 5a represents the geometry of the system. The white contour lines

corresponds to the points where the value of $H_{||}$ is equal to the values $0, -(1/4)H_c, -(1/2)H_c, -(3/4)H_c, -H_c$. In the black regions limited by the contour line labeled by 1 the material is demagnetized. As expected, the demagnetized regions are found around the inner equatorial point and the outer polar point. Fig. 5b shows the cumulative volumetric distribution of working points with respect to $B_{||}$ and expressed as fraction of the total volume V_{Tot} . From this graph we can read that the volumetric fraction of non-demagnetized material is $\approx 75\%$. It is also possible to read

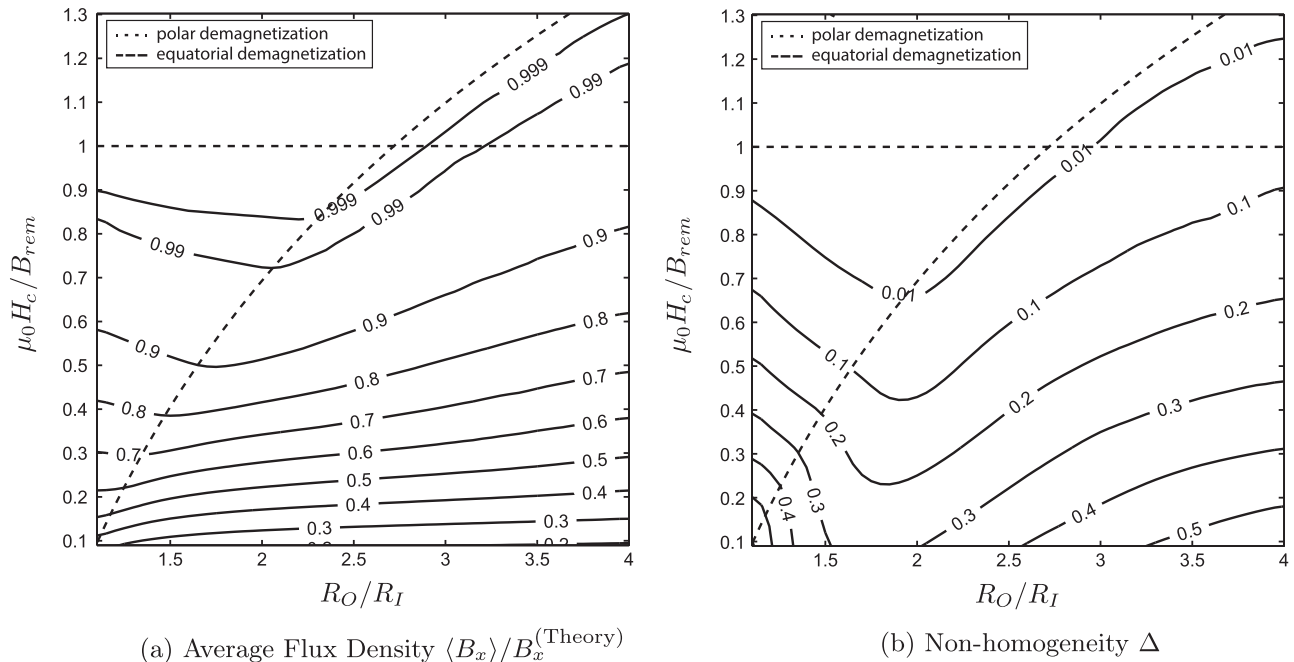
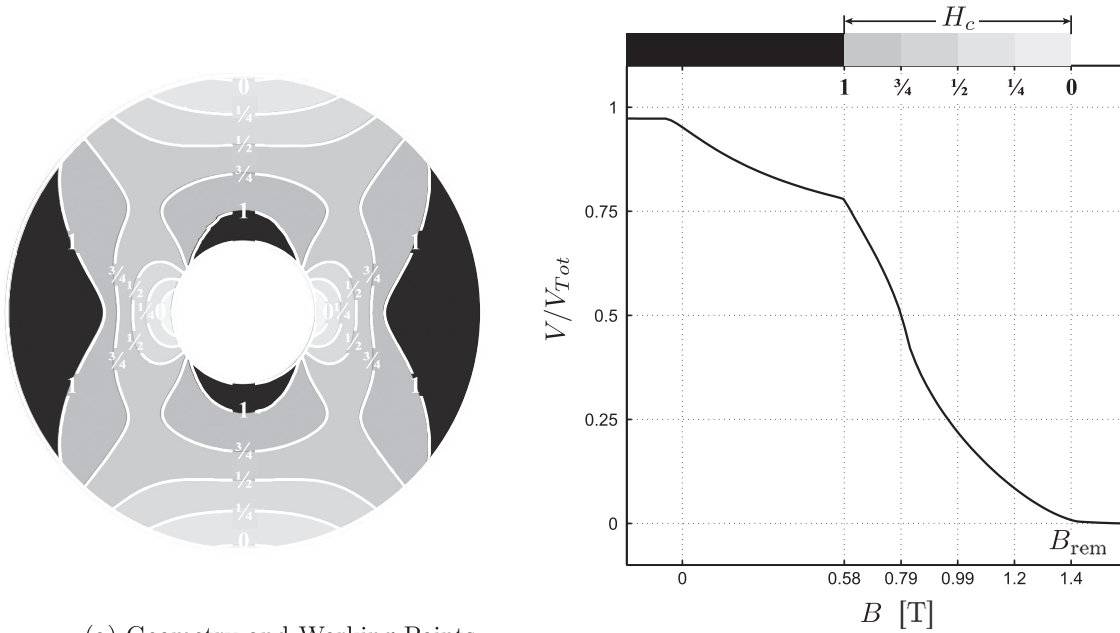


Fig. 4. (4a): Ratio $\langle B_x \rangle / B_x^{(Theory)}$ of the flux density in the air gap with respect to the ideal case. (4b): Value of the estimator Δ of the non-homogeneity of the field in the air gap (see Eq. (8)). The contour lines indicate for the left and right panels the value of $\langle B_x \rangle / B_x^{(Theory)}$ and Δ , respectively. The dashed lines represent the conditions for inner equatorial demagnetization expressed in Eq. (6), and for outer polar demagnetization expressed in Eq. (7). These conditions are calculated for the case $\mu_r^+ = \mu_r^- = 1$.



(a) Geometry and Working Points

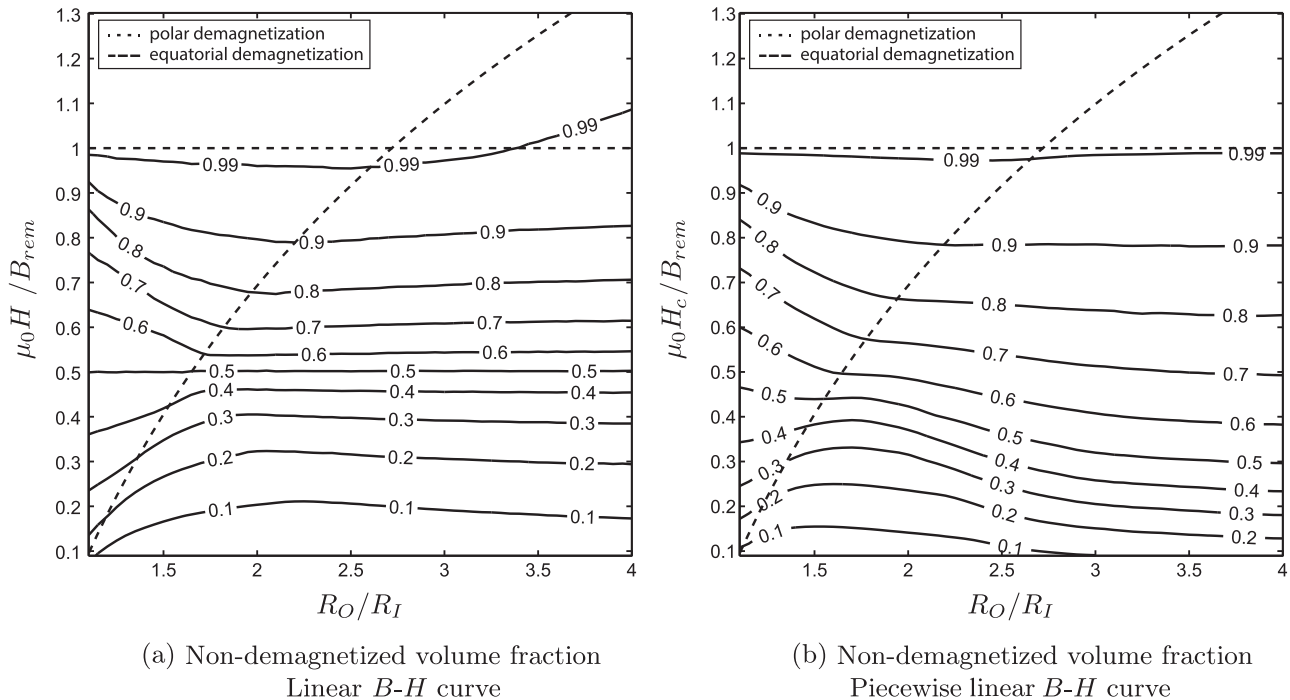
(b) Volumetric distribution of working points

Fig. 5. Illustration of the results for a particular choice of parameters: $R_O/R_I = 3.3$, $H_c = 0.65$ MA/m, ($\mu_0 H_c = 0.82$ T), $B_{rem} = 1.4$ T, and $\mu_r = 1$. (5a) represents the geometry. The white contour lines labeled by 0, 1/4, 1/2, 3/4 and 1, corresponds respectively to the points in which $H_{||}$ is equal to 0, $-(1/4)H_c$, $-(1/2)H_c$, $-(3/4)H_c$ and $-H_c$. The demagnetized regions are indicated by the color black and are limited by the contour lines labeled by 1. (5b) shows the cumulative volumetric distribution of working points, with respect to $B_{||}$ and normalized by the total volume V_{Tot} .

off the amount of material that could be replaced with a material with a lower coercivity without altering the performance: for example for $(1/2)H_c$ the volumetric fraction is $\approx 25\%$.

Proceeding systematically as in Section 3.1, we simulate the system for different values of $\mu_0 H/B_{rem}$ and of R_O/R_I , keeping the

relative permeabilities for the parallel and perpendicular directions $\mu_r^{||}$ and μ_r^{\perp} equal to 1.05 and 1.16, respectively. These results are shown in Fig. 6. For each combination of values of R_O/R_I , corresponding to the horizontal axis, and of $\mu_0 H/B_{rem}$, corresponding to the vertical axis, we calculate fraction of the total magnet



(a) Non-demagnetized volume fraction Linear B - H curve

(b) Non-demagnetized volume fraction Piecewise linear B - H curve

Fig. 6. Fraction of magnet in which the working point in the parallel direction lies above the values indicated on the magnetic field axis. The contour lines indicate the fraction with respect to the total magnet volume, as indicated by the labels. (6a) shows the simulations performed with the linear B - H relation, (6b) shows the simulations performed with the piecewise linear $B_{||}$ - $H_{||}$ curve corresponding to the coercivity that has the same value of the magnetic field indicated on the vertical axis. The dashed lines represent the condition for inner equatorial demagnetization expressed in Eq. (6), and the condition for outer polar demagnetization expressed in Eq. (7). These conditions are calculated for the case $\mu_r^{||} = \mu_r^{\perp} = 1$.

volume in which the H_{\parallel} component of the magnetic field is strictly larger than $-H_c$, indicated by the contour lines with their labels. This is equivalent to the fraction of volume for which the working points lie in the linear region of the B_{\parallel} - H_{\parallel} curve. We compare the results performed with a piecewise linear B - H relation, plotted in Fig. 6b, with simulations performed with a linear B - H relation with $\mu_r^{\parallel} = \mu_r^{\perp} = 1$, as in Eq. (1), plotted in Fig. 6a.

As expected from the results of Section 3.1, the linear and the piecewise linear model give the same result in the region in which the material is not demagnetized. This can be noticed by the fact that the region bounded by the dashed lines is in both cases above the contour line 0.99. However, outside this region of the graphs the two models give different results: the linear model indicates a volumetric distribution of working points symmetrically distributed around the middle value $\mu_0 H_{\parallel} / B_{rem} = 1/2$; the piecewise linear model indicates a greater extension of the demagnetized volume, resulting in the reduced performance observed before.

These results, and in particular Fig. 6a, can be used to determine how much of the expensive material with a high value of H_c can be replaced by a cheaper material with a low value of H_c without affecting the performance. This is done by selecting the areas of the magnet in which the working point does not leave the linear region of the B_{\parallel} - H_{\parallel} curve. The amount can be estimated by examining the vertical line corresponding to the desired value of R_O/R_I and observing the fraction of material that is able to work properly, given its coercivity.

As example of a multi-material magnet which is working properly, let us consider the choice of parameters $\mu_r = 1$, $H_c = 1.25$ MA/m, ($\mu_0 H_c = 1.57$ T), and $B_{rem} = 1.4$ T. Even with the same choice of R_O/R_I as in Fig. 5, this material is only demagnetized in a very small fraction of the volume close to the inner equatorial point. From Fig. 7b we can determine the amount of volume that can be replaced with a material with a lower coercivity, but the same remanence. In this case $\approx 18\%$ of the material can be replaced with a material with a coercivity 4 times smaller. We can also see that a coercivity greater than $(3/4)H_c$ is only required in a

small fraction of the magnet volume, $\approx 8\%$, limited by the corresponding contour line. In the case that four materials are available with coercivities respectively given by $H_n = (n/4)H_c$ with $n = 1, \dots, 4$, we can obtain the same performance of the full coercivity H_c by splitting the material into the following volume fractions:

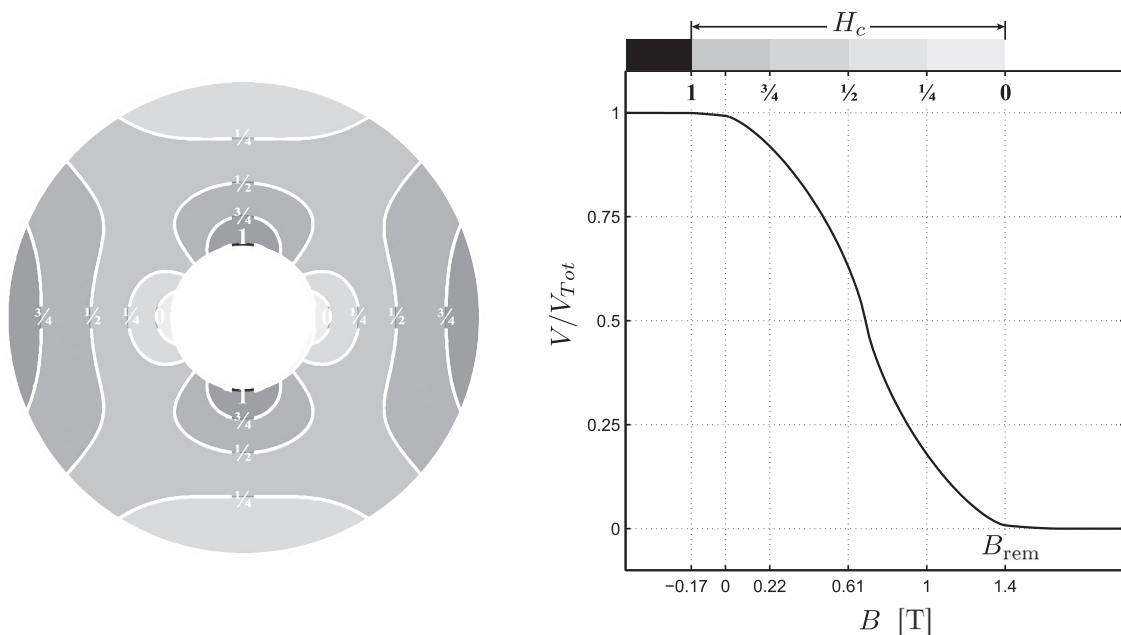
$$\left\{ V/V_{Tot}: H_{\parallel} \in [-H_n, -H_{n-1}] \right\}_{n=1,2,3,4} \approx \{18\%, 44\%, 30\%, 8\% \} \quad (9)$$

The coercivity of a NdFeB material, particularly at high temperatures, may be increased by adding dysprosium to the composition during the fabrication processes. Because of the elevated cost of dysprosium, materials with high coercivity are generally more expensive than materials with lower coercivity [15,24,25]. For this reason our method for indicating where the materials with low coercivity can be used without affecting the performance will result in an overall reduction in the cost of the materials.

4. Conclusions

We have presented a method able to predict the demagnetization effects in permanent magnet arrays due to the finite coercivity of the material. With this technique it is possible to quantify the decrease in the performance of the magnetic system and the parts of the magnet volume where demagnetization occurs. The starting point was a piecewise linear B - H relation characterized by the value of the coercivity H_c . We employed this method to investigate the case of the Halbach cylinder, for which the analytical solution is available, and the results of the piecewise linear model are consistent with the theoretical prediction.

Being based on finite elements method simulations, the same procedure can be applied to any geometry even when the analytical solution is not known. Moreover, it is straightforward to extend the same treatment to B - H relations which are not piecewise linear.



(a) Geometry and Working Points

(b) Volumetric distribution of working points

Fig. 7. Results of the simulation of a geometry with $R_O/R_I = 3.3$ and a material parametrized by $\mu_r = 1$, $H_c = 1.25$ MA/m ($\mu_0 H_c = 1.57$ T), and $B_{rem} = 1.4$ T. (7a) represents the geometry. The white contour lines labeled by 0, (1/4), (1/2), (3/4) and 1, corresponds respectively to the points in which H_{\parallel} is equal to 0, $-(1/4)H_c$, $-(1/2)H_c$, $-(3/4)H_c$ and $-H_c$. The very small demagnetized regions are limited by the contour line labeled by 1. (7b) shows the cumulative volumetric distribution of working points, with respect to B_{\parallel} and normalized by the total volume V_{Tot} .

We have shown that it is possible to replace part of the high coercivity material with lower coercivity materials without decreasing the performance of the magnetic array. This investigation will be relevant for many different applications, as a large variety of magnetic materials are available, and their costs may be very different.

Acknowledgements

This work was financed by the ENOVHEAT project which is funded by Innovation Fund Denmark (contract no 12-132673).

References

- [1] Vacuumschmelze GMBH & Co, KG, Pd 002 – Rare-Earth Permanent Magnets Vacodym/Vacomax, 2012.
- [2] O. Gutfleisch, M.A. Willard, E. Brück, C.H. Chen, S.G. Sankar, J.P. Liu, *Adv. Mater.* 23 (7) (2011) 821–842.
- [3] J.C. Mallinson, *IEEE Trans. Magn.* 9 (4) (1973) 678–682.
- [4] K. Halbach, *Nucl. Instrum. Methods* 169 (1980) 1–10.
- [5] G. Moresi, R. Magin, *Concept. Magn. Res.* 19B (2003) 35–43.
- [6] S. Applet, H. Kühn, F.W. Häsing, B. Blümich, *Nature Phys.* 2 (2006) 105–109.
- [7] H. Zijlstra, *Philips J. Res.* 40 (1985) 259–288.
- [8] P. Suominen, O. Tarvainen, H. Koivisto, *Rev. Sci. Instrum.* 75 (1) (2004) 59–63.
- [9] J.M.D. Coey, *J. Magn. Magn. Mater.* 248 (2002) 441–456.
- [10] R. Bjørk, C.R.H. Bahl, A. Smith, N. Pryds, *J. Appl. Phys.* 104 (1) (2008) 13910.
- [11] A. Kitanovski, J. Tušek, U. Tomc, U. Plaznik, M. Ozbolt, A. Poredoš, Springer, 2015.
- [12] F. Bloch, O. Cugat, G. Meunier, J.C. Toussaint, *IEEE Trans. Magn.* 34 (5) (1998) 2465–2468.
- [13] M. Kumada, T. Fujisawa, Y. Hirao, M. Endo, M. Aoki, T. Kohda, Y. Iwashita, I. Bolshakova, R. Holyaka, in: *Proceedings of 2nd Asian Particle Accelerator Conf.*, Beijing, China, 2001.
- [14] R. Bjørk, A. Smith, C.R.H. Bahl, *J. Magn. Magn. Mater.* 384 (2015) 128–132.
- [15] M.D. Kuz'min, K.P. Skokov, H. Jian, I. Radulov, O. Gutfleisch, *J. Phys. Condens. Matter* 26 (2014) 064205.
- [16] R. Bjørk, C.R.H. Bahl, A. Smith, *J. Magn. Magn. Mater.* 322 (2010) 133–141.
- [17] T.R.N. Mhiochàin, D. Weaire, S.M. McMurry, J.M.D. Coey, *J. Appl. Phys.* 86 (11) (1999) 6412–6424.
- [18] R. Bjørk, *J. Appl. Phys.* 109 (2011) 013915 1–6.
- [19] COMSOL Multiphysics, version 4.4, 2013.
- [20] Matlab, version 7.7.0.471 (R2008b), 2008.
- [21] J. Chavanne, O. Chubar, P. Elleaume, P. Van Vaerenbergh, in: *Proceedings of EPAC 2000*, Vienna, Austria, 2000, pp. 2316–2318.
- [22] Arnold Magnetic Technologies Corp. p. 6. – Cast ALNICO Permanent Magnets, 2003.
- [23] M. Katter, *IEEE Trans. Magn.* 41 (10) (2005) 1–3.
- [24] R.W. McCallum, L.H. Lewis, R. Skomski, M.J. Kramer, I.E. Anderson, *Annu. Rev. Mater. Res.* 44 (1) (2014) 451–477.
- [25] K. Ding, *EPJ Web Conf.* 75, 2014, 04005 pp. 1–3.

B.3 Globally Optimal Segmentation of Permanent-Magnet Systems

A. R. Insinga, R. Bjørk, A. Smith and C. R. H. Bahl

Physical Review Applied 5, (6), 064014, 1-16, (2016).

Globally Optimal Segmentation of Permanent-Magnet Systems

A. R. Insinga,^{*} R. Bjørk, A. Smith, and C. R. H. Bahl

*Department of Energy Conversion and Storage, Technical University of Denmark—DTU,
Frederiksborgvej 399, DK-4000 Roskilde, Denmark*

(Received 21 March 2016; revised manuscript received 26 May 2016; published 27 June 2016; publisher error corrected 1 July 2016)

Permanent-magnet systems are widely used for generation of magnetic fields with specific properties. The reciprocity theorem, an energy-equivalence principle in magnetostatics, can be employed to calculate the optimal remanent flux density of the permanent-magnet system, given any objective functional that is linear in the magnetic field. This approach, however, yields a continuously varying remanent flux density, while in practical applications, magnetic assemblies are realized by combining uniformly magnetized segments. The problem of determining the optimal shape of each of these segments remains unsolved. We show that the problem of optimal segmentation of a two-dimensional permanent-magnet assembly with respect to a linear objective functional can be reduced to the problem of piecewise linear approximation of a plane curve by perimeter maximization. Once the problem has been cast into this form, the globally optimal solution can be easily computed employing dynamic programming.

DOI: [10.1103/PhysRevApplied.5.064014](https://doi.org/10.1103/PhysRevApplied.5.064014)

I. INTRODUCTION

Permanent magnets play an important role in many scientific and industrial applications. Progress in the recent decades of research and development of new magnetic materials [1] has led to an immensely broadened range of applications of permanent magnets [2]. Applications of permanent magnets include rotary machines performing electromechanical energy conversion [3], magnetic actuators [4], magnetic gears [5], nuclear-magnetic-resonance devices [6,7], beam-focusing instruments [8,9], and wigglers and undulators [10].

In all these applications, it is always of the essence to optimize the design of the magnetic system, i.e., to increase the magnitude and precision of the generated field, and to reduce the volume and cost of the permanent-magnet materials. A wide range of different optimization techniques have been employed in this respect [11]. In general, it is advantageous to minimize the number of evaluations of the magnetic field solution, which is often performed with computationally expensive finite-element-method (FEM) techniques. However, because of the extent of the search space for this kind of problem, the advantage comes with a cost in terms of the optimality of the solution. Heuristic approaches, such as simulated annealing or, especially, genetic algorithms [12], are often preferred to deterministic algorithms in the attempt of avoiding to get stuck in local minima. In these schemes, there is always a trade-off between the computational complexity and the effectiveness of the algorithm in finding the optimal solution.

Other optimization approaches rely on the analytical calculation of the magnetic field [6,9,13,14]. In some cases,

it is possible to directly calculate the optimal solution based on analytical techniques. Even when this is not the case, the fast evaluation of the magnetic field solution allows the sampling of a large area of the considered search space, giving at least a close-to-optimal solution. The main limitation of this class of algorithms is the reduced dimension of the search space and the fact that only very few geometries are analytically solvable.

In this paper, we present an optimization method that can be applied to linear objective functionals and provides the globally optimal solution with single evaluation of the magnetic field solution and without the necessity of a starting guess. Restricting ourselves to linear objective functionals means that it is not possible to optimize, e.g., field homogeneity or, more generally, field quality. When the quality of the field with respect to a required distribution is critical, different strategies can be used to correct small field distortions [8,15,16].

Our approach is based on the reciprocity theorem [17], an energy-equivalence principle of magnetostatics. The presented method does not share the limitations of the analytical techniques since it can be used in combination with FEM to calculate the magnetic field solution for geometries that are not analytically solvable. The result is always the optimal remanent flux density field over the specified design area. The use of the reciprocity theorem for magnet optimization has previously been limited to continuously varying remanences or presegmented structures [18,19]. In this paper, we show how the theorem can be used to calculate the globally optimal shape of each magnet piece of a segmented structure with a given number of pieces. This procedure allows for the development of a set of tools that greatly aid the design process of permanent-magnet systems.

^{*}aroin@dtu.dk

This methodology assumes that all the materials exhibit a linear magnetic behavior. For hard permanent magnets, this approximation is justified as long as the demagnetizing and transversal fields are not too intense with respect to the coercivity and the anisotropic field. The effect of the nonlinear demagnetization characteristics can be predicted with numerical approaches such as the ones described in Ref. [20]. However, the optimality of the configuration determined within the linear approximation is not guaranteed when these effects are taken into account.

II. FRAMEWORK

A. Reciprocity theorem

We begin by considering the reciprocity theorem, which considers two distinct magnetic systems labeled 1 and 2 [17]. The theorem states that the volume integral of the scalar product between the magnetization of system 1, \mathbf{M}_1 , with the field of system 2, \mathbf{H}_2 , is equal to the integral of the scalar product between the magnetization of system 2, \mathbf{M}_2 , with the field of system 1, \mathbf{H}_1 ,

$$\int d^3x \mathbf{M}_1(\mathbf{x}) \cdot \mathbf{H}_2(\mathbf{x}) = \int d^3x \mathbf{M}_2(\mathbf{x}) \cdot \mathbf{H}_1(\mathbf{x}). \quad (1)$$

The reciprocity theorem assumes that the fields are constant in time and vanish at infinity and that there are no electrical currents. The relation between magnetization \mathbf{M} , magnetic field \mathbf{H} , and flux density \mathbf{B} is by definition $\mathbf{B} = \mu_0(\mathbf{H} + \mathbf{M})$.

We consider materials whose magnetic behavior is described by a linear constitutive relation $\mathbf{B} = \underline{\underline{\mu}} \cdot \mathbf{H} + \mathbf{B}_r$, where $\underline{\underline{\mu}}$ denotes the permeability tensor, and \mathbf{B}_r is the remanence vector. We also assume that the permeability tensor is symmetric and is the same in any point for systems 1 and 2. When these conditions are fulfilled, the theorem can be expressed as

$$\int d^3x \mathbf{B}_{r1}(\mathbf{x}) \cdot \mathbf{H}_2(\mathbf{x}) = \int d^3x \mathbf{B}_{r2}(\mathbf{x}) \cdot \mathbf{H}_1(\mathbf{x}). \quad (2)$$

The reciprocity theorem can be used to solve magnet design problems by considering an empty air gap and by aligning the remanence everywhere with the field generated by a *virtual* magnet placed in this air gap. We consider an objective functional \mathcal{S} , which is linear with respect to \mathbf{H}_1 , for example, maximizing the x component of the field averaged over a certain region. In general, a linear functional can be expressed in integral form:

$$\mathcal{S}[\mathbf{H}_1] = \int d^3x \mathbf{H}_1(\mathbf{x}) \cdot \mathbf{u}(\mathbf{x}), \quad (3)$$

where \mathbf{u} is an arbitrarily defined objective vector field. The integration domain can be reduced from the whole space to the region where the objective vector field \mathbf{u} is nonzero.

This region will be denoted by R_g ; it usually corresponds to an empty air gap. If the remanent flux density \mathbf{B}_{r2} of a *virtual* magnet is used as the objective vector field \mathbf{u} , Eq. (2) implies that $\mathcal{S}[\mathbf{H}_1]$ is also equal to

$$\mathcal{S}[\mathbf{H}_1] = \int d^3x \mathbf{H}_2(\mathbf{x}) \cdot \mathbf{B}_{r1}(\mathbf{x}), \quad (4)$$

where \mathbf{H}_2 is the field generated by the virtual remanence \mathbf{B}_{r2} , and \mathbf{B}_{r1} is the remanent flux density of the real magnet that is associated with the real field \mathbf{H}_1 . The functional \mathcal{S} has the dimensions of an energy. Again, the integration domain can be reduced to the region of space where the remanence of the real magnet is nonzero. This region denoted by R_m and called the magnet design region is assumed not to overlap with R_g . Equation (2) applies since R_m (R_g) will be the only region in which \mathbf{B}_{r1} (\mathbf{B}_{r2}) is not zero. The use of the reciprocity theorem for the optimization of a magnetic system is schematically illustrated in Fig. 1.

The theorem provides the solution to the following problem: assuming that the norm of the remanent flux density \mathbf{B}_{r1} is fixed, determine its optimal direction in any point of the region R_m such that the field \mathbf{H}_1 generated by \mathbf{B}_{r1} maximizes the integral of Eq. (3). The answer is evidently: the optimal remanence \mathbf{B}_{r1} should be aligned at every point with the virtual field \mathbf{H}_2 generated by \mathbf{B}_{r2} . To illustrate this result, we consider a simple example in which we wish to maximize the field in a given direction inside a cylindrical region with infinite length. This region will then be occupied by a virtual magnet with uniform remanent flux density. If the direction of the virtual remanence is transversal to the axis of the cylinder, for example, in the positive x direction, the field generated by it will lead to the

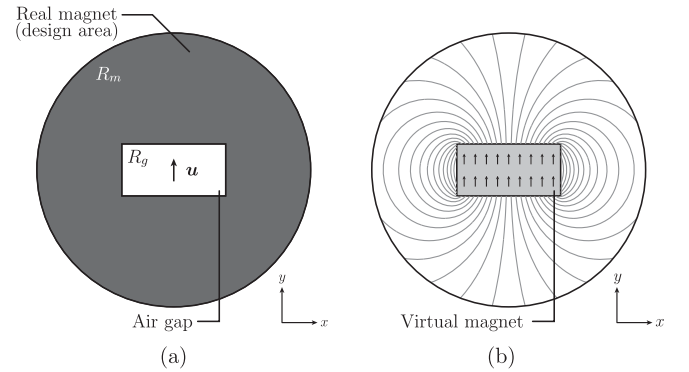


FIG. 1. (a) The use of the reciprocity theorem for magnet optimization is illustrated by considering a uniform objective field \mathbf{u} oriented in the positive y direction and defined over the rectangular air gap R_g . (b) The air gap R_g is filled with a virtual magnet magnetized in the same direction of the objective vector field \mathbf{u} . The reciprocity theorem implies that the optimal remanence is aligned with the field generated by the virtual magnet in any point of the design area R_m . The field lines of the virtual field \mathbf{H}_2 are shown in (b).

well-known Halbach cylinder solution [21], which, in cylindrical coordinates, is given by

$$\mathbf{B}_{r1}(r, \phi) \propto \cos(2\phi)\hat{e}_x + \sin(2\phi)\hat{e}_y. \quad (5)$$

This case of the Halbach cylinder is considered in detail in Sec. IV A.

B. Magnet border

We now consider the external border of the magnet. An important observation regarding Eq. (4) is that the different pieces of magnet contribute independently to the value of the objective functional \mathcal{S} : the optimal direction of the remanence in each point remains the same regardless of how the remanence is chosen elsewhere. The independence is a consequence of the fact that \mathbf{H}_1 is linear with respect to \mathbf{B}_{r1} , and \mathcal{S} is linear with respect to \mathbf{B}_{r1} . Moreover, once \mathbf{B}_{r1} is aligned to \mathbf{H}_2 at a point \mathbf{x} , the integrand of Eq. (4) becomes $\|\mathbf{H}_2(\mathbf{x})\|\|\mathbf{B}_{r1}(\mathbf{x})\| \geq 0$. This means that the contribution from that point of the magnet to the value of \mathcal{S} is proportional to the norm of the virtual field, which can, thus, be interpreted as a weight factor of the corresponding site in the magnet design area [18]. This fact can be used to predict the optimal border between hard magnets and air.

As we explain in Sec. II A, in order for Eq. (2) to be true, the magnetic susceptibility χ_m must be the same for the real and the virtual system, implying that it is not possible to determine the optimal susceptibility field, i.e., the optimal distribution of materials. However, if the susceptibility of the permanent-magnet material is zero, as is approximately true, e.g., for rare-earth hard magnets, we are not forced to decide in advance which areas of the magnet design region are to be filled with magnet and which areas are to be filled with air. Instead, we can determine the optimal border between magnet and air using the amount of available permanent-magnet material as a constraint.

As the contribution to the value of \mathcal{S} from a point of the design region is equal to $H_2 = \|\mathbf{H}_2\|$, it is better to utilize the permanent-magnet material in areas where the norm of the virtual field \mathbf{H}_2 is larger. This implies that the optimal borders between hard magnet and air are given by the level surfaces of the scalar field $H_2(\mathbf{x})$.

For the case of the Halbach cylinder, the norm H_2 of the virtual field \mathbf{H}_2 depends only on the radial coordinate and is proportional to $1/r^2$. This implies that the optimal external border of the magnet is always a cylindrical surface which is coaxial with the inner cylindrical cavity.

In the examples that we present in Sec. IV, we assume that the susceptibility of the permanent-magnet material is zero. However, it should be stressed that this requirement is necessary only for the purpose of determining the optimal border between magnet and air. All the remaining optimality results presented in this work remain true for any tensor permeability field $\underline{\mu}(\mathbf{x})$ which is symmetric.

Another interesting consequence of the reciprocity theorem concerns iron yokes, iron cores, or similar soft magnetic structures, which are often present in magnetic assemblies. If the magnet design region R_m is adjacent to a region containing a material with very high permeability, e.g., iron, the virtual field \mathbf{H}_2 in R_m will be almost normal to the border between the magnet and the highly permeable material (it will be exactly normal in the limit $\mu \rightarrow \infty$). Thus, if a permanent magnet is adjacent to an iron-filled region, it is never optimal for it to be magnetized in a direction that is not normal to the border between the magnet and iron, as this creates a short circuit for the flux lines to close without passing through the air-gap region. Therefore, the optimal remanence is always normal to the border between the magnet and iron.

C. Energy considerations

The method also suggests a practical technique for assembling systems composed of different pieces of permanent magnet. As it is explained in Ref. [22] for the case of the Halbach cylinder geometry, if a permanent magnet called the anchor is temporarily placed in the central air-gap region, it will exercise a force on the surrounding pieces of permanent magnet which will automatically align them in the Halbach configuration. The central anchor magnet plays the same role in this case as the virtual magnet in the optimization procedure presented here, and the value of \mathcal{S} corresponds to the mutual energy between the anchor magnet and the surrounding segments. This fabrication method can be extended to many different cases besides the Halbach cylinder geometry, as long as the forces resulting from the mutual interaction between the different magnet pieces are negligible compared to the force due to the anchor magnet.

Furthermore, by allowing configurations where the norm of the remanence is not uniform, the algorithm can provide solutions that are also maximally efficient, in the sense that they maximize the fraction of magnetic energy that the permanent magnet is able to generate outside of itself [23]. More specifically, among all of the possible remanence distributions \mathbf{B}_{r1} in R_m able to generate the same field \mathbf{B}_1 in R_g , the ideal remanence maximizes the figure of merit:

$$\mathcal{M} = \frac{\int_{R_g} d^3x \|\mathbf{B}_1(\mathbf{x})\|^2}{\int_{R_m} d^3x \|\mathbf{B}_{r1}(\mathbf{x})\|^2}. \quad (6)$$

The sufficient conditions for maximal energy efficiency to occur are

- (i) The magnet design region R_m and the air-gap region R_g are not overlapping.
- (ii) The union of R_g with R_m is equal to the whole space, except for the regions enclosed by material with infinite permeability.
- (iii) Inside R_g , the permeability is equal to μ_0 .

- (iv) Inside R_m , the permeability μ is uniform.
- (v) The real remanent flux density is chosen to be not only aligned but *proportional to* the virtual field \mathbf{H}_2 .

When the last two conditions are satisfied, the real remanent flux density is both solenoidal and irrotational, thus, satisfying the ideal remanence equations of Ref. [23]. When all the conditions above are satisfied, the magnetic structure in R_m is maximally energy efficient.

Within the same framework, it can be shown that the maximally energy-efficient border between the permanent magnet and the highly permeable material is given by a level surface of the magnetic scalar potential Φ_2 that generates the virtual field: $\mathbf{H}_2 = -\nabla\Phi_2$ [23].

III. OPTIMAL SEGMENTATION

We now address the question of how best to segment the solution with a continuously varying remanence into N uniformly magnetized segments. If the border of each segment is predetermined, the optimal remanence direction will just be the direction of the virtual field averaged over the volume of the segment. However, if the shape of the segments is not predetermined, the optimal border of each segment has to be determined from the optimization. We will now consider this problem as a function of the number of segments that the system is desired to be split into.

For simplicity, we consider two-dimensional problems, i.e., systems in which the extent in one dimension is greatly larger than along the other two dimensions, and no physical quantities are varying along this direction. An example is an infinitely long hollow cylinder.

The starting point to the solution of the segmentation problem is the observation that the optimal border between two adjacent segments always lies on a contour line of the direction of the virtual field \mathbf{H}_2 . The direction of \mathbf{H}_2 is determined by the angle $\psi = \arctan(H_y/H_x)$, where H_x and H_y are the two components of the virtual field \mathbf{H}_2 . The optimality of the contour lines of ψ is a consequence of the independence between the contributions to the value of \mathcal{S} from different points of the magnet. The derivation is given in Appendix A; intuitively, since the contribution from a point of the magnet is proportional to the scalar product between the virtual field in that point and the remanence of the real system, the orientation of the virtual field is the only relevant variable. A given point of the magnet is best assigned to the segment which gives the best match between the direction of the virtual field \mathbf{H}_2 and the remanence of the real magnet \mathbf{B}_{r1} . For the example of the Halbach cylinder of infinite length, the contour lines of ψ are coincident with the contour lines of the angular coordinate ϕ .

This observation considerably reduces the search space of the optimization problem: we are left with the simpler problem of determining which of the contour curves must be selected as borders between segments. Answering this question is equivalent to finding the best piecewise linear

approximation to a continuous curve, such that the perimeter of the piecewise curve is maximized. We start by illustrating the approach with a simple example before stating the general conditions for this equivalence to be true. Let us consider again the example of the Halbach cylinder and the corresponding optimal remanence \mathbf{B}_{r1} given by Eq. (5). As the angular coordinate ϕ goes from 0 to 2π , the vector $\mathbf{B}_{r1} \propto \mathbf{H}_2$ performs two complete revolutions. Instead of considering $\arctan(H_y/H_x)$, which has values in the interval $[-\pi, +\pi]$, we can introduce the accumulated angle which, in this case, is equal to 2ϕ , and assumes the values in the interval $[0, 4\pi]$. Below, we use ψ for this accumulated angle.

Once a starting value ψ_0 is fixed, it is possible to define the parametrized curve $\mathcal{H}(\psi_1)$ as

$$\mathcal{H}(\psi_1) = \int_{\mathcal{R}_{[\psi_0, \psi_1]}} d^2x \mathbf{H}_2(\mathbf{x}). \quad (7)$$

The curve has the dimension of magnetic field integrated over an area. The integration domain $\mathcal{R}_{[\psi_0, \psi_1]}$ is a subset of the design area R_m defined as

$$\mathcal{R}_{[\psi_0, \psi_1]} = \{\mathbf{x} : \psi(\mathbf{x}) \in [\psi_0, \psi_1]\} \cap R_m. \quad (8)$$

As shown in Appendix B, for the continuous case, the value of the objective functional \mathcal{S} is given by the length of the curve $\mathcal{H}(\psi)$. For the segmented case with splitting angles $\{\psi_j\}_{j=0, \dots, N}$, the value of \mathcal{S} reduces to the length of the piecewise linear curve inscribed in $\mathcal{H}(\psi)$:

$$\begin{aligned} \mathcal{S}_{\text{continuous}} &= \int_{\psi_0}^{\psi_0+4\pi} \left\| \frac{d}{d\psi} \mathcal{H}(\psi) \right\| d\psi \rightarrow \mathcal{S}_{\text{segmented}}^{(N)} \\ &= \sum_{j=0}^{N-1} \left\| \int_{\psi_j}^{\psi_{j+1}} \frac{d}{d\psi} \mathcal{H}(\psi) d\psi \right\|. \end{aligned} \quad (9)$$

For the case of the Halbach cylinder, the curve $\mathcal{H}(\psi)$ is given by *two* revolutions around a point. This implies that segmenting the Halbach magnet into N pieces will result in a reduction of the value of \mathcal{S} according to the familiar formula [21]:

$$\frac{\mathcal{S}_{\text{segmented}}^{(N)}}{\mathcal{S}_{\text{continuous}}} = \frac{N \sin(2\pi/N)}{2\pi}. \quad (10)$$

Any other possible way to segment this volume using the same number of segments results in a greater reduction. As an example, we consider a segmentation using seven pieces. The curve $\mathcal{H}(\psi)$ and the inscribed seven-segment piecewise linear approximation for the Halbach example are shown in Fig. 2(a), and the resulting optimal segmentation is shown in Fig. 2(b). Because of the symmetry, the choice of the starting point ψ_0 indicated in Figs. 2(a) and 2(b) as a black dot does

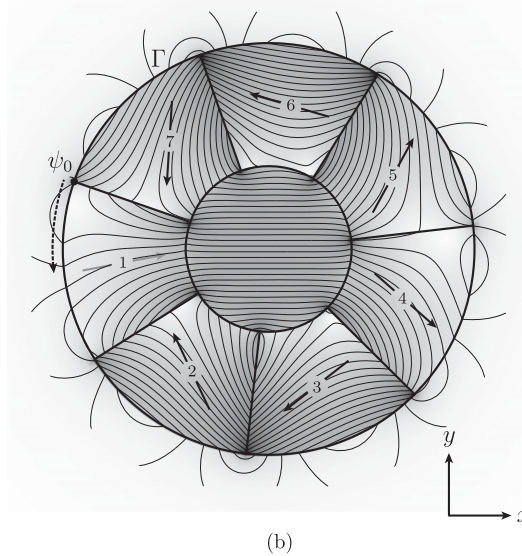
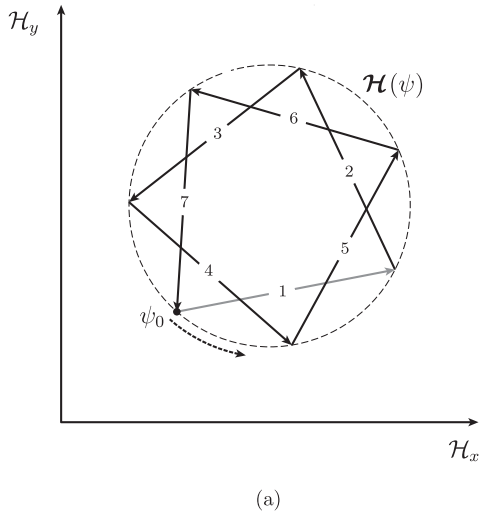


FIG. 2. Optimal segmentation of the Halbach cylinder geometry using seven segments. Because of the symmetry, the starting point indicated in both the panels by a black dot does not affect the value of the objective functional. (a) The curve $\mathcal{H}(\psi)$ and its segmentation. (b) Corresponding segmented geometry.

not affect the value of $\mathcal{S}_{\text{segmented}}^{(N)}$. This is not true in the general case.

We now examine the general case. We consider a connected two-dimensional design area R_m and a curve $\Gamma: t \in [0, 1] \rightarrow \mathbf{x}(t)$ inside this region, constructed in such a way that the vector \mathbf{H}_2 is always changing direction as we move along the curve, and the rotation of \mathbf{H}_2 is always in the same direction, for example, always counter-clockwise, as we move along the curve. The accumulated angle ψ is then monotonic. The role of Γ is to establish a one-to-one correspondence between the different ψ contour lines and the parameter $t \in [0, 1]$ with the continuity requirement that $\psi(t_1) \rightarrow \psi(t_2)$, for $t_1 \rightarrow t_2$. The choice of the curve Γ is not unique; however, all of the possible choices will lead to the same results, as long as the angle ψ is monotonic along the curve. It is possible to construct Γ by starting from an arbitrary point and proceeding in a way that each ψ contour is intercepted by Γ once and only once. Often the easiest choice is the external border of the design area.

The condition to be able to determine the globally optimal segmentation using our approach is that the union of all the ψ contour lines passing by the points of the curve Γ must fill the entire design area. A counterexample is illustrated in Fig. 3, where the curve Γ is coincident with the external border of the design area and represented by the thick black line. All the ψ contour lines are plotted inside the design area as thin black lines. As can be seen, none of the contour lines originating from the curve Γ are entering the pink shaded areas, and, therefore, the condition is not satisfied. Moreover, if the region enclosed by the dashed line is removed from the design area, the gray shaded region cannot be reached by any of the contour lines passing by Γ . We conjecture that these problems never occur for the case of a uniform objective field defined over a convex cavity, as long as the only hole of the design area is the cavity itself.

However, while this condition is conjectured to be sufficient, it does not exhaust the class of design objectives for which the globally optimal segmentation can be determined using our approach.

When the union of all the ψ contour lines intercepting Γ spans the whole design area, it is possible to reduce the problem of optimal segmentation to the problem of approximating the continuous curve $\mathcal{H}(\psi)$ with a piecewise linear curve so that the length is maximized. This fact is shown in Appendix B. The globally optimal solution to this problem can be determined employing dynamic programming [24].

If the curve Γ is closed, as it is in the Halbach example, the choice of the starting value ψ_0 can affect the value of \mathcal{S} : it is still possible to determine the dependence of \mathcal{S} on the starting point and find the optimal value of ψ_0 . However,

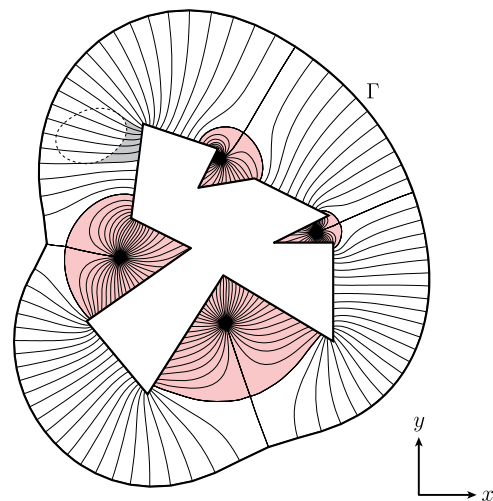


FIG. 3. Example of a geometry for which the ψ contour lines passing by the curve Γ do not span the whole design area. As explained in Sec. III, the globally optimal segmentation cannot be determined by our method for this case.

for the case of the Halbach cylinder with optimal external border, all the starting points are equivalent.

If the design area is not connected, each of the disconnected regions can be segmented independently using the same method. If the design area is not entirely spanned by the ψ contour lines passing by Γ , the picture is more complex, and this algorithm cannot determine the globally optimal solution. However, it remains true that the optimal borders between segments have to be contour lines of ψ . Moreover, it is still possible to find the optimal segmentation with respect to a limited search space.

Hitherto, we consider only two-dimensional systems. However, it is also possible to analyze the problem of segmenting a given design region R_m belonging to a three-dimensional system. It remains true that it is not optimal to split a region over which the direction of the virtual field is constant. This leaves 2 degrees of freedom such as the values of the azimuthal angle $\psi = \arctan(H_y/H_x)$ and the inclination angle $\vartheta = \arccos(H_z/\|\mathbf{H}\|)$ of the virtual field \mathbf{H}_2 . In this case, the problem consists of subdividing a region of the ψ - ϑ plane into simply connected subsets. The globally optimal solution to this problem cannot be determined using the same techniques that have been described for the two-dimensional case. It is still possible to approach a three-dimensional problem by considering the procedure described in Sec. V.

In the present section, we derive the framework to solve the problem of maximizing a linear functional with respect to the geometrical subdivision of a certain design area into a given number of uniformly magnetized segments. Since the value of the objective increases monotonically with the number of segments, approaching the limit given by the continuous case, the optimization problem is equivalent to minimizing the number of segments with a given value of the objective. The reason is that generally the manufacturing cost of a magnetic system increases with the number of subdivisions of the same volume of permanent magnet. However, the realization of segments whose borders are curved surfaces might be challenging and drive up the costs. One possible solution is to approximate the optimal shapes predicted by the theoretical approach with simplified geometries that are more feasible to produce. Another possibility is to consider the procedure described at the end of Appendix B, which has the purpose of constraining the family of possible segmentations to predefined shapes.

IV. EXAMPLES

The procedure outlined in Sec. III is now illustrated with different examples associated with figures showing the result of the finite-element-method simulation of the optimized configuration. The remanence always has the same norm for all the magnet segments, and its direction is indicated in the figures by the black arrows. The norm of the magnetic flux density \mathbf{B}_1 is indicated in gray scale,

darker shades corresponding to a higher value of the norm. The field lines of \mathbf{B}_1 are shown as thin black lines.

A. Halbach cylinder

We now examine in detail the case of the Halbach cylinder, which we discuss briefly in Sec. II.

We adopt cylindrical coordinates r and ϕ , and we denote the unit vectors in the radial and azimuthal directions by \hat{e}_r and \hat{e}_ϕ , respectively. The field \mathbf{H}_2 generated outside an infinitely long cylinder magnetized transversally to its axis is given by

$$\mathbf{H}_2(r, \phi) = \frac{MR_I^2}{r^2} [\cos(\phi)\hat{e}_r + \sin(\phi)\hat{e}_\phi], \quad (11)$$

where the axis of the cylinder is in the z direction, the magnetization is in the x direction, R_I is the radius of the cylinder, and M the norm of its magnetization. This cylinder is the virtual magnet for the Halbach case.

The norm of the virtual magnetic field H_2 is independent of ϕ , and the level curves of the norm are circles with their center in the origin. One of these circles is chosen as the external border. The points of the external border can be parametrized directly by the angle $\phi \in [0, 2\pi]$, and the orientation of the virtual field is described by the accumulated angle $\psi = 2\phi \in [0, 4\pi]$. The radius of the external border is denoted by R_O . The level curves of ψ are radial lines with constant ϕ . The vector $\mathcal{H}_{[\psi_0, \psi_1]}$ can be calculated explicitly:

$$\begin{aligned} \mathcal{H}_{[\psi_0, \psi_1]} &= \int_{\mathcal{R}_{[\psi_0, \psi_1]}} d^2x \mathbf{H}_2(x) \\ &= (MR_I^2) \int_{\psi_0/2}^{\psi_1/2} d\phi (\cos(\phi)\hat{e}_r \\ &\quad + \sin(\phi)\hat{e}_\phi) \int_{R_I}^{R_O} dr \frac{1}{r}, \end{aligned} \quad (12)$$

$$\begin{aligned} &= (MR_I^2) \log\left(\frac{R_O}{R_I}\right) \left(\hat{e}_x \int_{\psi_0/2}^{\psi_1/2} d\phi \cos(2\phi) \right. \\ &\quad \left. + \hat{e}_y \int_{\psi_0/2}^{\psi_1/2} d\phi \sin(2\phi) \right), \end{aligned} \quad (13)$$

$$\begin{aligned} &= (MR_I^2) \log\left(\frac{R_O}{R_I}\right) \frac{1}{2} (\hat{e}_x [\sin(\psi_1) \\ &\quad - \sin(\psi_0)] - \hat{e}_y [\cos(\psi_1) - \cos(\psi_0)]). \end{aligned} \quad (14)$$

Since $\psi \in [0, 4\pi]$, the curve $\mathcal{H}(\psi) = \mathcal{H}_{[\psi_0, \psi]}$ describes two revolutions around the point:

$$(-\sin(\psi_0)\hat{e}_x + \cos(\psi_0)\hat{e}_y)(MR_I^2) \log(R_O/R_I)/2 \quad (15)$$

with radius $R_B = (MR_I^2) \log(R_O/R_I)/2$. The initial point is in the origin: $\mathcal{H}(\psi_0) = \mathbf{0}$.

The length of this curve in the continuous case is equal to the value of \mathcal{S} and is given by $4\pi R_B$. Intuitively, since the curvature of the curve is constant, the best way to split it in N segments in order to maximize the length of the polygonal line is to use identical segments. If this curve is segmented using N identical segments (for the two revolutions), each segment will span an angle of $(4\pi)/N$. The side s of a regular polygon with N sides inscribed in a polygon of radius R is equal to $s = 2R \sin(\pi/N)$. Considering the double revolution, the ratio between the length of the vector \mathcal{H} associated with each segment and the length of the corresponding curve arc is given by

$$\frac{\mathcal{S}_N}{\mathcal{S}_{\text{continuous}}} = \frac{N \sin(2\pi/N)}{2\pi}, \quad (16)$$

which is the familiar formula for the segmented Halbach cylinder [21].

The $\mathcal{H}(\psi)$ curve and the geometry are shown in Figs. 2(a) and 2(b) for the case $N = 7$.

It is worth mentioning that the results of this section are also true for any multipole Halbach cylinder surrounded by air. This is shown by considering the analytical expression of the field generated by a multipole Halbach cylinder [25]. If the virtual remanence is defined over an infinitely long cylindrical shell R_g and is expressed as $\mathbf{B}_{r_2}(r, \phi) = B_r(r)[\cos(+p\phi)\hat{\mathbf{e}}_r + \sin(+p\phi)\hat{\mathbf{e}}_\phi]$, then the optimal real remanence is oriented as $\cos(-p\phi)\hat{\mathbf{e}}_r + \sin(-p\phi)\hat{\mathbf{e}}_\phi$. The design area is adjacent to R_g and is located on the external side of R_g if $p < 0$ and on the internal side of R_g if $p > 0$. The optimal external border of the design area is always a cylinder which is coaxial with R_m . Moreover, the optimal boundaries between adjacent segments are given by radial surfaces, all separated by equal angles. The ratio between

the value of \mathcal{S} in the segmented case and the value in the continuous case is still given by Eq. (16). In the continuous case, the field-generated \mathbf{H}_1 generated by the real remanence has exactly the same angular dependence as the virtual remanence:

$$\mathbf{H}_1 \propto r^{p-1}[\cos(+p\phi)\hat{\mathbf{e}}_r + \sin(+p\phi)\hat{\mathbf{e}}_\phi] \quad \text{for } p \neq 1. \quad (17)$$

The case analyzed above of uniform field in the x direction is given by $p = -1$, and the region R_g is a cylinder instead of a hollow cylindrical shell.

B. Rectangular cavity

A rectangular cavity is another example for which the equation of the virtual field is analytically solvable. In order to show the algorithm's results with an asymmetrical problem, a decentered circle is chosen as the external border of the design area, as is visible in Fig. 4(b).

The virtual remanence is uniform in the cavity in direction $\hat{\mathbf{e}}_y$. The accumulated angle ψ spans an angle of 4π as in the previous example. This implies that the curve $\mathcal{H}(\psi) = \mathcal{H}_{[\psi_0, \psi]}$ can be extended indefinitely on both sides according to

$$\mathcal{H}(\psi + 4\pi n) = \mathcal{H}(\psi) + n\mathcal{H}_{[\psi_0, \psi_0 + 4\pi]}, \quad (18)$$

where $\mathcal{H}_{[\psi_0, \psi_0 + 4\pi]}$ is the integral of the virtual field over the whole design region. The curve $\mathcal{H}(\psi)$ is plotted in Fig. 4(a) over a period of 8π . Selecting a different starting point moves the origin of the $\mathcal{H}_x - \mathcal{H}_y$ plane indicated as a black dot on different points of the curve $\mathcal{H}(\psi)$. Any interval $[\psi_0, \psi_0 + 4\pi]$ can be used for the segmentation corresponding to the different starting points on the external border of the magnet. The optimal position of the point ψ_0

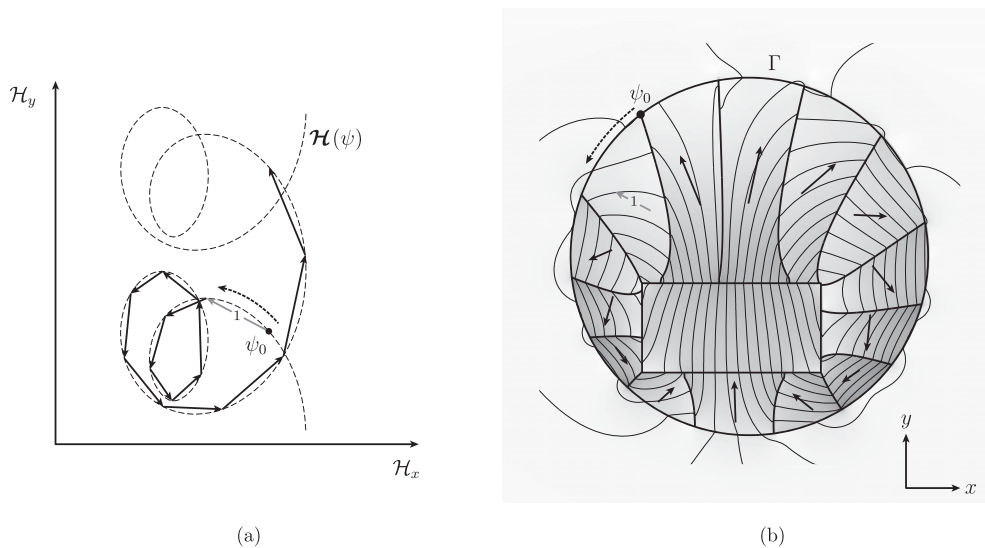


FIG. 4. The segmentation of a circular design region with a decentered rectangular cavity is shown in (b). The objective functional \mathcal{S} is the y component of the field integrated over the rectangular air gap. The curve $\mathcal{H}(\psi)$ and its optimal segmentation are shown in (a) as, respectively, a dashed curve and a collection of adjacent arrows. The arrows represent the optimal segmentation of the curve, their direction indicates the optimal direction of the remanence in each segment, and their length is proportional to the contribution to the value of \mathcal{S} from each segment. The norm of the remanence is the same for all segments.

for $N = 14$ segments is determined numerically from $\mathcal{H}(\psi)$ with a separate optimization step. The point $\mathcal{H}(\psi_0)$ is indicated by the black dot in Fig. 4(a) and corresponds to the point of the external border indicated in Fig. 4(b). The vectors \mathcal{H} resulting from the optimal segmentation are indicated as arrows in both the panels; the gray arrow indicates the direction of \mathcal{H} for the first segment.

C. Systems including iron

We now consider two examples which also involve high-permeability material. For these systems, we use FEM calculations to compute the virtual field. In both the cases pictured in Figs. 5(a) and 5(b), the position of the iron yokes and core is predetermined, but the border between hard magnets and air is optimal with the given volume constraint and so are the borders between the different segments. The parts of the geometry corresponding to the iron are represented as hatched areas.

The objective in the example of Fig. 5(a), which is a model of a permanent-magnet electric motor, is to create a quadrupole field directed radially and located in the air gap between the magnets and the external iron yoke. The virtual remanence is expressed in cylindrical coordinates as $\mathbf{B}_{r2}(\rho, \phi) = \hat{e}_\rho \sin(2\phi)$. The design area is the region between the internal border of the air gap and the external border of the iron core. To illustrate how the optimal border between iron and permanent magnet can be found, we put an arbitrary constraint on the magnet volume. In this example, we arbitrarily require that the magnet occupies 80% of the original design area and that the remaining part is filled with air. We then calculate the optimal border between magnet and air that is consistent with this constraint. The result is that the four regions adjacent to the inner iron core are excluded from the design area, as is visible in Fig. 5(a). Even though the objective of the optimization algorithm is the intensity of the field rather

than its quality, the result of this example reproduces the desired field shape quite accurately.

In case of Fig. 5(b), the objective is, again, as in the yokeless Halbach example, to maximize the field in the x direction averaged over the inner circular cavity. In this case, the design area is the region between the internal border of the iron yoke and the external border of the circular cavity. We arbitrarily require that the magnet occupies 70% of the original design area. The remaining part is then filled with air, and the optimization of the border between magnet and air determines the shape of the two empty regions that are visible in Fig. 5(b). Despite the fact that the virtual magnet of this example is identical to the one of the Halbach cylinder, the virtual field \mathbf{H}_2 is not given by Eq. (11) for this case, since the presence of the iron yoke affects the solution. The consequence is that the optimal direction of the remanence with respect to the linear objective is different for the two cases and so are the optimal borders between magnets and air and the ones between adjacent segments.

It is insightful to compare the yoked and yokeless cylinders for the ideal case of a remanence field of constant norm but continuously varying direction. Because of its self-insulation properties, an ideal Halbach cylinder whose remanence field is described by Eq. (5) generates the same field if an iron yoke is introduced at its external border. In the presence of the yoke, the Halbach solution, which is still optimal with respect to the purpose of generating a perfectly uniform field, is not the one producing the highest field intensity, i.e., maximizing the linear objective. Conversely, the field generated by the ideal solution corresponding to the highest intensity is not perfectly homogeneous.

Both examples in this section show the orthogonality between the optimal remanence and border between the magnet and iron. We see that the border between the magnet and air is always normal to the border between two segments. This is a consequence of the virtual field being both solenoidal and irrotational.

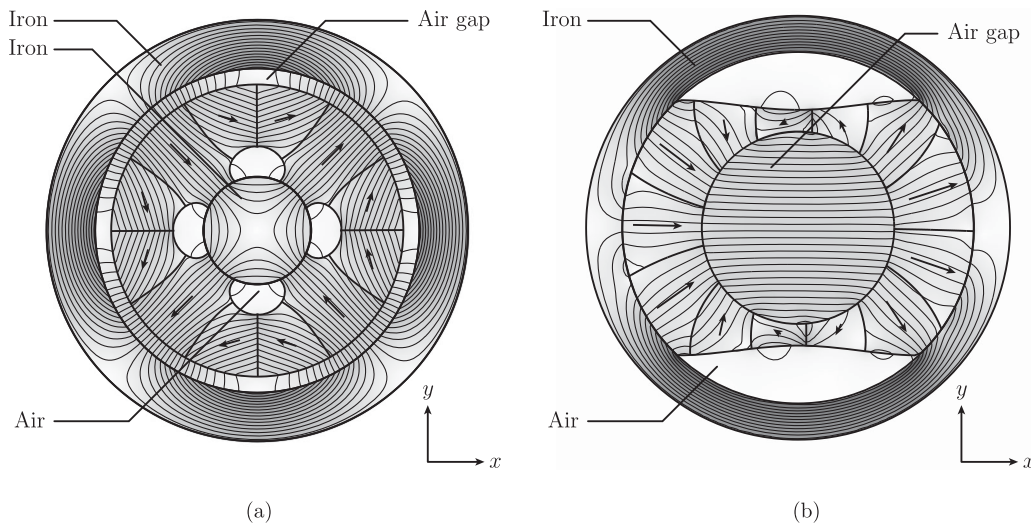


FIG. 5. Two examples of geometries involving iron parts and a constraint on the amount of magnetic material. (a) Quadrupole motor and (b) Yoked Halbach. In both examples the borders between the magnets and the parts of the design region filled with air have the optimal shape with respect to the constraint on the magnet volume. The arrows indicate the optimal segmentation of the curve $\mathcal{H}(\psi)$; thus, the length of each arrow corresponds to the contribution from that segment to the value of the objective \mathcal{S} .

D. Comparison with uniform field magnets

It is instructive to compare the results of our method, which can also be applied to maximize the field along one direction averaged over a closed air gap, with another design approach which starts with the assumption that the field is perfectly homogeneous.

Abele and Rusinek [26–28] developed an elegant framework for the design of segmented magnetic systems which can generate a perfectly uniform field \mathbf{H}_0 inside a closed cavity and are perfectly self-insulated from the surroundings. We consider the results in two-dimensional yokeless magnetic systems composed of a uniformly magnetized prism with triangular cross sections. We assume that the permanent-magnet material has zero susceptibility and that the norm B_r of the remanent flux density is constant. Any region of the system which is not occupied by magnet is occupied by air.

The closed cavity is a polygon with Q sides, which may be irregular. A single-layer structure in this framework must be composed of exactly $N = 3Q$ segments. Once the shape of the cavity is fixed, the geometry of the structure is entirely determined by two decisions: the ratio $K = H_0/B_r$ between the norm of the field inside the cavity and the norm of the remanence and the position of a point \mathbf{x}_F inside the cavity in which the magnetic scalar potential is zero. The direction of \mathbf{H}_0 determines the direction of the remanence of each segment, but it does not affect the geometry of the system. When the cavity is a regular polygon, the center of the polygon is the position of \mathbf{x}_F which minimizes the volume V_m of magnetic material and leads to the highest efficiency. An example is shown in Fig. 6(a): the cavity is an equilateral triangle, the field \mathbf{H}_0 is oriented in the y direction, and the point \mathbf{x}_F is in the center of the triangle.

This approach differs from the one presented in this paper since the resulting field is perfectly uniform, but the approach cannot be applied to any other objective, except the generation of a uniform dipole field. Moreover, there is a constraint on

the number of segments, and for single-layer structures, the volume of the magnet goes to infinity as H_0 goes to B_r . Since both are segmentation algorithms, it is interesting to compare the performance of the two approaches. This is best done by calculating the figure of merit \mathcal{M} introduced in Eq. (6). We consider magnetic assemblies designed to generate a field in the y direction; therefore, we replace \mathbf{B}_1 in the numerator of Eq. (6) with its y component. For the case of a uniform field, this replacement has no effect, but it is a more realistic way to estimate the efficiency of our method, since the field is not perfectly uniform. We also introduce the figure of merit η which characterizes the homogeneity of the field and is zero for a uniform field:

$$\eta = \frac{\langle B_1^2 \rangle - \langle B_1 \rangle^2}{\langle B_1^2 \rangle}. \quad (19)$$

The efficiency and uniformity with the two approaches are compared in Figs. 7(a) and 7(b) for different values of magnet volume V_m and for different shapes of the inner cavity: an equilateral triangle $Q = 3$ and octagon $Q = 8$ indicated by red and blue lines, respectively. We also consider a rectangular cavity $Q = 4$ with a width that is double the height, indicated by the green lines. The results are plotted as a function of the ratio $V_m : V_g$ between the volume of the magnet and the volume of the cavity V_g . The dashed lines indicate uniform field magnets realized with $N = 3Q$ segments, and the dotted or solid lines indicate the magnets optimized for field average using our approach. Since within our framework it is possible to choose of the number of segments, we consider the cases $N = 3Q$ and $N = 2Q$ indicated by the solid lines and the dotted lines, respectively. The efficiency of the Halbach cylinder with continuously varying remanence is indicated in Fig. 7(a) by the black dash-dot line.

Even if \mathcal{M} is not equivalent to the objective functional \mathcal{S} of our optimization approach, the results of this method

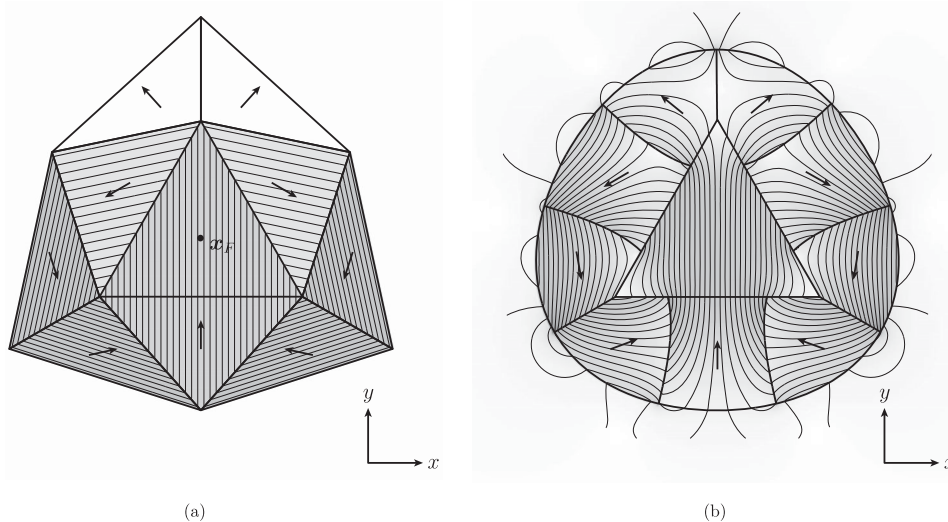


FIG. 6. Comparison between the two possible ways to segment the magnetic system designed to generate a field in the central triangular cavity and oriented in the y direction. (a) The segmented system which creates a perfectly uniform field inside the cavity. (b) The segmentation determined using our method, which maximizes the y component of the field averaged over the central cavity. The volume V_m of magnetic material is the same in the two cases. The arrows indicate the remanence inside each segment. The configuration of (a) produces a field that is also uniform inside each magnet segment. In the two blocks that are on top, the flux density is zero since $\mu_0 \mathbf{H}_1 = -\mathbf{B}_{r1}$.

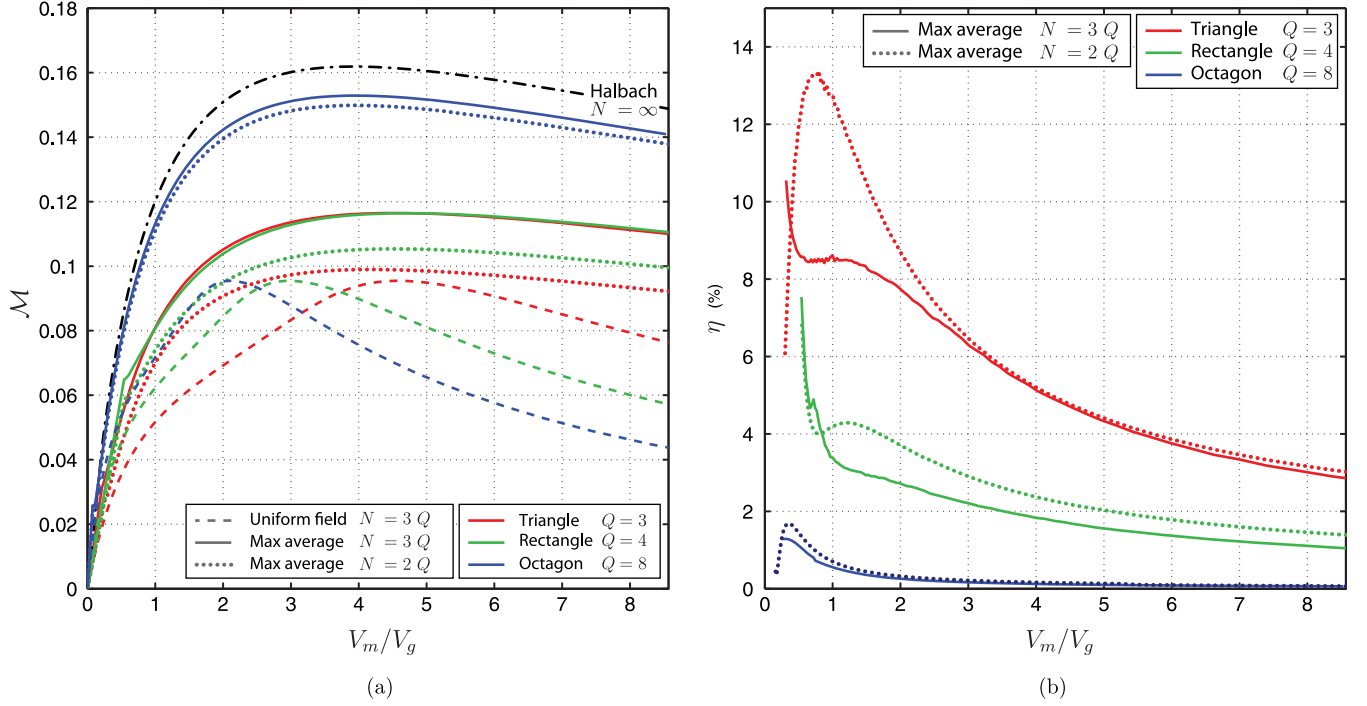


FIG. 7. Comparison between the performance of the two segmentation approaches for different shapes of the inner cavity. (a) The value of the efficiency figure of merit \mathcal{M} . (b) The value of the homogeneity figure of merit η . In both panels, the results are plotted as a function of the ratio $V_m:V_g$.

are characterized by a high efficiency when compared to the uniform field designs, even with a smaller number of segments. The choice of a magnet volume higher than the optimal, which results in higher values of field, does not decrease the efficiency with our method as it does for single-layer uniform field magnets.

The uniformity figure of merit η is shown in Fig. 7(b). The field is more uniform for the case of the rectangle than it is for the triangle and even more uniform for the case of the octagon. In all cases, the value of η is $\lesssim 5\%$ for magnet volumes above the maximum efficiency \mathcal{M} . The data points corresponding to very small magnet volumes are slightly affected by the numerical noise arising from the fact that the calculation of the curve $\mathcal{H}(\psi)$ is performed by a numerical integration. The estimation of the parameter η for small volumes is particularly affected by the noise, and, therefore, a few data points are omitted from Fig. 7(b). The limit $V_m \rightarrow 0$ is also not very relevant for practical applications since $\mathcal{M} \rightarrow 0$.

The result of the comparison between the two approaches shows the trade-off between field intensity and quality. Whenever the objective vector field $\mathbf{u}(\mathbf{x})$ is also a physically acceptable magnetic field, the configurations optimized with respect to the linear objective \mathcal{S} can be directly compared with configurations optimized by using other techniques that use as an objective the quality of the field. This class of optimization problems is formulated as the minimization of a nonlinear objective functional such as [19]

$$\mathcal{D}[\mathbf{H}_1] = \left(\int d^3x \|\mathbf{H}_1(\mathbf{x}) - \mathbf{u}(\mathbf{x})\|^2 \right)^{1/2}. \quad (20)$$

The linear objectives introduced in Sec. II A are suitable for magnet design problems where the main goal is to maximize the average intensity of the field in the direction given by $\mathbf{u}(\mathbf{x})$ using a fixed amount of permanent-magnet material. This problem is equivalent to minimizing the amount of permanent magnet that is necessary to obtain the same value of \mathcal{S} . Even though in many cases our approach is also able to reproduce with a good approximation the desired field shape \mathbf{u} , the accuracy of the generated field with respect to the required distribution is not the objective of the optimization method presented in this work. The design of magnetic systems for applications that require a very high field precision must be carried out with different techniques. A possibility is to combine the procedure described here with subsequent optimization schemes aimed at correcting small field distortions, such as the ones proposed in Refs. [8,15,16]. It is also worth mentioning that the relevance of linear functionals goes beyond those optimization problems that are directly described by this class of objectives, as the theoretical results obtained for linear functionals provide insight into general characteristics of magnet design problems.

V. THREE-DIMENSIONAL SYSTEMS

As we mention above, the segmentation procedure does not immediately generalize to three dimensions.

Nevertheless, one may ask to what extent the segmentation approach can be employed to optimize the segmentation of three-dimensional magnetic systems. The result presented in Appendix A is true for three-dimensional geometries as well: it is not advantageous to subdivide a region of constant direction of the virtual field, that is, a region $R(\vartheta, \psi)$ for which the inclination angle and the azimuthal angle of the virtual field are both constant. As we mention in Sec. III, the additional degree of freedom means that the globally optimal solution must be searched for among all the possible ways of partitioning the ϑ - ψ plane into a given number of regions. The procedure described in Appendix B does not provide the solution to this problem. On the other hand, applying the one-parameter segmentation procedure to the whole design area is too restrictive for most three-dimensional problems. One strategy is to apply the segmentation procedure separately to different parts of the design region identified beforehand. This preliminary decision can be based on considerations about the symmetries exhibited by the geometry of the magnetic system.

For the illustrative examples presented in this section, the symmetry suggests that the design area can be initially subdivided into smaller regions R_j ($j = 1, \dots, N$) separated by level surfaces of the inclination angle ϑ . Our procedure is then applied independently to each of the regions R_j to determine the values of the azimuthal angle ψ that optimize the splitting of R_j into N_j segments. It must be stressed that the subdivisions between the regions R_j and the combinations between the number of segments N_j assigned to each region have to be decided beforehand or determined with a separate optimization step.

The geometry of the first example shown in Fig. 8(a) is a three-dimensional generalization of the Halbach cylinder geometry considered in Sec. IV A. The objective is to maximize the z component of the field averaged over the internal spherical cavity. The ideal Halbach sphere with

continuously varying remanence produces in the bore a perfectly homogeneous flux density, whose norm is given by [6] $B_{\text{ideal}} = (4/3)B_r \log(R_O/R_I)$, where R_O and R_I are the external and internal radii of the spherical shell, respectively. The continuously varying remanence field optimized with our approach produces a field that is not perfectly homogeneous, but slightly more intense. The air gap average of the z component of the flux density for the ratio $R_O = 2R_I$, i.e. the value used in the example, is $B_{\text{continuous}} \approx 1.03B_{\text{ideal}}$.

We consider all the possible ways to subdivide this geometry into five regions delimited by level surfaces of the inclination angle ϑ of the virtual field \mathbf{H}_2 . Since \mathbf{H}_2 is the field generated by a uniformly magnetized sphere, the knowledge of the analytical solution allows us to take advantage of the symmetries to simplify the procedure. This means that we are able to consider all the possible combinations of number of segments N_j for each region and all the possible values of ϑ determining the subdivisions between these regions. The calculations show that the maximum value of the average air-gap flux density for this family of segmentations corresponds to $0.945B_{\text{continuous}}$.

Figure 8(a) shows the segmentation corresponding to the best combinations of the parameters for a total number of segments equal to $N_{\text{tot}} = 17$. Some of the magnet segments are not displayed in the picture; moreover, some of them are bisected by the plane $y = 0$, and the blue surfaces indicate internal cross sections of the bisected blocks, while the gray surfaces are the boundaries of the segments. Each of the two symmetrical polar regions is subdivided into three identical segments. Because of the symmetry, it is not advantageous to subdivide the equatorial region, as all the resulting segments will be magnetized in the z direction. Each of the two symmetrical regions between the poles and the equator is subdivided into five identical segments. The average air-gap flux density for this segmentation is $0.889B_{\text{continuous}}$.

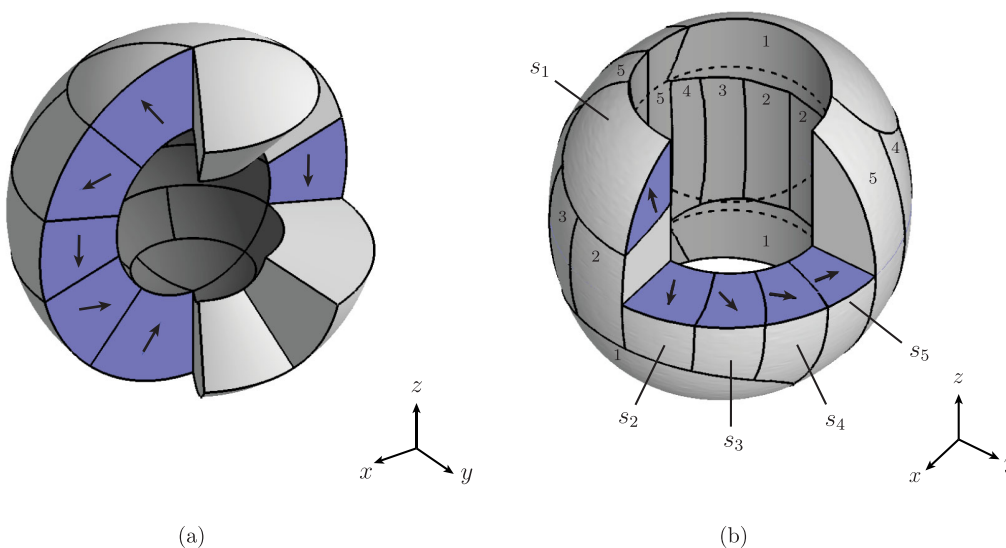


FIG. 8. Three-dimensional segmented magnetic structures optimized with respect to the average field inside the air gap. (a) Halbach sphere. The field is in the z direction, and the number of segments is $N_{\text{tot}} = 17$. (b) Finite-length Halbach cylinder. The field is in the x direction, and the number of segments is $N_{\text{tot}} = 20$.

The second example shown in Fig. 8(b) analyzes how the Halbach cylinder design can be modified when the effects of finite length in the z direction are taken into account. The objective is to maximize the x component of the field averaged over the region of the internal cylindrical cavity R_g that is delimited by the two circles indicated by the black dashed lines. Since for many applications it is desirable that the cavity is accessible from the top and from the bottom, the magnet design region extends only on the sides of the cylindrical cavity.

The figure represents a section of the geometry where the first octant is not displayed. Again, the blue surfaces represent sections cutting some magnet block in the middle, while the gray surfaces are all external boundaries of the blocks. As indicated by annotations on the graph, the magnet area is subdivided into five unique shapes denoted by s_1, \dots, s_5 . There are four copies of the shape s_1 , one for each quadrant of the x - z plane, and four copies of each of the shapes s_2, \dots, s_4 , one for each quadrant of the x - y plane. The total number of segments is, thus, $N_{\text{tot}} = 20$.

The external border of the magnet is a level surface of H_2 . Segments s_1 are delimited by level surfaces of ϑ , and the interfaces between segments s_2, \dots, s_4 are level surfaces of ψ . The regions occupied by each of the segments s_1 could have been subdivided as well, using levels of ψ ; however, as the direction of the virtual field is quite homogeneous over each of these regions, the advantage of this subdivision would have been minor. The x component of the flux density averaged over the air gap R_g is 5% greater for the magnetic system of Fig. 8(b) than it is for a conventionally segmented Halbach cylinder having the same magnet volume and the same number of segments N_{tot} .

It is noticed that the portion of the magnet area extending above the dashed lines is mainly occupied by segments s_1 and s_5 . This part of the magnet area can be thought of as an additional structure that can be attached to the conventional Halbach cylinder geometry in order to reduce the detrimental border effects and presents similarities with the structure proposed in Ref. [29].

VI. CONCLUSION

In conclusion, we present an approach which automatically gives the optimal design of magnetic systems with respect to any linear objective functional. For the case of hard magnets with zero susceptibility, the approach provides the globally optimal shape of the external border between magnet and air with a given volume constraint. The method also gives the globally optimal segmentation of two-dimensional systems with a given number of uniformly magnetized segments. This approach is versatile and being based on an analytical framework, it can be implemented into a fast and efficient algorithm, and the optimality is guaranteed.

ACKNOWLEDGMENTS

This work is financed by the ENOVHEAT project which is funded by Innovation Fund Denmark (Contract No. 12-132673).

APPENDIX A: Optimal segment borders

In this section, we show that an optimal segmentation consists of segments whose mutual borders are lines of constant direction of the virtual field. This we do by showing that any segmentation which has a curve section $R(\psi)$ of constant ψ divided between two segments can always be replaced by a segmentation which assigns $R(\psi)$ completely to one segment and which is at least as good as the original segmentation.

We start with the objective functional \mathcal{S} defined in Eq. (3) in terms of the field \mathbf{H}_1 and expressed in terms of the remanence \mathbf{B}_{r1} as

$$\mathcal{S}[\mathbf{H}_1] = \int d^2x \mathbf{B}_{r1}(\mathbf{x}) \cdot \mathbf{H}_2(\mathbf{x}), \quad (\text{A1})$$

where \mathbf{H}_2 is the virtual field. The optimization for the continuous case is immediate: we simply choose a remanence which in all points of the design region is aligned with \mathbf{H}_2 . Assuming that the remanence is constant in magnitude (and setting this magnitude equal to unity for convenience), we get the optimized value of the functional:

$$\mathcal{S}_{\text{continuous}} = \int_{R_m} d^2x \|\mathbf{H}_2(\mathbf{x})\|. \quad (\text{A2})$$

We now consider the segmentation of the design area R_m into N segments. We introduce the characteristic functions $\phi_n(\mathbf{x})$ that determine to which segment the point \mathbf{x} is assigned. They can assume only the values 0 or 1. If a given point \mathbf{x} is assigned to the k th segment, $\phi_k(\mathbf{x}) = 1$ while $\phi_{n \neq k}(\mathbf{x}) = 0$. The objective functional \mathcal{S} corresponding to the segmentation $\{\phi_n\}$ is then given by

$$\mathcal{S}[\{\phi_n\}] = \sum_{n=1}^N \mathbf{B}_{r1}(n) \cdot \int d^2x \phi_n(\mathbf{x}) \mathbf{H}_2(\mathbf{x}), \quad (\text{A3})$$

since $\mathbf{B}_{r1}(n)$ is constant on segment n . Now, the direction of the optimal remanence $\mathbf{B}_{r1}^{\text{opt}}(n)$ for the n th segment is clearly aligned with $\int d^2x \phi_n(\mathbf{x}) \mathbf{H}_2(\mathbf{x})$. As before, we can then write \mathcal{S} as

$$\mathcal{S}[\{\phi_n\}] = \sum_{n=1}^N \left\| \int d^2x \phi_n(\mathbf{x}) \mathbf{H}_2(\mathbf{x}) \right\|. \quad (\text{A4})$$

Thus, the problem of finding an optimal segmentation is equivalent to finding a set of characteristic functions $\{\phi_n\}$ which maximize the value of \mathcal{S} in Eq. (A4).

To proceed we make a change of integration variables. Each set $R(\psi_a) = \{\mathbf{x} : \psi(\mathbf{x}) = \psi_a\} \cap R_m$ defined by a particular value of ψ_a is a finite-length segment of a curve of

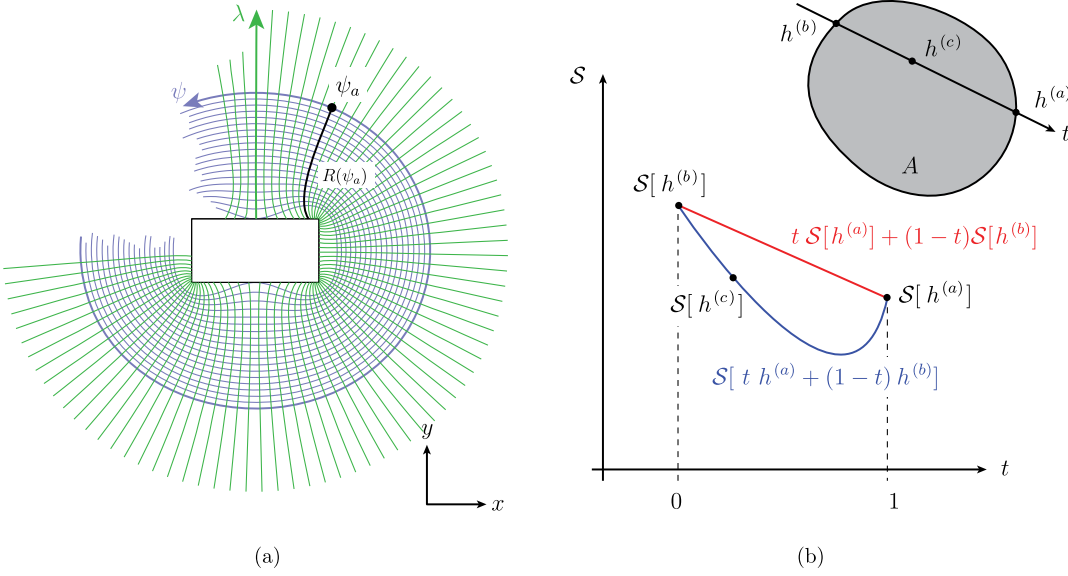


FIG. 9. (a) The coordinate transformation $\mathbf{x} \rightarrow (\psi, \lambda)$ is illustrated on an example geometry. (b) A convex set A and the value of the convex function S over a line segment traced between two points $h_n^{(a)}(\psi)$ and $h_n^{(b)}(\psi)$ belonging to the boundary of A , illustrating that either $S[h^{(a)}]$ or $S[h^{(b)}]$ is greater than or equal to the value of S for any other point on the line segment.

constant direction of the virtual field; it can be parametrized by some coordinate λ of finite range. We can then perform the coordinate transformation $\mathbf{x} \rightarrow (\psi, \lambda)$, as illustrated in Fig. 9(a). One possible choice for λ is the curve length along $R(\psi)$ from the external border of the design area. It is possible to show that if the permeability is uniform over the design area, the contour lines of ψ are also field lines of ∇H_2 . This implies that H_2 is monotonic along each $R(\psi)$ and is another possible choice for the parameter λ . We now write $\mathbf{H}_2(\mathbf{x})$ as $H_2(\mathbf{x})\hat{\mathbf{e}}_\psi$, where $\hat{\mathbf{e}}_\psi = \cos(\psi)\hat{\mathbf{e}}_x + \sin(\psi)\hat{\mathbf{e}}_y$. Then the functional \mathcal{S} can be written as

$$\mathcal{S} = \sum_{n=1}^N \left\| \int d\psi \hat{\mathbf{e}}_\psi \int_{R(\psi)} d\lambda \phi_n(\mathbf{x}(\psi, \lambda)) H_2(\mathbf{x}(\psi, \lambda)) g(\psi, \lambda) \right\|, \quad (\text{A5})$$

where $g(\psi, \lambda)$ is the absolute value of the determinant of the Jacobian of this transformation. Let us now define $h(\psi)$ as the total contribution to \mathcal{S} from the set $R(\psi)$:

$$h(\psi) = \int_{R(\psi)} d\lambda H_2(\psi, \lambda) g(\psi, \lambda). \quad (\text{A6})$$

We also define $h_n(\psi)$ as the amount of $h(\psi)$ that is assigned to the n th segment:

$$h_n(\psi) = \int_{R(\psi)} d\lambda \phi_n(\psi, \lambda) H_2(\psi, \lambda) g(\psi, \lambda). \quad (\text{A7})$$

Using the definition of the functions ϕ_n , it can immediately be seen that $h_n(\psi) \geq 0$ for all n and that the following relation holds for all ψ :

$$\sum_{n=1}^N h_n(\psi) = h(\psi). \quad (\text{A8})$$

The functional \mathcal{S} to be optimized can then be written as

$$\mathcal{S}[\{\phi_n\}] = \sum_{n=1}^N \left\| \int d\psi h_n(\psi) \hat{\mathbf{e}}_\psi \right\|. \quad (\text{A9})$$

The only dependence of \mathcal{S} on ϕ_n is through the functions $h_n(\psi)$. Finding an optimal segmentation is then equivalent to finding a set of optimal functions $h_n(\psi)$. This fact makes the search space \mathcal{X} equal to the space of all the N -dimensional vector functions defined over the interval of the real axis spanned by the values of ψ , subject to the conditions of non-negativity and the sum rule expressed in Eq. (A8). The sum between two elements $h^{(a)}$ and $h^{(b)}$ of \mathcal{X} is defined in the usual way:

$$\begin{aligned} \text{if } h^{(c)} &= h^{(a)} + h^{(b)} \text{ then} \\ h_n^{(c)}(\psi) &= h_n^{(a)}(\psi) + h_n^{(b)}(\psi), \quad \forall \psi, n. \end{aligned} \quad (\text{A10})$$

Similarly, multiplication of $h^{(a)}$ by the scalar c is defined through

$$\text{if } h^{(c)} = c h^{(a)} \text{ then } h_n^{(c)}(\psi) = c h_n^{(a)}(\psi), \quad \forall \psi, n. \quad (\text{A11})$$

These operations satisfy all the necessary properties that make \mathcal{X} a vector space.

We can show that the functional \mathcal{S} is convex with respect to $h_n(\psi)$. By definition, this means that if we consider two arbitrary vectors $h_n^{(a)}(\psi)$ and $h_n^{(b)}(\psi)$ and a scalar parameter $t \in [0, 1]$, the following property is always obeyed:

$$\begin{aligned} \mathcal{S}[t h^{(a)} + (1-t) h^{(b)}] &\leq (t) \mathcal{S}[h^{(a)}] + (1-t) \mathcal{S}[h^{(b)}] \\ &\leq \max(\mathcal{S}[h^{(a)}], \mathcal{S}[h^{(b)}]). \end{aligned} \quad (\text{A12})$$

This property can be shown by considering each member of the summation over n appearing in Eq. (A9) and applying the absolute homogeneity property of the norm and the triangle inequality.

We now restrict the search to a set $A \subset \mathcal{X}$ defined by the conditions of non-negativity and the sum rule of Eq. (A8):

$$A = \left\{ h_n(\psi) : \underbrace{\sum_{n=1}^N h_n(\psi) = h(\psi)}_{\text{equality}}, \quad \underbrace{h_n(\psi) \geq 0}_{\text{inequality}}, \quad \forall \psi \right\}. \quad (\text{A13})$$

We observe that the set A is convex, since for any two points $h_n^{(a)}(\psi)$ and $h_n^{(b)}(\psi)$ belonging to the set and a value of $t \in [0, 1]$, all the points on the line segment $th^{(a)} + (1-t)h^{(b)}$ also belong to the set.

Let us then consider a particular solution $h_n^{(c)}$ for which there is at least one value of ψ denoted ψ' for which $R(\psi')$ is subdivided between more than one segment. This assumption means that there exists an n' for which $h_{n'}^{(c)}(\psi')$ is strictly between 0 and $h(\psi')$. We now define two additional points $h^{(a)}$ and $h^{(b)}$, which for $\psi \neq \psi'$ are equal to $h_n^{(c)}$. For $\psi = \psi'$, we set

$$h_{n'}^{(a)}(\psi') = 0, \quad h_{n \neq n'}^{(a)}(\psi') = h(\psi') \frac{h_n^{(c)}(\psi')}{\sum_{j \neq n'} h_j^{(c)}(\psi')}, \quad (\text{A14})$$

and

$$h_{n'}^{(b)}(\psi') = h(\psi'), \quad h_{n \neq n'}^{(b)}(\psi') = 0. \quad (\text{A15})$$

Evidently, the point $h^{(a)}$ corresponds to a segmentation identical to $h^{(c)}$ except that $R(\psi')$ is assigned entirely to the segment n' . Similarly, $h^{(b)}$ has nothing of $R(\psi')$ assigned to n' . The line segment $th^{(a)} + (1-t)h^{(b)}$ for $t \in [0, 1]$ is entirely inside the set A , but for $t < 0$ or $t > 1$, we are outside of A . The points $h^{(a)}$ and $h^{(b)}$ are, thus, on the boundary of A , and the original point $h^{(c)}$ is an interior point of the segment corresponding to $t = h_{n'}^{(c)}(\psi')/h(\psi')$. Because of the convexity of \mathcal{S} , Eq. (A12) is obeyed for all the points on the line segment. Moreover, $t\mathcal{S}[h^{(a)}] + (1-t)\mathcal{S}[h^{(b)}]$, which is the right-hand side of Eq. (A12), is always smaller than or equal to its value at one of the end points, $h^{(a)}$ or $h^{(b)}$. This argument is illustrated in Fig. 9(b) and shows that either $h^{(a)}$ or $h^{(b)}$ gives a value of \mathcal{S} that is greater than or equal to $\mathcal{S}[h^{(c)}]$. Therefore, for any solution in which the set $R(\psi')$ is partially assigned to the segment n' , there is a solution giving a greater or equal value of \mathcal{S} ,

for which $R(\psi')$ is either entirely assigned to the segment n' or not at all.

Thus, we show that assigning each set $R(\psi)$ entirely to a single segment gives a value of \mathcal{S} which is equal to the maximum possible value achievable with N segments.

We are now left with the problem of determining how to assign each $R(\psi)$ to one of the N segments. However, until this point, we never enforced that the segments should be connected regions. This requirement implies that each segment corresponds to a single interval $[\psi_{n-1}, \psi_n]$:

$$h_n(\psi) = h(\psi), \quad \forall \psi \in [\psi_{n-1}, \psi_n]. \quad (\text{A16})$$

The border between the segments n and $n+1$ is, thus, given by the contour line $R(\psi_n)$, and the problem is reduced to the determination of the optimal splitting angles ψ_n (see Appendix B).

APPENDIX B: Optimal splitting angles

In this section, we show how to select which of the contour lines of ψ will lead to an optimal segmentation, given the total number of segments. Instead of $\arctan(H_y/H_x)$, we consider the accumulated angle ψ informally introduced in Sec. III. In order to define the accumulated angle precisely, we consider a curve $\Gamma: t \in [0, 1] \rightarrow \mathbf{x}(t)$, and we assume that \mathbf{H}_2 is rotating counterclockwise as we move along the curve. The purpose of Γ is to create a one-to-one correspondence between the contour lines $R(\psi_n)$ and the continuous parameter $t \in [0, 1]$. The accumulated angle is defined for each t as the angle ψ which is obtained by shifting $\arctan(H_y/H_x)$ by a number of complete revolutions, which is determined by requiring monotonicity and continuity. The monotonicity property means that $(d/dt)\psi[\mathbf{x}(t)] > 0, \forall t \in [0, 1]$. The continuity property means that if $t_a \rightarrow t_b$, then $\psi(t_a) \rightarrow \psi(t_b)$. If the curve Γ is closed, we also have the following continuity property across the starting point: if $t_a \rightarrow 0^+$ and $t_b \rightarrow 1^-$, then $\psi(t_b) - \psi(t_a) \rightarrow n2\pi$, where n is the number of revolutions performed by \mathbf{H}_2 from the first point $t = 0$ to the last point $t = 1$. The curve Γ can be constructed by starting from an arbitrary point and proceeding in a way such that each $R(\psi)$ is intersected once and only once. However, as long as ψ is monotonic, the result is the same for all the choices of Γ .

Since we assume that the union of all the ψ contour lines passing by the points of the curve Γ is coincident with the whole design area R_m , the definition of the accumulated angle ψ can be extended to any other point of R_m that is not on Γ .

We now define the region $\mathcal{R}_{[\psi_0, \psi_1]}$ as the set of points \mathbf{x} in the magnet design area in which the orientation angle ψ of the virtual field \mathbf{H}_2 is in the interval $[\psi_0, \psi_1]$,

$$\mathcal{R}_{[\psi_0, \psi_1]} = \{\mathbf{x} : \psi[\mathbf{H}_2(\mathbf{x})] \in [\psi_0, \psi_1]\} \cap R_m. \quad (\text{B1})$$

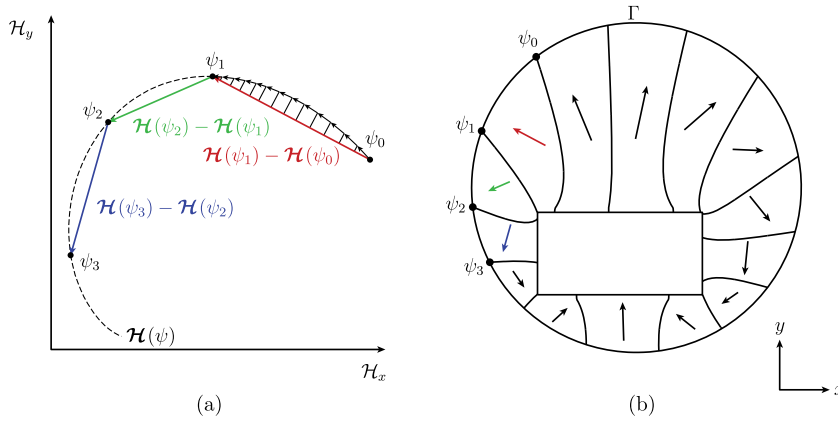


FIG. 10. In the continuous case, the optimal remanence is normalized and aligned at any point with the virtual field. This implies that the value of \mathcal{S} is given by the length of the curve $\mathcal{H}(\psi)$. In the segmented case, the contribution from a point belonging to a certain segment is proportional to the scalar product between the virtual field and the optimal remanence for that segment. This implies that the direction of the vector $\mathcal{H}(\psi_1) - \mathcal{H}(\psi_0)$ is also the optimal direction of the remanence, and its length is equal to the contribution from that segment to the total value of \mathcal{S} . (a) The curve $\mathcal{H}(\psi)$ and its segmentation. (b) The corresponding segmented geometry.

The regions so defined satisfy $\mathcal{R}_{[\psi_0, \psi_2]} = \mathcal{R}_{[\psi_0, \psi_1]} \cup \mathcal{R}_{[\psi_1, \psi_2]}$ for all $\psi_1 \in [\psi_0, \psi_2]$.

The integrated magnetic field vector associated with this region is

$$\mathcal{H}_{[\psi_0, \psi_1]} = \int_{\mathcal{R}_{[\psi_0, \psi_1]}} d^2x \mathbf{H}_2(\mathbf{x}) = \int_{\psi_0}^{\psi_1} d\psi h(\psi) \hat{\mathbf{e}}_\psi \quad (\text{B2})$$

with $h(\psi)$ defined in Eq. (A6). The symbol \mathcal{H} denotes the integral of a field over a region of space. These vectors satisfy the property $\mathcal{H}_{[\psi_0, \psi_2]} = \mathcal{H}_{[\psi_0, \psi_1]} + \mathcal{H}_{[\psi_1, \psi_2]}$ for all $\psi_1 \in [\psi_0, \psi_2]$.

Once a starting point $\psi_0 = \psi[\mathbf{x}(t=0)]$ is fixed, it is possible to parametrize the vectors associated with the different regions by just using the value ψ of the ending point; the following notation is used: $\mathcal{H}(\psi) = \mathcal{H}_{[\psi_0, \psi]}$. The velocity vector associated with this parametrized curve is denoted by $\mathbf{h}(\psi) = (d/d\psi)\mathcal{H}(\psi) = h(\psi)\hat{\mathbf{e}}_\psi$.

An example geometry and the corresponding curve $\mathcal{H}(\psi)$ are shown in Figs. 10(b) and 10(a), respectively.

In the continuous case, the contribution to \mathcal{S} from the interval $[\psi_0, \psi_1]$ is equal to the length of the corresponding arc of curve:

$$\begin{aligned} \mathcal{S}_{\text{continuous}} &= \int_{\mathcal{R}_{[\psi_0, \psi_1]}} d^2x \|\mathbf{H}_2(\mathbf{x})\| \\ &= \int_{\psi_0}^{\psi_1} d\psi \|\mathbf{h}(\psi)\| \\ &= \int_{\psi_0}^{\psi_1} d\psi h(\psi). \end{aligned} \quad (\text{B3})$$

In the segmented case, the contribution to \mathcal{S} is the length of the segment between the curve end points

$$\begin{aligned} \mathcal{S}_{\text{segmented}} &= \left\| \int_{\mathcal{R}_{[\psi_0, \psi_1]}} d^2x \mathbf{H}_2(\mathbf{x}) \right\| \\ &= \left\| \int_{\psi_0}^{\psi_1} d\psi \mathbf{h}(\psi) \right\| = \|\mathcal{H}(\psi_1) - \mathcal{H}(\psi_0)\|. \end{aligned} \quad (\text{B4})$$

When considering more than one segment, the value of $\mathcal{S}_{\text{segmented}}$ is given by the length of the polygonal line inscribed in $\mathcal{H}(\psi)$.

The problem of optimal segmentation is reduced to the problem of piecewise linear approximation of plane curves by perimeter optimization.

The globally optimal solution for this problem can always be found by employing a dynamic programming approach. This class of algorithms makes use of the optimal substructure exhibited by the problem in order to reduce its computational complexity. An algorithm for the curve approximation problem can be found in Ref. [24].

If the curve Γ is closed, it is possible to consider the dependence of \mathcal{S} on the starting point ψ_0 to determine the optimal starting point. A necessary but not sufficient condition for this is that the design area encloses the air gap completely. Once the curve $\mathcal{H}(\psi)$ is computed, this is not a computationally intensive procedure and can be performed as the last step of the optimization.

It is worthwhile to mention that the procedure described in this section can be generalized to different continuously parametrized segmentations in order to meet other design requirements. In this case, the final configuration is only optimal with respect to the considered search space. Let us consider the simple example of a rectangular design area R_m and the family of rectangular subsets:

$$\mathcal{R}_{[x_0, x_1]} = \{\mathbf{x} : x \in [x_0, x_1]\} \cap R_m. \quad (\text{B5})$$

The curve $\mathcal{H}(x)$ can be constructed from this parametrized set of rectangles as in Eq. (B2). The optimal segmentation of this curve with a given number of segments provides the set of values of x corresponding to the optimal splitting lines among the ones allowed by Eq. (B5). Any family of regions defined by a single parameter and obeying the same properties as described above can be considered with the purpose of constraining the shapes of the resulting segments as desired, by relaxing the condition of having an optimal shape of the border between two adjacent segments.

- [1] O. Gutfleisch, M. A. Willard, E. Brück, C. H. Chen, S. G. Sankar, and J. P. Liu, Magnetic materials and devices for the 21st century: Stronger, lighter, and more energy efficient, *Adv. Mater.* **23**, 821 (2011).
- [2] J. M. D. Coey, Permanent magnet applications, *J. Magn. Mater.* **248**, 441 (2002).
- [3] K. Yamazaki and Y. Kanou, Shape optimization of rotating machines using time-stepping adaptive finite element method, *IEEE Trans. Magn.* **46**, 3113 (2010).
- [4] L. Yan, I. M. Chen, C. K. Lim, G. Yang, W. Lin, and K. M. Lee, Design and analysis of a permanent magnet spherical actuator, *IEEE/ASME Trans. Mechatron.* **13**, 239 (2008).
- [5] J. Schönke, Smooth Teeth: Why Multipoles Are Perfect Gears, *Phys. Rev. Applied* **4**, 064007 (2015).
- [6] H. Zijlstra, Permanent magnet systems for NMR tomography, *Philips J. Res.* **40**, 259 (1985).
- [7] G. Moresi and R. Magin, Miniature permanent magnet for table-top NMR, *Concepts Magn. Reson.* **19B**, 35 (2003).
- [8] S. Becker, M. Bussmann, S. Raith, M. Fuchs, R. Weingartner, P. Kunz, W. Lauth, U. Schramm, M. El Ghazaly, F. Grüner, H. Backe, and D. Habs, Characterization and Tuning of Ultra-high Gradient Permanent Magnet Quadrupoles, *Phys. Rev. ST Accel. Beams* **12**, 102801 (2009).
- [9] B. Biswas, A magnetic quadrupole from rectangular permanent magnets, *Nucl. Instrum. Methods Phys. Res.* **605**, 233 (2009).
- [10] B. Diviacco, Performance optimization of pure permanent magnet undulators, *Proc. IEEE Part. Accel. Conf.* **2**, 1590 (1993).
- [11] R. Bjørk, C. R. H. Bahl, A. Smith, and N. Pryds, Improving magnet designs with high and low field regions, *IEEE Trans. Magn.* **47**, 1687 (2011).
- [12] S. Cheng and D. P. Arnold, Optimization of permanent magnet assemblies using genetic algorithms, *IEEE Trans. Magn.* **47**, 4104 (2011).
- [13] M. Markovic and Y. Perriard, Optimization design of a segmented Halbach permanent-magnet motor using an analytical model, *IEEE Trans. Magn.* **45**, 2955 (2009).
- [14] R. Ravaut, G. Lemarquand, and V. Lemarquand, Magnetic field created by a uniformly magnetized tile permanent magnet, *Prog. Electromagn. Res. B* **24**, 17 (2010).
- [15] M. G. Abele, H. Rusinek, F. Bertora, and A. Trequattrini, Compensation of field distortion with ferromagnetic materials and permanent magnets, *J. Appl. Phys.* **75**, 6990 (1994).
- [16] M. G. Abele, W. Tsui, and H. Rusinek, Methodology of pole piece design in permanent magnets, *J. Appl. Phys.* **99**, 08D903 (2006).
- [17] W. F. Brown, *Magnetostatic Principles in Ferromagnetism* (North-Holland Publishing Company, Amsterdam, 1962).
- [18] N. I. Klevets, Synthesis of magnetic systems producing field with maximal scalar characteristics, *J. Magn. Magn. Mater.* **285**, 401 (2005).
- [19] N. I. Klevets, Optimal design of magnetic systems, *J. Magn. Magn. Mater.* **306**, 281 (2006).
- [20] A. R. Insinga, C. R. H. Bahl, R. Bjørk, and A. Smith, Performance of Halbach magnet arrays with finite coercivity, *J. Magn. Magn. Mater.* **407**, 369 (2016).
- [21] K. Halbach, Design of permanent multipole magnets with oriented rare earth cobalt material, *Nucl. Instrum. Methods* **169**, 1 (1980).
- [22] C. K. Chandrana, J. A. Neal, D. Platts, B. Morgan, and P. Nath, Automatic alignment of multiple magnets into Halbach cylinders, *J. Magn. Magn. Mater.* **381**, 396 (2015).
- [23] J. H. Jensen and M. G. Abele, Maximally efficient permanent magnet structures, *J. Appl. Phys.* **79**, 1157 (1996).
- [24] Y. Sato, Piecewise linear approximation of planar curves by perimeter optimization, *Pattern Recogn.* **25**, 1535 (1992).
- [25] R. Bjørk, A. Smith, and C. R. H. Bahl, Analysis of the magnetic field, force, and torque for two-dimensional Halbach cylinders, *J. Magn. Magn. Mater.* **322**, 133 (2010).
- [26] M. G. Abele, Linear theory of yokeless permanent magnets, *J. Magn. Magn. Mater.* **83**, 276 (1990).
- [27] M. G. Abele and H. Rusinek, Optimum design of yokeless permanent magnets, *J. Appl. Phys.* **67**, 4644 (1990).
- [28] M. G. Abele, *Structures of Permanent Magnets* (John Wiley and Sons, New York, 1993).
- [29] R. Bjørk, C. R. H. Bahl, A. Smith, and N. Pryds, Optimization and improvement of Halbach cylinder design, *J. Appl. Phys.* **104**, 013910 (2008).

B.4 Optimally segmented permanent magnet structures

A. R. Insinga, R. Bjørk, A. Smith and C. R. H. Bahl

accepted for publication in IEEE Transactions on Magnetics

Optimally segmented permanent magnet structures

A. R. Insinga*, R. Bjørk, A. Smith and C. R. H. Bahl

Department of Energy Conversion and Storage
Technical University of Denmark

Frederiksborgvej 399, 4000 Roskilde, Denmark.

*Email: aroin@dtu.dk

Abstract—We present an optimization approach which can be employed to calculate the globally optimal segmentation of a two-dimensional magnetic system into uniformly magnetized pieces. For each segment the algorithm calculates the optimal shape and the optimal direction of the remanent flux density vector, with respect to a linear objective functional. We illustrate the approach with results for magnet design problems from different areas, such as a permanent magnet electric motor, a beam focusing quadrupole magnet for particle accelerators and a rotary device for magnetic refrigeration.

I. INTRODUCTION

With the development of new and powerful magnetic materials [1], the range of application of permanent magnets is expanding to many scientific and technological areas [2]. The geometry of the magnetic system must be optimized to achieve high efficiency and minimize the amount of permanent magnetic material. Among the wide range of geometry optimization techniques we can identify two important categories of algorithms: topology optimization methods and parametric shape optimization methods.

The purpose of *topology optimization* algorithms is to determine how to subdivide a given design area into regions occupied by materials with different magnetic properties, e.g., magnetic permeability or remanent flux density. Since the topological features of the allowed solution are not restricted by an initial design concept, these algorithms potentially lead to novel geometrical configurations. Typically, the implementation of this class of algorithms employs finite element analysis for the calculation of the magnetic field. The properties of the materials are linked to control fields which are optimized by numerically evaluating the sensitivity of the objective with respect to the control fields [3, 4, 5] and applying iterative techniques such as sequential linear programming or gradient descent. Alternatively, the control fields can be optimized with gradient-free heuristic approaches, such as genetic algorithms [6, 7, 8]. While being very versatile, topology optimization may produce solutions characterized by finely subdivided or jagged shapes which are not suitable for manufacturing. Avoiding this problem often requires fine tuning of some regularization parameter. Generally, topology optimization techniques present a trade-off between computational time and resolution of the mesh underlying the simulation.

In *parametric geometry optimization* the shapes of the boundaries between materials with different properties are linked to a finite number of control parameters. The magnetic

field for a given configuration may be determined with numerical techniques [9, 10], by analytically solving the partial differential equations [11, 12, 13], or by approximating the magnetic system with a simplified model [14]. When numerical methods are employed it is possible to consider arbitrary shapes and to take into account non-linear magnetic effects. With analytical approaches the computational time is very short, but they can only be applied to the geometries for which the solution is available. Moreover, analytical solutions generally assume linear magnetic behavior or even more ideal approximations, such as permanent magnets with permeability equal to one and soft magnetic material with infinite permeability. Parametric optimization techniques are intrinsically limited by the fact that the search space is determined beforehand: the diversity of the allowed configurations is restricted to variations around the same design concept.

The optimization approach discussed in this paper presents some of the advantages of both categories. Since it relies on an analytical result to determine the optimal remanent flux density at any point with a single finite element simulation, it can be implemented in a computationally efficient algorithm. Moreover, it does not share the limitations that are typical for parametric optimization. The method provides the globally optimal subdivision of a given design area into uniformly magnetized segments with respect to a linear objective functional. The optimality is guaranteed as long as each material in the system exhibits a linear magnetic behavior. Under the more restrictive assumption that the permeability of the permanent magnet material is close to 1 we are also able to determine the border between permanent magnet and air which maximizes the linear objective. Another possibility is to optimize the border between permanent magnet and soft magnetic material by considering the limit of infinite permeability.

Since the optimality results are derived under the specific assumptions about the magnetic behavior of the materials in the system, the optimization of magnetic systems which are expected to exhibit a highly non-linear behavior must be performed using other techniques. However, non-linear magnetic phenomena — such as demagnetization of the permanent magnets due to the finite coercivity and anisotropy field, or magnetic saturation of any soft magnetic materials — often cause detrimental effects which it is desirable to minimize. When these effects are expected to be small, it is possible to perform the optimization by assuming linear behavior, and check that the optimized configurations obtained in this way

are within the ranges for which the linear approximation is justified. It will be possible to apply small corrections to the geometry with a final optimization step which takes into account the non-linear behavior.

We illustrate the result of our optimization approach with three examples from different fields of application: a permanent magnet electric motor, a beam-focusing quadrupole magnet, and a rotary device for magnetic refrigeration at room temperature. Since the method always assumes a linear objective functional, we will also evaluate the goodness of each optimized configuration in terms of those features of the produced field which are most relevant to the corresponding application. We will also discuss quantitatively the variation of the field when it is computed under more realistic assumptions about the magnetic response of the materials in the system.

II. FRAMEWORK OF THE OPTIMIZATION METHOD

A. The reciprocity theorem and the Virtual Magnet method

Our optimization method is based on the *reciprocity theorem*, an energy equivalence principle of magnetostatics, which can be expressed by the following equation [15]:

$$\int dV \mathbf{B}_{r,1}(\mathbf{x}) \cdot \mathbf{H}_2(\mathbf{x}) = \int dV \mathbf{B}_{r,2}(\mathbf{x}) \cdot \mathbf{H}_1(\mathbf{x}) \quad (1)$$

where $\mathbf{B}_{r,1}(\mathbf{x})$ is the remanence of the system 1 at the point \mathbf{x} , \mathbf{H}_1 is the magnetic field generated by $\mathbf{B}_{r,1}$, and similarly for system 2. The integration domain of both the volume integrals extends over the whole space. However, if the integration domain of the left-hand side of (1) was replaced with the region where $\|\mathbf{B}_{r,1}\| > 0$ the result would be the same, and similarly for the right-hand side. The theorem in this form holds as long as there are no free currents, and all materials in the system obeys a linear \mathbf{B} - \mathbf{H} relation, i.e.: $\mathbf{B} = \underline{\underline{\mu}}\mathbf{H} + \mathbf{B}_r$. The permeability tensor field $\underline{\underline{\mu}}(\mathbf{x})$ must be the same for both the systems.

The theorem equates the energy possessed by the magnetic flux sources of system 1 when placed in the field generated by the flux sources of system 2 with the energy possessed by the flux sources of system 2 when placed in the field generated by the flux sources of system 1. We use this theorem in order to calculate the remanence field $\mathbf{B}_{r,1}$ which produces a magnetic field \mathbf{H}_1 which maximizes a given objective. The magnetic system 2 is a mathematical construction that is used to solve this optimization problem. For this reason, the system 1 will also be referred to as the *real system* and system 2 as the *virtual system*.

If the virtual remanence $\mathbf{B}_{r,2}$ is interpreted as an objective vector field [16, 17], the right-hand side of (1) can be seen as the definition of an objective functional \mathcal{S} . Any objective functional which is linear with respect to the field \mathbf{H}_1 can be expressed in this form. Equation (1) implies that the optimal direction of the real remanence $\mathbf{B}_{r,1}$, with respect to the objective functional \mathcal{S} , is aligned at any point with the virtual field \mathbf{H}_2 .

This approach also provides a way to quantify how much a specific point \mathbf{x} of the real magnet is contributing to the value

of the objective functional \mathcal{S} . Once the real remanence has been aligned at the point \mathbf{x} with the virtual field $\mathbf{H}_2(\mathbf{x})$, the contribution to the value of \mathcal{S} from the point \mathbf{x} is proportional to the norm $H_2(\mathbf{x}) = \|\mathbf{H}_2(\mathbf{x})\|$. If the relative permeability of the magnet is equal to 1, the border between magnet and air does not need to be determined in advance: the optimal border lies on a contour level of H_2 . Since the contribution of any given point to the value of \mathcal{S} is always positive, extending the magnet area can only increase the value of \mathcal{S} . This means that being able to determine the magnet border that maximizes \mathcal{S} in presence of a specific constraint on the total magnet volume is equivalent to minimizing the magnet volume that is necessary to obtain a given value of \mathcal{S} .

In some cases it is necessary to determine the border separating permanent magnet material from soft magnetic material, such as iron, characterized by such a high permeability that it can be approximated as infinite. In the regions where the permeability is finite, the virtual field \mathbf{H}_2 is normal to the borders with infinite-permeability regions. Being defined as $\mathbf{H}_2 = -\nabla\Phi_2$, the virtual field is also normal to the equipotential surfaces of its magnetic scalar potential Φ_2 . As pointed out in [18], to achieve maximal energy efficiency an equipotential surface of Φ_2 can be converted into the boundary between magnet region and highly permeable material so that the magnet is completely shielded from the outside.

B. Optimal Segmentation of 2D system

The determination of the virtual field \mathbf{H}_2 provides a continuously varying vector field which at any point gives the optimal direction of the real remanence $\mathbf{B}_{r,1}$. In practice, however, magnetic assemblies are realized by splitting the magnet into several uniformly magnetized segments. Because of the linearity, the different points of the magnet are independent, which implies that it is never optimal to split a region over which the direction of the virtual field \mathbf{H}_2 is uniform [19].

For two dimensional systems, the optimal border between two adjacent segments always lies on a contour level of the angle $\psi = \arctan(H_{2,y}/H_{2,x})$, reducing the optimal segmentation problem to the simpler one of selecting the optimal contours with a given total number of segments N_{Segments} .

It can be shown [19] that this problem is equivalent to the problem of approximating a continuous curve $\mathcal{H}(\psi)$ with an inscribed piecewise linear curve, in such a way that the perimeter of the piecewise curve is maximized. The continuous curve to be approximated is parametrized by the orientation ψ of the virtual field \mathbf{H}_2 . The curve has the dimension of magnetic field integrated over an area and is expressed by the following equation:

$$\mathcal{H}(\psi) = \int_{R_{[\psi_0, \psi_1]}} dS \mathbf{H}_2(\mathbf{x}) \quad (2)$$

The area of the surface element is denoted by dS , and the integration domain $R_{[\psi_0, \psi_1]}$ is defined as:

$$R_{[\psi_0, \psi_1]} = \{\mathbf{x} : \psi(\mathbf{x}) \in [\psi_0, \psi_1]\} \cap \{\text{Design Area}\} \quad (3)$$

The total extension of the design area can be decided arbitrarily depending on the geometrical constraints of each system. The problem of maximizing the perimeter of the piecewise linear approximation of \mathcal{H} can be solved with the desired degree of accuracy by employing dynamic programming [20].

III. OPTIMIZED MAGNETIC SYSTEMS

We present magnet design problems from different areas of application and show how our approach can be used to determine the optimally segmented solution. We will express the objective functional for each optimization problem by defining the objective vector field, which corresponds to the remanence $B_{r,2}$ of the virtual system. For each example we will show two figures. The first figure (as, e.g., Fig 1(a)) is an illustration of the geometry of the virtual system, including the virtual magnet area, shaded in pink, the design area, shaded in light blue, and the regions originally filled with soft magnetic material, shaded in gray. The virtual remanence vector field is represented by the red arrows, and the virtual field H_2 , which will be shown only inside the design area, is represented by blue arrows.

The second figure (as, e.g., Fig 1(b)) is the result of the Finite Element Method (FEM) simulation for the optimally segmented system performed using the commercial software COMSOL Multiphysics. The magnetic field is obtained by projecting on a triangular mesh the partial differential equation governing the magnetic vector potential and solving the resulting system of equations using the direct solver PAR-DISO, available with the software. The surface area of the mesh elements averaged over the design region is for all the examples $\approx 10^{-5}$ of the surface area of the design region. The real flux density B_1 is indicated in the figures by the black flux lines, and its norm is indicated by the color, darker shades corresponding to a higher norm. The direction of the optimal remanence for each segment is indicated by a black arrow.

Our approach allows us to choose freely the number of segments N_{Segments} to be used as a constraint in the optimization. The value of the objective functional will increase monotonically with the number of segments, converging asymptotically to the limit given by the case of a continuously varying remanence field. However, because of the symmetry exhibited by the geometry of each of the example optimization problems, if N_{Segments} is a multiple of 4 the optimally segmented magnetic system preserves the symmetry, and this results in the additional advantage of many segments having the same shape. We decided to use the value $N_{\text{Segments}} = 12$ for all the examples because 3 segments for each symmetric quadrant is a good trade-off between the goodness of the final result and the intent of minimizing the total number of segments which decreases the manufacturing cost of the magnetic assembly.

In all of the examples, the permanent magnetic material has a relative permeability $\mu = 1$, and a remanence of 1.4 T. The relative permeability of the soft magnetic material, such as iron, is set equal to $\mu = 1000$. The spatial dimensions of the examples will not be reported since the solution is invariant with respect to an isotropic rescaling.

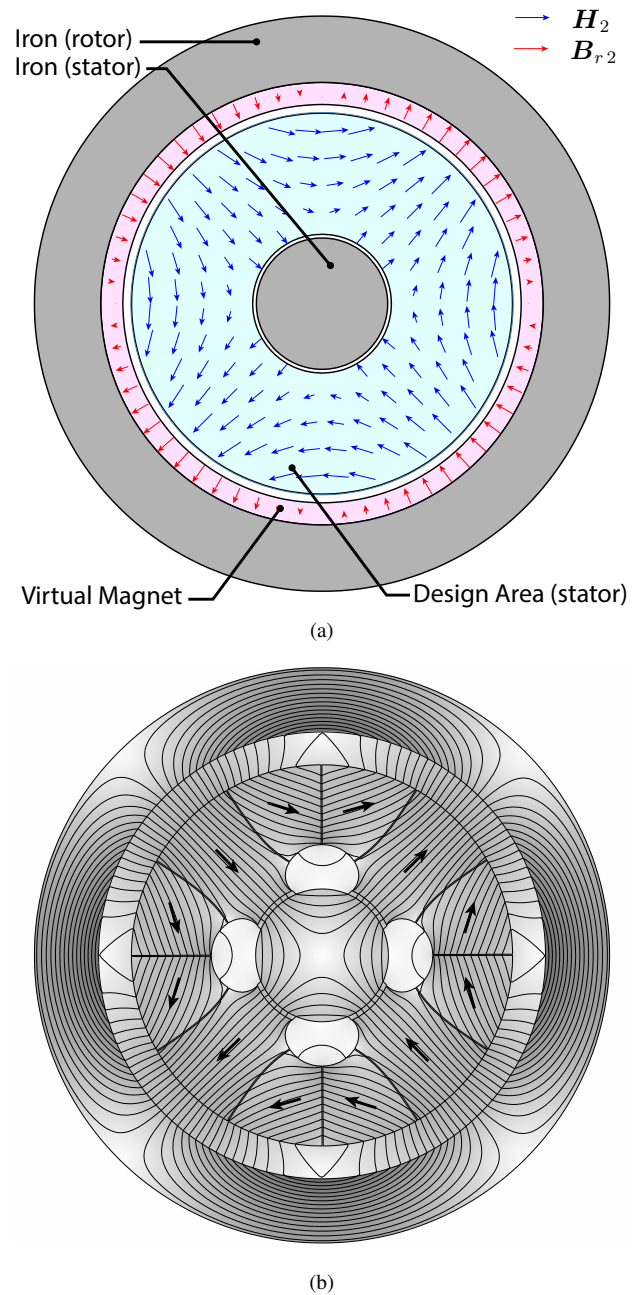


Fig. 1. Designing a magnet for an electric motor with the purpose of creating a sinusoidal radial field in the air gap between the stator and the rotor. Fig. 1(a): geometry of the virtual system. Fig. 1(b): FEM simulation of the optimal segmentation.

As a final verification step, the field generated by the optimized configuration of each example have been calculated using more realistic models for the magnetic behavior of the materials. In particular, the relative permeability of permanent magnets is set to $\mu = 1.05$, and the iron is modeled with the non-linear B - H curve included in the material library of COMSOL, which has a magnetic saturation of 2 T. Moreover, the magnetic field inside the permanent magnet material has been decomposed into the component that is parallel to the

remanence and the component that is normal. When the demagnetizing fields or transversal fields are too intense the linear approximation of the B - H relation may not be an accurate description of the magnetic behavior. The parallel and normal components of the field inside the permanent magnet material have been compared with typical values of, respectively, the coercive force and the anisotropy field of typical present-day rare-earth magnets. In all the examples these final validation tests confirmed that the underlying approximations were justified. In cases where this is not true, it will be possible to predict the effect of the non-linear demagnetization of permanent magnets by using numerical approaches such as the one presented in [21].

A. Electric Motor

The geometry of the virtual system for a four-poles surface-mounted permanent magnet electric motor is shown in Fig. 1(a). The iron core of the stator is surrounded by permanent magnet material. A small air gap is present between the stator and the external iron ring of the rotor (the rotor's slots are not represented). The virtual magnet area is located in the air gap, where the following virtual remanence is defined, with the purpose of minimizing the detrimental higher harmonics [13]:

$$\mathbf{B}_{r2} = \sin(2\phi) \hat{e}_\rho. \quad (4)$$

It is possible to apply a constraint on the total volume of permanent magnetic material. We arbitrarily set the volume of magnetic material to 90% of the total volume of the design region. We use this volume constraint to determine the optimal border between magnet and air by considering the norm of the virtual field \mathbf{H}_2 , as explained in section II-A. This results in the four holes adjacent to the iron core in the center, which are visible in Fig. 1(b). The desired properties of the solution

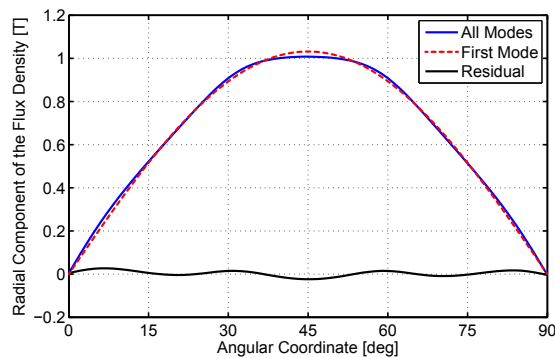


Fig. 2. The radial component of the air gap flux density for the electric motor example is plotted as a solid blue line. This curve has been decomposed into the first mode, plotted as a red dashed line, and the sum of all the other undesired harmonics, plotted as a solid black line.

can be checked by expanding in Fourier series the radial component B_ρ of the flux density $\mathbf{B}_1 = \mu_0 \mathbf{H}_1$ in the air gap between the stator and the rotor, close to external yoke. This is plotted in Fig. 2 for one quadrant of the geometry, given by the following interval of the angular coordinate: $\phi \in [0^\circ, 90^\circ]$.

The amplitude of the first harmonic is 0.9998 of the amplitude of the total signal, corresponding to 1.032 T. This implies that the total harmonic distortion, THD, is equal to 0.02. When the field is calculated taking into account the non-linear behavior of iron, and by setting the permeability of the magnets to $\mu = 1.05$, the amplitude of the first harmonic decreases to 1.020 T, but remains 0.9998 of the amplitude of the total signal, and thus the THD does not change.

B. Quadrupole magnet for Beam Focusing

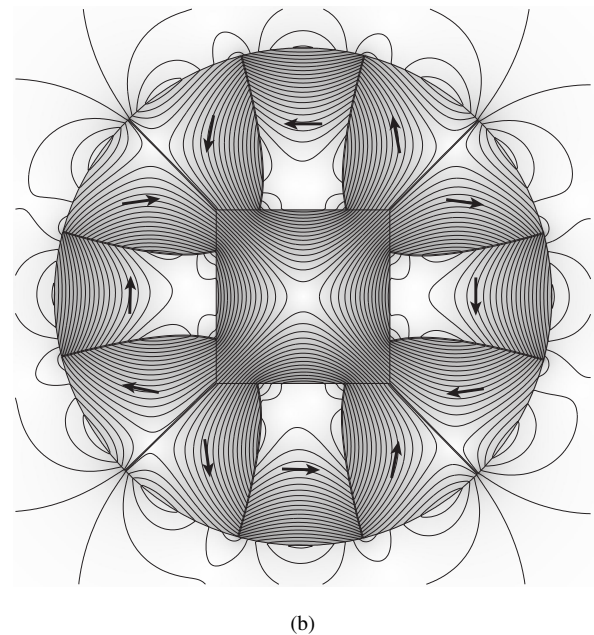
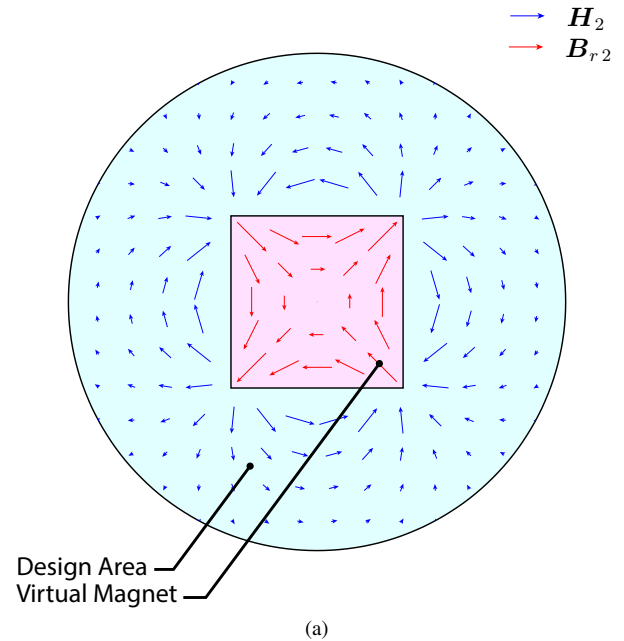


Fig. 3. Design of a quadrupole magnet with a square air gap and circular external border. The design is relevant for beam focusing applications in particle accelerator devices. Fig. 3(a): geometry of the virtual system. Fig. 3(b): FEM simulation of the optimal segmentation.

Quadrupole magnets are used in the field of particle acceleration for the purpose of focusing beams of charged particles [22]. The following virtual remanence, corresponding to a quadrupole field, is defined over the square cavity shown in Fig. 3(a):

$$\mathbf{B}_{r,2} = y \hat{e}_x + x \hat{e}_y. \quad (5)$$

The magnet area is limited by the external circle visible in the figure. The radius of the circle is determined by the desired field intensity. The results of the FEM simulation for the optimally segmented system is shown in Fig. 3(b). In order to evaluate the optimized magnetic system, we expand the field \mathbf{H}_1 in two components: a perfectly quadrupolar field $\mathbf{H}_Q(\mathbf{x})$, proportional to the virtual remanence $\mathbf{B}_{r,2}$ defined in (5), and the residual undesired component of the field, which we denote by $\Delta(\mathbf{x})$:

$$\mathbf{H}_1(\mathbf{x}) = \mathbf{H}_Q(\mathbf{x}) + \Delta(\mathbf{x}) \quad (6)$$

The field \mathbf{H}_Q is the second-order term of the interior cylindrical multipole expansion, and Δ is the sum of all the remaining terms. The calculation of the normalized amplitudes of the two components shows that the field \mathbf{H}_1 is quadrupolar within a very good approximation:

$$c_Q = \left(\frac{\int_{\Omega} dS \|\mathbf{H}_Q(\mathbf{x})\|^2}{\int_{\Omega} dS \|\mathbf{H}_1(\mathbf{x})\|^2} \right)^{1/2} = 0.993 \quad (7)$$

$$c_{\Delta} = \left(\frac{\int_{\Omega} dS \|\Delta(\mathbf{x})\|^2}{\int_{\Omega} dS \|\mathbf{H}_1(\mathbf{x})\|^2} \right)^{1/2} = 0.120 \quad (8)$$

The integration domain Ω is the whole square cavity. Because of the normalization we have: $c_Q^2 + c_{\Delta}^2 = 0.986 + 0.014 = 1$. When the magnetic behavior of permanent magnets and iron is calculated using the more realistic models described at the beginning of section III, the values of the coefficients change only slightly, thus giving: $c_Q = 0.992$ and $c_{\Delta} = 0.122$.

C. Magnetic Refrigeration

Fig. 4(a) shows the geometry of the virtual system for a rotary device for active magnetic refrigeration at room temperature. The following virtual remanence is defined, with the purpose of creating a high field in the pink shaded regions of the air gap and a low field in the angular sectors between them, as desirable for this kind of devices [23]:

$$\mathbf{B}_{r,2} = \text{sign}(x) \hat{e}_{\rho} \quad (9)$$

where x denotes the coordinate parameterizing the horizontal direction. As shown in Fig. 4(a), the virtual remanence is only defined in the high field regions of the air gap, which are situated on the two sides of the iron core.

We apply a constraint on the total volume of magnet material, which is equal to 5 times the volume of the high field region. This ratio is comparable to other published designs of magnetic refrigeration devices [24].

As explained in section II-A, we can convert an equipotential line of the virtual scalar potential Φ_2 into the external border between permanent magnet and soft magnetic material.

The level curves corresponding to the volume constraint are the kidney shaped lines shown on both the sides of the air gap in Fig. 4(b). After determining the boundary between magnet and iron, the outer border of the iron region can be determined arbitrarily, as long as magnetic saturation is avoided. We choose a circular external border which encloses the design area. The result of the FEM simulation is shown in

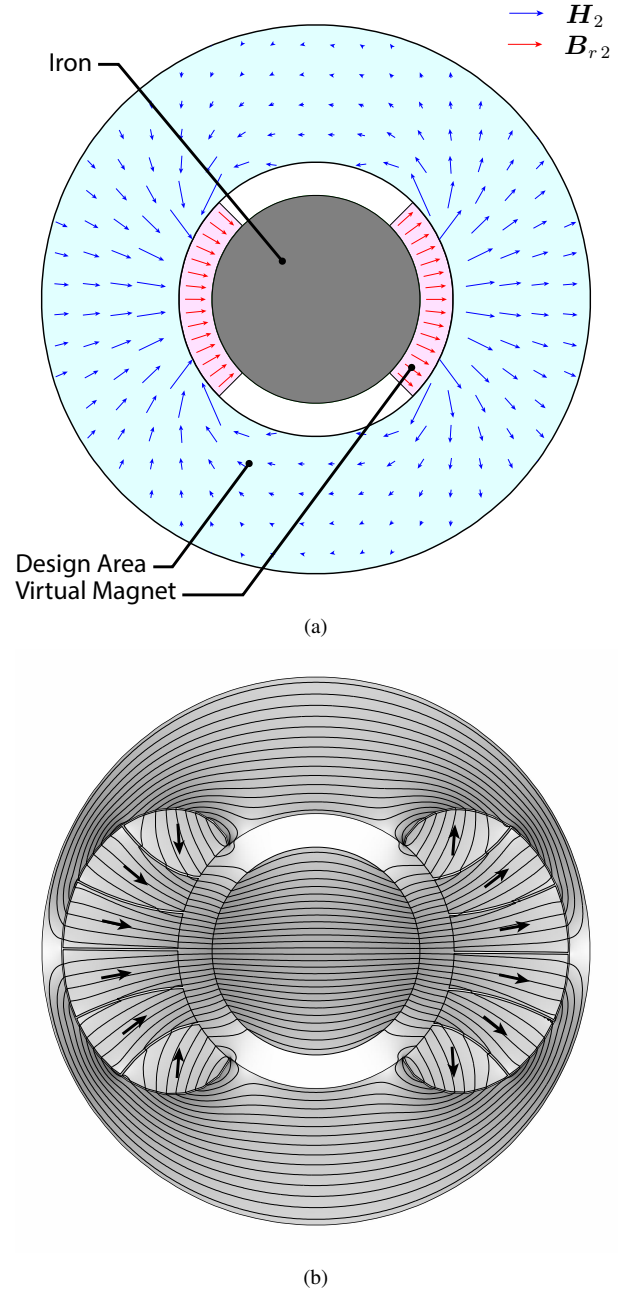


Fig. 4. Design of a magnetic assembly for application in magnetic refrigeration. The purpose of the magnetic system is to create high and low field regions in the air gap between the iron core and the external cylinder. Fig. 4(a): geometry of the virtual system. Fig. 4(b): FEM simulation of the optimal segmentation.

Fig. 4(b). The flux density norm averaged over the high field region is equal to 1.25 T and averaged over the low field region

is 0.13 T, which is a satisfactory result with respect to other published magnetic refrigeration devices [23]. The norm of the flux density evaluated at the middle radial position of the air gap is plotted in Fig. 5 as function of the angular coordinate ϕ in the interval $\phi \in [-90^\circ, 90^\circ]$. It would be possible to further reduce the average norm in the low field region by employing non-linear optimization techniques as the final step of the optimization process. When the field is calculated with the more realistic models for magnets and iron, the flux density norm averaged over the high field region decreases slightly to 1.23 T, while the low field region average remains 0.13 T.

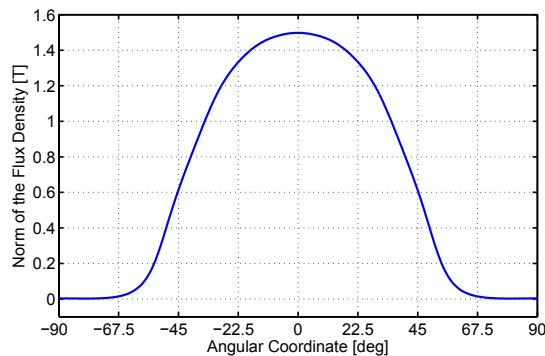


Fig. 5. Norm of the air gap flux density for the magnetic refrigeration example. The objective is to maximize the field in the interval $\phi \in [-45^\circ, 45^\circ]$

IV. CONCLUSIONS

We have briefly introduced a new method for optimal segmentation of magnetic systems, based on a linear objective functional. Its usefulness has been illustrated for three different applications of permanent magnet arrays.

Since the virtual field can be computed by means of FEM, this technique is applicable to any geometry, even when the analytical solution is not known.

The solution is globally optimal with respect to the considered geometry and objective functional. Moreover, the method can be implemented into a fast algorithm, since only one FEM computation is necessary.

It would be interesting to extend our approach by considering its generalization to the case of a non-linear objective functional. This problem could be solved with an iterative procedure involving the linear approximation to the objective functional at each step.

ACKNOWLEDGMENT

This work was financed by the ENOVHEAT project which is funded by Innovation Fund Denmark (contract no. 12-132673).

REFERENCES

[1] O. Gutfleisch, M. A. Willard, E. Brück, C. H. Chen, S.G. Sankar and J.P. Liu, *Magnetic materials and devices for the 21st century: stronger, lighter, and more energy efficient*, Adv. Mater. 23 (7), 821-42 (2011).

[2] J.M.D. Coey, *Permanent magnet applications*, J. Magn. Magn. Mater. 248, 441-456 (2002).

[3] J. S. Choi, J. Yoo, S. Nishiwaki and K. Izui, *Optimization of Magnetization Directions in a 3-D Magnetic Structure*, IEEE Trans. Magn. 46 (6), 1603-1606 (2010).

[4] S. Lim, S. Jeong and S. Min, *Multi-Component Layout Optimization Method for the Design of a Permanent Magnet Actuator*, IEEE Trans. Magn. 52 (3), 7205304, 1-4 (2016).

[5] E. Kuci, F. Henrotte, P. Duysinx, P. Dular and C. Geuzaine, *Design Sensitivity Analysis for Shape Optimization of Nonlinear Magnetostatic Systems*, IEEE Trans. Magn. 52 (3), 9400904, 1-4 (2016).

[6] S. Cheng and D. P. Arnold, *Optimization of Permanent Magnet Assemblies Using Genetic Algorithms*, IEEE Trans. Magn. 47 (10), 4104-4107 (2011).

[7] T. Sato, K. Watanabe and H. Igarashi, *Multimaterial Topology Optimization of Electric Machines Based on Normalized Gaussian Network*, IEEE Trans. Magn. 51 (3), 7202604, 1-4 (2015).

[8] S. Sato, T. Sato and H. Igarashi, *Topology Optimization of Synchronous Reluctance Motor Using Normalized Gaussian Network*, IEEE Trans. Magn. 51 (3), 8200904, 1-4 (2015).

[9] B.-K. Son, G.-J. Park, J.-W. Kim, Y.-J. Kim and S.-Y. Jung, *Interstellar Search Method With Mesh Adaptive Direct Search for Optimal Design of Brushless DC Motor*, IEEE Trans. Magn. 52 (3), 8201004, 1-4 (2016).

[10] M. Fasil, N. Mijatovic, B. B. Jensen, and J. Holboll, *Finite-Element Model-Based Design Synthesis of Axial Flux PMSM Motors*, IEEE Trans. Appl. Supercond. 26 (4), 0602905, 1-5 (2016).

[11] L. Wu and Z.-Q. Zhu, *Analytical Modeling of Surface-Mounted PM Machines Accounting for Magnet Shaping and Varied Magnet Property Distribution*, IEEE Trans. Magn. 50 (7), 8101511, 1-11 (2014).

[12] T. Shi, Z. Qiao, C. Xia, H. Li and Z. Song, *Modeling, Analyzing, and Parameter Design of the Magnetic Field of a Segmented Halbach Cylinder*, IEEE Trans. Magn. 48 (5), 1890-1898 (2012).

[13] M. Markovic and Y. Perriard, *Optimization Design of a Segmented Halbach Permanent-Magnet Motor Using an Analytical Model*, IEEE Trans. Magn. 45 (7), 2955-2960 (2009).

[14] D.-K. Lim, K.-P. Yi, D.-K. Woo, H.-K. Yeo, J.-S. Ro, C.-G. Lee and H.-K. Jung, *Analysis and Design of a Multi-Layered and Multi-Segmented Interior Permanent Magnet Motor by Using an Analytic Method*, IEEE Trans. Magn. 50 (6), 8201308, 1-8 (2014).

[15] W.F. Brown, *Magnetostatic principles in ferromagnetism*, North-Holland Publishing Company, Amsterdam, (1962).

[16] N.I. Klevets, *Synthesis of magnetic systems producing field with maximal scalar characteristics*, J. Magn. Magn. Mater. 285, 401-409 (2005).

[17] N.I. Klevets, *Optimal design of magnetic systems*, J. Magn. Magn. Mater. 306, 281-291 (2006).

- [18] J. H. Jensen and M. G. Abele, *Maximally efficient permanent magnet structures*, J. Appl. Phys. 79 (2), 1157-1163 (1996).
- [19] A. R. Insinga, R. Bjørk, A. Smith, and C. R. H. Bahl, *Globally Optimal Segmentation of Permanent-Magnet Systems*, Phys. Rev. Applied 5 (6), 064014, 1-16 (2016).
- [20] Y. Sato, *Piecewise linear approximation of planar curves by perimeter optimization*, Pattern Recognition 25 (12), 1535-1543 (1992).
- [21] A. R. Insinga, C.R.H. Bahl, R. Bjørk and A. Smith, *Performance of Halbach magnet arrays with finite coercivity*, J. Magn. Magn. Mater. 40, 369-376 (2016).
- [22] B. Biswas, *A magnetic quadrupole from rectangular permanent magnets*, Nucl. Instrum. Methods Phys. Res., Sect. A 605, 233-242 (2009).
- [23] R. Bjørk, C. R. H. Bahl, A. Smith and N. Pryds, *Improving Magnet Designs With High and Low Field Regions*, IEEE Trans. Magn. 47 (6), 1687-1692 (2011).
- [24] R. Bjørk, C. R. H. Bahl, A. Smith and N. Pryds, *Review and comparison of magnet designs for magnetic refrigeration*, Int. J. Refrigeration 33 (3), 437-448 (2010).

B.5 Topology optimized permanent magnet systems

R. Bjørk, C. R. H. Bahl and A. R. Insinga

submitted for publication in IEEE Transactions on Magnetics

Topology optimized permanent magnet systems

R. Bjørk, C. R. H. Bahl, A. R. Insinga

Department of Energy Conversion and Storage, Technical University of Denmark - DTU,
Frederiksborgvej 399, DK-4000 Roskilde, Denmark
e-mail: rabj@dtu.dk

Abstract—Topology optimization of permanent magnet systems consisting of permanent magnets, high permeability iron and air is presented. An implementation of topology optimization for magnetostatics is discussed and three examples are considered. First, the Halbach cylinder is topology optimized with iron and an increase of 15% in magnetic efficiency is shown, albeit with an increase of 3.8 pp. in field inhomogeneity - a value compared to the inhomogeneity in a 16 segmented Halbach cylinder. Following this a topology optimized structure to concentrate a homogeneous field is shown to increase the magnitude of the field by 111% for the chosen dimensions. Finally, a permanent magnet with alternating high and low field regions is considered. Here a Λ_{cool} figure of merit of 0.472 is reached, which is an increase of 100% compared to a previous optimized design.

I. INTRODUCTION AND TOPOLOGY OPTIMIZATION

Permanent magnets are used in a multitude of systems, ranging from motors to MRI systems (1). In all of these applications it is important to design the permanent magnet system in such a way that it has the highest possible performance for the given application.

A permanent magnet system can be designed based on parameter variation simulations, or through use of the reciprocity theorem which for a desired linear functional gives the optimal remanence distribution (2; 3). However, these approaches cannot be used to determine the optimal shape of the individual material pieces in a permanent magnet system. Although the reciprocity theorem can be used to determine the optimal border between permanent magnet and iron (4; 5), it cannot be used to determine the optimal shape of e.g. iron pieces alone.

To determine the optimal structure of a permanent magnet system, a topology optimization approach can be utilized. Topology optimization has been used for a multitude of applications including structural mechanics, beams and trusses as well as bio-mechanical and microelectro mechanical systems (6). For permanent magnet systems, topology optimization has previously been used to determine the optimal direction of the magnetization of a permanent magnet (7; 8) and for designing C-core actuators (9; 8). Topology optimization of rotor poles in electrical motors (7; 10), in order to minimizing stator slot effects (11) and the clogging torque (12), has also been investigated using topology optimized systems. Finally, topology optimized pole pieces for MRI systems, which have high requirements on field uniformity, has been studied in both 2D (13) and 3D (14).

Numerically, either a finite element approach or a phase field approach using genetic algorithm are typically presented. In the latter the area to be topology optimized is discretized into

pixels, each filled with a specific material (10; 15). This allows for magnets with e.g. a specific direction of magnetization to be specified. The pixelated geometry is then refined to increase the resolution in the model.

The previous topology studies of permanent magnet systems has been limited to very specific problems, typically in motor design. Topology optimization of general permanent magnet systems with varying geometrical parameters have not been considered, nor have systems where the optimal shape of bordering iron and permanent magnet pieces are considered, except for a single very specific case (9). Here, we will consider general topology optimization of permanent magnetic structure containing both permanent magnets, iron and air regions. We will consider three general permanent magnet applications and present topology optimized structures as function of various geometrical parameters for each of these. These optimized structures show a significantly improved performance compared to existing systems. First, the implementation of the topology optimization method is presented, followed by a study of a topology optimized Halbach cylinder, a topology optimized magnetic field concentrator and finally a topology optimized permanent magnet system with alternating high and low field regions.

II. METHOD AND IMPLEMENTATION

In this work, the finite element framework Comsol Multiphysics is used as the numerical implementation to perform the topology optimization simulations. The solver used is the Globally Convergent Method of Moving Asymptotes (GCMMA) solver, which is essentially a linear method with a three-level algorithm (16; 17). This solver is ideal for problems with a large number of control variables, making it suited for topology optimization. The mesh sensitivity of the topology optimized problem will be discussed in detail subsequently.

For each topology optimization problem considered here, a global objective is defined, termed Θ , that must be maximized through topology optimization. This objective must be a function of the topology of the system. The global objective of a permanent magnet system will vary depending on the application of the system. The most general optimization criteria is to obtain a permanent magnet system with the highest magnetic efficiency possible (15). The magnetic efficiency, or the magnetic figure of merit, is defined as (18)

$$M = \frac{\int_{V_{\text{field}}} \|\mathbf{B}\|^2 dV}{\int_{V_{\text{mag}}} \|\mathbf{B}_{\text{rem}}\|^2 dV}, \quad (1)$$

where V_{field} is the volume of the region where the magnetic field is created and V_{mag} is the volume of the permanent

magnets. The figure of merit is the ratio of the energy stored in the field region to the maximum amount of magnetic energy available in the magnetic material, and has a maximum value of $M = 0.25$ (18). The norm of the remanence is free to vary in the calculation of M , but in most practical applications a system with a fixed remanence within the permanent magnet is desired.

In a number of applications the magnetic figure of merit is not the logical choice of optimization variable, as either a varying remanence is not desirable or the price of the permanent magnet material is of less importance. In these applications the goal would typically be to generate as large a field as possible. Other applications such as MRI require a very uniform field, and thus here the optimization variable would be the relative standard deviation of the field.

We consider topology optimization of permanent magnet systems consisting of up to three materials: permanent magnets, high permeability iron and air. The permanent magnet material is assumed to have a linear $B - H$ relation with a permeability of $\mu = 1.05$ and a fixed remanence. The high permeability iron has a non-linear $B - H$ curve as provided in the Comsol material library. The saturation magnetization is around 2 T. Previous studies on non-linear materials have shown that it is important to account for the full $B - H$ curve of the materials (9).

In the problems considered in the following, a design region must be split into regions of two different distinct magnetic materials. In order to obtain a sharp geometrical transition between the different material types, a penalty function of a single control variable, p , is introduced that can switch between two material types. The control variable has a range between 0 and 1.

As an example, consider a design region that can either consist of permanent magnet material or high permeability iron. In this case, the relative permeability of the design region that is to be topology optimized between permanent magnet and high permeability iron is given as

$$\mu_r = (1.05 - \mu_{r,\text{iron}}) e^{-100p} + \mu_{r,\text{iron}} \quad (2)$$

where $\mu_{r,\text{iron}}$ is the relative permeability of iron and the relative permeability of the permanent magnet is $\mu_{r,\text{magnet}} = 1.05$. Note that $\mu_{r,\text{iron}}$ is a function of the norm of the magnetic field, H . Here if $p = 0$ the exponential factor is 1 and the material has the relative permeability of a permanent magnet. If $p = 1$, the exponential factor diminishes the first term, and the relative permeability is equal to $\mu_{r,\text{iron}}$. A somewhat similar approach was used in Refs. (11; 13). Likewise, the remanence of the topology optimized region is given as

$$\mathbf{B}_{\text{rem}} = e^{-100p} \mathbf{B}_{\text{rem, desired}} \quad (3)$$

where $\mathbf{B}_{\text{rem, desired}}$ is the desired remanence of the permanent magnet, i.e. in the case of $p = 0$ the permanent magnet has the desired remanence while for $p = 1$ the remanence is essentially zero. Similarly a region can be topology optimized between high permeability iron and air by changing the factor of 1.05 in Eq. (2) to 1.00, equal to the relative vacuum permeability, and setting $\mathbf{B}_{\text{rem, desired}} = 0$ in Eq. (3).

Numerical simulations have shown that the resulting topology optimized geometry depends on the initial value of p . This is a result of the build-in variation of the parameter in Comsol multiphysics during the optimization step. A series of simulations was conducted that determined that the optimal initial value was $p = 0.003$, as this produced a topology optimized geometry with the highest performance.

We consider three different applications of topology optimization in the following. First, the creating of a uniform field in a cylinder bore using a Halbach cylinder is considered. Following this, the concentration of a uniform magnetic field is considered and finally generating a magnetic field with adjacent high and low field regions is considered.

III. HALBACH CYLINDER

The Halbach cylinder is a cylindrical magnet system that generates a homogeneous magnetic field in the cylinder bore. This system has been used for nuclear magnetic resonance (NMR) equipment (19; 20), magnetic refrigeration devices (21; 22) and medical applications (23). In a continuous Halbach cylinder the components of the remanence are given in cylindrical coordinates as (24)

$$\begin{aligned} B_{\text{rem},r} &= B_{\text{rem}} \cos(p\phi) \hat{r} \\ B_{\text{rem},\phi} &= B_{\text{rem}} \sin(p\phi) \hat{\phi} \end{aligned} \quad (4)$$

We consider a $p = 1$ cylinder that generates a homogeneous magnetic field in the cylinder bore. This Halbach cylinder has a maximum magnetic efficiency parameter of $M \approx 0.162$, far from the theoretic maximum value of 0.25 (25; 26). Being able to increase this value would be of great interest for all the above mentioned applications.

In general there are three ways to increase the magnetic efficiency of a given magnet design. These are using magnets with a varying norm of the remanence, altering the direction of the remanence or replacing parts of the magnetic design with a high permeability soft magnetic material. For the Halbach cylinder design, we consider a design with a constant fixed remanence. Therefore, to improve the Halbach cylinder design, it must be investigated if parts of the cylinder can be replaced with a high permeability soft magnetic material, without severely decreasing the produced field. The goal of a topology optimized Halbach cylinder is to improve the magnetic efficiency of the design such that a higher magnetic field could be generated using a lesser amount of magnet.

The whole cylindrical Halbach magnet is considered as the topology optimization area, as shown in Fig. 1. The material in a point on the cylinder is either permanent magnet with a remanence given by Eq. (4) or iron with soft magnetic properties as stated previously. The objective function that is maximized is

$$\Theta = \frac{\langle B \rangle}{A_{\text{mag}}} \quad (5)$$

where $\langle B \rangle$ is the average magnetic flux density in the cylinder bore and A_{mag} is the area of the permanent magnet, i.e. the area of the cylinder that is not iron.

For the Halbach cylinder, the norm of the remanence is constant as is the area of the high field region, i.e. the

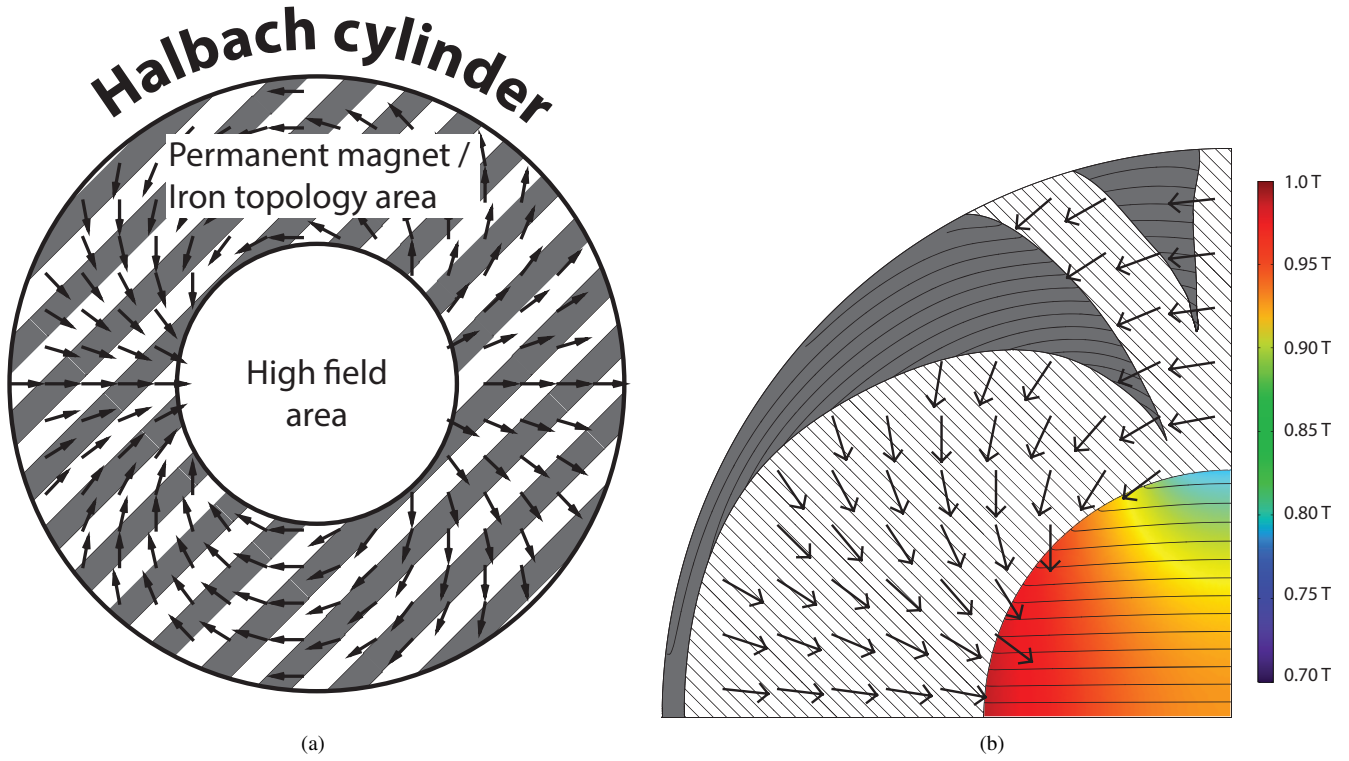


Fig. 1. a) The Halbach geometry to be topology optimized. The hatched grey area indicates the area to be topology optimized. The arrows indicate the fixed direction of remanence, if the material in question is a permanent magnet. b) A quarter of the topology optimized system for $R_o/R_i = 2.3$.

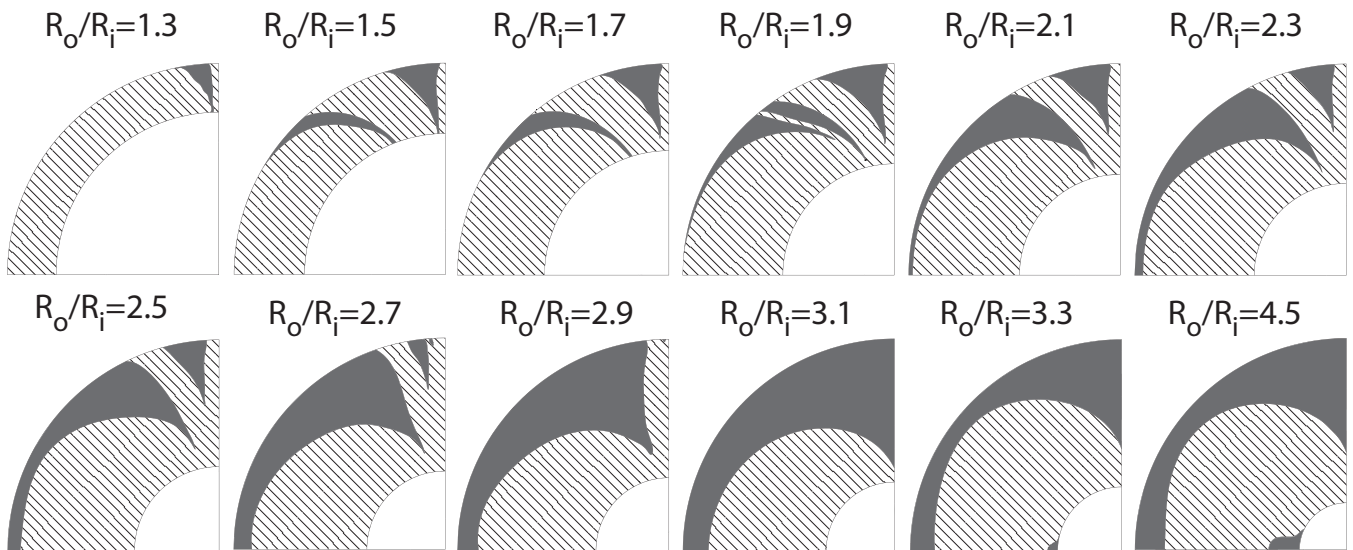


Fig. 2. The topology optimized geometries as function of the ratio between the outer and the inner radius. The grey areas are iron and the hatched areas are permanent magnet with a remanence given by Eq. 4.

cylinder bore. This means that the figure of merit, M , reduces to a proportionality between the integral of the magnetic flux density squared and the volume of the magnet squared. However, in practical applications it is usually required that the Halbach cylinder generate as strong a field as possible, using the least amount of magnetic material. This corresponds to the Θ defined in Eq. 5. If the generated field is completely homogeneous, maximizing Θ also maximizes M .

The geometry resulting from the topology optimization process depend on the ratio between the outer and the inner radius of the Halbach cylinder, R_o and R_i respectively. The computed topology optimized geometries are shown in Fig. 2. As can be seen from the figure, the fractional area of iron increases as function of the ratio of the outer and inner radius. The topology optimization produces iron regions with features with very sharp ends. These are similar to structures seen by Ref. (11), although in that case it was for borders between iron and air, and not iron and permanent magnet as is the case here.

The figure of merit, M , for the topology optimized designs is shown in Fig. 3a as function of $\langle B \rangle / B_{\text{rem}}$. For the Halbach cylinder, the figure of merit can explicitly be calculated (18; 26). This expression is also shown in the figure. As can be seen from the figure, the topology optimized design is superior to the Halbach cylinder for all values of the field generated. The generated field increases monotonically with an increase in R_o/R_i . However, the stronger field generated comes at the expense of the homogeneity of the field in the bore. The relative standard deviation of the field in the bore as a function of the average norm of the field is shown in Fig. 3b. The relative standard deviation is given as $\frac{\sigma}{\langle B \rangle} = \frac{\sqrt{\langle (B - \langle B \rangle)^2 \rangle}}{\langle B \rangle}$. The field is quite homogeneous with a relative standard deviation below 8% for all fields considered. The large change of the standard deviation at the data point at $\langle B \rangle / B_{\text{rem}} = 0.25$ is due to a change in the topology of the system from one to two iron regions, as can also be seen in Fig. 2 from $R_o/R_i = 1.3$ to 1.5. Note that for a Halbach cylinder, the field is completely homogeneous and the standard deviation is zero. The standard deviation of a segmented 8 or 16 piece Halbach cylinder is also shown, and the topology optimized structure is seen to have a relative standard deviation very similar to the 16 segmented Halbach.

As an example, at the optimal Halbach efficiency of $\langle B \rangle / B_{\text{rem}} = 0.796$, the figure of merit is $M = 0.186$ for the topology optimized design, an improvement of 15% compared to the Halbach cylinder. This improvement comes at the expense of a small increase in relative standard deviation of the field in the bore to $\frac{\sigma}{\langle B \rangle} = 3.8\%$. This system has $R_o/R_i = 2.3$ and is illustrated in Fig. 1b.

IV. CONCENTRATING A HOMOGENEOUS FIELD

We now consider a homogeneous magnetic field across a region of space and wish to see if a structure that concentrates the magnetic field in a given area can be designed using topology optimization. This could be a device similar to the meta-material flux enhancer presented in Ref. (27), except using purely ferromagnetic material. In this system the choice

between materials is iron and air, contrary to the choice between permanent magnet and iron in the Halbach cylinder case considered previously.

We consider a geometry as shown in Fig. 4a. The area to be topology optimized is shaped as a square, surrounding a circular high field region. The diameter of the circular high field region is half the side length of the surround square. The area to be topology optimized can in a given point have a permeability in the range of $\mu_r = 1$ to 4000, i.e. from free space to that of unsaturated iron. Following the computation, the computed geometry is verified with the actual nonlinear $B - H$ of iron. The topology optimization criteria, Θ , is a maximization of the average field throughout the bore, i.e. without regard for field uniformity,

$$\Theta = \langle B \rangle \quad (6)$$

We can estimate the amount that the magnetic field can at most be concentrated by following the approach of Ref. (27). Although this approach has only been shown to be valid for circular geometries, it will never the less provide an estimate for the geometry considered here. In this framework the increase in field is proportional to the difference in cross-sectional length of the geometry perpendicular to the magnetic field. Here this is the side length of the square topology area divided by the diameter of high field region, i.e. a factor of two.

The computed topology optimized structure is shown in 4b using the actual nonlinear $B - H$ curve. In this structure the field is enhanced from a surrounding homogeneous 1 T magnetic field to an average field of $\langle B \rangle = 1.46$ T in the high field area, an increase of 46%. The field generated is not uniform, but this was also not a requirement of the optimization algorithm. The increase in field of 46% is less than the maximum possible 100% increase. However, as only material with $\mu_r \geq 1$ is used, it is not possible to completely shield the system from flux leakage.

This structure was also optimized in 3D, where the high field region was a sphere and the topology optimization region surround the sphere was shaped as a cube. The resulting structure in this case was a structure similar to that in Fig. 4b, except rotated around the sphere, as shown in Fig. 5. Here the averaged field was increased to $\langle B \rangle = 2.11$ T, an increase of 111% compared to the surrounding field.

Here the same approach as above leads to a maximum concentrating factor of $8/\pi = 2.54$, i.e. the side length of the iron region divided by the circumference of the high field region. Again, a smaller increase than the theoretical limit is seen, due to the same reasons as argued above.

A. Pole pieces

We now extend the above analysis to a system that includes permanent magnets as the flux sources. We consider a geometry as shown in Fig. 6, i.e. a system with pole pieces to focus and enhance a magnetic field. The geometry consists of two square permanent magnets, two regions that are to be topology optimized between air and iron and a smaller square area where the magnetic field is to be maximized. The

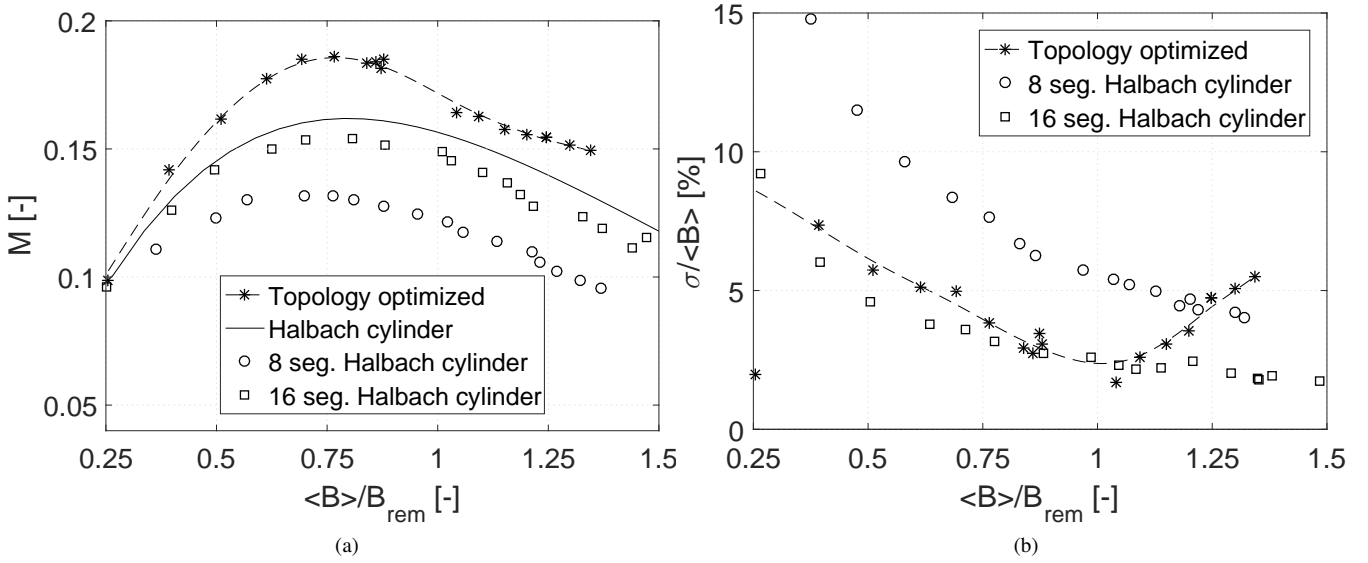


Fig. 3. a) The figure of merit, M , and b) the relative standard deviation of the field generated in the cylinder bore, both as function of the average field generated in the bore normalized by the remanence. The lines are guides to the eye.

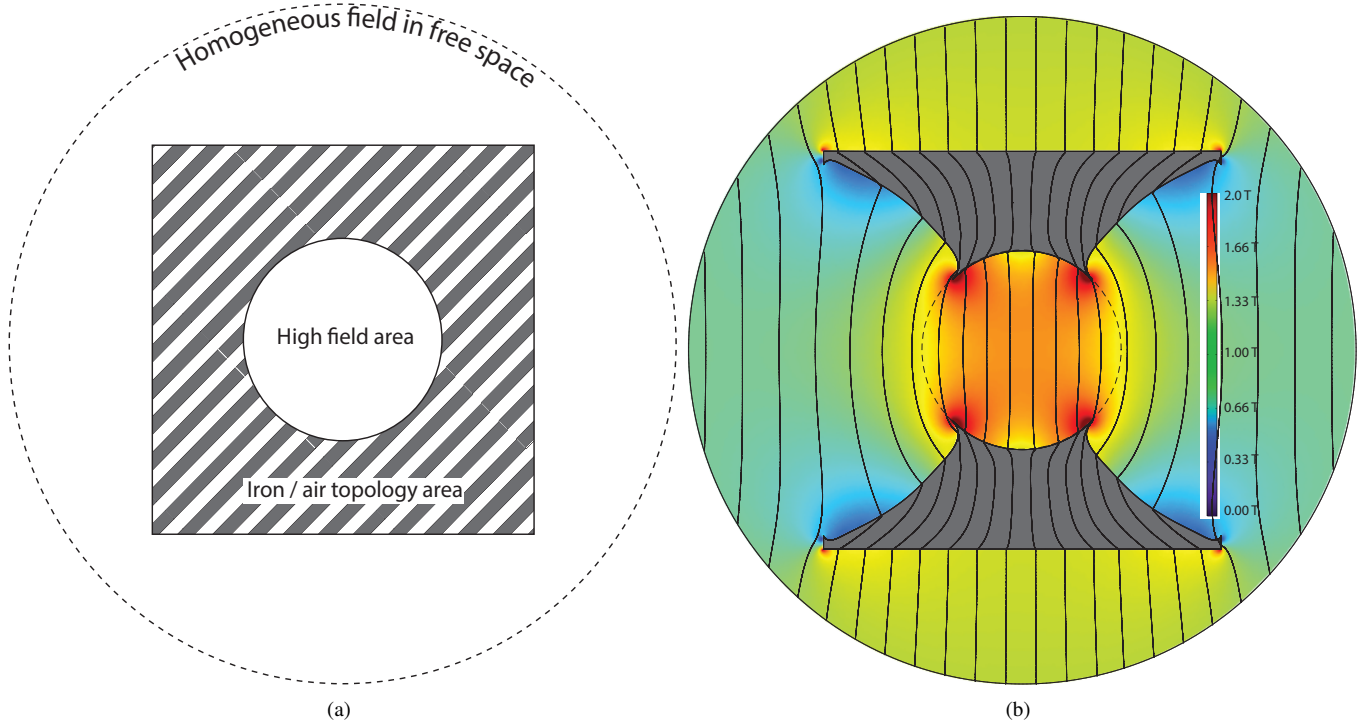


Fig. 4. a) The geometry of the system considered. The hatched grey area indicate the area to be topology optimized. b) The topology optimized structure determined.

side length of the high field region is half of the side length of the permanent magnets. The flux lines are imagined closed between the two permanent magnets through an iron circuit. Numerically, this is accomplished through periodic boundary conditions.

We consider a permanent magnet with a remanence of 1 T. We wish to determine the topological shape of iron that can concentrate the magnetic field into the high field area. Contrary to the case above, both a strong and homogeneous field is desired. Therefore, the optimization function to be maximized

is given as

$$\Theta = \frac{\langle B \rangle^\delta}{\sqrt{\langle (B - \langle B \rangle)^2 \rangle}} \quad (7)$$

In this expression the nominator is the average norm of the field, while the denominator is the standard deviation of the field. The factor δ is used to prioritize a strong but inhomogeneous field by increasing the absolute value of the nominator.

In order to evaluate the effectiveness of the topology optimization algorithm, we compare the generated topologies with

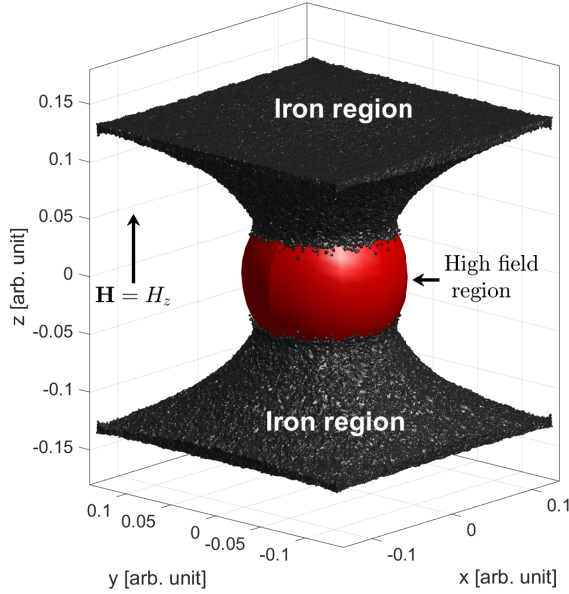


Fig. 5. The geometry of the 3D topology optimized structure. The iron regions as well as the high field region is indicated.

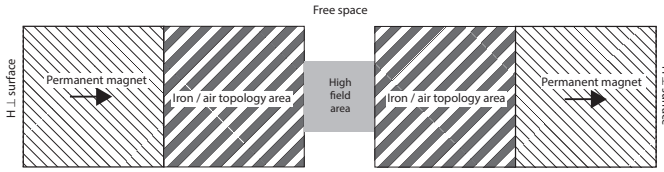


Fig. 6. The pole piece geometry simulated. The hatched grey area indicate the area to be topology optimized. The two permanent magnets are considered in contact through an iron yoke.

a standard trapezoidal-shaped pole piece, i.e. a geometry where the area to be topology optimized is replaced by a trapezoid of iron with varying side angle. Interestingly, the magnetic field produced in the air gap by the trapezoid geometry also be computed using a simple magnetic circuit approach for this geometry, including flux leakage in the model (28). There is a difference of less than 10% between finite element calculations and the magnetic circuit model for the geometry.

The relative standard deviation of the field in the high field area as function of $\langle B \rangle$ is shown in Fig. 7a for both the topology optimized geometries as well as for the trapezoidal geometries. The parameter δ is varied to control the strength of the generated field. As can be seen from the figure, the topology optimization algorithm is not able to determine a geometry that is better than the simple trapezoidal shape for the considered geometry. The dependence of the topology optimization on the δ parameter can be seen in Fig. 7b. Here it is clearly seen that as δ is increased, a higher field in the high field region is prioritized, at the expense of the homogeneity of the field.

V. MAGNETIC REFRIGERATION

We now consider permanent magnet structures, for which the low field regions are also of importance. This is relevant for magnetic refrigeration, where the permanent magnet system must provide adjacent regions of high and low field, between which a magnetocaloric material can be moved. Realizing this in practice without substantial flux leakage is difficult, although a number of magnet designs have realized a large difference between high and low field regions (22).

To more easily compare a topology optimized geometry with previous results, we consider a permanent magnet system geometry previously optimized using an alternative approach (29; 30). This geometry consists of two concentric Halbach cylinders, that generate four high field and four low field regions in the space between the cylinders. The radii of the system are identical to those given in Ref. (29), namely an inner and outer radius of the inner magnet of 10 mm and 70 mm respectively, and corresponding radii of the outer magnet of 100 mm and 135 mm, respectively. The remanence of the outer magnet is given by Eq. 4 with $p = 2$, while the inner magnet has $p = -2$. The geometry is illustrated in Fig. 8a. The topology optimization routine will here distinguish between permanent magnet material and iron.

The optimization criteria must be designed to favor either a large difference in magnetic field between the high and low field regions or a small amount of permanent magnet used to create this field difference. The expression to be maximized is

$$\Theta = \delta \frac{\langle B_{\text{high}}^{2/3} \rangle - \langle B_{\text{low}}^{2/3} \rangle}{A_{\text{mag}}} A_{\text{field}} \quad (8)$$

Here $\langle B_{\text{high}}^{2/3} \rangle$ is the average of the magnetic field to the power of 2/3 in the high field region, and similarly for the low field region, and A_{field} and A_{mag} are the areas of the high field volume and the area of permanent magnet material, respectively. Note that as the geometry is fixed the area of the high field region is $A_{\text{field}} = \pi/2 ((100 \text{ mm})^2 - (70 \text{ mm})^2)$. The power of 2/3 is used because the magnetocaloric effect approximately scales with this power around Curie temperature for most relevant magnetocaloric materials (31; 32). The parameter δ can be increased to increase the difference in field strength produced by the magnet, albeit with a higher amount of permanent magnet material.

The geometry is topology optimized for $\delta = 1 - 50$. An example of one of the topology optimized structures is shown in Fig. 8b. The efficiency of the resulting designs can be determined by calculating the Λ_{cool} parameter (33), which is proportional to Eq. (8) except without δ in the first factor. The Λ_{cool} and the M figure of merit value for the topology optimized designs are shown in Fig. 9 as function of the difference in field to the power of 2/3. Two different remanence values of 1.2 T and 1.4 T were used, as Λ_{cool} does not account for the influence of this parameter. The topology optimized structures are compared with the structure optimized using conventional optimization (29) and with $B_{\text{rem}} = 1.4 \text{ T}$. As can be seen from the figure, the topology optimized structures are significantly better than the conventionally optimized structure. With regards to the magnetic efficiency, M , the structures

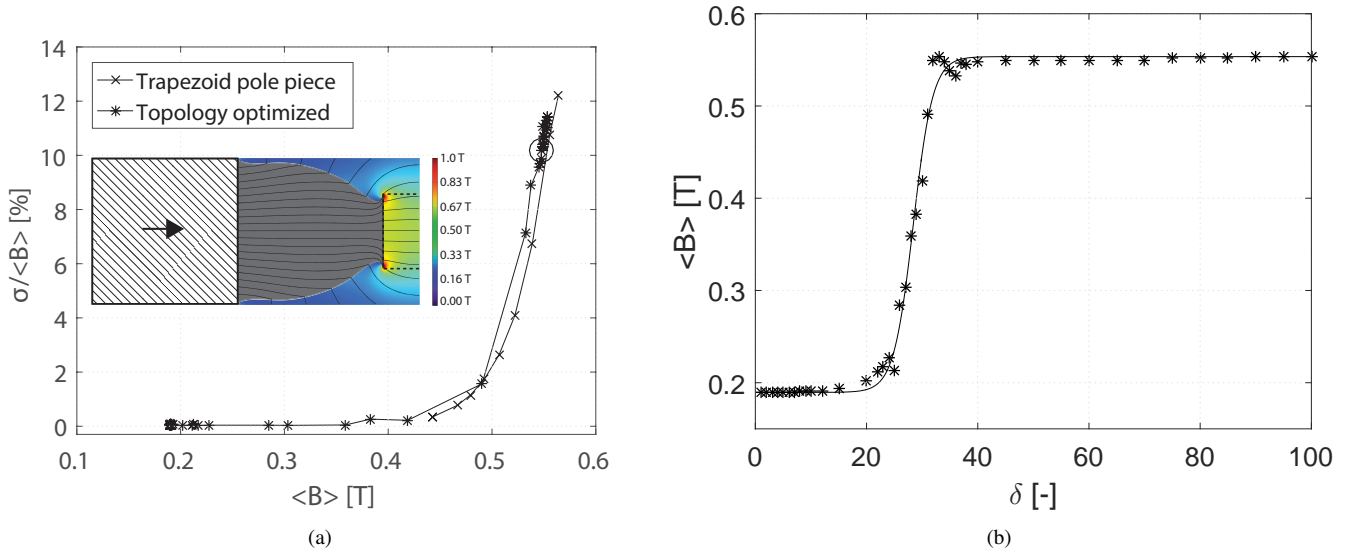


Fig. 7. a) The homogeneity of the field in the high field area as function of the average norm of the field in the same area. Both the results from topology optimized geometries as well as for a trapezoidal shape pole piece is shown. The inset shows the geometry for $\delta = 40$, which is the data point marked with a circle. b) The average norm of the magnetic field as function of the δ parameter. The line is a guide to the eye.

with different but constant remanence perform identically, as expected.

It should be noted that the low difference in flux density is a result of the dimensions of the geometry. Had larger magnets been utilized, the difference in flux density would have increased substantially.

VI. DISCUSSION

The objective function as well as the resulting improvement for each of the above cases is shown in Table I. As can clearly be seen, topology optimization can be used to design permanent magnet systems with significantly increased performance, compared to existing designs.

In the above implementation of topology optimization for permanent magnets, we have considered permanent magnets with a specified distribution of remanence. It is possible also to consider topology optimized problems where the remanence can freely vary in orientation throughout the design region by introducing a control variable describing e.g. the angle of the remanence with respect the chosen coordinate system. However, this is computationally very intensive and therefore such problems have not been considered above.

For the calculations above self-demagnetization has not been considered, but as long as the assemblies remain small (26) or magnets with high coercivity are used (34), this is not necessary. Furthermore, the manufacturability or the designs has not been considered. Numerical methods exist to optimally segment permanent magnet structures (4), which can be applied to segment and reduce the complexity of the topology produced systems for different applications (5).

The mesh sensitivity of the topology optimized problems considered were investigated using the Halbach cylinder geometry defined above. The average field in the cylinder bore as function of the number of mesh elements is shown in Fig. 10. As can be seen from the figure, the solution clearly converge

to a fixed value. The choice for number of mesh elements used for all simulations throughout this article corresponds to the highest number of mesh elements shown in Fig. 10.

VII. CONCLUSION

In conclusion, we have presented topology optimization of permanent magnet structures consisting of permanent magnets, high permeability iron and air. Three examples were considered. First, the Halbach cylinder was topology optimized by inserting iron, and an increase of 15% in magnetic efficiency was obtained with only an increase of 3.8 pp. in field inhomogeneity - a value similar to the inhomogeneity in a 16 segmented Halbach cylinder. Following this a topology optimized structure to concentrate a homogeneous field was computed, and was shown to increase the magnitude of the field by 111%. Finally, a permanent magnet with alternating high and low field regions was considered. Here a Λ_{cool} figure of merit of 0.472 was obtained, which is an increase of 100% compared to a previous optimized design.

ACKNOWLEDGEMENTS

This work was financed by the ENOVHEAT project, which is funded by Innovation Fund Denmark (contract no 12-132673).

REFERENCES

- [1] J. M. D. Coey, "Permanent magnet applications," *J. Magn. Mater.*, vol. 248, pp. 441, 2002.
- [2] N. I. Klevevts, "Synthesis of magnetic systems producing field with maximal scalar characteristics," *J. Magn. Mater.*, vol. 285, pp. 401, 2005.
- [3] N. I. Klevevts, "Optimal design of magnetic systems," *J. Magn. Mater.*, vol. 306, pp. 281, 2006.

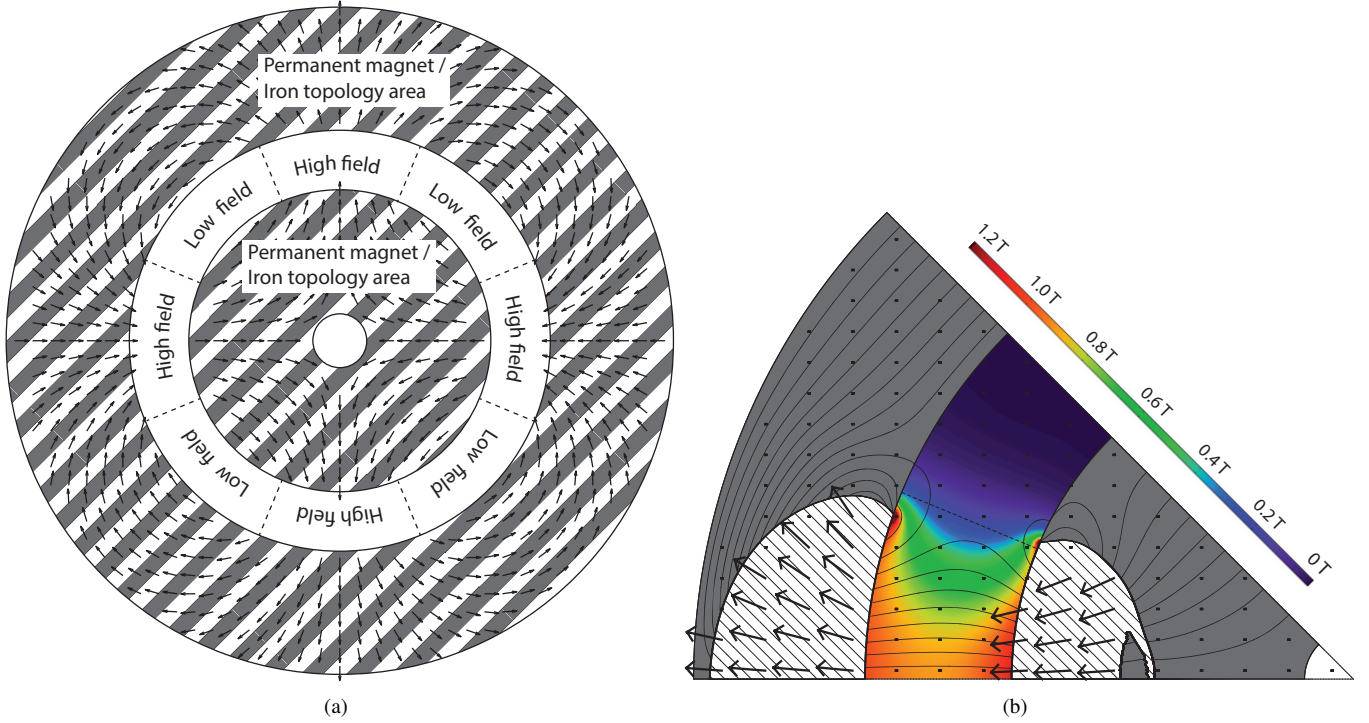


Fig. 8. a) The geometry of the system considered. b) The topology optimized structure determined, with $B_{rem} = 1.4$ T. Due to symmetry only a section of the geometry is shown.

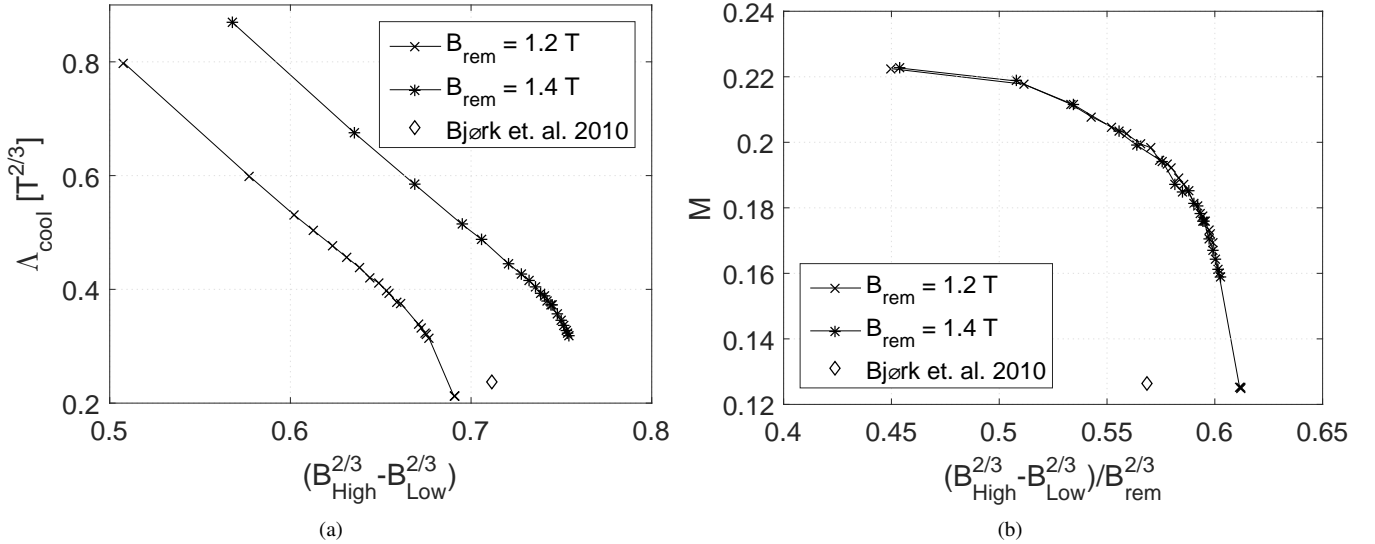


Fig. 9. The increase in a) Δ_{cool} and b) the figure of merit, M , as function of the difference in field to the power of 2/3.

- [4] A. R. Insinga, R. Bjørk, A. Smith, C. R. H. Bahl, "Globally optimal segmentation of permanent magnet systems," *Phys. Rev. Appl.*, vol. 5, pp. 064014, 2016.
- [5] A. R. Insinga, R. Bjørk, A. Smith, C. R. H. Bahl, "Optimally segmented permanent magnet structures," accepted for publication in *IEEE Trans. Magn.*, 2016.
- [6] M. P. Bendsoe, O. Sigmund, "Topology optimization: theory, methods, and applications," *Springer Science & Business Media*, 2013.
- [7] S. Wang, D. Youn, H. Moon, J. Kang, "Topology optimization of electromagnetic systems considering magnetization direction," *IEEE Trans. Magn.*, vol. 41, pp. 1808, 2005.
- [8] J. S. Choi, K. Izui, S. Nishiwaki, "Multi-material optimization of magnetic devices using an allen-cahn equation," *IEEE Trans. Magn.*, vol. 48, pp. 3579, 2012.
- [9] J. Lee, S. Wang, "Topological shape optimization of permanent magnet in voice coil motor using level set method," *IEEE Trans. Magn.*, vol. 48, pp. 931, 2012.
- [10] T. Ishikawa, P. Xie, N. Kurita, "Topology optimization of rotor structure in permanent magnet synchronous motors considering ease of manufacturing," *IEEJ J. Ind. Appl.*,

TABLE I
 THE VALUE FOR THE HALBACH CYLINDER IS TAKEN AT $R_o/R_i = 2.3$, WHILE THE VALUE FOR MAGNETIC REFRIGERATION IS TAKEN AT
 $\langle B_{\text{high}}^{2/3} \rangle - \langle B_{\text{low}}^{2/3} \rangle = 0.71 \text{ T}^{2/3}$.

Type	Objective function, Θ	Optimal value	Improvement (reference)
Halbach cylinder	$\frac{\langle B \rangle}{V_{\text{mag}}}$	$M = 0.186$	15% (25)
Homogeneous field	$\langle B \rangle$	$\langle B \rangle = 2.11 \text{ T}$	111%
Pole pieces	$\frac{\langle B \rangle^\delta}{\sqrt{(\langle B \rangle - \langle B \rangle)^2}}$	Identical to trapezoidal pole piece	None
Magnetic refrigeration	$\delta \langle B_{\text{high}}^{2/3} \rangle - \langle B_{\text{low}}^{2/3} \rangle \frac{A_{\text{field}}}{A_{\text{mag}}}$	$\Lambda_{\text{cool}} = 0.472 \text{ T}^{2/3}$	100% (29)

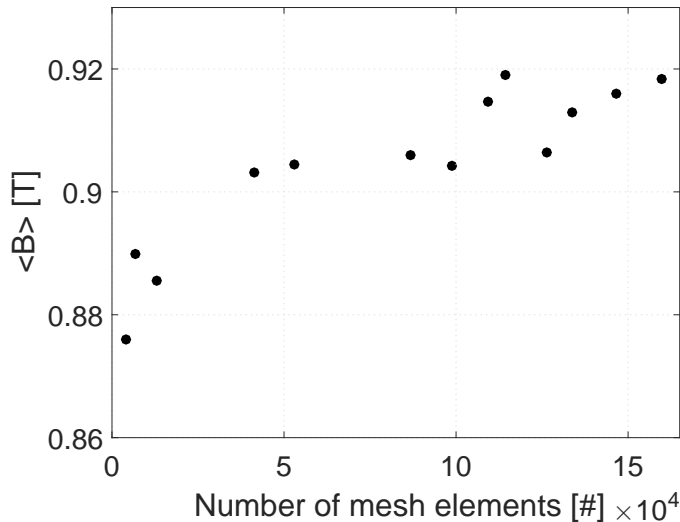


Fig. 10. The average value of the flux density in a topology optimized Halbach cylinder with a ratio of the inner and outer radius of $R_o/R_i = 2.3$ as function of the number of triangular elements in the mesh. The line is a guide to the eye.

- vol. 4, pp. 469, 2015.
- [11] J. S. Choi, T. Yamada, K. Izui, S. Nishiwaki, H. Lim, J. Yoo, "Optimal shape design of flux barriers in ipm synchronous motors using the phase field method," *COMPEL: Int. J. Comp. Math. Elec. Elec. Eng.*, vol. 33, pp. 998, 2014.
- [12] P. Putek, K. Gausling, A. Bartel, K. M. Gawrylczyk, E. J. W. ter Maten, R. Pulch, M. Gnther, "Scientific Computing in Electrical Engineering. Vol. 23 of Mathematics in Industry," *Springer*, 2016.
- [13] J. Lee, J. Yoo, "Topology optimization of the permanent magnet type MRI considering the magnetic field homogeneity," *J. Magn. Magn. Mater.*, vol. 322, pp. 1651, 2010.
- [14] T. Tadic, B. G. Fallone, "Three-dimensional nonaxisymmetric pole piece shape optimization for biplanar permanent-magnet MRI systems," *IEEE Trans. Magn.*, vol. 47, pp. 231, 2011.
- [15] S. Cheng, D. P. Arnold, "Optimization of permanent magnet assemblies using genetic algorithms," *IEEE Trans. Magn.*, vol. 47, pp. 4104, 2011.
- [16] Svanberg, K., "The method of moving asymptotes a new method for structural optimization," *Int. J. Numer. Methods Eng.*, vol. 24, pp. 359, 1987.
- [17] Svanberg, K., "A class of globally convergent optimization methods based on conservative convex separable approximations," *SIAM J. Optim.*, vol. 12, pp. 555, 2002.
- [18] J. H. Jensen, M. G. Abele, "Maximally efficient permanent magnet structures," *J. Appl. Phys.*, vol. 79, pp. 1157, 1996.
- [19] G. Moresi, R. Magin, "Miniature permanent magnet for table-top NMR," *Concepts Magn. Reson. Part B (Magn. Reson. Eng.)*, vol. 19B(1), pp. 35, 2003.
- [20] S. Appelt, H. Kühn, F. W. Häsing, B. Blümich, "Chemical analysis by ultrahigh-resolution nuclear magnetic resonance in the earth's magnetic field," *Nature Phys.*, vol. 2, pp. 105, 2006.
- [21] A. Tura, A. Rowe, "Design and testing of a permanent magnet magnetic refrigerator," *Proc. 2nd Int. Conf. Magn. Refri. Room Temp., Portoroz, Slovenia*, pp. 363, 2007.
- [22] R. Bjørk, C. R. H. Bahl, A. Smith, Pryds, N., "Review and comparison of magnet designs for magnetic refrigeration," *Int. J. Refri.*, vol. 33, pp. 437, 2010.
- [23] A. Sarwar, A. Nemirovski, B. Shapiro, "Optimal halbach permanent magnet designs for maximally pulling and pushing nanoparticles," *J. Magn. Magn. Mater.*, vol. 324, pp. 742, 2012.
- [24] K. Halbach, "Design of permanent multipole magnets with oriented rare earth cobalt material," *Nucl. Instrum. Methods*, vol. 169, 1980.
- [25] J. M. D. Coey and T. R. Ni Mhiochain, "Permanent magnets," *In: High Magnetic Fields, Edt: F. Herlach and N. Miura, World Scientific Publishing*, pp. 25, 2003.
- [26] R. Bjørk, A. Smith, C. R. H. Bahl, "The efficiency and the demagnetization field of a general halbach cylinder," *J. Magn. Magn. Mater.*, vol. 384, pp. 128, 2015.
- [27] C. Navau, J. Prat-Camps, A. Sanchez, "Magnetic energy harvesting and concentration at a distance by transformation optics," *Phys. Rev. Lett.*, vol. 109, pp. 263903, 2012.
- [28] H. A. Leupold, E. Potenziani II, "A Permanent Magnet Circuit Design Primer, Army Research Laboratory, ARL-TR-946," 1996.
- [29] R. Bjørk, C. R. H. Bahl, A. Smith, D. V. Christensen, N. Pryds, "An optimized magnet for magnetic refrigeration," *J. Magn. Magn. Mater.*, vol. 322, pp. 3324, 2010.
- [30] R. Bjørk, C. R. H. Bahl, A. Smith, N. Pryds, "Improving

- magnet designs with high and low field regions,” *IEEE Trans. Magn.*, vol. 47, pp. 1687, 2011.
- [31] R. Bjørk, C. R. H. Bahl, M. Katter, “Magnetocaloric properties of $\text{LaFe}_{13-x-y}\text{Co}_x\text{Si}_y$ and commercial grade Gd.,” *J. Magn. Magn. Mater.*, vol. 322, pp. 3882, 2010.
- [32] A. Smith, C. R. H. Bahl, R. Bjørk, K. Engelbrecht, K. K. Nielsen, N. Pryds, “Materials challenges for high performance magnetocaloric refrigeration devices,” *Adv. Energy Mater.*, vol. 2, pp. 1288, 2012.
- [33] R. Bjørk, C. R. H. Bahl, A. Smith, N. Pryds, “Optimization and improvement of halbach cylinder design,” *J. Appl. Phys.*, vol. 104, pp. 13910, 2008.
- [34] A. R. Insinga, C. R. H. Bahl, R. Bjørk, A. Smith, “Performance of halbach magnet arrays with finite coercivity,” *J. Magn. Magn. Mater.*, vol. 407, pp. 369, 2016.

B.6 Performance-oriented analysis of a hybrid magnetic assembly for a heat-pump magnetocaloric device

A. R. Insinga, A. Smith, C. R. H. Bahl and R. Bjørk

6th IIF-IIR International Conference on Magnetic Refrigeration at Room Temperature, Thermag VI

PERFORMANCE-ORIENTED ANALYSIS OF A HYBRID MAGNETIC ASSEMBLY FOR A HEAT-PUMP MAGNETOCALORIC DEVICE

A. R. INSINGA, A. SMITH, C. R. H. BAHL, R. BJØRK

Department of Energy Conversion and Storage, Technical University of Denmark
Risø Campus, Roskilde, Denmark – aroin@dtu.dk

ABSTRACT — Conventional active-regenerator magnetocaloric devices include moving parts, with the purpose of generating an oscillating magnetic field in the magneto-caloric material, placed inside the regenerator. In this work a different design is analyzed, for application in a magnetocaloric heat pump. In this design all the parts of the machine are static and the oscillating field is generated by varying the currents of electromagnets included in the hybrid magnetic assembly. The use of different permanent magnet materials is compared with the perspective of maximizing the coefficient of performance of the device.

1. INTRODUCTION

The magnetic assemblies designed for magnetocaloric refrigeration are necessarily realized without using electromagnets, since the heat produced by the Joule effect would decrease the overall performance of the device. In order to work, any magnetocaloric device must produce a time oscillating magnetic field inside the magnetocaloric material. When the magnetic assembly is realized without the use of electromagnets, there are two main options[1] to produce the field oscillation inside the material: rearrange different parts of the magnetic assembly to modify the field, or displace the material itself in different positions characterized by different values of magnetic field. Both the options have some disadvantages: additional design challenges are introduced, the lifespan of some components of the machine is reduced because of friction and vibrations associated with the motion. A magnetocaloric heat pump does not share this limitation with the refrigerators and the use of a hybrid magnetic assembly, which includes also electromagnets, is feasible. The Joule dissipation in the coils of the electromagnets will generate an additional heating output. Moreover a new option is available to produce the oscillating field inside the magnetocaloric material: the coil-current of the electromagnets can be varied to alter the magnetic field while all the parts of the device are stationary. This design solution is not affected by the disadvantages of moving machines, and would also result in a minor noise production. One prototypical geometry for a static machine with hybrid magnetic assembly will be analysed, with the perspective of maximizing the net performance of the magnetocaloric heat pump.

2. METHODS

We will consider one prototypical geometry for static machines with hybrid magnetic assembly and describe the methods we employed to model this system. The geometry is schematically illustrated in Fig. 1 and consists in a high-permeability material (iron) core composed by two loops (left and right loop).

A permanent magnet magnetized in the vertical direction is placed in the central branch of the circuit. Two air gaps, which will host the magnetocaloric regenerators, are located in the middle of the left and right branches. Finally, two electric coils are wrapped around the left and right branches of the circuit (in the figure the coils are placed right around the air gaps, but any position would be equivalent as long as each coil is interlocked with the respective iron-core loop).

The geometry is modelled as a magnetic circuit composed by its different elements connected through common nodes. Each element is characterized by uniform magnetic field, H , and flux density, B , and by a couple of geometric parameters: length and cross-section area. In analogy with an electric-circuit, the system is governed by a conservation equation for each node and one for each loop. Gauss's law for magnetism implies the conservation of the magnetic flux at each node. Ampere's law implies that the line integral of H over each loop is equal to the electrical current flowing through the loop. The final ingredient to complete the model is a constitutive B - H relation for each material. This means that there is no flux leakage from the air gaps. In this analysis the following materials will be considered: air, iron, neodymium-iron-boron (NdFeB) magnet and aluminium-nickel-cobalt (AlNiCo) magnet. The demagnetization branch of the B - H curve of each of the relevant materials (except air) is plotted in the left panel of Fig. 2. We developed a model in Matlab that interpolates the constitutive relations from a set of (B,H) points passed as input, and then numerically solves the resulting magnetic-circuit equations. The program

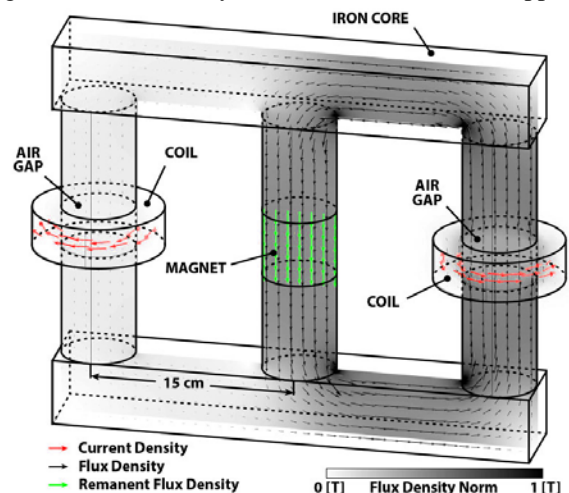


Fig. 1. Schematic illustration of the double-loop geometry. The right air gap is in the high-field state.

returns as outputs the values of the flux density inside each air gap. The results given by this simplified model are less realistic than what could be obtained with a finite element analysis of the geometry, but the computational cost is much lower, making it a suitable tool for a preliminary analysis.

The operation of the device (i.e. the time dependence of the coil-currents) is determined by the characteristics of the thermodynamical cycle of the magnetocaloric material. The focus of this work will be on cycles for which the materials spend half of the cycle time in high-field state and the other half in a low-field state. In this device the coils augment the field in one of the air gaps while simultaneously reducing it in the other for one half of the cycle. During the other half of the cycle the high-field and low-field air gaps are switched. The current is parameterized by the high-field state current value, I_H , and the low-field state value, I_L . In every moment of the cycle both these currents are occurring simultaneously on the two coils. Instead of using these parameters, however, the following expressions are used: $I_H = I \cos \phi$, $I_L = I \sin \phi$. In this way the net power, α , spent by the machine by Joule dissipation, is not dependent on the ‘current-angle’ ϕ , but only on the square I^2 of the ‘current-amplitude’, that is equal to the sum of the squares of the two components. The performance of the device is expressed by the Coefficient Of Performance, COP, which is defined[2] as the ratio between the output heating power and the input power: $COP = (Q_C + P_0 + \alpha)/(P_0 + \alpha)$, where P_0 is the net ‘base’ power (i.e. the power spent by the machine in other parts than the electric coils, for example the pump of the heat-exchange fluid), and Q_C is the cooling power generated by the magnetocaloric effect. It is assumed[3] that the cooling power is given by $Q_C = \gamma \Lambda_B = \gamma (B_H^{2/3} - B_L^{2/3})$, where γ is the cooling factor and B_H and B_L are respectively the high and low values of the norm of the flux density.

3. RESULTS

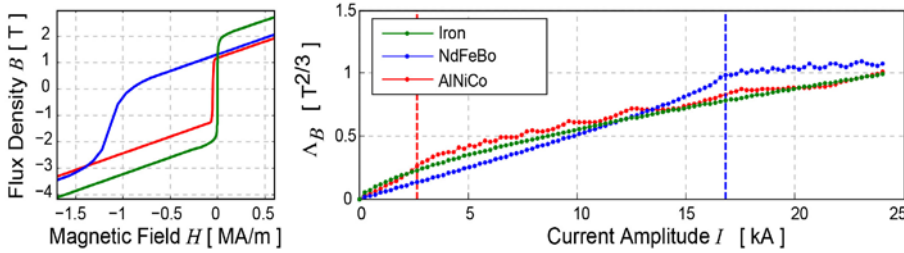


Fig. 2. Left panel: Demagnetization branch of the B - H curves of the relevant materials. Right panel: value of Λ_B as a function of I , for the optimal choice of ϕ .

The analysis based on this model can be used to optimize different geometrical and operational parameters of the heat-pump device. The starting point is to determine the optimal value of ϕ for each value of I and each permanent magnet material. This result is shown in the right panel of Fig. 2. The value of Λ_B (vertical axis) is plotted as a function of I (horizontal axis) for the different materials corresponding to the B - H curves plotted in the left panel. The plotted $\Lambda_B(I)$ curves correspond to the optimal choice of ϕ for a given value of I .

The vertical dashed lines correspond to the minimum value of I necessary to completely cancel the field B_L for each material. The plot indicates that for very low values of I the best performance would be obtained by replacing the permanent magnet material with iron. For higher current values, (approximately between the red dashed line and the blue dashed line), AlNiCo would be the better-performing material. For even higher current values the best choice would be NdFeB, but the value of Λ_B remains of the same order of magnitude of the other materials. These results are consequences of the $2/3$ exponents weighting the fields, B , in the expression of Λ_B . Because of these exponents, it is more convenient to reduce B_L than it is to increase B_H . For values of I large enough to cancel B_L , the optimal ϕ is determined by the condition that the flux density in the low field region is not reversed (thus increasing its norm). For this reason AlNiCo, or even iron, could perform better than NdFeB for some values of I .

4. CONCLUSIONS

This analysis has been used to determine, for arbitrary values of base power P_0 and cooling factor γ , the optimal values of ϕ and I , and the better-performing material. The optimality parameter is the coefficient of performance COP of the final heat-pump device, which, once the values of P_0 and γ are known, can be predicted by this model. Within this framework it is possible to compare the performance of this geometry or similar static devices, with the performance of more conventional designs with moving parts. This work was financed by the ENOVHEAT project which is funded by the Danish Council for Strategic Research (contract no 12-132673) within the Programme Commission on Sustainable Energy and Environment.

REFERENCES

- [1] R. Bjørk, C.R.H. Bahl, A. Smith, N. Pryds, “Comparison of adjustable permanent magnetic field sources”, J. Magnetism and Magnetic Materials, 2010, 322 (22): pp. 3664-3671.
- [2] J.A. Lonzano, K. Engelbrecht, C. R. H. Bahl, K. K. Nielsen, D. Eriksen, U. L. Olsen, J. R. Barbosa, Jr., A. Smith, A.T. Prata, N. Pryds, “Performance analysis of a rotary active magnetic refrigerator”, J. Applied Energy 2010, 111: pp. 669-680.
- [3] R. Bjørk, “Designing a magnet for magnetic refrigeration”, PhD Thesis, 2010.

B.7 Optimization of Hybrid Magnetic Systems

A. R. Insinga, R. Bjørk, A. Smith and C. R. H. Bahl

AIM 2016 - Advances In Magnetism Conference

Optimization of Hybrid Magnetic Systems

Andrea R. Insinga¹, Rasmus Bjørk¹, Anders Smith¹ and Christian R. H. Bahl¹

¹Department of Energy Conversion and Storage – Technical University of Denmark
 Frederiksborgvej, 399 – 4000 Roskilde, Denmark
aroin@dtu.dk

Abstract—We present an optimization approach that can be employed for the design of hybrid magnetic systems consisting of permanent magnets combined with electromagnets. We consider a geometry composed of different independent coils and uniformly magnetized segments. We address the problem of maximizing a non-linear objective functional with respect to the direction of the remanence of each segment and with respect to the current density flowing inside each coil. Our approach exploits the linearity of the field with respect to the sources to quickly evaluate the objective functional for any given configuration, and apply different optimization techniques, which would have otherwise been prohibitive.

Index Terms—Electromagnet, optimization methods, permanent magnet, system design.

I. INTRODUCTION

Permanent magnets and electromagnets have different strengths and limits, which usually make one of the two options more suitable than the other for a particular application[1].

Permanent magnets allow the creation of a field at no energy cost, making them particularly advantageous for energy conversion applications, when efficiency is especially important. However, the only way to create a time-dependent field employing permanent magnets is to move the parts of the magnetic system with respect to each other, which is often done with an electric motor. Electromagnets on the other hand are very versatile as they allow modification of the field they produce by simply changing the current density flowing in the different coils of the system.

For some applications, the best option could be to combine permanent magnets with resistive magnets into a hybrid magnetic system, which exploits the benefits of the two flux sources.

II. METHODS

We present an optimization approach which we developed to optimize hybrid magnetic systems with respect to a given objective functional S . Many optimization algorithms require a large number of evaluations of the objective functional and each evaluation requires the solution of the magnetic field equations for the considered geometry. This is often done by employing computationally expensive Finite Element Methods (FEM) and therefore many optimization algorithms are unfeasible. Our method is based on the linearity of the generated magnetic field \mathbf{H} with respect to the remanent flux density \mathbf{B}^{rem} and current density \mathbf{J} producing it. We consider a system whose geometry is pre-determined: the permanent

magnet is divided into N uniformly magnetized segments, and the resistive magnet is divided into M coils, each with uniform current density. It is possible to compute the field \mathbf{H}_j generated by each permanent magnet segment in any point of space in terms of a linear combination of the components of its remanence vector. Similarly, the field \mathbf{H}_k generated by each coil is proportional to the current density in the coil. The total field \mathbf{H} is then given by the superposition of the individual fields generated by each segment and by each coil, which we compute in advance for each orthogonal component of \mathbf{B}^{rem}_j and \mathbf{J}_k :

$$\mathbf{H}(\mathbf{x}) = \sum_j^N \mathbf{H}_j(\mathbf{x}; \mathbf{B}_j^{rem}) + \sum_k^M \mathbf{H}_k(\mathbf{x}; \mathbf{J}_k) \quad (1)$$

The optimization problem is to maximize the value of a functional $S[\mathbf{H}]$ with respect to the direction of the remanence for each segment, and with respect to the current density for each coil. We also apply a constraint on the total power dissipated by the coils (assumed non-superconducting) because of the Joule effect.

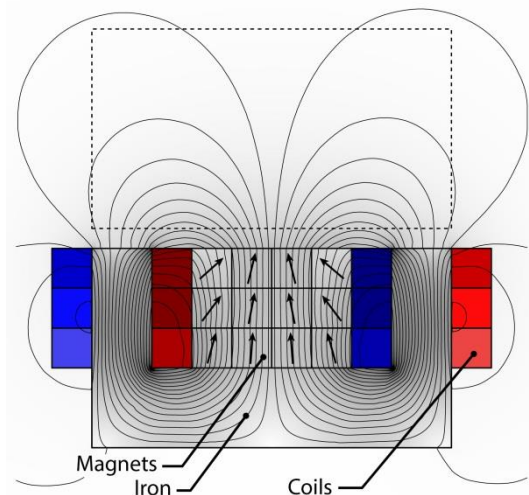


Fig. 1. Magnetic system optimized for maximum attractive force in the area enclosed by the dashed line.

For each optimization problem we initially consider a suitable linear functional L , which approximates the actual non-linear objective functional S . Any functional L that is linear with respect to the field \mathbf{H} can be expressed in terms of an objective vector field \mathbf{u} defined over a certain region Ω :

$$L[\mathbf{H}] = \int_{\Omega} dV \mathbf{H}(\mathbf{x}) \cdot \mathbf{u}(\mathbf{x}) \quad (2)$$

Because of the linearity, the contribution to the value of L from each magnet and each coil is independent. This implies that the globally optimal solution with respect to L can be easily computed. We use this solution as the initial guess to

solve the non-linear problem employing different optimization algorithms, such as gradient descent, simulated annealing and the Nelder–Mead method. These methods require a large number of function evaluations which we are able to perform rapidly thanks to the fact that we compute in advance the individual field generated by each source.

III. RESULTS

We illustrate the usefulness of our method by presenting two-dimensional optimized designs from three different applications of magnetic systems. We express the objective functional for each optimization problem by defining the objective vector field \mathbf{u} .

For each example we show a figure with the result of the FEM simulation of the optimized system. The flux density \mathbf{B} is indicated by the black flux lines, and its norm is indicated by the grayscale, darker shades corresponding to a higher norm. The optimal direction of the remanence for each magnet segment is indicated by a black arrow, and the current density for each coil is indicated by the colored overlay. Blue indicates current density flowing into the plane and red indicates current density flowing out of the plane. Darker shades indicate a higher current density norm.

A. Force Optimization

We consider a system designed to maximize the attractive force on magnetizable bodies. For this purpose we maximize the negative y component of the gradient of the norm of the field [2]:

$$S[\mathbf{H}] = - \int_{\Omega} dV \hat{e}_y \cdot \nabla \|\mathbf{H}(\mathbf{x})\|^2 \quad (3)$$

where Ω is the area enclosed by the dashed line shown in Fig. (1). The initial linear functional is defined as:

$$L[\mathbf{H}] = + \int_{\Omega} dV \mathbf{H}(\mathbf{x}) \cdot \hat{e}_y \quad (4)$$

Our optimization process leads to the optimized result shown in Fig. 1.

B. Quadrupole Magnet

Quadrupole magnets are employed in particle accelerators with the purpose of focusing beams of charged particles[3].

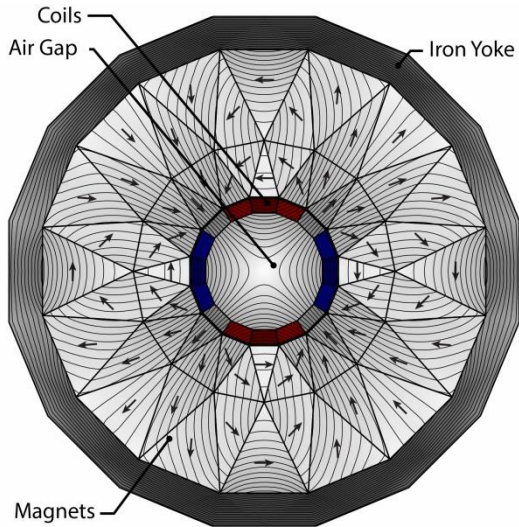


Fig. 2. Quadrupole hybrid magnet designed to focus a charged particle beam.

We start the optimization procedure with the linear objective L defined in the circular air gap Ω shown in Fig. 2:

$$L[\mathbf{H}] = \int_{\Omega} dV y H_x + x H_y \quad (5)$$

After the linear optimization step we consider the following non-linear objective functional:

$$S[\mathbf{H}] = \int_{\Omega} dV \|\Delta(\mathbf{x})\| \quad (6)$$

where Δ is the the vector difference between the field \mathbf{H} and its quadrupolar component.

C. Magnetic Refrigeration

Magnetic systems for active magnetic refrigeration at room temperature are designed to produce a field with high and low field regions adjacent to each other[4]. We consider the rotary magnetic system whose geometry is shown in Fig. 2.

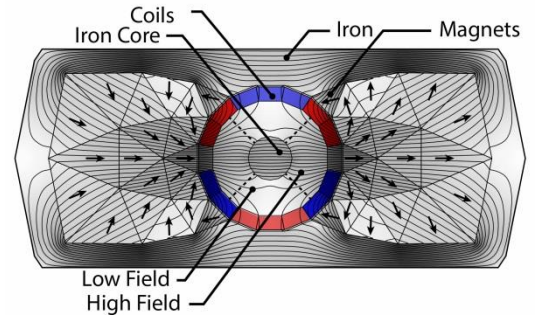


Fig. 3. Magnetic system for a rotary device for magnetic refrigeration.

The high and low field regions are both located in the air gap between the external cylinder and the iron core in the center. The high field regions Ω_H are on the sides of the iron core, and the low field regions Ω_C are above and below the iron core. They are separated by the dashed lines shown in the Fig. 3. We consider an objective vector field oriented towards the positive x direction and defined over the high field region:

$$L[\mathbf{H}] = \int_{\Omega_H} dV \mathbf{H}(\mathbf{x}) \cdot \hat{e}_x \quad (7)$$

Since the magnetocaloric effect scales as the norm of the field elevated to the power of $2/3$, we consider the following non-linear objective functional[4]:

$$S[\mathbf{H}] = \int_{\Omega_H} dV \|\mathbf{H}(\mathbf{x})\|^{2/3} - \int_{\Omega_C} dV \|\mathbf{H}(\mathbf{x})\|^{2/3} \quad (8)$$

IV. CONCLUSION

We observed that starting the optimization process by solving a suitable linear problem is a valuable aid in solving the considered non-linear problems.

REFERENCES

- [1] M. G. Abele, "Generation of highly uniform fields with permanent magnets," *J. Appl. Phys.*, vol. 76, no. 10, 1994.
- [2] A. Sarwar, A. Nemirovski, and B. Shapiro, "Optimal Halbach Permanent Magnet Designs for Maximally Pulling and Pushing Nanoparticles," *J. Magn. Magn. Mater.*, vol. 324, pp. 724-754, 2012.
- [3] G. Tosin, P. P. Sanchez, J. F. Citadini and C. C. Vergasta, "Super hybrid quadrupoles," *Nucl. Instrum. Methods Phys. Res.*, vol. A674, pp. 67-73, 2012.
- [4] R. Björk, C. R. H. Bahl, A. Smith and N. Pryds, "Improving Magnet Designs With High and Low Field Regions," *IEEE. Trans. Magn.*, vol. 47, no. 6, 2011.

B.8 Generating the optimal magnetic field for magnetic refrigeration

R. Bjørk, A. R. Insinga, A. Smith and C. R. H. Bahl

7th IIF-IIR International Conference on Magnetic Refrigeration at Room Temperature, Thermag VII

GENERATING THE OPTIMAL MAGNETIC FIELD FOR MAGNETIC REFRIGERATION

R. Bjørk*, A. R. Insinga, A. Smith, C. R. H. Bahl

Department of Energy Conversion and Storage, Frederiksborgvej 399, 4000 Roskilde, Denmark

*Corresponding author. E-mail: rabj@dtu.dk

ABSTRACT

In a magnetic refrigeration device the magnet is the single most expensive component, and therefore it is crucially important to ensure that an effective magnetic field as possible is generated using the least amount of permanent magnets. Here we present a method for calculating the optimal remanence distribution for any desired magnetic field. The method is based on the reciprocity theorem, which through the use of virtual magnets can be used to calculate the optimal remanence distribution. Furthermore, we present a method for segmenting a given magnet design that always results in the optimal segmentation, for any number of segments specified. These two methods are used to determine the optimal magnet design of a 12-piece, two-pole concentric cylindrical magnet for use in a continuously rotating magnetic refrigeration device.

Keywords: Permanent magnet, Design, Remanence, Optimization, Segmentation, Virtual

1. INTRODUCTION

Generating a strong magnetic field is of great importance in magnetic refrigeration. Most magnetic refrigeration devices use permanent magnets to accomplish this task, as these do not require any energy input to generate a magnetic field. However, permanent magnets are expensive and thus it is important to utilize them most efficiently. This means that the permanent magnet structure must generate the high magnetic field using the least amount of magnet material possible; indeed the magnet is the most expensive component in a magnetic refrigeration device [1,2].

Previously, design of permanent magnet systems for magnetic refrigeration have relied on adapting existing well-known geometries, such as the Halbach cylinder or the “C”-shaped magnet, to a given regenerator geometry [3,4]. An optimization method exists that can be used to optimize a given magnet design [5], but it requires an existing geometry and remanence distribution. The large spread in efficiency of published magnet designs [6] indicates the very diverse methods used to design magnets for magnetic refrigeration, but also the potential for improving performance.

Here we present a method that can determine the optimal distribution of remanence and the border of the magnet for any desired magnetic field. Furthermore, we present a method for segmenting a given magnet design that always results in the optimal segmentation, for any number of segments specified.

2. THE RECIPROCITY THEOREM AND THE OPTIMAL MAGNET

The optimization method presented here is not applied to a predefined magnet design but is based solely on the desired magnetic field. The foundation for determining the optimal distribution of permanent magnet material is the so-called reciprocity theorem in magnetostatics, which can be expressed as [7]:

$$\int \mathbf{B}_{r,1}(\mathbf{x}) \cdot \mathbf{H}_2(\mathbf{x}) dV = \int \mathbf{B}_{r,2}(\mathbf{x}) \cdot \mathbf{H}_1(\mathbf{x}) dV \quad (1)$$

This equation is an energy equivalence between two magnetic systems, 1 and 2. The equation states that the magnetic energy in system 1 in virtue of its remanence, $\mathbf{B}_{r,1}$, when placed in the field generated system 2, \mathbf{H}_2 , is equal to the energy in system 2 with remanence $\mathbf{B}_{r,2}$, when placed in the field generated by system 1, \mathbf{H}_1 . The integration is performed over all space. However, since $\mathbf{B}_{r,1}$ is only non-zero in places where permanent magnet material is present in system 1, and likewise for system 2, we can limit the integrals in Eq. (1) to these regions. In deriving Eq. (1) we have assumed that there are no free currents in the system and that the materials

in the system obeys a linear $\mathbf{B} - \mathbf{H}$ relation, $\mathbf{B} = \mu\mathbf{H} + \mathbf{B}_r$, where the permeability, μ , must be the same for both systems [8].

The theorem in Eq. (1) can be used to determine the optimal remanence, $\mathbf{B}_{r,1}$, that produces a given desired magnetic field, \mathbf{H}_1 . We consider a *virtual* magnet system that has a virtual remanence, $\mathbf{B}_{r,2}$, parallel to the desired magnetic field, \mathbf{H}_1 , in every point in the air gap [9,10]. Then the right hand side of equation Eq. (1) will be maximized as $\mathbf{B}_{r,2} \parallel \mathbf{H}_1$. The left hand side will thus also be maximized if the real remanence is aligned to the field produced by the virtual remanence everywhere. An illustration of this concept is shown in Fig. 1, for a system where we want to generate a magnetic field as shown on the figure to the left, i.e. a field that is radial in two air gaps and zero between these. Firstly, virtual magnets are ‘placed’ in the air gap, with a remanence identical to the desired magnetic field. These virtual magnets generate a magnetic field, shown in the right hand side of Fig. 1. The optimal remanence in the design area is then aligned everywhere to this virtual magnetic field, to maximize the averaged projection of the produced field onto the desired virtual remanence.

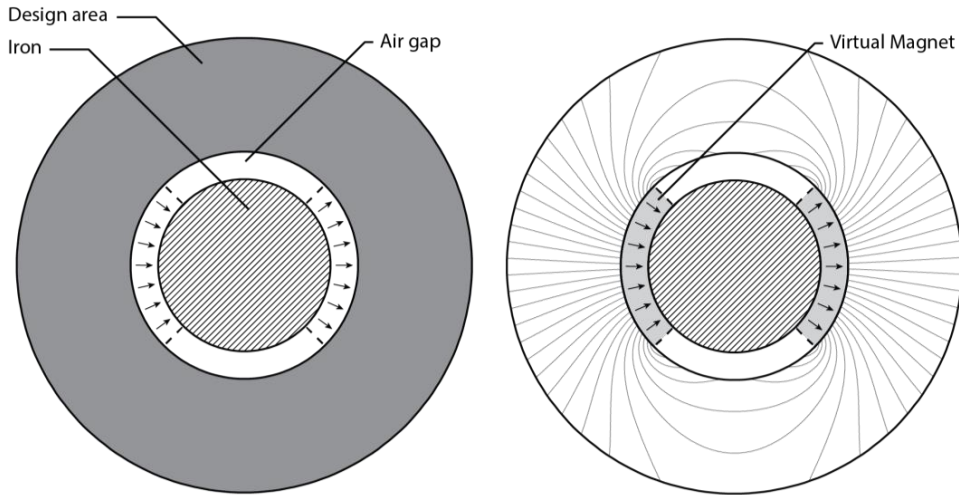


Figure 1. An illustration of the reciprocity theorem. The left-hand figure show the design area as well as the desired magnetic field in the air gap. The right-hand figure show the corresponding virtual system, with virtual magnets with a remanence identical to the desired magnetic field of the real system and the field produced by these.

It is also seen from Eq. (1) that once the real remanence is aligned to the virtual field \mathbf{H}_2 in a given point \mathbf{x} , the contribution of that site to the integral in Eq. (1) is proportional to the norm H_2 . This means that if the magnet is surrounded by air ($\mu_r = 1$) the optimal border between magnet and air will be a contour level of H_2 , as points inside a contour level of H_2 will contribute more to the integral in Eq. (1) than points outside. If the magnet design area is surrounded by a high permeability material, e.g. iron, the optimal border can also be calculated. Assuming an infinite permeability for iron, the virtual field \mathbf{H}_2 will be normal to the border of the areas with iron present. The magnetic field can also be written as the gradient of a magnetic scalar potential, $\mathbf{H}_2 = -\nabla\Phi_2$. Here the magnetic field is also normal to contours of Φ_2 . Thus, there is an analogy between these two cases. By choosing a contour of Φ_2 as the border of the magnet, we can ensure that the energy efficiency of the system is maximized [11]. If the relative permeability of the surrounding matter is neither 1 nor infinite, an iterative approach can be used to determine the border between magnet and the surroundings.

3. OPTIMAL SEGMENTATION

Once a remanence vector field has been selected, be it optimal or not, the magnetic structure must be segmented before it can be realized. When segmenting a magnet design, the system is split into uniformly magnetized segments. Previously segmentation of magnet designs was done by numerically determining the optimization direction of the remanence on a predefined segmented geometry. However, it has recently been shown that it is possible to determine the globally optimal segmentation of a 2D magnetic system [8].

Because of superposition, the field generated by each point in the magnet is independent from the other points. One can show that this implies that it is never optimal to split a region over which the direction of the virtual field \mathbf{H}_2 is uniform [8], which for 2D systems can be shown to be equivalent with the fact that the optimal border between two adjacent segments must lie on a contour of $\psi = \arctan(H_{2,y} / H_{2,x})$. We are thus left with choosing the optimal contours that gives the desired number of segments. This problem can be shown to be equivalent with maximizing the perimeter of a piecewise linear approximation of a continuous curve $H_{int}(\psi_2)$ defined as the integral of \mathbf{H}_2 between two contours ψ_1 and ψ_2 [8]. It is possible to determine the globally optimal solution to the curve approximation problem up to the desired precision by dynamic programming using numerical techniques described elsewhere [8].

4. EXAMPLE

We will consider an example to illustrate the applicability of the techniques presented above for use in designing magnets for magnetic refrigeration. We consider a rotating magnet design with an outer cylindrical magnet, an inner iron cylinder and two high field regions and two low field regions in the air gap between the cylinders. This is a geometry well known from literature [12]. We assume an inner radius of the air gap of 0.125 m, and an outer radius of 0.165 m. The total high field cross-sectional area is thus 182 cm². The magnet is assumed to have a maximum outer radius of 0.33 m. We consider a design where the part of the outer cylinder that is not permanent magnet is iron, which here is assumed to have a permeability of $\mu_r = 1000$. The remanence of the permanent magnets is 1.4 T.

The remanence of the permanent magnets is 1.4 T.

We desire a magnetic field in the high field air gaps similar to the field illustrated in Fig. 1. In order to design the magnet, we follow the procedure described above. First, virtual magnets with a remanence equal to the desired magnetic field are ‘placed’ in the high field air gaps. The remanence in the design area is then aligned to the field produced by these virtual magnets. Finally a contour of the magnetic scalar potential of the virtual field, Φ_2 , is chosen as the border between the magnet and the surrounding iron. The choice of contour of Φ_2 is a choice of the area of the permanent magnet. Following this, segmentation into 12 pieces is chosen, following the optimal segmentation technique described above.

The difference in average field between the high and the low field regions as function of the fraction of the outer cylinder that is permanent magnet material is shown in Fig. 2a. Also shown in this figure is the Λ_{cool} figure of merit parameter for the magnet design [6]. As can be seen from the figure, at a difference in average field of 1 T, a value of $\Lambda_{cool} = 0.35 \text{ T}^{2/3}$ can be obtained, a value significantly higher than previously reported values [6]. An illustration of the resulting design is shown in Fig. 2 below for the case of a cross-sectional

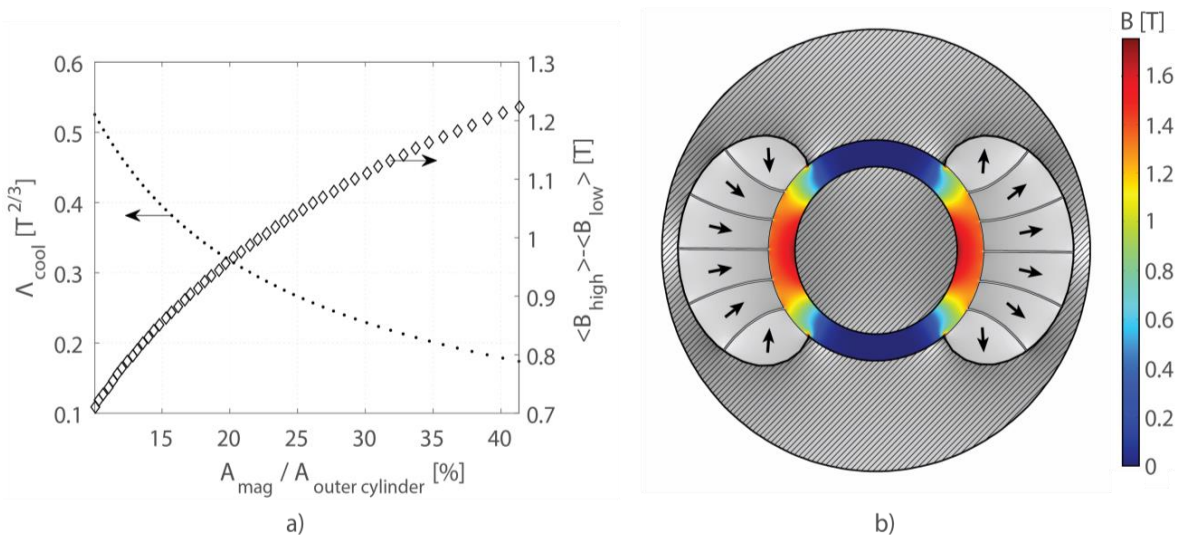


Figure 2: a) The Λ_{cool} and the difference in averaged field between the high and low field regions as function of the amount of permanent magnet material and b) the optimal magnet design for the case of $A_{mag} / A_{outer\ cylinder} = 36\%$.

magnet area of 930 cm², i.e. $A_{mag}/A_{outer\ cylinder} = 36\%$ for this design. The average field in the high field region is 1.25 T, while the average field in the low field region is 0.13 T.

The methods described above always produce the magnet with optimum remanence and optimum segmentation for the desired field distribution in the air gap. However, as can also be seen from Fig. 2, the shape of the individual magnet segments are not polyhedral as is usually required for cheap manufacturing. Thus, a further simplification of the determined magnet design might be needed.

5. CONCLUSIONS

We have presented two methods for designing the optimum magnet. One method can be used to determine the optimal distribution of remanence that produces a desired magnetic field. The other method can segment a given magnet design into optimally shaped segments. The methods were used to segment a magnet design typically used for rotating magnetic refrigeration devices, and the field produced was characterized. The Λ_{cool} figure of merit was found to be significantly higher than previously reported values in literature.

ACKNOWLEDGMENTS

This work was financed by the ENOVHEAT project, which is funded by Innovation Fund Denmark (contract no 12-132673).

REFERENCES

- [1] A. Tura, A. Rowe, "Concentric Halbach cylinder magnetic refrigerator cost optimization", *International Journal of Refrigeration* **37**, 106 (2014).
- [2] R. Bjørk, C. R. H. Bahl, K. K. Nielsen, "The lifetime cost of a magnetic refrigerator", *International Journal of Refrigeration* **63**, 48 (2016).
- [3] P. V. Trevizoli, J. A. Lozano, G. F. Peixer, J. R. Barbosa Jr., "Design of nested Halbach cylinder arrays for magnetic refrigeration applications", *Journal of Magnetism and Magnetic Materials* **395**, 109 (2015).
- [4] J. Tušek, S. Zupan, A. Šarlah, I. Prebil, A. Poredoš, "Development of a rotary magnetic refrigerator", *International Journal of Refrigeration* **33**, 294 (2010).
- [5] R. Bjørk, C. R. H. Bahl, A. Smith, N. Pryds, "Improving magnet designs with high and low field regions", *IEEE Transactions on Magnetics* **47**, 1687 (2011).
- [6] R. Bjørk, C. R. H. Bahl, A. Smith, N. Pryds, "Review and comparison of magnet designs for magnetic refrigeration", *International Journal of Refrigeration* **33**, 437 (2010)
- [7] W.F. Brown, "Magnetostatic principles in ferromagnetism", North-Holland Publishing Company, Amsterdam (1962).
- [8] A. R. Insinga, R. Bjørk, A. Smith, C. R. H. Bahl, "Globally optimal segmentation of permanent magnet systems", submitted for publication in *Physical Review Applied* (2016).
- [9] N.I. Klepets, "Synthesis of magnetic systems producing field with maximal scalar characteristics", *Journal of Magnetism and Magnetic Materials*. **285**, 401 (2005).
- [10] N.I. Klepets, "Optimal design of magnetic systems", *Journal of Magnetism and Magnetic Materials* **306**, 281 (2006).
- [11] J. H. Jensen, M. G. Abele, "Maximally efficient permanent magnet structures", *Journal of Applied Physics* **79**, 1157 (1996).
- [12] D. Eriksen, K. Engelbrecht, C. R. H. Bahl, R. Bjørk, K. K. Nielsen, A. R. Insinga, N. Pryds, "Design and experimental tests of a rotary active magnetic regenerator prototype", *International Journal of Refrigeration* **58**, 14 (2015).

Bibliography

- [1] O. Gutfleisch, M. A. Willard, E. Brück, C. H. Chen, S.G. Sankar, and J.P. Liu, *Magnetic materials and devices for the 21st century: stronger, lighter, and more energy efficient*, *Adv. Mater.* **23** (7), 821-842, (2011).
- [2] R. W. McCallum, L. H. Lewis, R. Skomski, M. J. Kramer, and I. E. Anderson, *Practical Aspects of Modern and Future Permanent Magnets*, *Annu. Rev. Mater. Res.* **44** (1), 451-477, (2014).
- [3] H. R. Kirchmayr, *Permanent magnets and hard magnetic materials*, *J. Phys. D: Appl. Phys.* **29** (11), 2763-2778, (1996).
- [4] J. M. D. Coey, *Permanent Magnet Applications*, *J. Magn. Magn. Mater.* **248** (3), 441-456, (2002).
- [5] M. Katter, *Angular Dependence of the Demagnetization Stability of Sintered Nd-Fe-B Magnets*, *IEEE Trans. Magn.* **41** (10), 3853-3855, (2005).
- [6] J. Chavanne, O. Chubar, P. Elleaume, and P. Van Vaerenbergh, *Nonlinear numerical simulation of permanent magnets*, *Proc. EPAC Conf.*, 2316-2318, (2000).
- [7] L. Dupré, and J. Melkebeek, *Electromagnetic hysteresis modelling : from material science to finite element analysis of devices*, *International COMPUMAG Society Newsletter* **10** (3), 4-15, (2003).
- [8] J. Prat-Camps, A. Sanchez, and C. Navau, *Superconductor/ferromagnetic metamaterials for magnetic cloaking and concentration*, *Supercond. Sci. Technol.* **26** (7), 074001, 1-7, (2013).
- [9] J. Prat-Camps, C. Navau, and A. Sanchez, *Experimental realization of magnetic energy concentration and transmission at a distance by metamaterials*, *Appl. Phys. Lett.* **105** (23), 234101, 1-3, (2014).
- [10] *Rare-Earth Permanent Magnets Vacodym/Vacomax*, *Vacuumschmelze GMBH & Co, KG*, 1-72, (2014).
- [11] *Soft Magnetic Materials and Semi-finished Products*, *Vacuumschmelze GMBH & Co, KG.*, 1-30, (2002).
- [12] *Cast ALNICO Permanent Magnets*, *Arnold Magnetic Technologies Corp.*, (2003).
- [13] *Neodymium Sintered - Standard Grades*, *Bakker Magnetics*, (2014).
- [14] K. Binnemans, P. T. Jones, B. Blanpain, T. V. Gerven, Y. Yang, A. Walton, and M. Buchert, *Recycling of rare earths: a critical review*, *J. Clean Prod.* **51**, 1-22, (2013).
- [15] J. W. Darcy, H. M. Dhammika Bandara, B. Mishra, B. Blanpain, D. Apelian, and M. H. Emmert, *Challenges in Recycling End-of-Life Rare Earth Magnets*, *JOM* **65** (11), 1381-1382, (2013).

- [16] T. S. Jang, D. H. Lee, A. S. Kim, S. Namgung, H. W. Kwon, and D. H. Hwang, *Recovery of high coercivity of the powders obtained by crushing Nd-Fe-B sintered magnet scraps*, *Phys. Stat. Sol. (a)* **201** (8), 1794-1797, (2004).
- [17] K. Ding, *The Rare Earth Magnet Industry and Rare Earth Price in China*, *EPJ Web. Conf.* **75**, 04005, 1-3, (2014).
- [18] M. D. Kuz'min, K. P. Skokov, H. Jian, I. Radulov, and O. Gutfleisch, *Towards high-performance permanent magnets without rare earths*, *J. Phys. Condens. Matter* **26** (6), 064205, 1-5, (2014).
- [19] *Critical Materials Factsheet*, Center for Sustainable Systems, University of Michigan, Pub. No. CSS14-15 1-2, (2015).
- [20] P. M. Tlali, R. J. Wang, and S. Gerber, *Magnetic gear technologies: A review*, *IEEE Int. Conf. on Electr. Machines (ICEM)*, 544-550, (2014).
- [21] B. V. Jayawant, *Electromagnetic suspension and levitation*, *IEE Proc. Pt. A Reviews* **129** (8), 549-581, (1982).
- [22] D. Eaton, J. Rama, and S. Singhal, *Magnetic bearing applications & economics*, *IEEE Proc. Petroleum and Chemical Industry Conference (PCIC)*, 1-9, (2010).
- [23] J. Schönke, *Smooth Teeth: Why Multipoles Are Perfect Gears*, *Phys. Rev. Applied* **4** (6), 064007, 1-8, (2015).
- [24] J. Chell, and C. Zimm, *Permanent Magnet Assembly*, *US Patent 7148777 B2*, (2006).
- [25] C. Zimm, A. Boeder, J. Chell, A. Sternberg, A. Fujita, S. Fujieda, and K. Fukamichi, *Design and performance of a permanent-magnet rotary refrigerator*, *Int. J. Refrigeration* **29** (8), 1302-1306, (2006).
- [26] B. F. Yu, Q. Gao, B. Zhang, X. Z. Meng, and Z. Chen, *Review on research of room temperature magnetic refrigeration*, *Int. J. Refrigeration* **26** (6), 451-477, (2003).
- [27] A. Kitanovski, J. Tušek, U. Tomc, U. Plaznik, M. Ožbolt, and A. Poredoš, *Magnetocaloric Energy Conversion, From Theory to Applications*, *Springer*, (2015).
- [28] K. Yamazaki, and Y. Kanou, *Shape Optimization of Rotating Machines Using Time-Stepping Adaptive Finite Element Method*, *IEEE Trans. Magn.* **46** (8), 3113-3116, (2010).
- [29] L. Yan, I. M. Chen, C. K. Lim, G. Yang, W. Lin, and K. M. Lee, *Design and Analysis of a Permanent Magnet Spherical Actuator*, *IEEE/ASME Trans. Mechatron.* **13** (2), 239-248, (2008).
- [30] S. Applet, H. Kühni, F.W. Häsing, and B. Blümich, *Chemical analysis by ultrahigh-resolution nuclear magnetic resonance in the Earths magnetic field*, *Nat. Phys.* **2** (2), 105-109, (2006).
- [31] H. Zijlstra, *Permanent magnet systems for NMR tomography*, *Philips J. Res.* **40** (5), 259-288, (1985).

- [32] G. Moresi, and R. Magin, *Miniature permanent magnet for table-top NMR*, *Concepts Magn. Reson.* **19B** (1), 35-43, (2003).
- [33] P. Suominen, O. Tarvainen, H. Koivisto, and D. Hitz, *Optimization of the Halbach-type magnetic multipole for an electron cyclotron resonance ion source*, *Rev. Sci. Instrum.* **75** (1), 59-63, (2004).
- [34] S. Becker, M. Bussmann, S. Raith, M. Fuchs, R. Weingartner, P. Kunz, W. Lauth, U. Schramm, M. El Ghazaly, F. Grüner, H. Backe, and D. Habs, *Characterization and tuning of ultrahigh gradient permanent magnet quadrupoles*, *Phys. Rev. ST Accel. Beams* **12** (10), 102801, 1-7, (2009).
- [35] B. Biswas, *A magnetic quadrupole from rectangular permanent magnets*, *Nucl. Instrum. Meth. A* **605** (3), 233-242, (2009).
- [36] B. Diviacco, *Performance Optimization of Pure Permanent Magnet Undulators*, *Proc. IEEE Part. Accel. Conf.* **2**, 1590-1592, (1993).
- [37] G. Tosin, P. P. Sanchez, J. F. Citadini, and C. C. Vergasta, *Super hybrid quadrupoles*, *Nucl. Instrum. Meth. A* **674**, 67-73, (2012).
- [38] R. Baartman, *Quadrupole shapes*, *Phys. Rev. ST Accel. Beams* **15** (7), 074002, 1-8, (2012).
- [61] S. Cheng, and D. P. Arnold, *Optimization of Permanent Magnet Assemblies Using Genetic Algorithms*, *IEEE Trans. Magn.* **47** (10), 4104-4107, (2011).
- [40] R. Ravaut, G. Lemarquand, and V. Lemarquand, *Magnetic field created by a uniformly magnetized tile permanent magnet*, *Prog. Electromagn. Res. B* **24** 17-32, (2010).
- [41] C. K. Chandrana, J. A. Neal, D. Platts, B. Morgan, and P. Nath, *Automatic alignment of multiple magnets into Halbach cylinders*, *J. Magn. Mater.* **381**, 396-400, (2015).
- [42] L. Debnath, and P. Mikusinski, *Introduction to Hilbert Spaces with Applications*, 3rd Edition, *Academic Press*, (1990).
- [43] D. Maringer, *Heuristic Optimization, Portfolio Management with Heuristic Optimization*, *Springer*, 38-76, (2005).
- [44] P. Śolín, *Partial Differential Equations and the Finite Element Method*, *John Wiley and Sons*, (2005).
- [45] W. H. Press, S. A. Teukolsky, W. T. Vetterling, and B. P. Flannery, *Numerical Recipes, The Art of Scientific Computing*, 3rd Edition, *Cambridge University Press*, (2007).
- [46] Y. Sato, *Piecewise linear approximation of planar curves by perimeter optimization*, *Pattern Recognition* **25** (12), 1535-1543, (1992).
- [47] F. Bloch, O. Cugat, G. Meunier, and J. C. Toussaint, *Innovating approaches to the generation of intense magnetic fields : design and optimization of a 4 Tesla permanent magnet flux source*, *IEEE Trans. Magn.* **34** (5), 2465-2468, (1998).

- [48] M. Kumada, T. Fujisawa, Y. Hirao, M. Endo, M. Aoki, T. Kohda, Y. Iwashita, I. Bolshakova, and R. Holyaka, *Development of 4 tesla permanent magnet*, *IEEE Proc. 2nd Asian Particle Accelerator Conf.* **5**, 3221-3223, (2001).
- [49] C. C. Hwang, M. H. Wu, and S.P. Cheng, *Influence of pole and slot combinations on cogging torque in fractional slot PM motors*, *J. Magn. Magn. Mater.* **304** (1), e430-e432, (2006).
- [50] N. Bianchi, and S. Bolognani, *Design Techniques for Reducing the Cogging Torque in Surface-Mounted PM Motors*, *IEEE Trans. Ind. Appl.* **38** (5), 1259-1265, (2002).
- [51] H. A. Leupold, and E. Potenzianni II, *A Permanent Magnet Circuit Design Primer*, *Army Research Laboratory*, 1-65, (1996).
- [52] D.-K. Lim, K.-P. Yi, D.-K. Woo, H.-K. Yeo, J.-S. Ro, C.-G. Lee, and H.-K. Jung, *Analysis and Design of a Multi-Layered and Multi-Segmented Interior Permanent Magnet Motor by Using an Analytic Method*, *IEEE Trans. Magn.* **50** (6), 8201308, 1-8, (2014).
- [53] P. Liang, F. Chai, Y. Bi, Y. Pei, and S. Cheng, *Analytical model and design of spoke-type permanent-magnet machines accounting for saturation and nonlinearity of magnetic bridges*, *J. Magn. Magn. Mater.* **417**, 389-396, (2016).
- [54] L. Wu, and Z.-Q. Zhu, *Analytical Modeling of Surface-Mounted PM Machines Accounting for Magnet Shaping and Varied Magnet Property Distribution*, *IEEE Trans. Magn.* **50** (7), 8101511, 1-11, (2014).
- [55] T. Shi, Z. Qiao, C. Xia, H. Li, and Z. Song, *Modeling, Analyzing, and Parameter Design of the Magnetic Field of a Segmented Halbach Cylinder*, *IEEE Trans. Magn.* **48** (5), 1890-1898, (2012).
- [56] M. Markovic, and Y. Perriard, *Optimization Design of a Segmented Halbach Permanent-Magnet Motor Using an Analytical Model*, *IEEE Trans. Magn.* **45** (7), 2955-2960, (2009).
- [57] A. Sarwar, A. Nemirovski, and B. Shapiro, *Optimal Halbach Permanent Magnet Designs for Maximally Pulling and Pushing Nanoparticles*, *J. Magn. Magn. Mater.* **324** (5), 742-754, (2012).
- [58] J. S. Choi, J. Yoo, S. Nishiwak, and K. Izui, *Optimization of Magnetization Directions in a 3-D Magnetic Structure*, *IEEE Trans. Magn.* **46** (6), 1603-1606, (2010).
- [59] S. Lim, S. Jeongl, and S. Min, *Multi-Component Layout Optimization Method for the Design of a Permanent Magnet Actuator*, *IEEE Trans. Magn.* **52** (3), 7205304, 1-4, (2016).
- [60] E. Kuci, F. Henrotte, P. Duysinx, P. Dular, and C. Geuzaine, *Design Sensitivity Analysis for Shape Optimization of Nonlinear Magnetostatic Systems*, *IEEE Trans. Magn.* **52** (3), 9400904, 1-4, (2016).
- [61] S. Cheng, and D. P. Arnold, *Optimization of Permanent Magnet Assemblies Using Genetic Algorithms*, *IEEE Trans. Magn.* **47** (10), 4104-4107, (2011).

- [62] T. Sato, K. Watanabe, and H. Igarashi, *Multimaterial Topology Optimization of Electric Machines Based on Normalized Gaussian Network*, *IEEE Trans. Magn.* **51** (3), 7202604, 1-4, (2015).
- [63] S. Sato, T. Sato, and H. Igarashi, *Topology Optimization of Synchronous Reluctance Motor Using Normalized Gaussian Network*, *IEEE Trans. Magn.* **51** (3), 8200904, 1-4, (2015).
- [64] J. C. Mallinson, *One-sided fluxes - A magnetic curiosity?*, *IEEE Trans. Magn.* **9** (4), 678-682, (1973).
- [65] K. Halbach, *Design of permanent multipole magnets with oriented rare earth cobalt material*, *Nucl. Instrum. Methods* **169** (1), 1-10, (1980).
- [66] M. Pozzi, N. Mijatovic, and B. B. Jensen, *Topology Optimization of a High-Temperature Superconducting Field Winding of a Synchronous Machine*, *IEEE Trans. Appl. Supercond.* **23** (6), 51-56, (2013).
- [67] H. Polinder, J. A. Ferreira, B. B. Jensen, A. B. Abrahamsen, K. Atallah, and R. A. McMahon, *Trends in Wind Turbine Generator Systems*, *IEEE J. Sel. Topics Power Syst.* **1** (3), 174-185, (2013).
- [68] S. Högberg, F. B. Bendixen, N. Mijatovic, B. B. Jensen, and J. Holbøll, *Influence of Demagnetization-Temperature on Magnetic Performance of Recycled Nd-Fe-B*, *IEEE Proc. International Electric Machines Drives Conf. (IEMDC)*, 1242-1246, (2015).
- [69] M. Fasil, N. Mijatovic, B. B. Jensen, and J. Holbøll, *Performance Variation of Ferrite Magnet PMBLDC Motor With Temperature*, *IEEE Trans. Magn.* **51** (12), 1-6, (2015).
- [70] M. Fasil, C. Antaloae, N. Mijatovic, B. B. Jensen, and J. Holbøll, *Improved dq-axes Model of PMSM Considering Airgap Flux Harmonics and Saturation*, *IEEE Trans. Appl. Supercond.* **26** (4), 1-6, (2016).
- [71] T. T. Overboom, J. W. Jansen, E. A. Lomonova, and F. J. F. Tacke, *Design and Optimization of a Rotary Actuator for a Two-Degree-of-Freedom z - ϕ -Module*, *IEEE Trans. Ind. Appl.* **46** (6), 2401-2409, (2010).
- [72] K. J. Meessen, J. J. H. Paulides, and E. A. Lomonova, *Force Calculations in 3-D Cylindrical Structures Using Fourier Analysis and the Maxwell Stress Tensor*, *IEEE Trans. Magn.* **49** (1), 536-545, (2013).
- [73] R. Zanis, J. W. Jansen, and E. A. Lomonova, *Modeling and Design Optimization of A Shaft-Coupled Motor and Magnetic Gear*, *Actuators* **5** (1), 1-10, (2016).
- [74] W. F. Brown Jr., *Magnetostatic Principles in Ferromagnetism*, North-Holland Publishing Company, (1962).
- [75] J. D. Jackson, *Classical Electrodynamics*, 3rd Edition, John Wiley and Sons, (1998).
- [76] A. E. Fitzgerald, C. Kingsley Jr., S. D. Umans, and *Electric Machinery*, 6th Edition, McGraw-Hill, (2003).

- [77] J. L. Paulsen, J. Franck, V. Demas, and L.-S. Bouchard, *Least Squares Magnetic-Field Optimization for Portable Nuclear Magnetic Resonance Magnet Design*, *IEEE Trans. Magn.* **44** (12), 4582-4590, (2008).
- [78] Z. Haznadar, Ž. Štih, and S. Berberović, *The least square deviations criterion and inverse-source magnetostatic problems*, *Int. J. Appl. Electrom.* **15** (1), 207-212, (2002).
- [79] S. Bégot, E. Voisin, P. Hiebel, J. M. Kauffmann, and E. Artioukhine, *Resolution of linear magnetostatic inverse problem using iterative regularization*, *Eur. Phys. J. AP* **12** (2), 123-131, (2000).
- [80] N. I. Klevets, *Synthesis of magnetic systems producing field with maximal scalar characteristics*, *J. Magn. Magn. Mater.* **285** (3), 401-409, (2005).
- [81] N. I. Klevets, *Optimal design of magnetic systems*, *J. Magn. Magn. Mater.* **306** (2), 281-291, (2006).
- [82] M. G. Abele, and H. Rusinek, *Optimization of multilayered magnetic structures*, *J. Appl. Phys.* **73** (10), 5446-5448, (1993).
- [83] M. G. Abele, *Equivalent structures of permanent magnets and electric currents designed to generate uniform fields*, *J. Appl. Phys.* **75** (10), 6993-6995, (1994).
- [84] M. G. Abele, H. Rusinek, F. Bertora, and A. Trequattrini, *Compensation of field distortion with ferromagnetic materials and permanent magnets*, *J. Appl. Phys.* **75** (10), 6990-6992, (1994).
- [85] M. G. Abele, W. Tsui, and H. Rusinek, *Methodology of pole piece design in permanent magnets*, *J. Appl. Phys.* **99** (8), 08D903, 1-3, (2006).
- [86] J. H. Jensen, and M. G. Abele, *Maximally efficient permanent magnet structures*, *J. Appl. Phys.* **79** (2), 1157-1163, (1996).
- [87] M. G. Abele, *Linear theory of yokeless permanent magnets*, *J. Magn. Magn. Mater.* **83** (1-3), 276-278, (1990).
- [88] M. G. Abele, and H. Rusinek, *Optimum design of yokeless permanent magnets*, *J. Appl. Phys.* **67** (9), 4644-4646, (1990).
- [89] M. G. Abele, *Structures of permanent Magnets: Generation of Uniform Fields*, *John Wiley and Sons*, (1993).
- [90] P. Joshi, P. S. Williams, L. R. Moore, T. Caralla, C. Boehm, G. Muschler, and M. Zborowski, *Circular Halbach array for fast magnetic separation of hyaluronan-expressing tissue progenitors*, *Anal. Chem.* **87** (19), 9908-9915, (2015).
- [91] R. Bjørk, A. Smith, and C. R. H. Bahl, *Analysis of the magnetic field, force, and torque for two-dimensional Halbach cylinders*, *J. Magn. Magn. Mater.* **322** (1), 133-141, (2010).
- [92] R. Bjørk, C. R. H. Bahl, A. Smith, D. V. Christensen, and N. Pryds, *An optimized magnet for magnetic refrigeration*, *J. Magn. Magn. Mater.* **322** (21), 3324-3328, (2010).

- [93] R. Bjørk, C. R. H. Bahl, A. Smith, and N. Pryds, *Comparison of adjustable permanent magnetic field sources*, *J. Magn. Magn. Mater.* **322** (22), 3664-3671, (2010).
- [94] R. Bjørk, A. Smith, and C. R. H. Bahl, *The efficiency and the demagnetization field of a general Halbach cylinder*, *J. Magn. Magn. Mater.* **384** (22), 128-132, (2015).
- [95] R. Bjørk, *The magnetic properties of the hollow cylindrical ideal remanence magnet*, *J. Magn. Magn. Mater.* **416**, 321324, (2016).
- [96] R. Bjørk, C. R. H. Bahl, A. Smith, and N. Pryds, *Improving Magnet Designs With High and Low Field Regions*, *IEEE Trans. Magn.* **47** (6), 1687-1692, (2011).
- [97] R. Bjørk, C. R. H. Bahl, A. Smith, and N. Pryds, *Optimization and improvement of Halbach cylinder design*, *J. Appl. Phys.* **104** (1), 013910, 1-9, (2008).
- [98] R. Bjørk, C. R. H. Bahl, A. Smith, and N. Pryds, *Review and comparison of magnet designs for magnetic refrigeration*, *Int. J. Refrigeration* **33** (3), 437-448, (2010).
- [99] J. A. Lozano, K. Engelbrecht, C. R. H. Bahl, K. K. Nielsen, D. Eriksen, U. L. Olsen, J. R. Barbosa Jr., A. Smith, A.T. Prata, and N. Pryds, *Performance analysis of a rotary active magnetic refrigerator*, *Appl. Energy* **111**, 669-680, (2013).
- [100] A. Smith, C. R. H. Bahl, R. Bjørk, K. Engelbrecht, K. K. Nielsen, and N. Pryds, *Materials Challenges for High Performance Magnetocaloric Refrigeration Devices*, *Adv. Energy Mater.* **2** (11), 1288-1318, (2012).
- [101] R. Bjørk, and K. Engelbrecht, *The influence of the magnetic field on the performance of an active magnetic regenerator (AMR)*, *Int. J. Refrigeration* **34** (1), 192-203, (2011).
- [102] R. Bjørk, *Designing a magnet for magnetic refrigeration*, Ph.D. Thesis, Technical University of Denmark - DTU, (2010).
- [103] D. Eriksen, K. Engelbrecht, C. R. H. Bahl, R. Bjørk, K. K. Nielsen, A. R. Insinga, and N. Pryds, *Design and experimental tests of a rotary active magnetic regenerator prototype*, *Int. J. Refrigeration* **58**, 14-21, (2015).
- [104] A. R. Insinga, C.R.H. Bahl, R. Bjørk, and A. Smith, *Performance of Halbach magnet arrays with finite coercivity*, *J. Magn. Magn. Mater.* **407**, 369-376, (2016).
- [105] A. R. Insinga, R. Bjørk, A. Smith, and C.R.H. Bahl, *Globally Optimal Segmentation of Permanent-Magnet Systems*, *Phys. Rev. Applied* **5**, (6), 064014, 1-16, (2016).
- [106] A. R. Insinga, R. Bjørk, A. Smith, and C.R.H. Bahl, *Optimally segmented permanent magnet structures*, accepted for publication in *IEEE Trans. Magn.*, (2016).

